

School of Civil and Mechanical Engineering

**Development and Design of Non-corrosive Precast Dry Beam-
column Joints Containing Fibre-reinforced Polymer Composites**

Tang Tuan Ngo

ORCID: 0000-0002-7098-061X

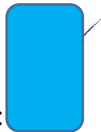
**This thesis is presented for the Degree of
Doctor of Philosophy
of
Curtin University**

September 2021

Declaration

To the best of my knowledge and belief, this thesis contains no material previously published by any other person except where due acknowledgement has been made.

This thesis contains no material which has been accepted for the award of any other degree or diploma in any university.

Signature:  (TANG TUAN NGO)

Data:21/9/2021.....

ABSTRACT

Beam-column joints play a vital role in the behaviours of moment-resisting frames. Lessons from various earthquakes have indicated that if the joints are damaged, the building may collapse, even though beams and columns remain intact. Most of the existing studies have focused on monolithic and wet joints due to their good performance in load-carrying capacity, stiffness, energy dissipation (ED), and ductility. However, there have been still some disadvantages in these joint types, such as longer construction time, higher construction cost, low-quality control, and more negative impacts on the environment, as compared to precast joints. For precast dry joints, beams and columns are cast in factories before they are assembled in construction sites. Therefore, the application of precast dry joints could effectively resolve the above disadvantages of the conventional monolithic joints. Nevertheless, the application of precast joints in practice is still limited compared to monolithic joints due to disadvantages related to strength, ductility, and corrosion resistance. For example, corrosion of the connecting elements may lead to deterioration or even destruction of the entire building. Additionally, the expenditure to maintain and repair deteriorated members in some circumstances can be incredibly more costly than the original new ones. Therefore, it is necessary to propose new precast dry joint types which can replace the conventional monolithic joints while satisfying the requirements for applications in non-seismic and seismic regions and requiring minimum maintenance to overcome corrosion-related deterioration.

Moreover, natural or man-made disasters can generate impact loading, which usually occur suddenly without any warnings. Rockfalls and landslides are two of many typical examples of these disasters which occur in many areas across the world due to various reasons such as erosion and earthquake. Rockfalls and landslides can destroy infrastructure and buildings, potentially costing millions of dollars per event. Surprisingly, there is still a lack of standards and design guides for concrete structures against impact loads, especially beam-column joints due to the inadequate studies and understanding of the structural performances under impact loads. The response and failure pattern of structures under impact loading are different from those under static and earthquake loads. Consequently, the current standards for static and earthquake loadings could not be applied to design structures against impact and blast loads. For

the above reasons, investigating the dynamic response of concrete structures including, beams, columns, and beam-column joints is deemed necessary.

Another challenging issue around the globe is the alarming increase of CO₂ emission from cement production due to the ever-growing demand for construction. CO₂ emission is also responsible for global warming which has negative effects on human health and our planetary ecology. Therefore, it is urgently needed to discover new “green” binders which could completely or partially replace the ordinary portland cement in construction. The application of geopolymer concrete (GPC) into the construction sector is a new trend attracting a growing amount of research and applications. The use of GPC to replace ordinary Portland concrete (OPC) offers numerous benefits including, but not limited to, reuse of industrial wastes, reduction of CO₂, excellent acid resistance, good bond strength between GPC and reinforcements, and high strength. Therefore, GPC is a so-called “green” material in the construction industry. It means GPC can effectively replace OPC to reduce industrial waste and carbon footprint releasing into the atmosphere while GPC members still satisfy structural requirements.

Recognising all the above challenging issues, the studies presented in this dissertation successfully developed new sustainable, durable and resilient precast concrete beam-column joints with excellent performance for use in both earthquake and non-earthquake regions. The newly developed joints provide numerous advantages that cannot be found in typical monolithic beam-column joints such as (1) faster construction, (2) better quality control, (3) easier replacement and repairing of damaged components, i.e., more resilient to adverse effects, (4) recycling industry by-product materials and (5) unsusceptible to corrosion damage. Various new and advanced materials were used in this new joint including GPC, fibre reinforced concrete (FRC) with synthetic and steel fibres, and fibre reinforced polymer (FRP) bolts and FRP rebars. The application of GPC in this project not only effectively reuse the industrial and residential wastes but also reduce CO₂ emission, therefore contributing to the development of sustainable and carbon-zero construction technology. Moreover, the use of FRP material can increase the life span of structures due to its durable and non-corrosive properties and reduce the lifecycle maintenance cost of the structure. There have been no such precast joints available in the market. The excellent performance of the newly developed joints has been experimentally,

numerically and analytically verified under normal structural design loads, as well as cyclic and impact loads. Hence, these newly proposed precast joint types can be used to replace the conventional monolithic joints in construction. To facilitate the practical application, analytical models and design procedures of the new joints have been also developed in this dissertation.

This dissertation consists of seven Chapters. An overview of research objectives, methodologies are presented in Chapter 1. A newly proposed dry joint for moment-resisting frames was investigated in Chapter 2. The exciting results indicated that the proposed dry joints showed better performances compared to the reference monolithic joint in terms of load-carrying capacity, energy dissipation, and stiffness. Therefore, the proposed dry joints can be plausibly applied to prefabricated constructions in non-seismic and seismic areas. To increase the shear and tensile resistances of the joints, steel rebars are often used but the number of rebars is limited due to the congestion in this location. Considering these issues, the use of FRC in these joints was investigated in Chapter 3 and demonstrated to be a good choice to significantly improve their performance. An analytical model to estimate the capacity of the proposed dry joint using OPC and FRC was also proposed in Chapter 3. Although the ambient-cured GPC and precast beam-column joints offer many advantages as mentioned previously, there are no studies investigating the performance of precast beam-column joints made of GPC in the literature yet. Therefore, the behaviour of ambient-cured GPC dry and monolithic joints was investigated in Chapter 4. A comprehensive design procedure of the GPC dry joint was also proposed in this chapter. In Chapter 5, numerical models using ABAQUS were built to further examine the performances of beam-column joints tested in Chapters 3 and 4. The influences of some parameters which could not be measured in experiments were investigated in Chapter 5. Finally, to offer more options for designers and users, a newly proposed hybrid joint using synthetic and steel fibres was proposed in Chapter 5. The application of synthetic and steel fibres significantly increased the capacities of the hybrid joints. Therefore, the use of hybrid joints could effectively resolve the disadvantage of dry joints related to a poorly architectural appearance. In Chapter 6, the impact performance of monolithic and proposed dry joints using GFRP bolts, GFRP reinforcements, and different fibre types subjected to pendulum impact was investigated. The proposed dry joints reinforced with fibres and GFRP bars showed better behaviour in terms of energy dissipation, reduced damage

level, and reduced maximum and residual displacement as compared to the monolithic joints. In addition, the application of GFRP reinforcements, GFRP bolts, synthetic fibres in both precast and monolithic joints effectively mitigates the corrosion while still satisfies design requirements in both strength and ductility. Finally, the new findings and recommendations for future studies are summarised in Chapter 7.

ACKNOWLEDGMENT

First and foremost, I want to express my deepest gratitude to my supervisors John Curtin Distinguished Professor Hong Hao and my co-supervisor Dr Thong Pham who have provided enlightening guidance, valuable advice, continuous support throughout my PhD candidature. I have enjoyed my PhD journey, and I learnt a lot from you.

Also, I would like to thank my wife, my mother, and my daughter, for their love and encouragement during these last three and half years. I would never have finished my PhD study without their encouragement and support in my academic life.

I would like to extend my acknowledge to VIED Scholarship, Curtin University and Quy Nhon University for the support for my full doctoral scholarship. Also, I want to thank the financial support from the Australian Research Council Laureate Fellowships FL180100196 for the funding of my experiments and other research involvement.

My gratitude is to A/Prof Duc Tung Doan, A/Prof Binh Ha Nguyen, A/Prof Giang Nguyen, A/Prof Ngoc My Do, and Prof Van Hoi Pham for believing in me and supporting me academically and personally to win a scholarship for my PhD study.

I also highly appreciate Mr Mario Guenette from Pultrall Inc, Mr Gary Goodall from BOSFA Pty Ltd, Mr Des Vlietstra from BarChip Pty Ltd, and Mr Greg Sieders from Bluey Pty Ltd for the material sponsorship. I deeply acknowledge the support of A/Prof De-Cheng Feng, Dr Tan D. Le, Dr Sajjad Sayyar Roudsari, and Dr Xian-Xing (Lambert) Li for the Umat code and guidance of ABAQUS.

Lastly, I would like to thank my friends and PhD peers, Dr Tung Tran, Dr Cheng Yuan, Dr Tan D. Le, Mr Emad Pournasiri, Dr Huawei Li, Mr Jhutan Kuri, Mr Nhi Vo, Mr Duong Tran, and Mr Zhixing Li who helped me a lot during the process of my experimental tests.

LIST OF PUBLISHED WORK

This thesis contains the accepted papers and submitted manuscript which are rearranged to form this dissertation, as outlined below.

Chapter 2

Ngo TT, Pham TM, Hao H. Ductile and dry exterior joints using CFRP bolts for moment-resisting frames. Structures 2020;28:668-84.

<https://doi.org/10.1016/j.istruc.2020.09.020>

Chapter 3

Ngo TT, Pham TM, Hao H. Effects of steel fibres and prestress levels on behaviour of newly proposed exterior dry joints using SFRC and CFRP bolts. Eng Struct 2020;205:110083.

<https://doi.org/10.1016/j.engstruct.2019.110083>

Chapter 4

Ngo TT, Tran TT, Pham TM, Hao H. Performance of geopolymer concrete in monolithic and non-corrosive dry joints using CFRP bolts under cyclic loading. Compos Struct 2020:113394.

<https://doi.org/10.1016/j.compstruct.2020.113394>

Chapter 5

Ngo TT, Pham TM, Hao H, Wensu C, Ngoc San H. Experiment and numerical study on newly proposed dry and hybrid concrete joints with GFRP bolts and GFRP reinforcements under cyclic loading. 2021 (*Responding to reviewers' comments*).

Chapter 6

Ngo, TT, Pham TM, Hao H, Chen W, Elchalakani M. Performance of monolithic and dry joints with GFRP bolts reinforced with different fibres and GFRP bars under impact loading. Eng. Struct 2021;240:112341.

<https://doi.org/10.1016/j.engstruct.2021.112341>

STATEMENT OF CONTRIBUTION OF OTHERS

This project was initiated by Prof Hong Hao and Dr Thong Pham who significantly helped the candidate define the overall scope, objective and methodology for the project. The research works presented in this dissertation were primarily carried out by the PhD candidate, Mr Tang Tuan Ngo, including the literature review, design of the specimens and test setup, preparation of specimens, doing the tests, analysing and interpreting experimental results, developing numerical models, proposing new analytical models for the proposed precast joints, and preparing the first drafts of manuscripts. Dr Thong Pham and Prof Hong Hao then provided additional intellectual input in the discussions of the results and revised the manuscript. Dr Thanh Tung Tran, Dr Wensu Chen, and Dr Mohamed Elchalakani supported Mr Tang Tuan Ngo in the experimental process in Chapters 4 and 6. Dr Ngoc San Ha helped to validate the results of the numerical model with the testing data in Chapter 5. The steel fibres, synthetic fibres, GFRP reinforcements, and GFRP bolts, which were used for the experiments reported in Chapters 5 and 6, were sponsored by BOSFA Pty Ltd, BarChip Pty Ltd, Pultrall Inc, and Bluey Pty Ltd, respectively. The financial support was provided by the Australian Research Council Laureate Fellowships FL180100196. The signed contribution forms are attached in the appendix.

LIST OF RELEVANT ADDITIONAL PUBLICATIONS

The additional publications during my PhD candidature, which are relevant to the dissertation but not forming part of it with the bibliographical details are listed below.

Award for excellence

Pham TM, **Ngo TT**, Hao H. Award for excellence in Technology and Innovation for developing a new sustainable and resilient precast concrete beam-column joint type from the concrete institute of Australia (2021).

Journal papers

1. Li H, Chen W, Huang Z, Hao H, **Ngo TT**, Pham TM, Yeoh KJ. Dynamic response of monolithic and precast concrete joint with wet connections under impact loads. (*Accepted for publication in Engineering Structures*).
2. Li H, Chen W, Huang Z, Hao H, **Ngo TT**, Pham TM. Dynamic response of beam-to-column joint subjected to different impact scenarios. 2021 (*Under review*).
3. Tran TT, Pham TM, Huang Z, Chen W, **Ngo TT**, Hao H, Elchalakani M. Effect of fibre reinforcements on shear capacity of geopolymer concrete beams subjected to impact loads. 2021 (*Accepted for publication in International Journal of Impact Engineering*).

Conference proceeding papers

1. **Ngo, TT**, Pham TM, and Hao H (2021). Performance of monolithic and precast dry beam-column joints using GFRP bolts and GFRP reinforcements under impact loading. *24th International Conference on Composite Structures (ICCS24)*. Porto, Portugal.
2. Pham, TM, **Ngo TT**, Hao H, and Tran, TT (2021). Investigation of ambient-cured GPC dry and monolithic beam-column joints using CFRP bolts under cyclic loading. *Concrete 2021*. Perth, WA, Australia.
3. Tran, TT, Pham TM, **Ngo TT**, and Hao H (2021). Fibre-reinforced ambient-cured geopolymer concrete for sustainable and resilient structures: from experiment to analytical predictions. *Concrete 2021*. Perth, WA, Australia.

4. **Ngo, TT**, Pham TM, and Hao H (2019). Use of CFRP bolts in dry beam-column joints for sustainable prefabrication constructions. *APFIS2019*. Surfers Paradise, Gold Coast, Australia.

5. Hao, H, **Ngo TT**, and Pham TM (2019). Performance of dry exterior beam-column joints using CFRP bolts and SFRC under cyclic loading. *Australian Earthquake Engineering Society 2019 Conference*. Newcastle, NSW, Australia.

Industrial project

Bi, K, Pham TM, Zuo H, and **Ngo TT** (2020). Laboratory test of an altCONNECT frame. For Yenem engineering services. Curtin University.

TABLE OF CONTENTS

ABSTRACT	3
ACKNOWLEDGMENT	7
LIST OF PUBLISHED WORK	8
STATEMENT OF CONTRIBUTION OF OTHERS	9
LIST OF RELEVANT ADDITIONAL PUBLICATIONS	10
TABLE OF CONTENTS	12
LIST OF FIGURES	16
LIST OF TABLES	21
CHAPTER 1: INTRODUCTION	23
1.1 Background	23
1.2 Research objectives	29
1.3 Research outlines	30
ABSTRACT	33
2.1 Introduction	34
2.2 Experimental program.....	36
2.2.1 Design of the specimens.....	37
2.2.2 Mechanical properties of materials	39
2.2.3 Specimen preparation and test setup.....	41
2.2.4 Experimental results and discussion	42
2.3 Analytical calculations	62
2.4 Summary	69
CHAPTER 3: EFFECTS OF STEEL FIBRES AND PRESTRESS LEVELS ON BEHAVIOUR OF NEWLY PROPOSED EXTERIOR DRY JOINTS USING SFRC AND CFRP BOLTS	71
ABSTRACT	71

3.1 Introduction	72
3.2 Experimental program.....	75
3.2.1 Design of the specimens.....	75
3.2.2 Mechanical properties of materials	78
3.2.3 Test setup	79
3.2.4 Experimental results and discussion	81
3.3 Analytical calculations	98
3.3.1 Failure at fixed-end	99
3.3.2 Failure in the middle zone.....	100
3.4 Summary	103
CHAPTER 4: PERFORMANCE OF GEOPOLYMER CONCRETE IN MONOLITHIC AND NON-CORROSIVE DRY JOINTS USING CFRP BOLTS UNDER CYCLIC LOADING.....	105
ABSTRACT.....	105
4.1 Introduction.....	106
4.2 Experimental program and analytical calculations	109
4.2.1 Design of the experimental specimens.....	109
4.2.2 Mechanical properties of materials	110
4.2.3 Test setup	113
4.2.4 Analytical model to estimate the maximum applied loads and the main failure position	115
4.2.5 Experimental results and discussion	121
4.2.6 Verification of predicted results.....	136
4.3 Summary	137
CHAPTER 5: EXPERIMENT AND NUMERICAL STUDY ON NEWLY PROPOSED DRY AND HYBRID CONCRETE JOINTS WITH GFRP BOLTS AND GFRP REINFORCEMENTS UNDER CYCLIC LOADING.....	139
ABSTRACT.....	139

5.1 Introduction	140
5.2 Experimental program.....	143
5.2.1 Details of beam-column joints	144
5.2.2 Test setups	148
5.2.3 Material properties	150
5.3 Experimental results and discussion	152
5.3.1 Global performances and failure modes	152
5.3.2 Hysteretic responses.....	158
5.3.3 Energy dissipation capacity.....	160
5.3.4 Drift ratio and maximum applied loads	162
5.4. Numerical simulation with ABAQUS software.....	165
5.4.1 Description of the finite element model.....	165
5.4.2 Effect of concrete-end-plate thickness	174
5.5 Summary	179
CHAPTER 6: PERFORMANCE OF MONOLITHIC AND DRY JOINTS WITH GFRP BOLTS REINFORCED WITH DIFFERENT FIBRES AND GFRP BARS UNDER IMPACT LOADING	181
ABSTRACT.....	181
6.1. Introduction	182
6.2 Experimental program.....	185
6.2.1 Details of beam-column joints and test setup	185
6.2.2 Pendulum impact system and data acquisition system	188
6.2.3 Material properties	191
6.3 Experimental results and discussion	193
6.3.1 Comparisons between monolithic joint and proposed dry joint.....	193
6.3.2 Effects of fibres and different kinds of fibres	208
6.4 Summary	217
CHAPTER 7: CONCLUSIONS AND RECOMMENDATIONS	220

7.1 Findings.....	220
7.2 Recommendation for future works.....	223
References	224
APPENDIX I: FIGURES IN CHAPTER 6	234
APPENDIX II: STATEMENTS OF CONTRIBUTION OF CO-AUTHORS .	241
APPENDIX III: COPYRIGHT CLEARANCE	243
BIBLIOGRAPHY DISCLAIMER	245

LIST OF FIGURES

Fig. 1-1 Comparison of CO ₂ footprint intensities between eight concrete types [37].	27
Fig. 1-2. Summary of different tests performed in the main chapters.	32
Fig. 2-1. Design of the monolithic and dry precast joints (in millimeter).	37
Fig. 2-2. Details of the reinforcements, strain gauges, aluminium bars, formworks, and plastic tubes.	38
Fig. 2-3. Details of strain gauges and load cells.	40
Fig. 2-4. A typical test setup.	41
Fig. 2-5. Loading history.	42
Fig. 2-6. Failure modes.	43
Fig. 2-7. Strain of longitudinal reinforcement (a) and on concrete (b).	45
Fig. 2-8. Load versus strain of the strain gauges in the aluminium bars.	46
Fig. 2-9. Force path and cause of inclined cracks.	48
Fig. 2-10. Load-displacement hysteretic responses of tested specimens.	49
Fig. 2-11. Envelopes of hysteretic curves of all the specimens.	50
Fig. 2-12. Definitions of the yield displacement and the ultimate displacement.	53
Fig. 2-13. Energy dissipation curves of the tested specimens.	55
Fig. 2-14. Equivalent viscous damping ratio curves of the tested specimens.	57
Fig. 2-15. Hysteretic energy dissipation and effective stiffness for cyclic response.	58
Fig. 2-16. Comparison of peak to peak stiffness.	58
Fig. 2-17. The progressive failure process.	59
Fig. 2-18. Opening of joints at the top and bottom surface of the concrete-end-plate.	61
Fig. 2-19. The failure of CFRP bolts when being prestressed with a high level using a torque wrench.	61
Fig. 2-20. Bolt forces at the top and bottom zone of the concrete-end-plate.	62
Fig. 2-21. Definition of the effective joint area.	65

Fig. 2-22. Global equilibrium of exterior joints.....	66
Fig. 2-23. Comparisons between the experiments and analytical results.	68
Fig. 2-24. Variations between the experiments and analytical results.....	68
Fig. 3-1. Designs of the precast specimen (left) and monolithic specimen (right) (unit: mm).	76
Fig. 3-2. Details of the reinforcements.	77
Fig. 3-3. Positions of load cells on the bolts and strain gauges on the concrete-end-plate.	78
Fig. 3-4. Details of the test setup.	80
Fig. 3-5. Cyclic loading history.	80
Fig. 3-6. Hysteretic load-drift ratio relationship of test specimens.....	82
Fig. 3-7. Load-drift ratio envelopes of all the specimens.	83
Fig. 3-8. Load versus strain of (a) the concrete-end-plate and (b) longitudinal reinforcements.....	84
Fig. 3-9. Failure patterns.....	85
Fig. 3-10. Explaining the cause of inclined cracks.	87
Fig. 3-11. Strain of the strain gauges on the aluminium bars.	88
Fig. 3-22. Average load-carrying capacity and the corresponding drift ratio.....	92
Fig. 3-13. Definition of the yielding point.	94
Fig. 3-14. Comparison of energy dissipation capacity.	96
Fig. 3-15. Effective stiffness and energy dissipation under cyclic loads.....	96
Fig. 3-16. Comparison of the effective stiffness.....	97
Fig. 3-17. Global equilibrium of an exterior joint.	99
Fig. 3-18. Tensile forces of the top and bottom bolts.	102
Fig. 3-19. Comparisons between the experimental and analytical results.	103
Fig. 4-1. Positions of load cells and LVDTs.....	109
Fig. 4-2. Design of (a) monolithic joint and (b) dry joint (unit: mm).....	110
Fig. 4-3. Details of CFRP bolts (unit: mm).	111

Fig. 4-4. Details of the test setup.	114
Fig. 4-5. Cyclic loading scheme.	115
Fig. 4-6. Definition of the effective joint area.	117
Fig. 4-7. Global equilibrium of the monolithic joint.	117
Fig. 4-8. Global equilibrium of the proposed precast joint.....	118
Fig. 4-9. Crack patterns.....	122
Fig. 4-10. Data of strain gauges on longitudinal rebars of beams and columns.	123
Fig. 4-11. Progressive development of cracks.	124
Fig. 4-12. Strain of aluminium bars embedded inside of concrete to measure concrete strain.....	125
Fig. 4-13. Arrangement of rebars in the concrete-end-plate.....	127
Fig. 4-14. Comparison of hysteretic load-drift ratio responses.	128
Fig. 4-15. Comparison of energy dissipation capacity.	129
Fig. 4-16. Load-drift ratio envelope curves.	130
Fig. 4-37. Comparison of average load-carrying capacity and drift ratio.....	132
Fig. 4-18. Method to determine the yielding point and failure point.....	134
Fig. 4-19. Tensile forces of CFRP bolts.	136
Fig. 5-1. Dimensions of the monolithic joint (a), hybrid joint (b), and dry joint (c) (unit: mm).	145
Fig. 5-2. 3D-views of the newly proposed hybrid joint.....	146
Fig. 5-3. Details of reinforcements, shear keys, and formworks.	147
Fig. 5-4. Setup for applying prestress to GFRP bolts.	148
Fig 5-5. Typical test setup of hybrid joints.	149
Fig 5-6. Loading history.	149
Fig. 5-7. Details of (a) GFRP bolts and (b) GFRP spiral stirrups.....	151
Fig. 5-8. Failure modes.	153
Fig. 5-9. Data of strain gauges attached on (a) longitudinal reinforcements and (b) stirrups at middle joints.....	155

Fig. 5-10. Hysteretic responses of all the specimens.	159
Fig. 5-11. Envelope curves of the tested specimens.	160
Fig. 5-12. Energy dissipation of all the specimens.	162
Fig. 5-13. Comparison of peak load and drift ratio.	163
Fig. 5-14. Main components of the dry and hybrid joints; (a & b) dry joint, (c) hybrid joint, (d) monolithic joint.	166
Fig. 5-15. The effects of compression-softening on reinforced concrete [55].	167
Fig. 5-16. Comparison of hysteretic and envelope curves between experiment and numerical simulation results.	171
Fig. 5-17. Comparison of failure modes between experiment and numerical simulation of Specimens D6-GR-S-T100 (a-b), M2-GR (c-d), and H4-GR-T100 (e-f) at the peak load.	173
Fig. 5-18. Tensile stress in GFRP reinforcements: (a) dry joint and (b) monolithic joint.	173
Fig. 5-19. Shear stress distribution on dry joints with different CEP thickness.	176
Fig. 5-20. Principal compressive stress flow.	177
Fig. 5-21. Comparison of the peak load and drift ratio.	178
Fig. 6-1. Details of monolithic specimen (Left) and precast specimen (Right) (unit: mm).	187
Fig. 6-2. Details of reinforcements, shear keys, and the test specimens.	187
Fig. 6-3. Setup for applying prestress for GFRP bolts.	188
Fig. 6-4. Test setup for pendulum impact tests.	190
Fig. 6-5. Impact velocity in the tests.	190
Fig. 6-6. Photos of (a) StFs; (b) SyFs; (c) GFRP bolts and nuts; and (d) GFRP spiral stirrups.	192
Fig. 6-7. Typical impact responses of joints with 3-stage classification at the impact point.	194
Fig. 6-8. Beam lateral displacement of (a) Specimens M1-NF and (b) P4-NF at 2.5 m/s impact.	195

Fig. 6-9. Comparison of damage modes (Specimens M1-NF vs P4-NF; Impact loading vs cyclic loading).	198
Fig. 6-10. Strain of longitudinal reinforcements on the beams of Specimens M1-NF and P4-NF.	201
Fig. 6-11. Impact force-time histories of Specimens (a) M1-NF and (b) P4-NF. ...	203
Fig. 6-12. Impact forces and reaction forces of Specimens (a) M1-NF and (b) P4-NF.	204
Fig. 6-13. Displacement-time histories of Specimens (a) M1-NF and (b) P4-NF...	205
Fig. 6-14. Definition of three types of energy.	207
Fig. 6-15. Energy comparison of Specimens M1-NF and P4-NF.	208
Fig. 6-16. Damage modes of the monolithic specimens.....	211
Fig. 6-17. Damage modes of the precast specimens.....	212
Fig. 6-18. Impact forces of Specimen M3-1StF-35.	213
Fig. 6-19. Impact forces of two precast joints with fibres (a) P5-1SyF-48 and (b) P6-1StF-35.....	214
Fig. 6-20. Displacement-time histories of Specimens (a) M2-1SyF-48, (b) P5-1SyF-48, and (c) P6-1StF-35.	216
Fig. 6-21. Energy dissipation comparison of Specimens M2-1SyF-48, P5-1SyF-48, and P6-1StF-35.	217
Fig. 6-A1. Crack development of Specimens M1-NF and P4-NF at 2.5 m/s and 3.3 m/s.....	236
Fig. 6-A2. Crack development of Specimen M3-1StF-35.....	237
Fig. 6-A3. Crack development of Specimens P5-1SyF-48 and P6-1StF-35.....	240

LIST OF TABLES

Table 1. Comparison between different joint types	25
Table 2-1. Steel reinforcements and aluminium bars properties.	39
Table 2-2. Properties of CFRP bolts, nuts and plates.....	39
Table 2-3. Load-carrying capacity and drift ratios of all the tested specimens.....	52
Table 2-4. Displacement and ductility of all the tested specimens.	54
Table 2-5. The values of V_{jmax} from the experiment and V_n in the standards.....	68
Table 3-1. Steel reinforcements and aluminium bars properties.	79
Table 3-2. Details of CFRP bolts, nuts, and plates [76].	79
Table 3-3. Details of load-carrying capacities with corresponding drift ratios.....	91
Table 3-4. Displacement and ductility of all the tested specimens.	94
Table 3-5. The comparisons of P_{max} between the experiment and analytical model.	102
Table 4-1. Mixture proportions of 1 m ³ GPC and OPC.	112
Table 4-2. Chemical compositions of FA and GGBFS.	112
Table 4-3. Rebar properties.	113
Table 4-4. Details of CFRP bolts and nuts [76].	113
Table 4-5. The comparisons between the experimental and theoretical results of P_{max} and V_{jh}	121
Table 4-6. Maximum applied loads with corresponding DRs.....	131
Table 4-7. Ductility of tested specimens.	133
Table 5-1. Specimen design.	144
Table 5-2. Mixture proportions of 1 m ³ plain concrete [149] and filled concrete...	150
Table 5-3. Properties of GFRP bolts and nuts [150].	151
Table 5-4. Mechanical properties of GFRP reinforcements [151].	151
Table 5-5. Description of specimens built on ABAQUS.	175
Table 6-1. Descriptions of the prepared specimens.....	185

Table 6-2. GFRP reinforcement properties.	191
Table 6-3. Details of two types of fibres.	192
Table 6-4. Details of GFRP bolts and nuts.....	193

CHAPTER 1: INTRODUCTION

1.1 Background


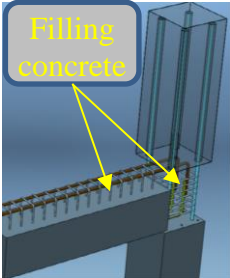
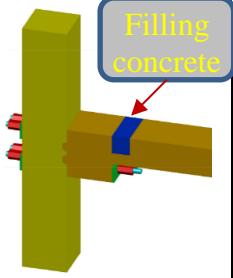
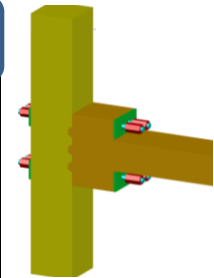
Beam-column joints play a crucial role in reinforced-concrete (RC) structures under earthquake loading because they support adjacent members such as beams and columns and maintain the structures' integrity [1]. There are two types of beam-column joints including conventional monolithic and precast joints. The precast joints can be categorized into three main types including dry, wet, and hybrid joints. The beams and columns in dry joints are completely cast in the factories and they are delivered to the construction site for assembling so no formwork is required. Bolts and tendons are often used to connect precast beams to precast columns. Although most parts of the beams and columns in wet joints are also cast in the factories, concrete needs to be filled into the joint area after the assembling process. The formwork and scaffold are required until the filled concrete can resist the load. Hybrid joints lay in between wet and dry joints. The concrete also needs to be filled but without or requires only simple formwork. It is because the filling concrete in hybrid joints can resist the load after the assembling process. The comparisons between these joint types are presented in Table 1. Recently, dry and hybrid beam-column joints in precast concrete structures attract increasing interest because these joint types offer various benefits such as shorter construction time, lower construction cost, easier control of construction quality, less environmental impact, more effective applications of the new technologies and materials (e.g., 3D-printing, geopolymer, and fibre reinforced concrete), and easier replacing and recycling of damaged components toward resilient structures [2], compared to the conventional monolithic joints. Nevertheless, the application of dry and hybrid joints in practice is still limited, compared to monolithic joints. Beams and columns in precast structures are cast separately in factories before they are delivered to the construction site for assembly. Strength, ductility, drift ratio (DR) and energy dissipation capacity of precast joints are often lower than those of the monolithic joints owing to discontinuity of concrete and reinforcement in the precast joints. In addition, the connecting components in the conventional precast joints (e.g., steel bolts, tendons, and plates) might not be properly protected against corrosion. Therefore, it may cause deterioration or even collapse of the buildings, especially when the building is located near the sea [3]. For example, According to Koch et al. [4], \$8.3

billion is the annual costs of corrosion for highway bridges in the USA, including maintenance costs for replacing structurally deficient bridges (\$3.8 billion), for concrete bridge decks (\$2.0 billion), for concrete substructures (\$2.0 billion), and for painting of steel bridges (\$0.5 billion). In some circumstances, the cost of maintenance and repairing of damaged components can be higher than that of making new ones [5, 6]. Recognising the above advantages and disadvantages of precast joints, this dissertation proposed new precast joints which can utilise full advantage of precast joints while effectively resolving their disadvantages. The proposed precast joints in this dissertation consist of the following innovations:

Excellent performance for use in seismic-prone regions: Most of the current studies on the beam-column joints have concentrated on the monolithic and wet joints owing to their good performances [7-9]. There have been a limited number of studies investigating dry joints in the literature. A few studies [10-12] examined the dry joints under cyclic loading using unbonded steel tendons to connect beams and columns. Other studies used steel bolts to connect the beams and columns in the dry joints [13, 14]. Many of these studies showed undesirable behaviours in terms of the load-carrying capacity, drift ratio, and energy absorption capability, compared to monolithic joints. This dissertation developed the dry joint type using concrete-end-plates (CEP) and bolts which was previously proposed in a big project called “US-PRESSS” of the USA in 1990s but was discarded since then due to its poor behaviours, i.e., could not meet the seismic design requirements. That project included two main phases and its results were reported in Saqan [14] dissertation and journal paper [15], in which some precast joint types were proposed and experimentally investigated. The dry joint with CEP and bolts in the study showed poor performances, compared to other precast joint types. For example, DR of the dry joint in that project [14] was only 1.5% which was lower than the minimum requirement of various standards, such as ACI T1.1-01 [16] (3.5%), CSA A23.3-07 [17] (2.5%), and ASCE 41-06 [18] (2%), for earthquake resistance designs. For many years, there has been no progress on the development of this type of dry joint. This dissertation identifies the shortcomings of the dry joints investigated in [14], suggests improvements for it to meet the seismic resistance design requirements such as changing the scale of CEP thickness, using steel spiral in CEP, and applying different fibre types (steel and synthetic fibres). Furthermore, to overcome the sustainability and durability problem, the performances of using

geopolymer concrete to replace Portland cement concrete, and use FRP bars and bolts to replace steel bars and bolts in construction of the dry joints are also investigated. To improve the constructability and aesthetic view of the large bulky concrete end plate, hybrid joint is also proposed. The newly proposed precast joints (i.e., dry and hybrid joints) showed excellent performances and can be effectively applied in seismic-prone areas.

Table 1. Comparison between different joint types

Parameters	Monolithic joints	Wet joints	Hybrid joints	Dry joints
Cast location	Construction site	Factory and construction site	Factory (mostly) and construction site (some)	Factory
Formwork and scaffold	Yes	Yes	No	No
Longitudinal rebars of the beam to column	Continuous	Continuous	Discontinuous	Discontinuous
Construction time on site	Highest	>	>	Lowest
Tensile resistance	Longitudinal rebars	Longitudinal rebars	Bolts, tendons	Bolts, tendons
Illustration				

Cite of figures	[19]	[20]	[21]	[21]
-----------------	------	------	------	------

Application of sustainable GPC to reduce CO₂ emission: The application of GPC into the construction sector is an emerging trend which has attracted a growing number of studies and applications. Due to the significantly increasing construction demand, the alarming increase of CO₂ emission from cement manufacturing was reported in various previous studies [22-24]. As an estimation, if there is no effective strategy to reduce the CO₂ emission from the global cement industry, 2.34 billion tons of CO₂ will be released into the atmosphere by 2050 [22]. Therefore, the use of GPC to replace ordinary Portland concrete (OPC) can potentially reduce carbon footprint (See Fig. 1-1) and bring various benefits including, but not limited to, significant recycling of industrial wastes [24], excellent acid resistance [25], good bond strength between GPC and reinforcements [26], and high flexural strength [27]. However, despite the obvious advantages of GPC, the use of GPC in construction is still scarce owing to a lack of design standards. Most of existing studies focused on optimising GPC mixture design while little has been conducted to investigate structural responses of GPC structures, especially beam-column joints. Xie et al. [28] proposed that GPC with 50% slag, 50% fly ash and 0.5 water/binder ratio could be an optimal mixture in terms of mechanical behaviours and workability. Wang et al. [29] and Rafeet et al. [30] indicated that the mechanical properties of GPC including compressive strength and elastic modulus could be improved when increasing the slag/fly ash ratio. In addition, most of existing studies investigated the mechanical properties of heat-cured GPC since it offered less creep and drying shrinkage, higher compressive strength and bond strength, better resistance in acid and sulphate environments when compared to ambient-cured GPC [31, 32]. For instance, Wang et al. [29] suggested that GPC components should be cured under 80 °C for 12-24 hours to achieve good mechanical properties. Meanwhile, the evidence about the performance of GPC structures are still insufficient and sometimes contradictory. For instance, Nguyen et al. [33] and Visintin et al. [34] claimed that the current standards of OPC could be applied to design the GPC beams and columns because the performances of heat-cured GPC and OPC beams and columns were relatively similar. Nevertheless, some recent studies [35, 36] suggested an opposite observation that the strength of ambient-cured and over-reinforced GPC

beams and columns was overestimated by conventional sectional analysis procedures. In addition, no previous studies investigated the performance of GPC precast joints and no analytical models were proposed to estimate the capacity of monolithic and precast joints in the existing literature. Recognising the above gaps in the literature, this dissertation [24] investigated the performances of both GPC monolithic and precast joints and further proposed an analytical model to predict the load-carrying capacity of these joint types.

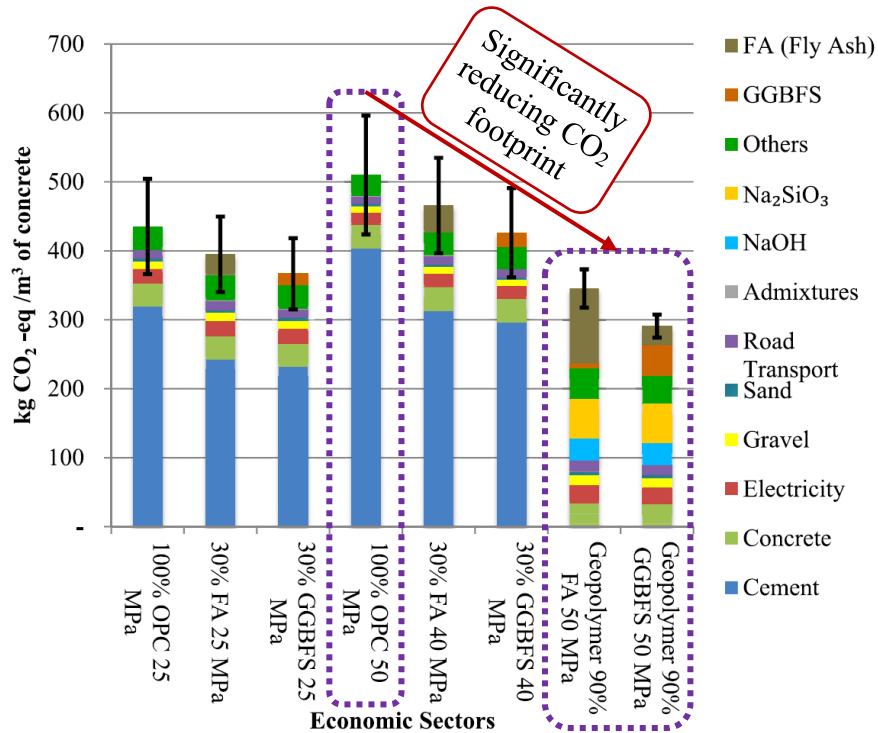


Fig. 1-1 Comparison of CO₂ footprint intensities between eight concrete types [37].

Use of fibre reinforced concrete to improve ductility: In addition, high ductility in the beam-column joints is a desirable property to avoid brittle failure of structures. It was observed in many earthquakes that failures of the beam-column joints could cause the collapse of the building even though no damage occurred on the beams and columns [19, 38, 39]. Therefore, improving the ductility of the beam-column joints, especially in GPC components due to the brittleness of GPC is essential to ensure the application of joints. In addition, numerous studies [40-44] indicated that shear and tensile stresses in the joint areas may cause brittle failure in beam-column joints. This brittle shear failure results in various serious consequences since it often occurs suddenly without any warnings before the total collapse of buildings [1, 45]. Various recent devastating earthquakes across the world demonstrated this dangerous brittle failure, such as the

1995 Hyogo-ken (Japan), the 1999 Kocaeli (Turkey), and the 1999 Chi-Chi (Taiwan) earthquakes. To deal with the above issues, different fibre types (e.g., steel and synthetic fibres) were applied in the studies of this dissertation [2, 21, 46]. The specification and dosage of fibres are critical to obtaining excellent behaviours of structures. The fibre specification in these studies was chosen based on its pull-out behaviour and rupture strength while the optimal fibre dosage was selected to achieve maximum capacity and energy absorption. As a result, the proposed precast beam-column joints using OPC and GPC with fibres showed excellent performances in terms of ductility, peak load, energy dissipation, and DR. For example, DR of the proposed precast joints reached 3.5% satisfying various standards (e.g., CSA A23.3-07 [17], ASCE 41-06 [18], and ACI T1.1-01 [16]) for structures in earthquake-prone regions.

Excellent impact resistance: Recent years also witnessed increasing attention to investigating structural response under impact loading. Structures which are attacked by impact forces usually suddenly collapse without any warnings bringing deadly threats to human beings. For example, due to landslides, rockfalls, and debris flow runouts, Australia lost approximately 82 million dollars and at least 138 human lives between the period of 1842 and 2011 [47]. Although impact force due to natural disasters causes serious consequences, there have been no standards for structural designs against impact loads. Unfortunately, the current standards for structures under static and seismic loads could not be used to design structures under impact loading since different loading rates may induce different failure modes. For example, shear stress causes severe damage under impact loads while flexural cracks govern the main failure of the identical beam under static loads [48-50]. Therefore, it is crucial to understand and accurately predict the dynamic responses of structures under impact loads. For beam-column joints under impact and blast loads, only two studies [51, 52] that conducted experiments to investigate dynamic responses of monolithic beam-column joints can be found. Aluminium honeycomb core was used to absorb a large amount of impact energy (49%) compared to specimens without the honeycomb plate. It is noted that there has been no existing study that has investigated precast joints under impact loads in the literature yet. This dissertation is one of the first to investigate the performances of the precast joints under impact loads. The experimental results indicated that the proposed precast joints showed excellent performances under multiple impacts. Especially, the application of steel and synthetic

(plastic) fibres significantly increased the capacities of the joints due to increasing shear resistance. For instance, severe damage was observed on specimens without fibres while only minor cracks occurred on specimens using steel and synthetic fibres. The above results demonstrated that the proposed precast joints were applicable in rockfall and landslide regions to replace the monolithic joints and satisfy the requirements of resilience structures under impact loading. More details and discussions about the desirable performances of the proposed precast joints will be presented in the subsequent chapters.

1.2 Research objectives

The primary objective of this dissertation is to propose the non-corrosive dry beam-column joints which can effectively replace conventional monolithic joints to be applied in the earthquake and impact-prone areas. To achieve this objective, three main approaches were utilised in this dissertation, including experiment, analytical analysis, and numerical simulation. The specific research tasks of this dissertation are summarised below:

1. Proposing new precast joints (e.g., dry and hybrid joints) to reduce the construction time and construction cost.
2. Conducting experiments to investigate the performances of the proposed precast joints under cyclic and impact loads. The main parameters to investigate the joint performance include failure modes, drift ratio, ductility, maximum applied load/peak load, stiffness, energy dissipation, and residual displacement.
3. Using new and advanced materials to resolve corrosion and improve structural performances (i.e., FRP bolts/plates, FRP reinforcements, synthetic fibres).
4. Investigating the behaviours of both precast and monolithic joints made of “green materials” GPC to recycle industrial wastes and reduce CO₂ footprint.
5. Proposing new analytical models to assist engineers to design the newly proposed precast joints using the mentioned relatively new materials (OPC, GPC, SFRC, and FRP bolts/plates).
6. Using numerical models to investigate several parameters which could not be straightforwardly measured from experiments (e.g., stress flow and stress distribution). After validating the numerical models with the testing data, the

results of experiments and assumptions of the proposed analytical models were examined, and the optimal value of CEP thickness was determined.

1.3 Research outlines

This dissertation includes seven chapters. The first chapter presents the introduction of this dissertation including the background of the research, research objectives and research outlines. The main contents of the next six chapters are summarised as follows:

Chapter 2 presents the performances of newly proposed dry joints using CEP and CFRP bolts. One monolithic joint and several dry joints with different parameters/designs, namely CEP thickness, using steel spiral reinforcements and different bolt types, were tested under cyclic loading. The performances of the proposed dry joints are compared with those of the reference monolithic joint in terms of failure modes, drift ratio, ductility, maximum applied load, energy dissipations, and stiffness. This chapter demonstrates that the proposed dry joints offer good performances and, therefore, they can effectively replace monolithic joints. In addition, the available standards and analytical models are used to estimate the loading capacity of the proposed dry joints.

Chapter 3 reports experimental and analytical investigations on the structural performance of the proposed dry joints reinforced with different fibres. Some parameters which significantly affect the joints performances are also investigated in this chapter such as the effects of prestress forces in bolts. Based on the results of experiments, a new analytical model to design the OPC and SFRC dry joints with CEP and bolts is proposed.

Chapter 4 focuses on the performance of GPC dry vs GPC monolithic joints. The behaviours of GPC joints will be compared with the corresponding OPC joints in terms of the failure mode, drift ratio, ductility, maximum applied load, and energy dissipation. After understanding the performances of both GPC dry and monolithic joints, an analytical model is proposed to help engineers in designing precast and monolithic GPC joints.

Chapter 5 investigates the behaviours of the newly proposed hybrid joints. This hybrid joint type was developed based on the dry joints in Chapters 2, 3, and 4. This

new joint type is expected to mitigate the disadvantages of the dry joints related to poor and bulky appearances, as well as offering more options for engineers when designing precast concrete structures. The non-corrosive materials including FRP reinforcements, FRP bolts, and synthetic fibres are applied in this chapter to replace the conventional steel material. In addition, a numerical model is developed and validated against the experimental results. The validated numerical model is then used to investigate some parameters which could not be measured by the experiments such as stress flow, and stress distribution. The optimal value of the CEP thickness is suggested via the results of the numerical analyses.

In **Chapter 6**, the impact performances of the dry and monolithic joints are tested and compared. These comparisons help to study the dynamic responses of the proposed dry joints and monolithic joints under impact loading. The effectiveness of using different fibres to reinforce the joints on resisting impact load is discussed in this chapter in terms of damage level, lateral displacement and residual displacement.

Finally, **Chapter 7** summarises the main findings of this dissertation, as well as recommendations for future works.

It is worth mentioning that this dissertation is compiled from the technical papers prepared by the candidate during his PhD study. Each technical paper forms a chapter from Chapter 2 to Chapter 6. The published technical papers in the chapters are formatted by the author as per the requirements from Curtin University. Some definitions and figures may be reintroduced for readers' convenience and the logical flow of the chapters. The flow chart was also used to summarise the different tests in each chapter, as shown in Fig. 1-2

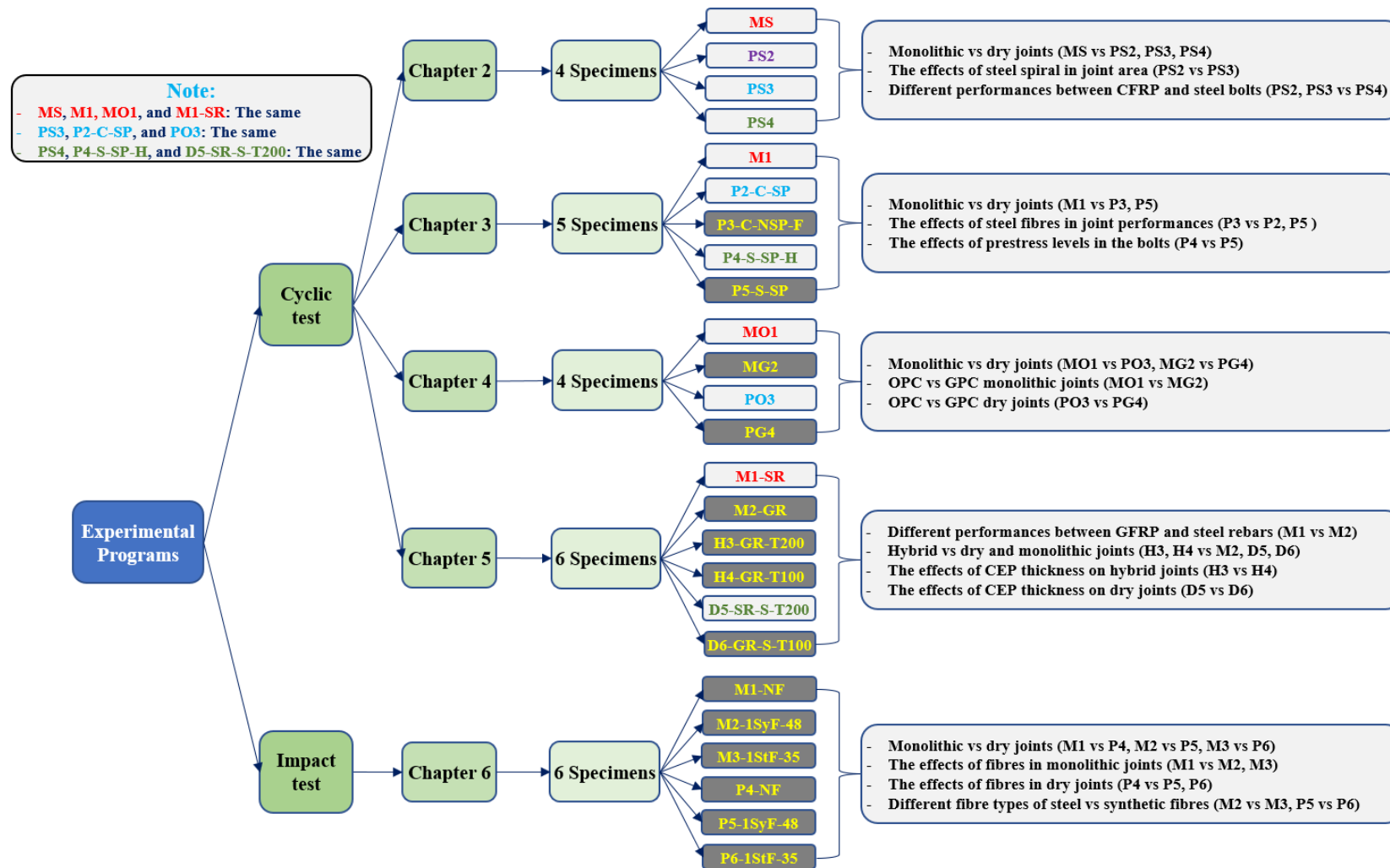


Fig. 1-2. Summary of different tests performed in the main chapters.

CHAPTER 2: DUCTILE AND DRY EXTERIOR JOINTS USING CFRP BOLTS FOR MOMENT-RESISTING FRAMES

ABSTRACT¹

This chapter proposes a new dry joint type for moment-resisting frames by using carbon fibre reinforced polymer (CFRP) bolts and plates. This is one of the very rare studies focusing on the potential of using CFRP bolts to connect beams to columns in the precast beam-column joints. CFRP bolts have been recognised for their good performances, which could effectively resolve a very costly issue of corrosion in the common dry joints using steel bolts, plates, and tendons. Cyclic loading was applied to test four specimens until 85% of the post-peak load. The results indicated that the proposed dry joints showed better performances compared to the reference monolithic joint in the load-carrying capacity, energy dissipation, and stiffness, which increased by 27-61%, 45-75%, and 27-55%, respectively. Particularly, drift ratio of all the proposed joints exceeded 3%, which is higher than the requirements for ductile joints in various standards. The ductility of the proposed joints was also more preferable than the reference monolithic joint (i.e. 2.2 vs 2.4). These exciting results suggest that these new dry joints can be plausibly applied to prefabricated constructions in non-seismic and seismic-prone areas. In addition, the proposed dry joints offer numerous advantages, compared to the traditional monolithic joints, in terms of construction time and construction-quality control.

¹ This work was published in **Structures** with the full bibliographic citation as follows:

Ngo TT, Pham TM, Hao H. Ductile and dry exterior joints using CFRP bolts for moment-resisting frames. *Structures* 2020;28:668-84.
<https://doi.org/10.1016/j.istruc.2020.09.020>

2.1 Introduction

Beam-column joints play a vital role in the behaviours of moment-resisting frames. They support the development of the ultimate capacity of adjacent members. This characteristic can only be achieved when the joints between beams and columns have sufficient strength and stiffness so that internal forces between members could transmit together. Lessons from various earthquakes have indicated that if the joints are destroyed, the building would collapse, although beams and columns are still undamaged [38, 53].

Most of existing studies have focused on monolithic, wet, or hybrid joints [7-9, 54] due to their good performance in peak load, stiffness, energy dissipation, ductility, and hysteretic behaviours. However, there have been still some disadvantages in these joint types, such as longer construction time, higher construction cost, more difficulties to control construction quality, and negative effects on the environment as compared to dry joints. Beams and columns in the dry joints are cast in factories before they are assembled in construction sites. Therefore, the application of dry joints could effectively resolve the above disadvantages of monolithic, wet, or hybrid joints [46, 55]. Nevertheless, the application of dry joints in reality is still limited compared to monolithic joints due to disadvantages related to strength, ductility, and corrosion resistance. Since beams and columns are cast separately and are connected later by bolts and tendons, dry joints are usually weaker than monolithic joints. For example, dry joints using cleat angles and stiffeners have not been recommended for use in earthquake-prone regions [56]. In precast concrete structures, especially with traditional dry joints, corrosion is more likely to occur because connecting elements might be not protected properly by concrete. The corrosion of the connecting elements leads to deterioration or even destruction of the entire buildings [3, 57]. Additionally, the expenditure to maintain and repair deteriorated members in some circumstances can be incredibly more costly than the original new ones [5, 6].

Meanwhile, fibre reinforced polymers (FRP) have gained its increasing popularity in civil engineering because they offer favourable features, such as lightweight, high strength, easy implementation, fatigue resistance, and good corrosion resistance [58, 59]. Recently, FRP bolts have been introduced to the market but its application for structural engineering is still limited. GFRP and CFRP bolts are the popular types, in

which GFRP bolts are more favoured because they are more cost-effective [60, 61]. The use of FRP bolts has not been popular in construction because the shear capacity of these bolts is relatively low as compared to steel bolts. FRP bolts are very strong in tension but weak in shear [62, 63].

Recently, CFRP and Basalt tendons have been applied in precast segmental concrete beams and normal beams to replace steel tendons for effective mitigation of corrosion problems [64, 65]. The functions of FRP tendons and FRP bolts are similar in tensile behaviour and prestress needs to be applied to these bolts/tendons before applying external loads. However, the application of FRP tendons in the structures is quite challenging compared to steel tendons due to the anchorage problem. This is because of the relatively low shear and compressive capacity of FRP materials so that anchors could fail by excessive principal stresses, local crushing, and interfacial slippage [66]. Therefore, the use of conventional anchorage methods for FRP tendons is not reliable and difficult to predict anchorage failure patterns. In addition, FRP sheets have been popularly applied to strengthen beam-column joints [58, 67]. Conventional steel reinforcements were replaced by GFRP bars to minimize corrosion [62, 68]. However, most of existing studies focus on wet and hybrid joints while there are very few studies on precast beam-column joints with FRP bolts. Feroldi and Russo [69] investigated precast beam-column joints using pultruded plates and C-shape FRP bars to replace steel plates and C-shape steel bars in steel structures. Since steel bolts were used to connect the beams and columns, these joints were still susceptible to corrosion of the metal parts. To date, no publication is available in literature yet to use FRP bolts and plates to connect beam-column joints.

Among various types of concrete dry joints, those with concrete-end-plates and bolts show various advantages, compared to other dry joint types. In this joint type, the concrete-end-plates are used to connect the beams to the adjacent columns using steel bolts. This type of dry joints can be easily installed and post-tensioned with no required formwork. Despite their advantages, only few studies focus on the behaviours and applications of this joint [13-15]. Saqan [14] and Palmieri et al. [15] conducted an experiment with large-scale specimens and an analytical investigation on this dry joint type. Among the five large-scale joints studied, the internal beam-column joint with the concrete-end-plates and steel bolts showed the worst behaviours, specifically in the

load-carrying capacity, drift ratio, and energy absorption capability. The experimental results indicated that the concrete-end-plates failed due to concrete crushing at the top and bottom zones. It was explained that concrete stress in compression struts reached its compressive strength at a low drift ratio of 1.5% and caused damage [14, 15]. Possibly, due to these negative results, the dry joint type using concrete-end-plates and steel bolts was overlooked. As a result, there is a lack of studies on the behaviours of this dry joint type.

It is clear from the literature that the advantages of dry joints can only be leveraged if more research is done to improve the capacities of these joints in terms of ductility, energy dissipation, stiffness, load-carrying capacity, and corrosion resistance. The current study, therefore, aims to propose dry beam-column joints for non-seismic and seismic-prone locations by using corrosion-resistant CFRP bolts to replace conventional steel bolts. Steel spirals are placed in the top and bottom zone of concrete-end-plates to confine concrete and increase the capacity of the joints. The effects of the thickness of the concrete-end-plates are also investigated. After applying various innovations, the proposed dry joints yield sufficient ductility and load-carrying capacity, as well as solving the issue of corrosion effectively. The use of CFRP bolts in the proposed joints is critical to increase the lifetime of structures and reduce the construction time and maintenance costs, which helps to promote the use of these dry joints in the construction sector.

2.2 Experimental program

This study proposes a new corrosion-resistant joint type that exhibits sufficient strength and ductility to be used in both non-seismic and seismic-prone regions. To evaluate the dry joint performance using CFRP bolts and steel bolts under quasi-static cyclic loads, four specimens were cast and tested until failure, including a monolithic specimen (MS), a precast specimen 2 (PS2) with CFRP bolts and no steel spirals in the concrete-end-plate, a precast specimen 3 (PS3) with CFRP bolts and steel spirals, and a precast specimen 4 (SP4) with steel bolts and steel spirals. Spirals were used in the concrete-end-plate to confine concrete and improve the capacity of the concrete-end-plate and thus the joint. All the bolts in the precast specimens had the same diameter of 20 mm. Details of the specimen design and the test setup are presented in the following sections.

2.2.1 Design of the specimens

Four exterior beam-column joints with a scale of 1/3 of an eight-floor building were designed according to ACI 550R-96 [70] and ACI 352R-02 [71]. The design was based on the design philosophy of strong columns and weak beams. The two previous studies by Hanaor and Ben-Arroyo [13] and Saqan [14] were also used as references to design the precast beam-column joints since there have been no existing standards for the precast joints using bolts and concrete-end-plates. The columns in all the specimens had the same length of 1280 mm with a square-shaped cross-section of 200×200 mm². Four 16-mm deformed steel bars were used as longitudinal reinforcements. 10-mm stirrups with a spacing of 70 mm were used as shear reinforcements for the columns (Fig. 2-1).

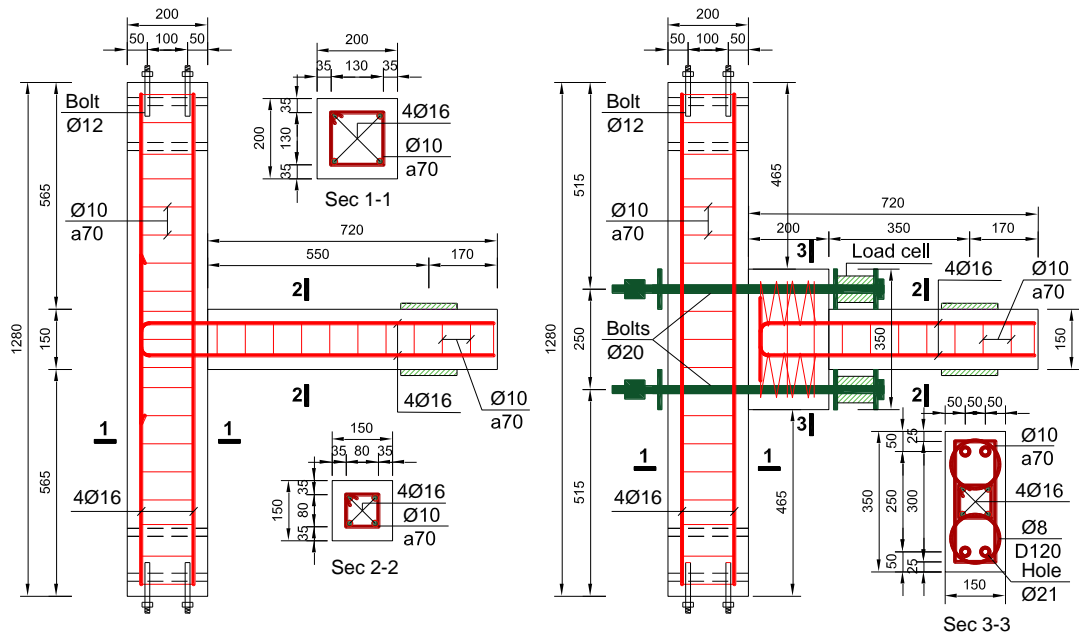


Fig. 2-1. Design of the monolithic and dry precast joints (in millimeter).

The beams of the precast specimens had a T-shape and included two parts: (1) the concrete-end-plate and (2) Beam A. This study adopted the guides of ACI 318-11 [72] and Wight and MacGregor [73] to design Beam A. The beam section in all the specimens was reinforced with four 16-mm deformed steel bars with a reinforcement ratio of 2.2%. Additionally, 10-mm stirrups with a spacing of 70 mm were used as shear reinforcements. The dimensions of the concrete-end-plate were 350×150×200 mm³ while those of Beam A was 150×150×520 mm³ as shown in Fig. 2-1. According

to Saqan [14], the capacity of the precast beam-column joint using the concrete-end-plates and steel bolts was comparably low since the crushing of the concrete appeared at the concrete-end-plate at a low drift ratio of 1.5 %. Therefore, in this research, 8-mm steel spirals at a spacing of 30 mm were used to confine the concrete and increase the compressive strength at the concrete-end-plates (see Fig. 2-2). This design was expected to improve the capacity of these precast beam-column joints.

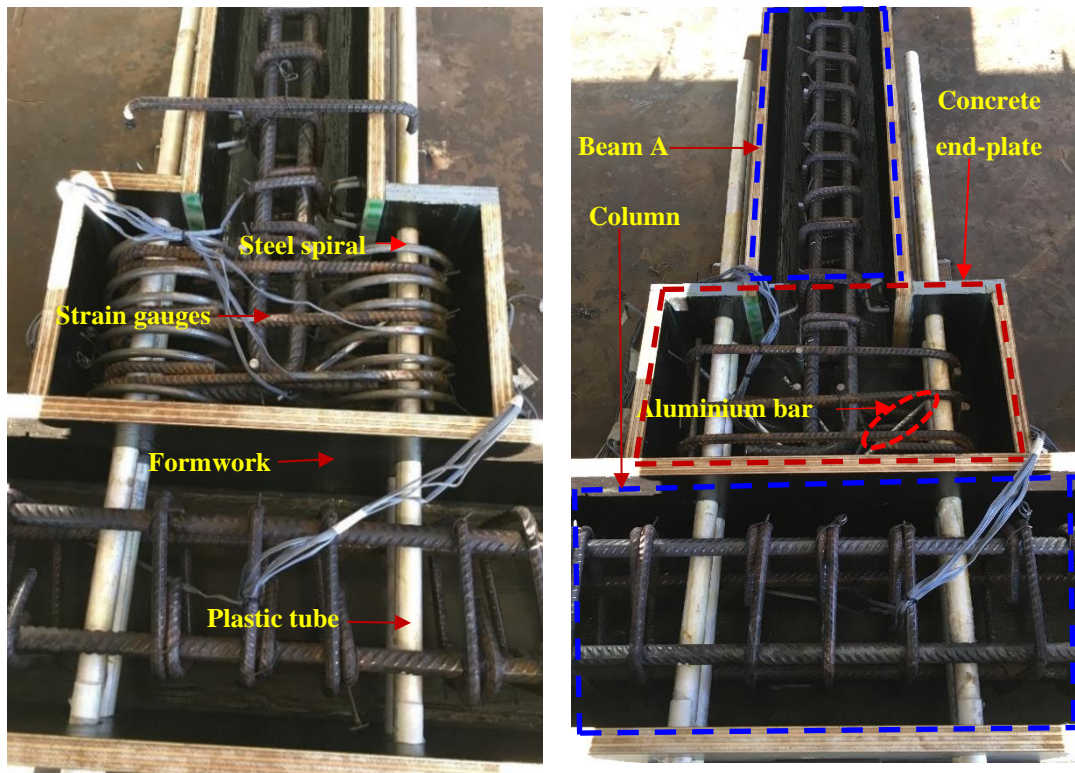


Fig. 2-2. Details of the reinforcements, strain gauges, aluminium bars, formworks, and plastic tubes.

To evaluate the effectiveness of the steel spirals, it is necessary to determine the exact strength of the concrete in the compressive zone during the test. Aluminium bars with a diameter of 6.1 mm were placed in the assumed direction of the concrete struts. Strain gauges were stuck to these bars to monitor the concrete strain as shown in Fig. 2-2. A cutting machine was used to create notches on the aluminium bars. These notches helped to increase the bond between the concrete and the aluminium bars. The concrete cover of all the beams and columns was 35mm as required in ACI 318-11 [72]. Details of all the reinforcements, steel spirals, and CFRP bolts are shown in Tables 2-1 and 2-2.

Table 2-1. Steel reinforcements and aluminium bars properties.

Bar size	Area	f_y	f_u	E_s	Remarks
(mm)	(mm ²)	(MPa)	(MPa)	(GPa)	
8	50	377	522	200	Spirals
10	78	560	675	200	Stirrups
16	201	597	706	200	Longitudinal reinforcements
6.3	31	110	150	69	Measuring the strain of concrete inside the concrete-end-plates

Table 2-2. Properties of CFRP bolts, nuts and plates.

Type	Dimension	Weight	Tensile strength	Shear strength	Bending strength	Compressive strength	Ultimate load	Elastic modulus	Impact strength
	(mm)	(g)	(MPa)	(MPa)	(MPa)	(MPa)	(kN)	(GPa)	(kJ/m ²)
Bolts	D20	376	≥ 850	≥ 160	480	760	≥ 267	100	185
Nuts	N20	44	-	-	-	-	100	100	-
Plates	150×90×20	540	-	-	-	-	≥ 100	100	-

Note: - = not given.

The most challenging issue in the prefabrication of these precast specimens was to ensure that the four bolts went through the beams and the columns smoothly when assembling the joints. To resolve this issue, the formworks for columns and beams were set up together as real joints. The holes inside the beams and columns were created by embedding plastic tubes with an outside diameter of 21 mm into the steel cages before the concrete was poured. Details of plastic tube disposition are shown in Fig. 2-2. In the two previous studies [13, 14], the tensile force in the bolts, a crucial parameter to determine the behaviours of the proposed joint type, was not reported. In the current experiment, two 20-ton load cells were used to measure the tensile forces in the bolts as shown in Fig. 2-3.

2.2.2 Mechanical properties of materials

Concrete properties are determined according to AS 1012.8.1-14 [74] and AS 1012.9.1-14 [75] as the averaged values from three 100×200 mm cylinders. The average compressive strength (f'_c) and tensile strength (f_{ct}) of concrete on the testing day was 38.4 MPa and 3.8 MPa, respectively. The ultimate tensile strengths of the reinforcements were 522 MPa for 8-mm bars, 675 MPa for 10-mm bars, and 706 MPa

for 16-mm bars. Other properties of these steel bars and aluminium bars which were provided by the manufacturer are presented in Table 2-1.

CFRP bolts were supplied by J and R Metalwork Industry Pty Ltd [76]. As informed by the manufacturers, GB/T 1447-05 [77] was used to evaluate the mechanical properties of CFRP bolts. The number of samples for the testing was 20-30 with a length of 800-1000 mm. The tensile strength, shear strength, and elastic modulus of 20-mm CFRP bolts were 850 MPa, 160 MPa, and 100 GPa, respectively. It is noted that the capacity of the entire bolts is restrained primarily by the capacity of the nuts with the ultimate load of 100 kN for the 20-mm bolts. The detailed properties of CFRP bolts, nuts, and plates are presented in Table 2-2. In addition, M20-metric steel bolts with class 8.8 had the proof load, yield stress, ultimate strength of 580 MPa, 640 MPa, and 800 MPa, respectively [78].

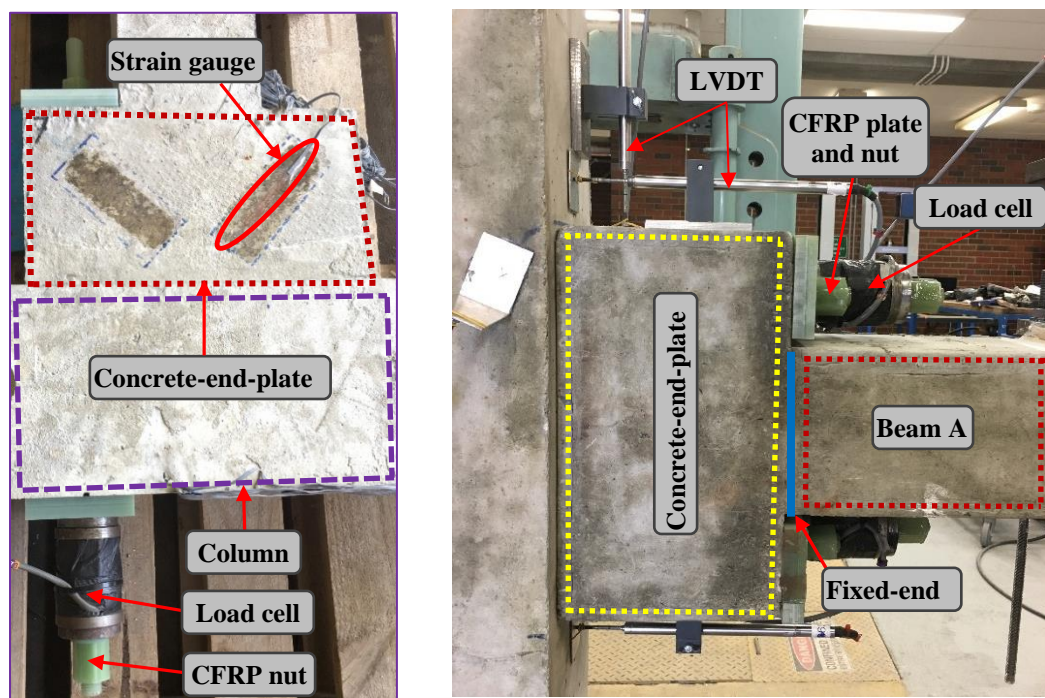


Fig. 2-3. Details of strain gauges and load cells.

Strain gauges with a length of 5 mm were bonded to stirrups, longitudinal reinforcements, and aluminium bars to measure the strain of reinforcements and the assumed concrete struts. Additionally, to measure the strain of concrete in diagonal struts of the concrete-end-plate, 60-mm strain gauges were glued on these estimated areas. Detailed strain gauges are presented in Figs. 2-2 and 2-3.

2.2.3 Specimen preparation and test setup

A steel brush and a compressed air gun were used to clean the holes and remove dust before the test setup. The column was the first to be connected to the reaction frame. Then, the beam was lifted by a forklift and connected to the column with four bolts. The setup process in this experiment is also applicable in reality. Four bolts with a diameter of 20 mm went through the four holes with a diameter of 21 mm on the beams and columns. CFRP or steel plates were placed into the bolts before nuts were tightened by a torque wrench to avoid concentrated stress around the bolts. According to the information provided by the manufacturer, 80 Nm of torque was recommended to apply to the CFRP nuts. Due to the low torsion resistance of CFRP bolts, low prestress levels were applied on CFRP bolts. The prestress levels in specimens PS2, PS3, and PS4 were 4.1, 6.5, and 51 kN, respectively.

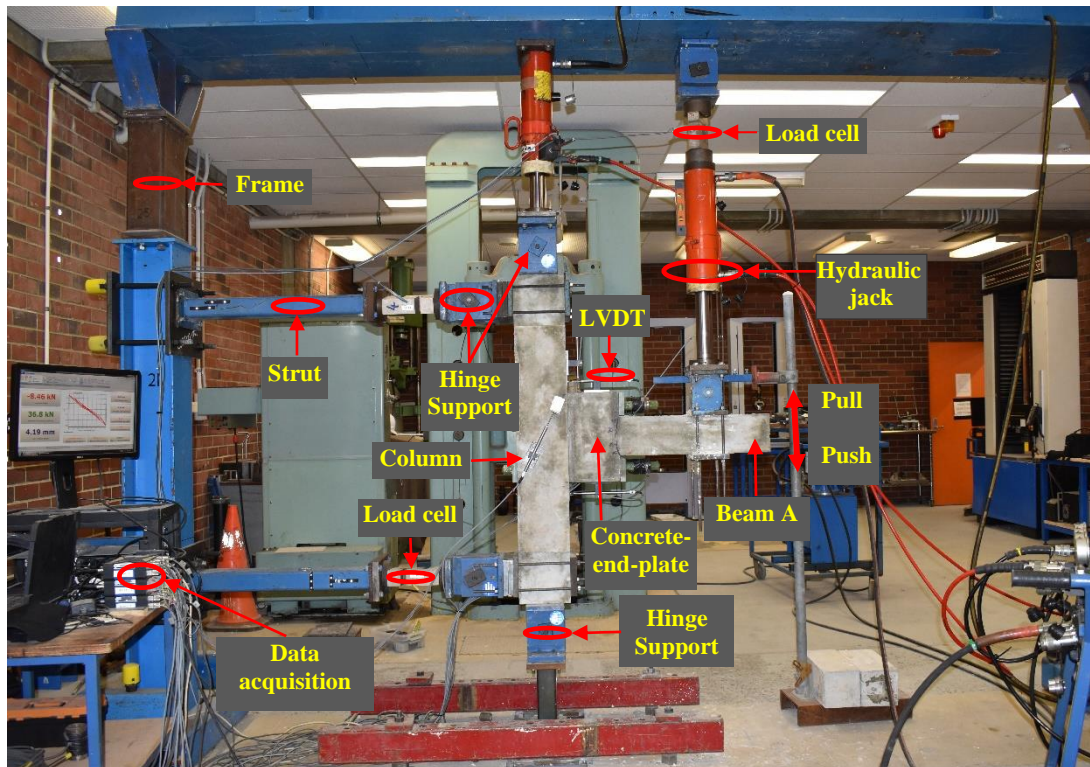


Fig. 2-4. A typical test setup.

For the test setup, a hydraulic jack was used to apply the vertical restraint on the column top with an axial force of 15 kN ($0.01f'_cA_c$). Since the effect of the axial force is not the focus of this chapter, it was maintained as low as possible. It was reported in a previous study that higher axial force is beneficial to the capacity of the joints [79]. Therefore, this chapter aims to investigate the most unfavourable case of joints.

Another hydraulic jack was used to apply the vertical quasi-static cyclic loading at the beam tip. The jack was installed at 650 mm from the column centre. The details of the test setup are presented in Fig. 2-4. The beam-column joints were tested under cyclic loading until 85% post-peak load. The loading history, which was based on ACI T1.1-01 [16], is shown in Fig. 2-5. Due to the time limitation, two load cycles were conducted at each loading level under displacement control at the level of 6-9 mm/min.

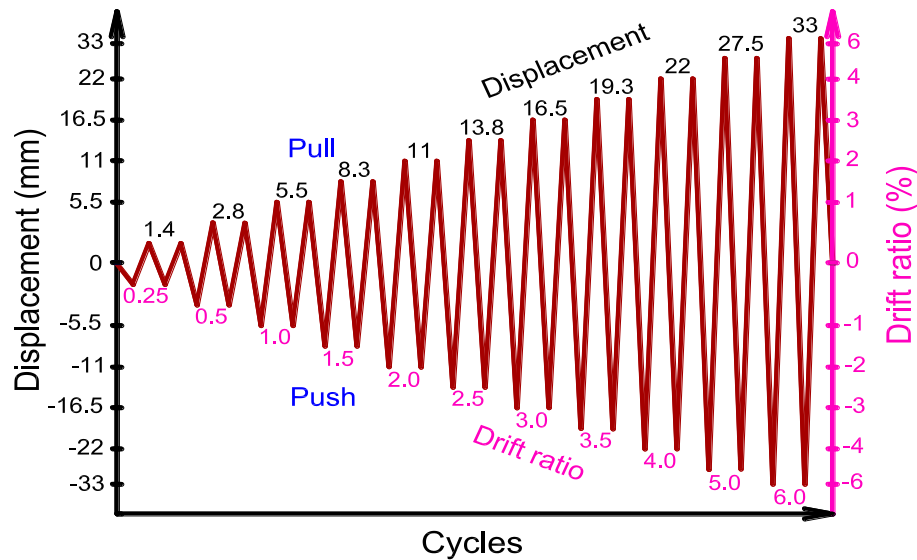


Fig. 2-5. Loading history.

2.2.4 Experimental results and discussion

2.2.4.1 General behaviours and failure patterns

Fig. 2-6 shows the failure modes of all the tested specimens. All the precast specimens experienced no visible cracks on the columns. As expected, the column showed good performance without any failure, which satisfied the criteria for weak beams-strong columns. The maximum tensile force in the CFRP bolts did not reach its strength limit. For example, the maximum tensile force of the CFRP bolts in Specimen PS3 was only 34% of its ultimate tensile force (see Table. 2-2). Therefore, no failure was observed in the CFRP bolts. Additionally, although no corbels or brackets were used for all the precast specimens, no slips were recorded during the tests, which was demonstrated by LVDT data (almost zero). The main failure of Specimens MS and PS4 occurred at the beams whereas Specimens PS2 and PS3 exhibited failure at the joints. More observations and discussions on the failure modes will be presented in Section 2.2.4.2.

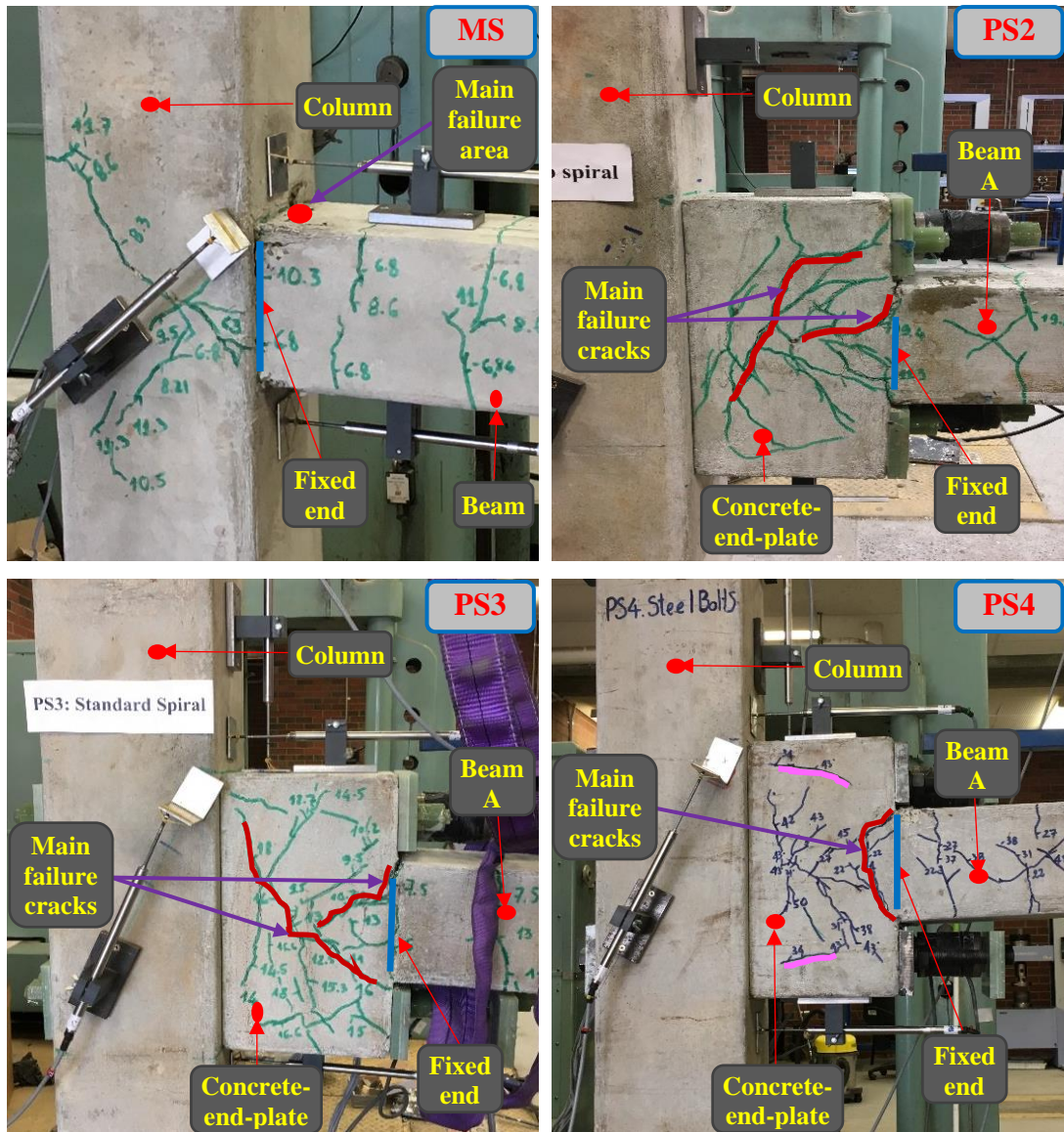


Fig. 2-6. Failure modes.

The reference Specimen MS exhibited flexural cracks on the beam and inclined cracks in the joint. The vertical flexural cracks were observed firstly on the beam when the beam soffit was in tension. These cracks were located at distances of 1, 100, and 220 mm from the face of the column at $\pm 0.7\%$ (± 4.0 mm) drift ratio corresponding to the tip displacement of ± 4.0 mm. For convenience, hereby the number in the bracket after the drift ratio shows the corresponding tip displacement. There were no shear cracks on the beam as shown in Fig. 2-6(MS). Then, the inclined cracks appeared and propagated into the joint zone after 1% drift ratio. These inclined cracks firstly formed in the middle of the joint before developing toward two corners of the column. The maximum width of the inclined crack achieved approximately 1.5 mm at 5.5% drift

ratio. Minor crushing of concrete occurred at the fixed-end when drift ratio reached 2%. The monolithic specimen MS achieved the maximum capacity at the drift ratio of 5.0%. Eventually, the crushing of concrete and vertical cracks at the fixed end caused the failure of Specimen MS.

As shown in Fig. 2-6, Specimens PS2 and PS3 exhibited the same failure patterns and the same crack development modes. The flexural crack initially formed at the fixed end at $\pm 0.5\%$ drift ratio ($\pm 2.5\text{mm}$). When drift ratio reached $\pm 0.6\%$ ($\pm 3.3\text{ mm}$), the inclined cracks had a tendency to propagate into the middle zone of the concrete-end-plate. At the initial stage, two vertical cracks at the fixed end were formed because the tensile strain of concrete at this section reached its maximum value due to sufficient bending moments. In the following stages, the longitudinal reinforcements started to significantly contribute to the flexural resistance and did not show considerable damage but some cracks. Meanwhile, inclined cracks gradually developed in the middle zone of the concrete-end-plate with an increase of the inclined angle (see Fig. 2-6). These inclined cracks initiated in the middle and then developed to the top and bottom of the concrete-end-plate and caused the failure.

Fig. 2-7 shows the data of strain gauges of the longitudinal reinforcements and the concrete-end-plates in all the tested specimens. The dots in this figure indicate their maximum strain at each cycle. The data of strain gauges at drift ratio of 3.0% ($\pm 16.4\text{ mm}$) on Specimen PS3 in Fig 2-7 indicate that the strain of longitudinal reinforcements ($2559\ \mu\epsilon$) almost reached the yielding point ($2980\ \mu\epsilon$) and the tensile strain of concrete ($1334\ \mu\epsilon$) exceeded the ultimate tensile strain ($131\ \mu\epsilon$). The maximum tensile strain of concrete was determined based on its tensile strength (f_{ct}). Therefore, two main inclined cracks (see red curves on Fig. 2-6) significantly opened with a width of approximately 2-3 mm, which caused the main failure for Specimens PS2 and PS3. Additionally, there were no shear cracks on Beam A of Specimens PS2 and PS3.

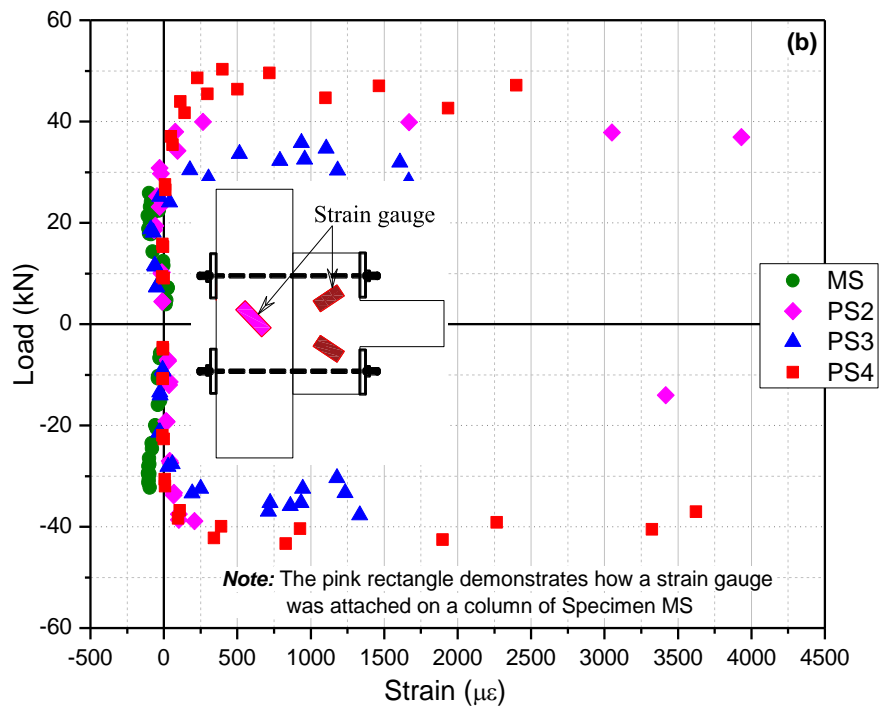
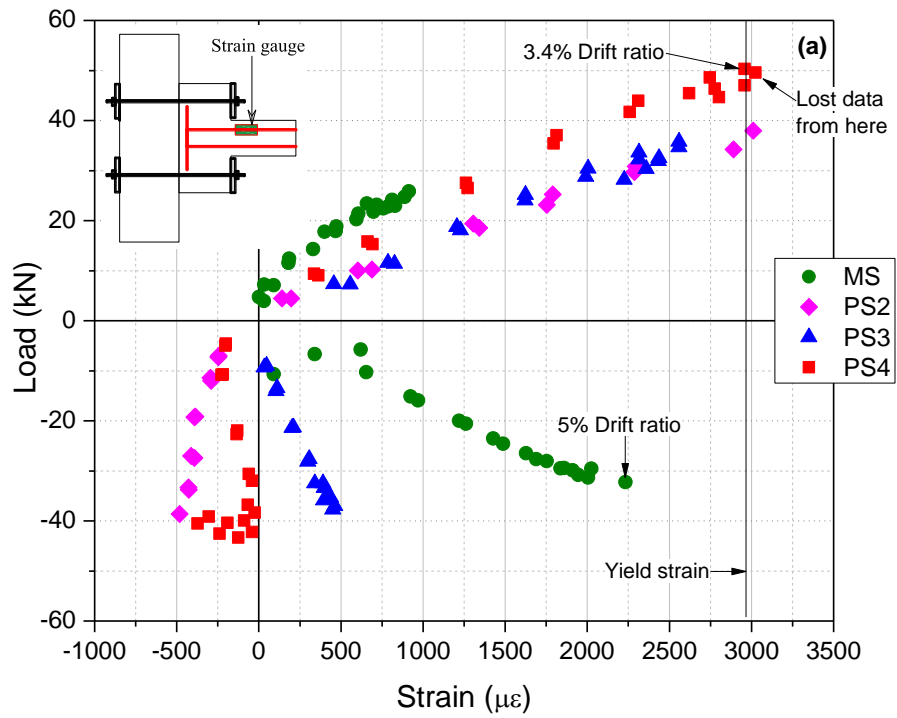


Fig. 2-7. Strain of longitudinal reinforcement (a) and on concrete (b).

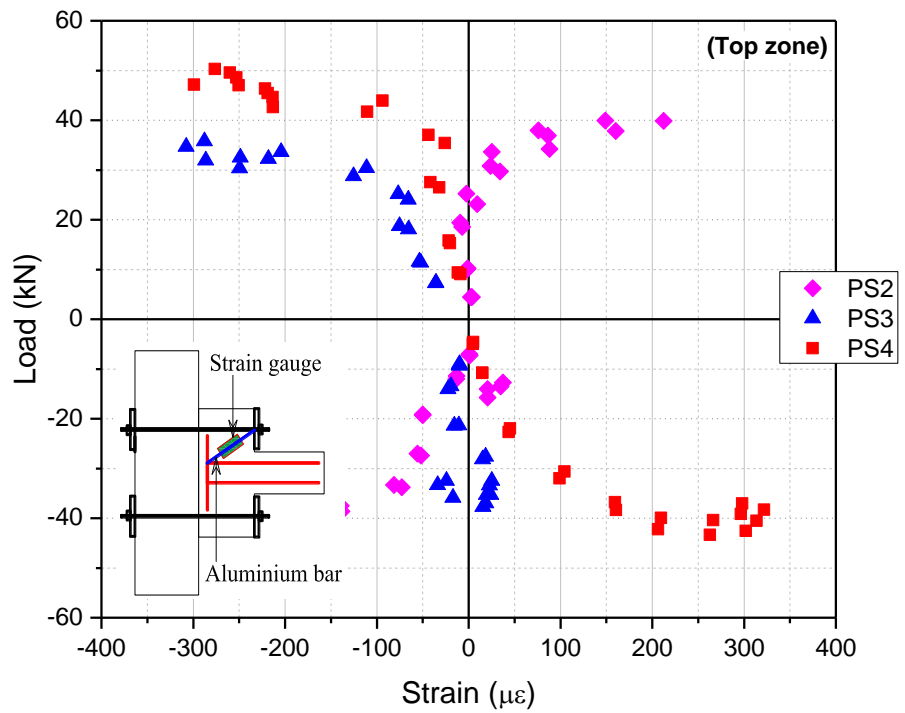
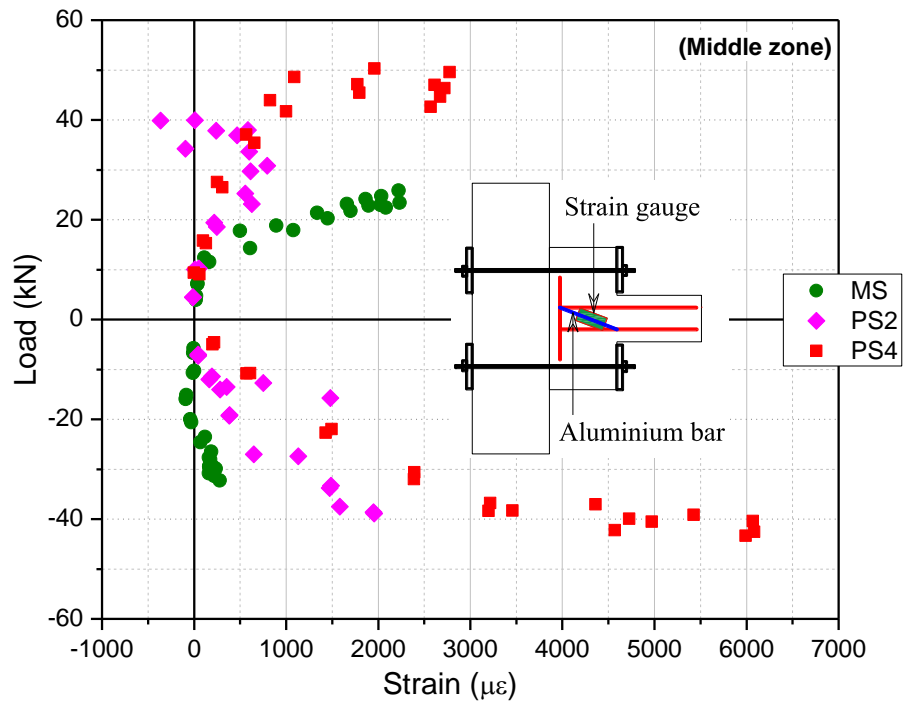


Fig. 2-8. Load versus strain of the strain gauges in the aluminium bars.

Specimen PS4 showed different failure patterns as compared to Specimens PS2 and PS3. The two inclined cracks, which formed a V-shape, initially appeared from the two corners between Beam A and the concrete-end-plate (see the red curve in Fig. 2-6(PS4)). These inclined cracks occurred soon after the load was applied at the beam tip at 0.3% drift ratio (± 1.65 mm). At 0.8% drift ratio, the inclined cracks developed from the fixed end into the middle areas of the concrete-end-plate. It is different from Specimens PS2 and PS3 due to the effects of the prestress level of the bolts. The inclined cracks of Specimen PS4 occurred mainly in the middle and only one inclined crack appeared at the top and bottom of the concrete-end-plate after achieving the peak load of 50.3 kN with 3.0% drift ratio (see the pink curves in Fig. 2-6(PS4)). The prestress level of Specimen PS4 was higher than those of Specimens PS2 and PS3 by approximately 12.4 and 7.8 times, respectively. The high prestress level in the bolts might have helped to improve the confined capacity of the concrete in the top and bottom zones of the concrete-end-plate [13]. From 2.8% drift ratio, the concrete on the top and bottom of the concrete-end-plate began to crush, and the red curve crack opened approximately 4-5 mm, which caused the main failure in Specimen PS4 as shown in Fig. 2-6(PS4)).

Fig. 2-7 shows the strain at the surface of the concrete-end-plate while Fig 2-8 presents the strain inside the concrete-end-plate measured on the aluminium bars at the possible struts. In Fig. 2-8, the maximum measured strain inside the middle zone was much higher than that at the top and bottom zones of the concrete-end-plates. For instance, the maximum measured tensile strain inside the middle zone and the top zone at 4% drift ratio of Specimen PS4 was $4971 \mu\epsilon$ and $314 \mu\epsilon$, respectively. Therefore, it can be concluded that the tensile stress inside the top and bottom zones was lower than that inside the middle zone. As a result, the proposed dry joints failed differently from those in the previous study by Saqan [14] who reported that the main failure was the compression strut at the top and bottom zone of the concrete-end-plate. To further analyse the failure mechanism, Fig. 2-9 presents a sketch of force paths in the concrete-end-plate, T_1 vs T_2 and T_3 are the tensile forces of the bolts and reinforcements and T_4 , q_1 vs q_2 , and q_3 are the compressive forces of the reinforcements, CFRP plates, and the bottom zones. Theoretically, there are two possibilities for the failure of the joints governed by either compressive or tensile strength of concrete [73]. The data of strain gauges in Figs. 2-7(b) and 2-8 indicate that the compressive strain in the compression

struts of the concrete-end-plate was relatively small ($< 110 \mu\epsilon$) and did not reach the maximum compressive strain of concrete, whereas the tensile strain of concrete ($> 1334 \mu\epsilon$) well exceeded its maximum tensile strain ($131 \mu\epsilon$). Therefore, it is suggested that the major cracks and failure of these precast specimens were caused by the tensile strain of concrete. This mechanism could be explained by the two effects: (1) the angle of possible struts and (2) the bond between reinforcements and concrete. There were two possible struts (i.e., Struts AB and AC) that might occur on concrete-end-plates as shown in Fig. 2-9. The angle of Strut AB was quite small (approximately 34°) and the bond stress (b in Fig. 2-9) between the reinforcements and the concrete had the tendency to resist the tensile force (T_3) in the reinforcements. Therefore, the tensile force (T_3) in the reinforcements at node B was low which led to the low compressive stress of concrete around node B. For Strut AC, it had a larger angle (50°) and higher compressive stress as compared to that of Strut AB. Meanwhile, the failure of Specimens PS2 and PS3, as shown in Fig. 2-6, reveals that the red inclined cracks were established due to the tensile stress. From observations during the tests and the above analyses, it could be concluded that tensile cracks (AB and AC) caused the failure of the specimens.

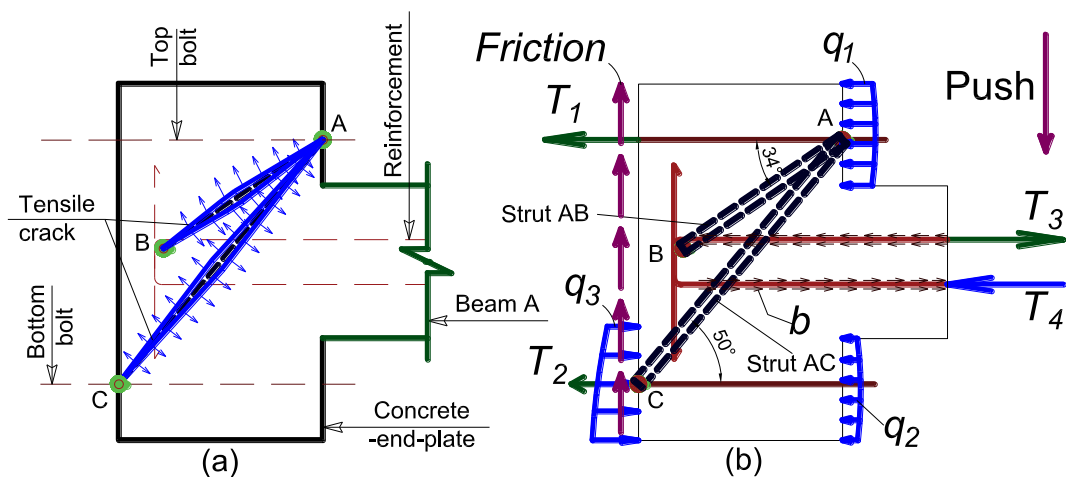


Fig. 2-9. Force path and cause of inclined cracks.

2.2.4.2 Hysteretic behaviours

The hysteretic responses of all the specimens were almost symmetrical in both the push and pull directions (see Fig. 2-10) because both the top and bottom

reinforcements in the beams were similar, with a diameter of 16 mm. However, the hysteretic curves were asymmetrical after the peak loads due to large and irreversible deformation, which is consistent with the results of the previous studies [14, 15]. Linear responses were observed in the envelope curves of all the precast specimens until 3% drift ratio. These responses were due to the linear responses of the CFRP bolts and steel bolts during the tests. In addition, the longitudinal reinforcements did not yield until 3% drift ratio (see Fig. 2-7), thus the main failure of the precast specimens was governed by the concrete properties. After this stage, the load started to decrease. Various cracks on the concrete-end-plates caused a significant reduction in the load-carrying capacity after 3% drift ratio. From 4% drift ratio, the envelope curves had a tendency to remain constant as indicated in Fig. 2-11. This performance could be explained with a reference to the strength hardening of the reinforcements. Stresses in the reinforcements still increased after reaching peak load, so the failure shifted from the joint to the beam after 4% drift ratio as also observed in the previous study [62].

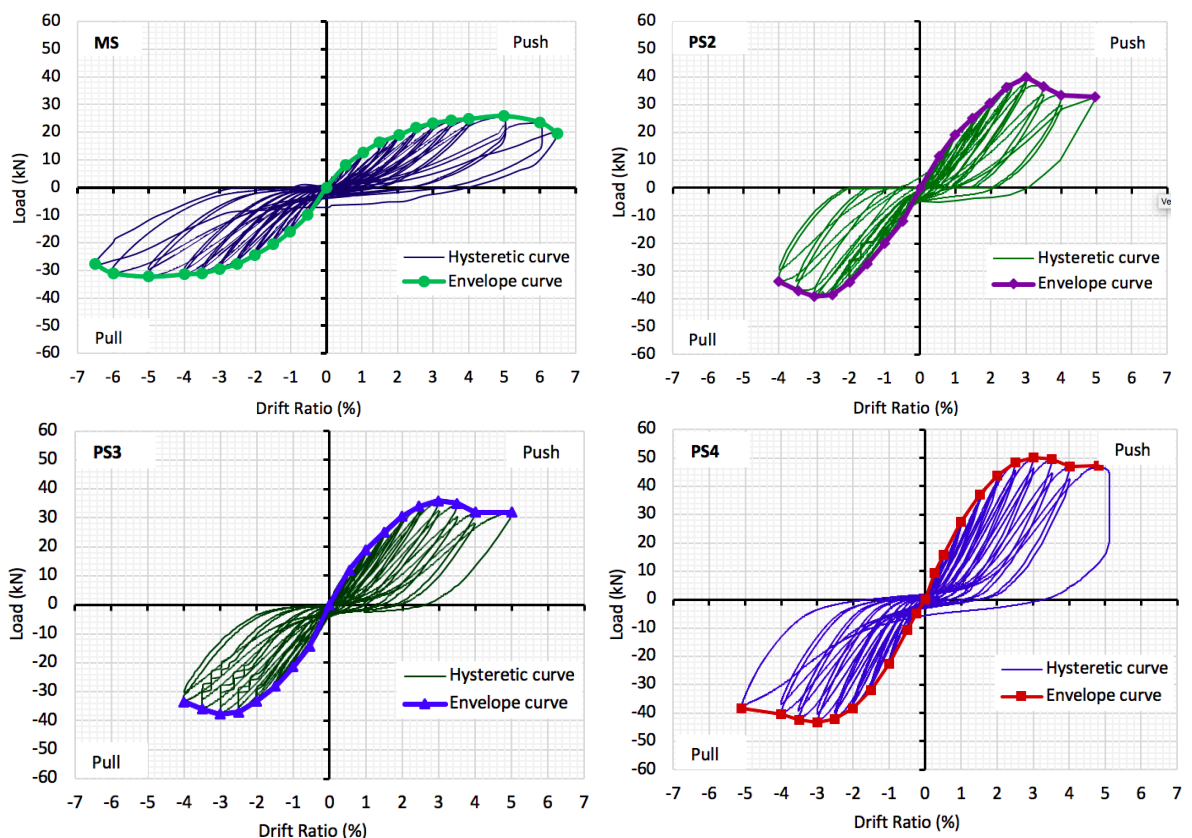


Fig. 2-10. Load-displacement hysteretic responses of tested specimens.

To further understand the behaviours of all the specimens, the maximum design loads of the beams were estimated and presented in Fig. 2-11. Design loads of 28 kN and 44

kN were applied to the monolithic beam and precast beams, respectively. Specimens MS and PS4 reached their peak loads of 32.3 kN at 5% drift ratio and 50.3 kN at 3% drift ratio. These maximum loads were higher than the estimated capacities of the corresponding beams. This variation might result from the difference between the nominal tensile strength and the actual strength of the reinforcements. Taken all the above results together, it is clear that the main failure of Specimens MS and PS4 occurred at the beams, whereas that of Specimens PS2 and PS3 occurred at the joints, as discussed in section 2.2.4.1.

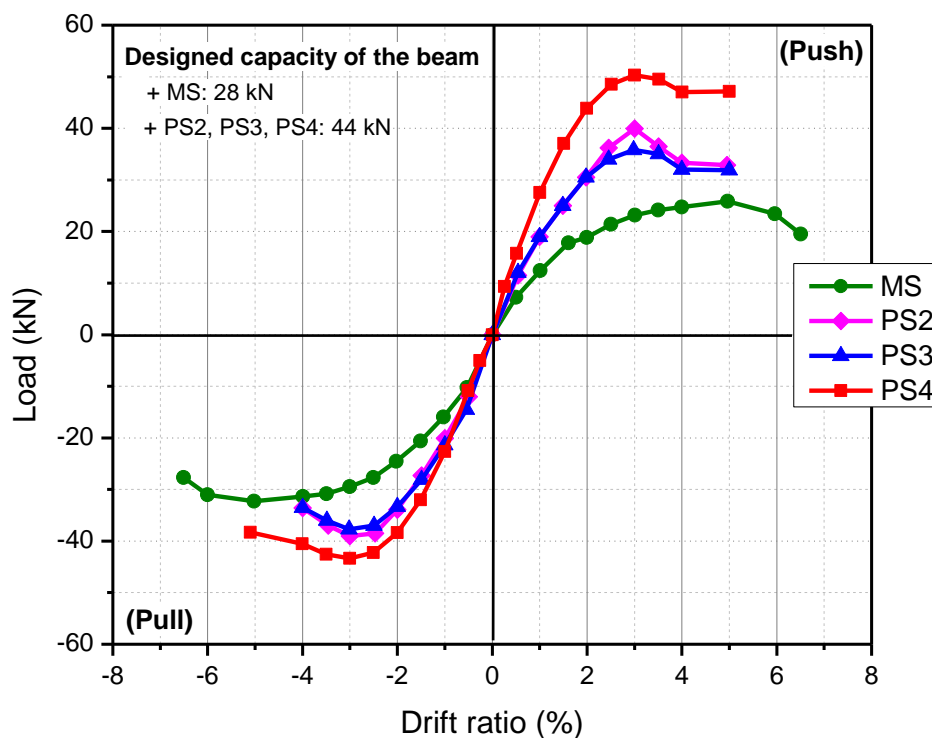


Fig. 2-11. Envelopes of hysteretic curves of all the specimens.

In general, the responses of Specimen MS showed nonlinear behaviours from 1% drift ratio until failure. Up to 1% drift ratio, Specimen MS exhibited elastic behaviours and dissipated little energy because there was no evidence of a significant pinching and stiffness degradation. It is noted that the pinching indicates the energy dissipation capacity of specimens and it often occurs when there is a significant variation of the area inside hysteresis loops. After 1% drift ratio, pinching continuously increased due to the crack developments. Specimen MS began to yield at 2.7% drift ratio before reaching the maximum load at 5% drift ratio. From 5% to 6.5% drift ratio, the load

capacity continuously dropped and the Specimen MS was damaged at 6.5% drift ratio. Until the end of the test, the longitudinal reinforcements in Specimen MS did not yield as shown in Fig. 2-7(a) ($2233 \mu\epsilon < 2980 \mu\epsilon$) while concrete crushing at the fixed end caused a load decrease in Specimen MS. The reduction in the load-carrying capacity of all the specimens after the peak load could be mainly attributed to tensile cracks in the concrete-end-plate, crushing of concrete and flexural cracks at the fixed end, as previously explained.

2.2.4.3 Drift ratio and load-carrying capacities

The drift ratio is an essential parameter to evaluate the joint performances. The drift ratio is defined as follows:

$$R = \Delta/l \quad (2-1)$$

where Δ is the vertical displacement of the beam at the loading point and l is the distance from the loading point to the column face ($l = 550$ mm).

The drift ratio of a monolithic beam-column joint is reported to range approximately from 4% to 5%, which well satisfies the requirements of many standards. For example, ACI T1.1-01 [16], CSA A23.3-07 [17], and ASCE 41-06 [18] require drift ratio of 3.5%, 2.5% and 2% to ensure the life safety in earthquake-prone regions, respectively. For drift ratio of dry joints with concrete-end-plates and steel bolts, previous studies reported a value of 1.5% [14]. Therefore, the application of this dry joint type is still limited in earthquake-prone regions. Interestingly, the drift ratio of the currently tested specimens was satisfactory to be applied in earthquake-prone regions.

Table 2-3 shows the peak loads and the corresponding drift ratios of all the specimens. In general, the proposed dry joints showed good performances including drift ratio and load-carrying capacities as compared to those from the previous studies [13-15]. Specimen MS exhibited a ductile load-displacement response with the highest drift ratio of 5%, corresponding to the average peak load of 29.1 kN. This peak load is the lowest load-carrying capacity among all the tested specimens. All the precast specimens exhibited the same drift ratio of 3% at the peak loads. This value was higher than 2.5% and 2% required by CSA A23.3-07 [17], and ASCE 41-06 [18], respectively, to ensure life safety. Specimen PS2 reached the peak load of 39.5 kN at

a drift ratio of 3%, which was 35.8% higher than that of the Specimen MS. For Specimens PS3 and PS4, the maximum loading capacities were also significantly increased with an average peak load of 36.8 kN and 46.8 kN, respectively, which were 26.6% and 61.2%, higher than that of Specimen MS.

Table 2-3. Load-carrying capacity and drift ratios of all the tested specimens.

Name	Peak load (kN)		Increase (%)		Average (kN)	Increase (%)	Drift ratio at peak load (%)	
	Push	Pull	Push	Pull			Push	Pull
MS	25.8	32.3	-	-	29.1	-	5.0	5.0
PS2	39.9	39.0	54.6	20.8	39.5	35.8	3.0	3.0
PS3	35.8	37.7	38.6	16.9	36.8	26.6	3.0	3.0
PS4	50.3	43.3	94.7	34.3	46.8	61.2	3.0	3.0

Note: - = not applicable.

In the previous study by Saqan [14], which investigated the same kind of joints, the failure occurred at the compression strut at the top and bottom zones of the concrete-end-plate. Therefore, the current chapter used steel spirals to confine concrete in this region and thus improve the load-carrying capacity and the drift ratio. Interestingly, the ultimate load and the drift ratio of Specimens PS2 and PS3 were almost the same, indicating that the use of spirals did not improve the performances of the joints. This phenomenon can be explained by the change of the failure modes. The precast specimens in this chapter failed due to tensile cracks of concrete in the middle zone of the concrete-end-plate which was different from the previous study [14]. The change in the failure modes was discussed in Section 2.2.4.2. Meanwhile, Specimen PS4 with steel bolts had the same drift ratio of 3% but a higher maximum load (27.2%) as compared to those of Specimen PS3 with CFRP bolts. According to previous studies [46, 80, 81], high prestress levels improved the maximum load of joints. Therefore, the improvement in the ultimate load of the specimen with steel bolts was attributed to the prestress level in the bolts. Due to low torsion resistance, the CFRP bolts were prestressed at a lower force than the steel bolts (6.5 kN vs 51 kN). Further study is necessary to investigate the effect of these parameters on the load-carrying capacity of joints.

2.2.4.4 Ductility of joints

Ductility is a crucial parameter to evaluate the bearing capacity of a building under earthquake loading. High ductility considerably minimises a reduction in strength and brittle failure of a building. In addition, ductility significantly affects the energy dissipation capacity of structures during inelastic deformations. In this chapter, ductility is defined as the ratio of the ultimate displacement (Δ_u) to displacement at the yield loads (Δ_y), as presented in Eq. 2-2 [82]:

$$\mu = \Delta_u / \Delta_y \quad (2-2)$$

The yielding deformation in a reinforced concrete structure is determined inconsistently in different studies since the relationship between the load and displacement does not exhibit a clear yielding point due to the nonlinear behaviours of materials [82]. In this study, the yield displacement is determined at the point corresponding to the 75% of the ultimate load H_u while the ultimate displacement corresponds to the displacement at 85% the post-peak load as shown in Fig. 2-12 [83].

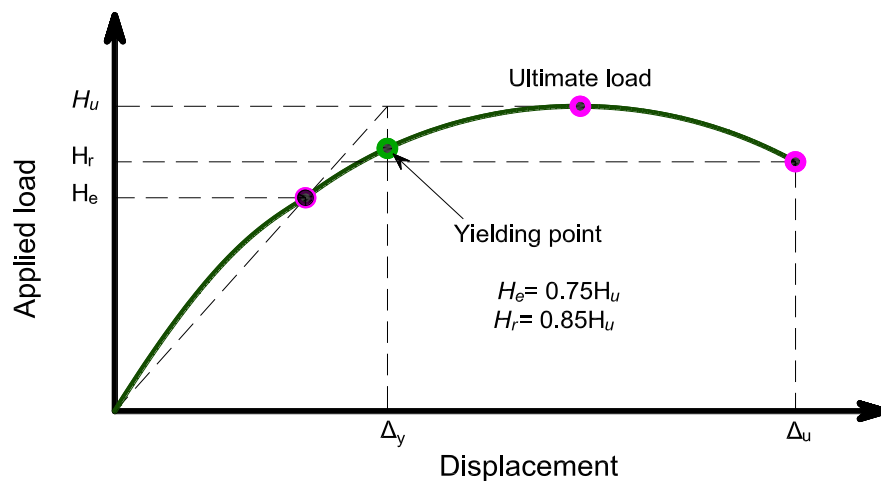


Fig. 2-12. Definitions of the yield displacement and the ultimate displacement.

In the current chapter, the maximum displacement of Specimens PS3 and PS4 stopped at 27.6 mm and 28.1 mm due to the limitation of the hydraulic jack, which corresponded to 90% peak load. Therefore, the ultimate displacement of Specimens PS3 and PS4 was determined corresponding to 90% of the peak load. The load-carrying capacity of Specimens PS3 and PS4 had a tendency to remain unchanged in the push direction from 4% drift ratio until the end of the tests due to the change of

failure mode from the joints into the beams. Therefore, the ultimate displacements of Specimens PS3 and PS4 were quite high, preventing the brittle failure and giving engineers warnings before the total collapse of the structures.

Table 2-4. Displacement and ductility of all the tested specimens.

Name	Force	H_u	$0.75H_u$	Δ_y	$0.85H_u$	Δ_u (85%)	$\mu = \Delta_u / \Delta_y$	Average (μ)	Decrease (%)
		(kN)	(kN)	(mm)	(kN)	(mm)			
MS	Push	25.8	19.4	15.6	22.0	35.8	2.3	2.4	-
	Pull	32.3	24.2	14.5	27.4	35.6	2.5		
PS2	Push	39.9	29.9	14.2	33.9	21.5	1.5	1.7	-29.2
	Pull	39.0	29.3	12.0	33.2	22.4	1.9		
PS3	Push	35.8	26.9	12.2	32.2*	27.5*	2.3	2.1	-12.5
	Pull	37.7	28.3	11.1	34.0*	21.5*	1.9		
PS4	Push	50.3	37.7	11.4	45.3*	26.5*	2.3	2.3	-4.2
	Pull	43.3	32.5	11.4	39.0*	26.3*	2.3		

Note: - = not applicable.

* at 90% of the post-peak load.

Table 2-4 summarizes displacements at the yielding and ultimate stages of all the specimens in the two directions as well as the ductility ratio. Specimens PS3 and PS4 almost achieved the same ductility level as the reference Specimen MS, which were 2.1, 2.3, 2.4, respectively. For Specimen PS2, it showed less ductile behaviours than Specimens PS3, PS4, and MS, with the ductility ratio approximately 19.0%, 26.1%, and 29.2% less than that of the three specimens, respectively. Specimen PS3 showed a higher ductility than that of Specimen PS2 as given in Table 2-4 even though they had quite similar designs except for the prestressing force and steel spirals. This difference results from the varied ultimate displacements. Although the ultimate displacement of Specimen PS3 (27.5 mm) was calculated at 90% of the post-peak load, it was still higher than that of Specimen PS2 (22.4 mm) at 85% of the post-peak load. This result was because the load-carrying capacity of Specimen PS2 significantly dropped after achieving the peak load in the push direction. Furthermore, using the steel spirals with an appropriate pitch helped to increase the ductility due to an increase in ultimate displacement in Specimens PS3 and PS4 [84]. The ductility of Specimens PS3 and PS4 were quite similar (2.1 vs 2.3) because the behaviours of these specimens were governed by concrete and steel reinforcements while the CFRP bolts and steel bolts were over-designed with high capacity and were not yielded up to failure. The

similarity also proves that CFRP bolts can be used to replace steel bolts to resolve the corrosion problem effectively.

2.2.4.5 Energy dissipation capacities and equivalent viscous damping ratio

In order to evaluate the energy dissipation capacity of the beam-column joints, the dissipated energy and equivalent viscous damping ratio are determined based on the hysteretic loops.

2.2.4.5.1 Energy dissipation capacities

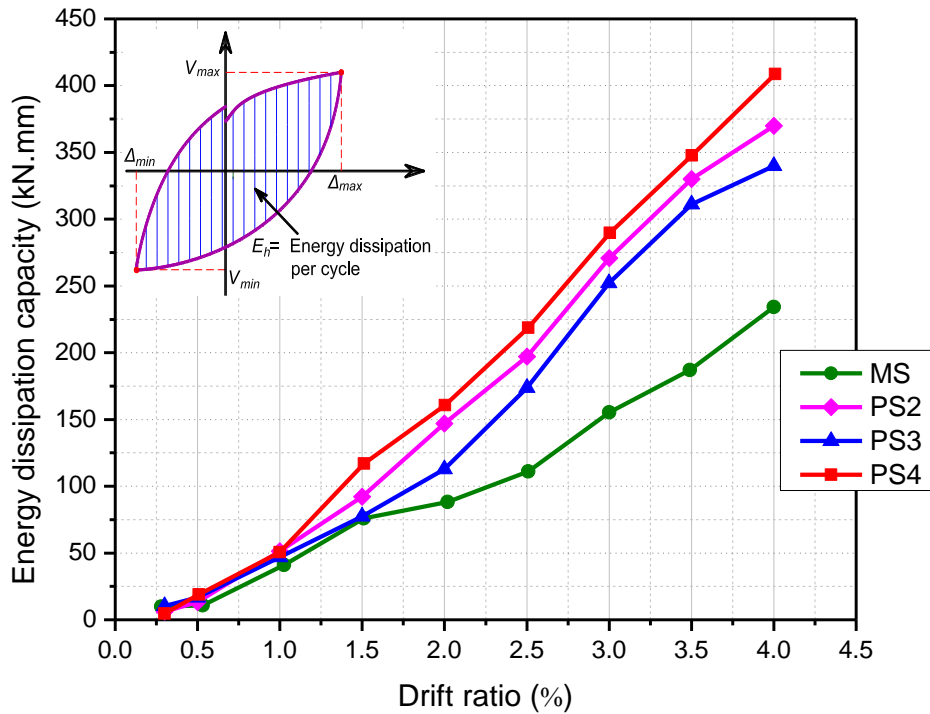


Fig. 2-13. Energy dissipation curves of the tested specimens.

The energy dissipation capacity is an essential parameter to examine how effective a joint withstands earthquake loading. A beam-column joint subjected to quasi-static cyclic loading is classified as ductile if a sufficient amount of energy is dissipated without a significant decline of its strength and stiffness [56, 85]. The energy dissipation at a specific load cycle due to inelastic action is calculated as the area enclosed (A_h) inside the hysteretic loop in that cycle. Fig. 2-13 presents the energy dissipation capacity versus the drift ratio of the specimens. All the specimens exhibited similar patterns of energy dissipation from the initial stage to drift ratio of 1% because

they behaved elastically up to 1% drift ratio. However, the overall dissipated energy of Specimen MS was less than that of the precast specimens from the drift ratio of 1% until failure because the area (A_h) in each cycle of Specimen MS was smaller than that of the precast specimens as shown in the hysteresis loops in Fig. 2-10. The energy dissipation at 4% drift ratio of Specimens PS2, PS3, and PS4 was 57.9%, 45.1%, and 74.5% higher than that of Specimen MS, respectively. Therefore, it can be concluded that the proposed dry joints showed good energy dissipation capacity and were suitable for applications in the seismic-prone regions.

2.2.4.5.2 Equivalent viscous damping ratio

The equivalent viscous damping ratio represents the ability in reducing the peak response amplitudes from inelastic deformation during an earthquake excitation [86]. The equivalent hysteretic damping ratio in a specific loading cycle is calculated based on the area inside an absolute load-displacement hysteresis loop A_h to 2π times the elastic strain energy absorbed in an equivalent linear elastic system as follows [86]:

$$\xi_{eq} = \frac{A_h}{2\pi V_m \Delta_m} \quad (2-3)$$

where V_m and Δ_m are the average peak load and displacement values in the i^{th} cycle, respectively, and eq stands for *equivalent*.

The equivalent viscous damping ratio of Specimens MS, PS2, PS3, and PS4 was presented in Fig. 2-14. From 0.3 to 0.5% drift ratio, the equivalent viscous damping ratio of Specimens MS, PS2, and PS3 significantly dropped while that of Specimen PS4 increased slightly. This phenomenon was because there was a high bending moment in Specimen MS and low prestress level in CFRP bolts of Specimens PS2 and PS3 which caused a higher initial displacement at an early stage if compared to Specimen PS4.

Up to the drift ratio of 2%, the reference Specimen MS showed a higher equivalent viscous damping ratio than Specimens PS3 and PS4. At the drift ratio of 2.5%, the equivalent viscous damping ratio of Specimens PS2, PS3, and PS4 was almost equal and higher than that of Specimens MS. However, when the drift ratio is greater than 2.5%, the equivalent viscous damping ratio of all the specimens slightly increased and all the precast specimens exhibited a higher equivalent viscous damping ratio than that

of Specimen MS. This reduction of Specimen MS was attributed to pinching in the curves, concrete crushing, and shear stress, which contributed to narrowing the hysteresis loop.

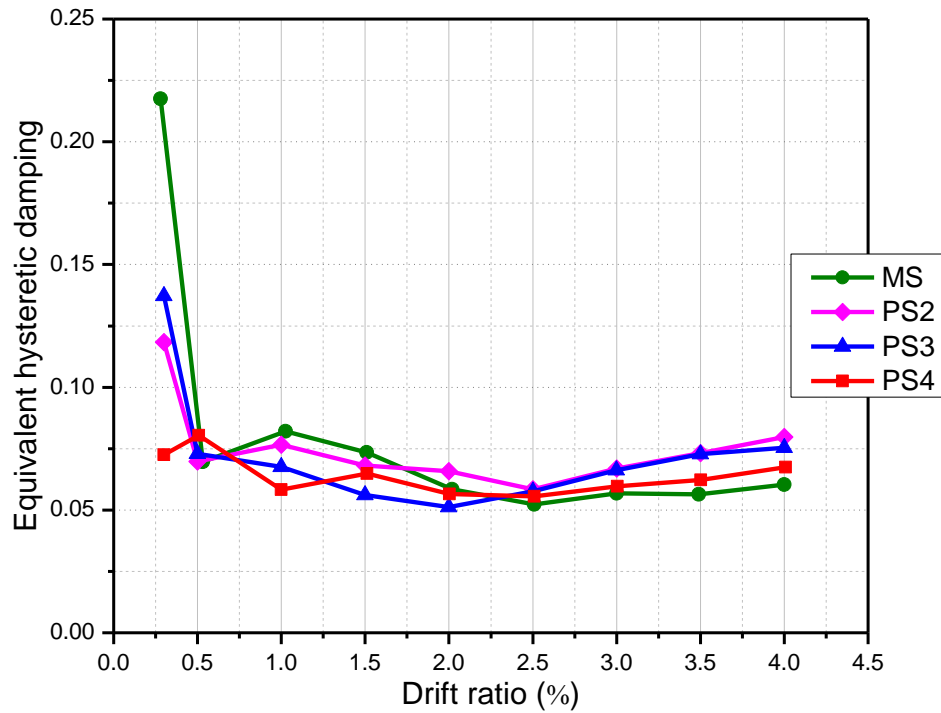


Fig. 2-14. Equivalent viscous damping ratio curves of the tested specimens.

2.2.4.6 Stiffness degradation

Stiffness degradation of specimens under quasi-static loading is usually defined by the secant stiffness changes of the load-displacement curves. However, when connecting the push and pull peaks of each cycle in the cyclic tests, the line does not go through the origin. In the current study, the effective stiffness was utilized to evaluate the stiffness degradation of the specimens in the cyclic tests. The slope of the line, which connected the push and pull peak loads, was used to determine the effective stiffness at each drift ratio (Fig. 2-15). The stiffness of all the specimens monotonically declined with the increase in the applied load. This observation is due to the numerous cracks formed at the concrete-end-plates and the crushes of concrete as shown in Fig. 2-6. The comparisons in the effective stiffness degradation among all the specimens are shown in Fig. 2-16.

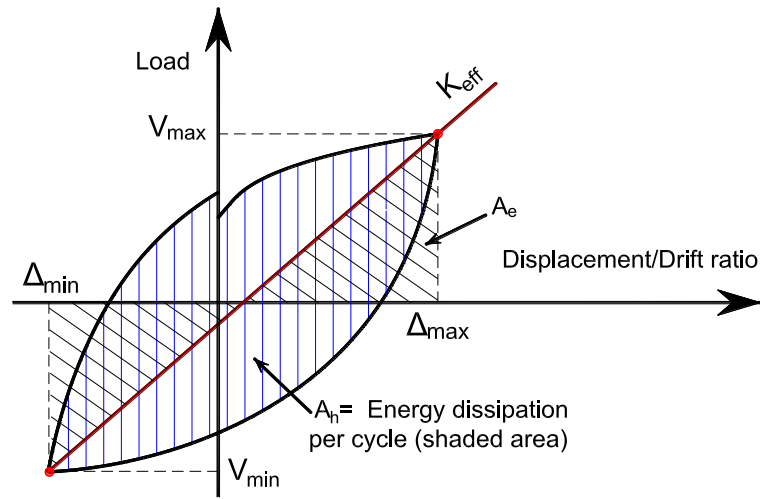


Fig. 2-15. Hysteretic energy dissipation and effective stiffness for cyclic response.

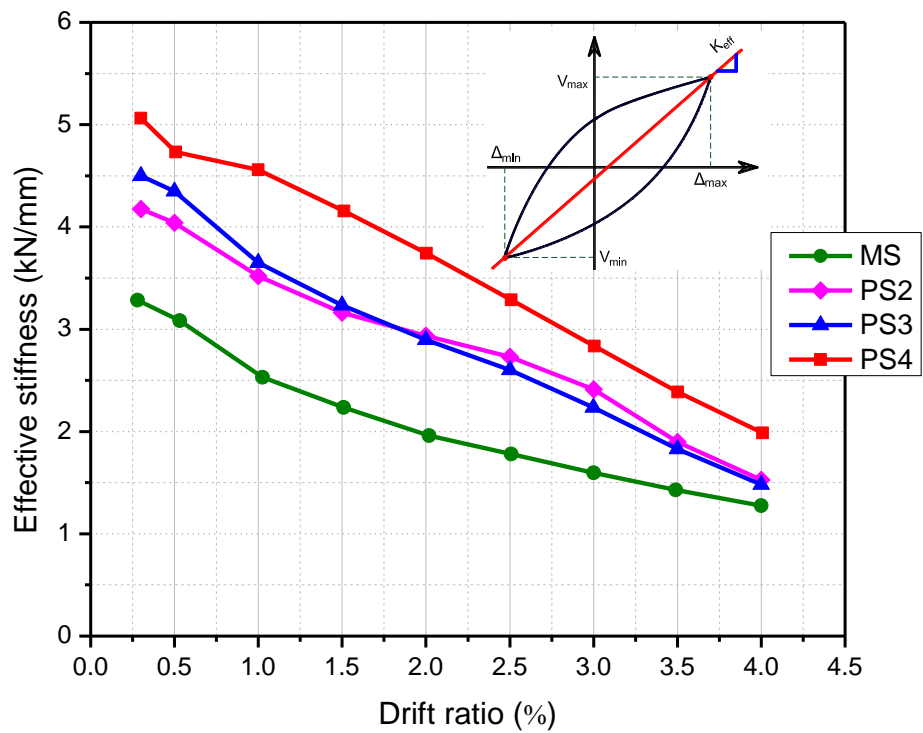


Fig. 2-16. Comparison of peak to peak stiffness.

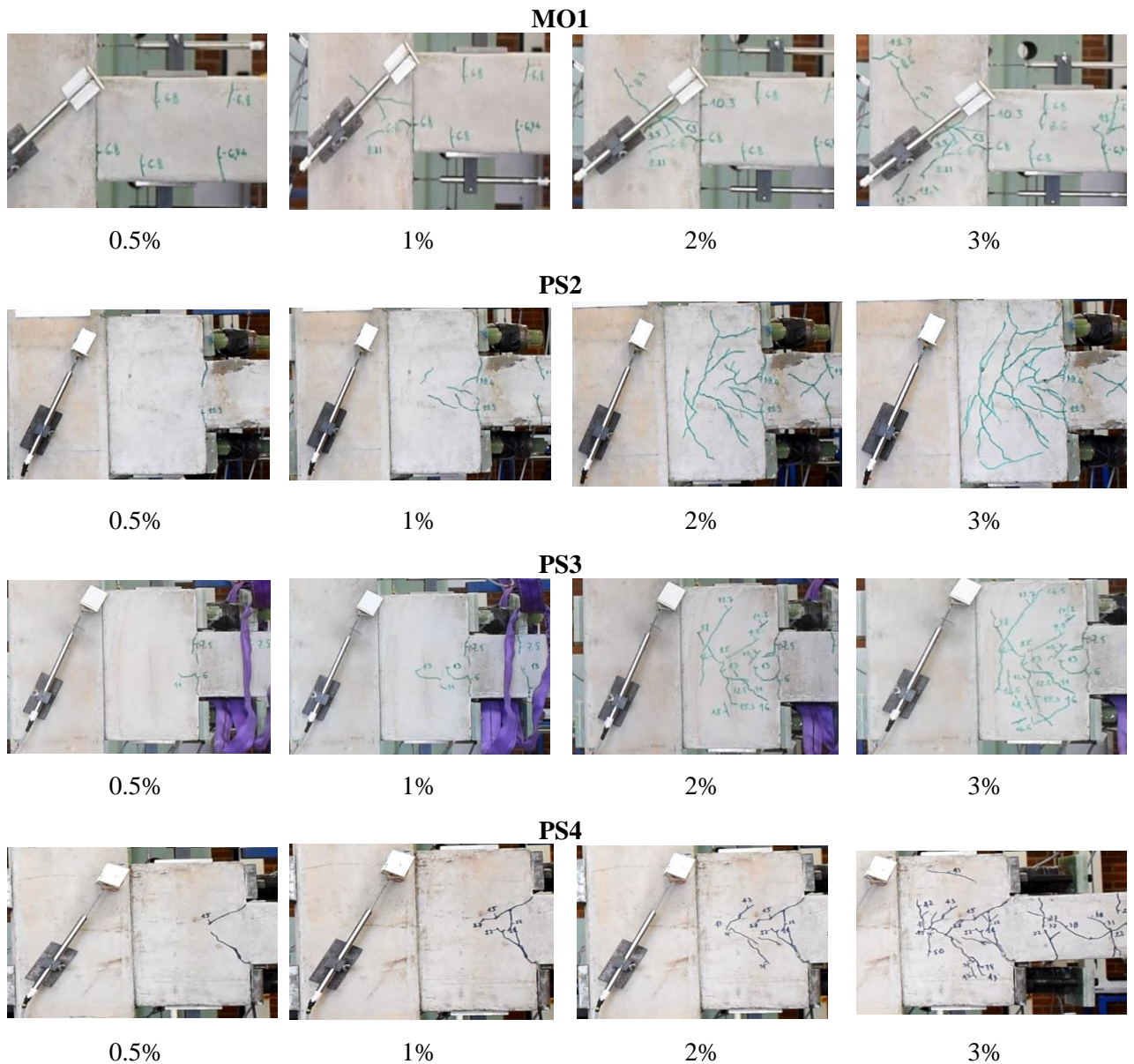


Fig. 2-17. The progressive failure process.

In general, all the precast specimens showed higher effective stiffness than Specimen MS until the drift ratio reached 4% because EI/l ratio of all the precast specimens was higher than that of Specimen MS (where EI and l are the flexural rigidity and the length of a member, respectively). The effective stiffness of all the specimens continuously reduced from the beginning of the test although the envelope curves (Fig. 2-11) showed nearly linear responses in the initial stage. This phenomenon is possible because the development of concrete cracks occurred early in this stage (Fig. 2-17). Additionally, the data of strain gauges at 0.5% drift ratio also indicated that the strain of concrete exceeded the value of $30\%\epsilon'_c$, so the concrete started to experience

nonlinear responses. The stiffness degradation trends of Specimens PS2 and PS3 were quite similar to each other, from drift ratio of 1% to 4%. The initial stiffness at 0.3% drift ratio of Specimens MS, PS2, and PS3 was less than that of Specimen PS4, by approximately 35.3%, 17.6%, and 11.8% respectively, because the elastic modulus of steel bolts (200 GPa) in Specimen PS4 was higher than that of CFRP bolts (100 GPa). As a result, Specimen PS4 exhibited the highest stiffness among the tested specimens.

2.2.4.7 Joint openings

The joint opening is not expected in this precast joint type during the service condition. However, when an excessive load (above the serviceability level) is applied to the joint, it may open and then close after the load reduces. Joint openings of Specimens PS2, PS3, and PS4 at the top surface and the bottom surface of the concrete-end-plate are shown in Fig. 2-18. It can be noted that the three specimens using the bolts to connect beams and columns reached the maximum opening at the drift ratio of 2.5%. This phenomenon may be explained that the elongation of the bolts reached the ultimate values at 2.5% drift ratio and then the development of the cracks on the concrete-end-plate, the fixed end, and Beam A mainly contributed to the deflection at the beam tip. Therefore, although the load-carrying capacity still increased at 3% drift ratio, the joint opening slightly decreased.

Fig. 2-18 showed that the joint opening of Specimen PS4 was very small (almost zero) while those of Specimens PS2 and PS3 were approximately 2.0 mm and 1.6 mm at 2.5% drift ratio, respectively. This phenomenon resulted from the effects of prestress levels in the bolts and the elastic modulus of the bolts. The prestress levels in steel bolts of Specimen PS4 were approximately 51 kN while those in the CFRP bolts of Specimens PS2 and PS3 were only 4.1 kN and 6.5 kN, respectively. The torsion resistance of CFRP bolts was quite low so they could not be prestressed to a high level. High prestress levels on CFRP bolts could lead to premature damage to the bolts as shown in Fig. 2-19. Meanwhile, the tensile forces in the top and bottom bolts at the concrete-end-plate measured by load cells during the tests are shown in Fig. 2-20. At the drift ratio from 0.3% to 1.5%, these tensile forces in Specimens PS2 and PS3 were similar due to the role of the prestress forces in the initial stage. After that, the load-carrying capacity of Specimen PS2 was higher than that of Specimen PS3. Therefore, the tensile forces in the CFRP bolts of Specimen PS2 were also higher than those of

Specimen PS3. Consequently, the maximum joint opening in Specimen PS2 was higher than that of Specimen PS3 as shown in Figs. 2-18 and 2-20. It is suggested that the CFRP bolts need to be prestressed to a higher level to minimize the joint opening. Further study is deemed necessary to overcome the problem associated with the low torsion capacity of the FRP bolts.

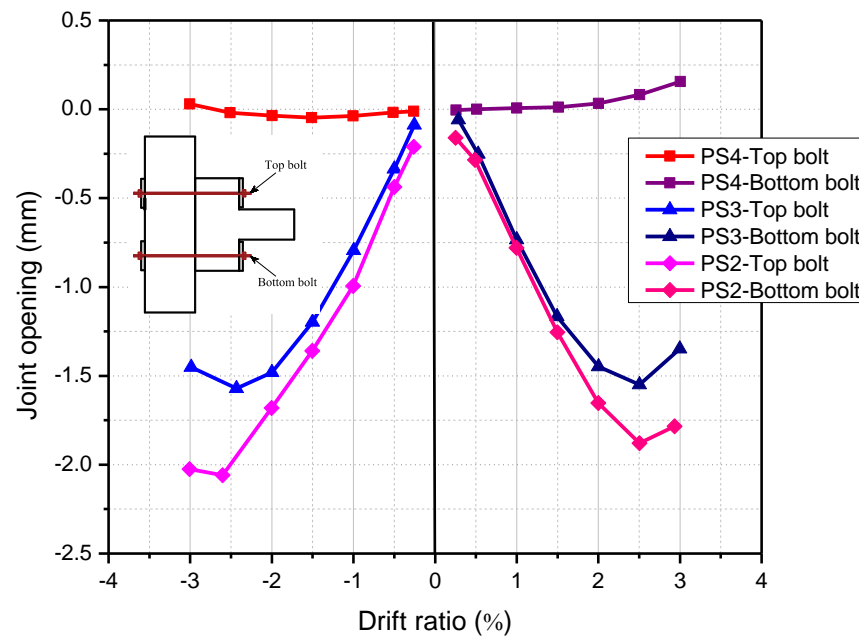


Fig. 2-18. Opening of joints at the top and bottom surface of the concrete-end-plate.



Fig. 2-19. The failure of CFRP bolts when being prestressed with a high level using a torque wrench.

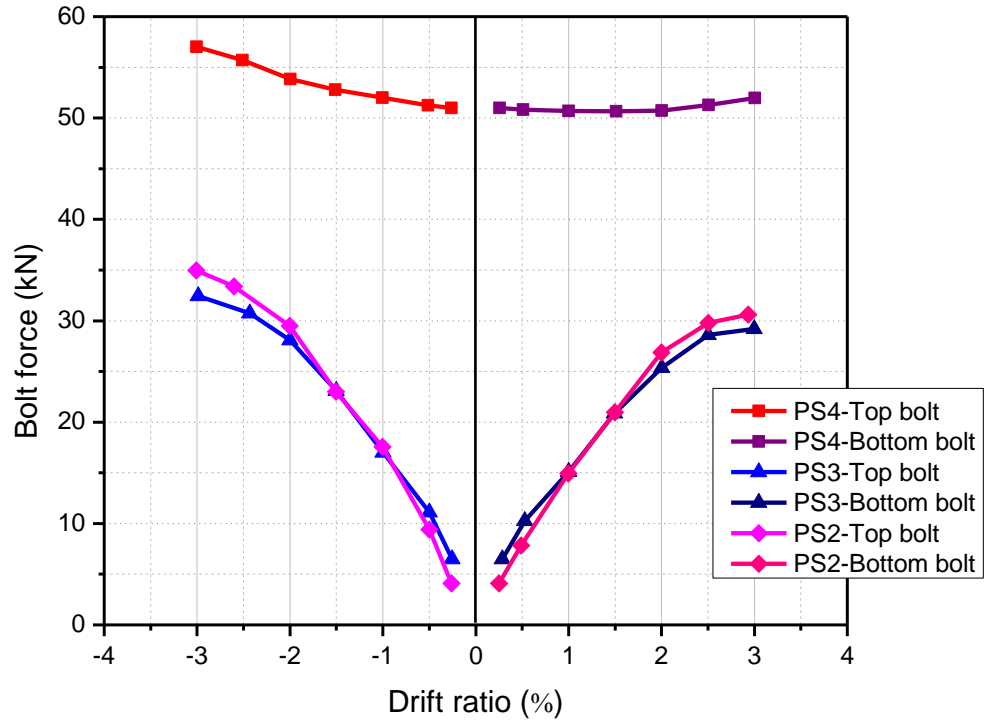


Fig. 2-20. Bolt forces at the top and bottom zone of the concrete-end-plate.

2.3 Analytical calculations

In this section, the design models for beam-column joints from previous studies are adopted to examine their suitability in predicting the capacity of the precast joints using CFRP bolts and steel bolts. The examined standards include ACI 318-11 [72], NZS 3101-06 [87], BS EN 1998-1-04 [88], AIJ-2010 [89]. It is worth mentioning that all these standards and Hwang and Lee [90] model were proposed for the analysis of monolithic beam-column joints. So far, there have been no models to calculate the nominal shear capacity of the bolted precast beam-column joints. ACI 318-11 [72] recommended the following equation to calculate the nominal shear capacity of monolithic beam-column joints:

$$V_n = \gamma \sqrt{f'_c} A_j \quad (2-4)$$

where γ refers to a set of constants related to the confinement of the joints, $\gamma = 1.7$ for joints confined by beams on all four faces, $\gamma = 1.2$ for joints confined by beams on two or three faces, $\gamma = 1.0$ for other cases, f'_c is the compressive concrete strength, A_j is the

effective joint area, and b_j and h_{col} are the effective joint width and depth, respectively, b_b and b_c are the width of beam and column, respectively, determination of b_b , b_c , h_{col} , and x is shown in Fig. 2-21,

$$A_j = b_j h_{col}, b_j = \min\{b_b + 2x, b_b + h_{col}\} \text{ if } b_c \geq b_b, b_j = b_c \text{ if } b_c < b_b$$

NZS 3101-06 [87] suggested the following equation to estimate the shear resistance of monolithic beam-column joints:

$$V_n = \min\{0.2f'_c A_j, 10 \text{ MPa} A_j\} \quad (2-5)$$

where $A_j = b_j h_{col}$, b_j has the same value of b_j in the model of BS EN 1998-1-04 [88].

BS EN 1998-1-04 [88] proposed the following equation for monolithic beam-column joints:

$$V_n = \lambda \eta f_{cd} \sqrt{1 - \left(\frac{v_d}{\eta}\right)} A_j \quad (2-6)$$

where λ depends on the joint types, $\lambda = 1$ for interior joints, $\lambda = 0.8$ for exterior joints, $\eta = 0.6 \left(1 - \frac{f'_c}{250}\right)$ is the reduction factor on concrete compressive strength due to tensile strains in the transverse direction, $f_{cd} = \frac{f'_c}{1.5}$ is the design value of concrete compressive strength, v_d is the normalized axial force in the column above the joints, $v_d = \frac{N_{Ed}}{A_c f_{cd}}$, N_{Ed} is an axial force from the analysis for the seismic design situation, A_c is the section area of the concrete column,

$A_j = b_j h_{jc}$, $b_j = \min\{b_c, b_b + 0.5h_{col}\}$ if $b_c \geq b_b$, $b_j = \min\{b_b, b_c + 0.5h_{col}\}$ if $b_c < b_b$, and h_{jc} is the distance between layers of column reinforcement.

AIJ-2010 [89] adopted the following equation to compute the nominal shear strength of beam-column joints:

$$\text{For mean value:} \quad V_{n,mean} = \alpha f'_c{}^{\beta} A_j, \quad (2-7)$$

$$\text{For lower value:} \quad V_{n,lower} = k \phi_j 0.8 f'_c{}^{0.7} A_j \quad (2-8)$$

where α , β , and k are based on the joint types, in which $\alpha = 0.8$, $\beta = 0.712$, and $k = 1.0$ for interior joints, $\alpha = 0.59$, $\beta = 0.718$, and $k = 0.7$ for exterior joints.

$\phi_j = 1.0$ for joints confined by beams on all four faces, $\phi_j = 0.85$ for other cases,

$A_j = b_j h_{col}$, $b_j = b_b + \min\left\{\frac{b_{a1}}{2}, \frac{h_{col}}{2}\right\} + \min\left\{\frac{b_{a2}}{2}, \frac{h_{col}}{2}\right\}$, values of b_b , b_{a1} , b_{a2} and h_{col} are shown in Fig. 2-21.

Hwang and Lee [90] suggested the following softened strut and tie model for beam-column joints:

$$V_n = K \zeta f'_c A_{str} \cos\theta \quad (2-9)$$

where $K = K_h + K_v - 1$ is tie index, K_h and K_v are horizontal and vertical tie indexes for under-reinforced cases, $K_h = 1 + (\bar{K}_h - 1)F_{yh}/\bar{F}_h \leq \bar{K}_h$, $K_v = 1 + (\bar{K}_v - 1)F_{yv}/\bar{F}_v \leq \bar{K}_v$,

$\bar{K}_h = \frac{1}{[1-0.2(\gamma_h + \gamma_h^2)]}$, $\bar{K}_v = \frac{1}{[1-0.2(\gamma_v + \gamma_v^2)]}$, \bar{K}_h and \bar{K}_v are horizontal and vertical tie indexes with enough horizontal and vertical reinforcements,

$\bar{F}_h = \gamma_h \bar{K}_h \zeta f'_c A_{str} \cos\theta$, $\bar{F}_v = \gamma_v \bar{K}_v \zeta f'_c A_{str} \sin\theta$, \bar{F}_h , \bar{F}_v are horizontal and vertical tie forces which horizontal and vertical ties reach yielding at failure,

$F_h = A_{th} E_s \varepsilon_h \leq F_{yh}$, $F_v = A_{tv} E_s \varepsilon_v \leq F_{yv}$, F_h and F_v are horizontal and vertical tie forces, F_{yh} and F_{yv} are yielding forces of horizontal and vertical ties, A_{th} and A_{tv} are the areas of horizontal and vertical ties, E_s is the elastic modulus of steel bars, ε_h and ε_v are the strains of horizontal and vertical ties, θ is the angle between the diagonal strut and the horizontal direction, γ_h , and γ_v are the force distribution coefficient, $\gamma_h = \frac{2 \tan\theta - 1}{3}$, $\gamma_v = \frac{2 \cot\theta - 1}{3}$, ζ is the softening coefficient, $\zeta \approx 3.35/\sqrt{f'_c} \leq 0.52$, $A_{str} = a_s b_s$, a_s and b_s are the depth and width of the diagonal strut, respectively,

$$a_s = a_c = \left(0.25 + 0.85 \frac{N}{A_g f'_c}\right) h_{col} \quad (2-10)$$

The effective area A_j , presented in ACI 318-11 [72], NZS 3101-06 [87], BS EN 1998-1-04 [88], AIJ-2010 [89], is shown in Fig. 2-21. In all the above standards, the column

width b_c is often larger than the effective joint width b_j . b_j in NZS 3101-06 [87] and in BS EN 1998-1-04 [88] is the same and h_{jc} in BS EN 1998-1-04 [88] is lower than h_{col} in ACI 318-11 [72], NZS 3101-06 [87], AIJ-2010 [89]. These differences lead to the effective joint areas A_j in BS EN 1998-1-04 [88] the lowest.

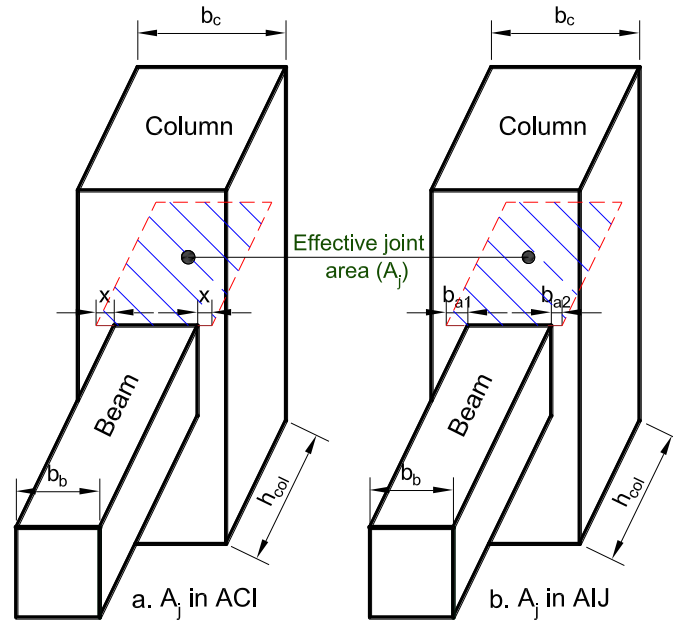


Fig. 2-21. Definition of the effective joint area.

Hwang and Lee [90] model proposed an assumption to determine the effective area of the diagonal struts A_{str} . The depth a_b of the compression zone in the beam was neglected in calculating a_s because only a small compression zone in the beam suffered from crushing. Hence, the depth of the struts can be computed by $a_s = a_c$. Additionally, the width of the diagonal strut b_s is defined as the effective width b_j of joints as recommended in ACI 318-11 [72]. In ACI 318-11 [72], BS EN 1998-1-04 [88], and AIJ-2010 [89], the effects of the confinement from the adjacent beams were investigated, whereas those effects were not mentioned in NZS 3101-06 [87]. Additionally, only BS EN 1998-1-04 [88] considered the effect of the axial load on the column. When the axial load decreases, there is an increase in the nominal shear capacity V_n in the joints (see Eq. 2-6). The concrete compressive strength is a crucial parameter to estimate the nominal shear capacity of beam-column joints. In addition, the tensile forces in the longitudinal reinforcements and the bolts were taken from data of the strain gauges and the load cells to calculate the joint shear force V_{jmax} in Specimens PS3 and PS4. For Specimen PS2, the yield stress was used to calculate

tensile forces in longitudinal reinforcements due to unreliable data of strain gauges on this specimen. The data of the strain gauges and the load cells are shown in Fig. 2-7 and Fig. 2-20.

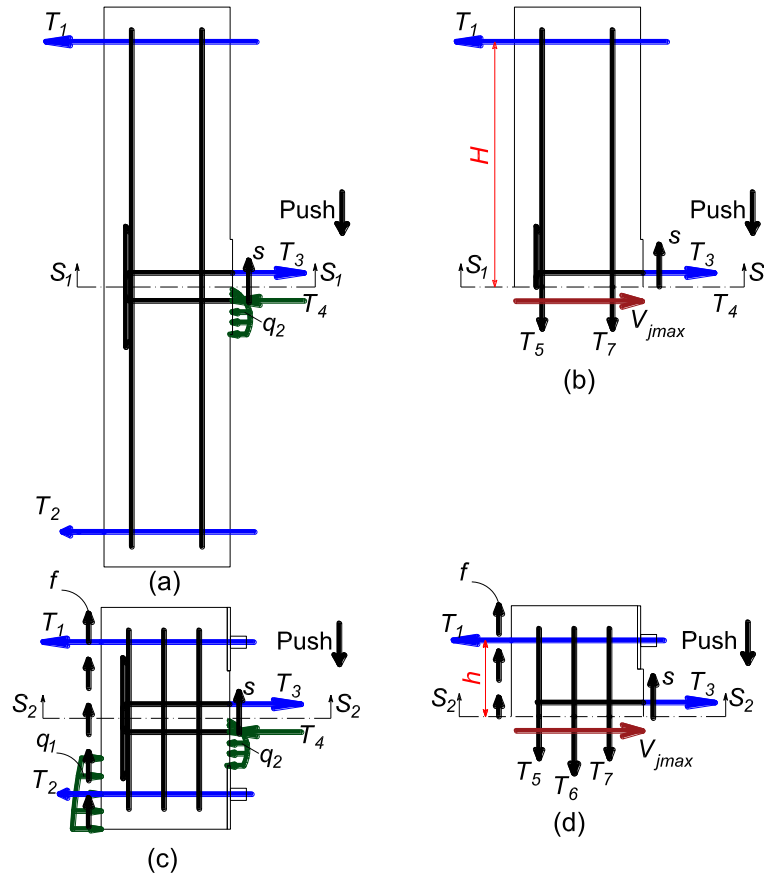


Fig. 2-22. Global equilibrium of exterior joints.

Fig. 2-22 illustrates the equilibrium conditions to calculate the shear capacity (V_{jmax}) in the joint. This value is determined as follows:

$$V_{jmax} = T_3 - T_1 \quad (2-11)$$

where T_1 is either the reaction force at column top of the monolithic specimen or tensile force in the bolts of precast specimens, T_3 is the tensile force in the longitudinal reinforcements. T_1 depends on H and h which are the distance from T_1 of monolithic and precast specimens to the central axis of the beam, respectively. From the equilibrium condition, T_1 is inversely proportional to H and h , in which H is significantly greater than h . This result indicates that the shear capacity (V_{jmax}) of Specimen MS is higher than that of Specimens PS3 and PS4. The shear capacity in the

experiment (V_{jmax}) and the nominal shear capacity V_n of all the tested specimens are listed in Table 2-5. Considering the data in Table 2-5, Fig. 2-23 and Fig. 2-24, it is clear that the safety factor of Hwang and Lee [90] model was higher than those of all the standards.

As can be seen from Figs. 2-23 and 2-24, most of the standards and Hwang and Lee [90] model predicted the shear capacity of Specimen MS with significant variations because the main failure mode of Specimen MS occurred in the beam at the fixed end. For all the precast specimens, all the standards and Hwang and Lee [90] model predicted the nominal shear capacity of the joints with variations up to 96.1%, as shown in Table 2-5. This result can be explained that the failure mechanism, which was used to calculate the nominal shear capacity V_n in the standards and Hwang and Lee [90] model, was different from the failure mechanism in these precast specimens. In all the standards, the nominal shear capacity was generally evaluated based on the diagonal compressive strut mechanism whereas the tensile cracks and the concrete crushing governed the main failure of these specimens, as discussed in the above sections. In addition, all the standards and Hwang and Lee [90] model do not consider the effects of prestress levels in the bolts. Further studies towards analytical models for this type of beam-column joint is deemed necessary.

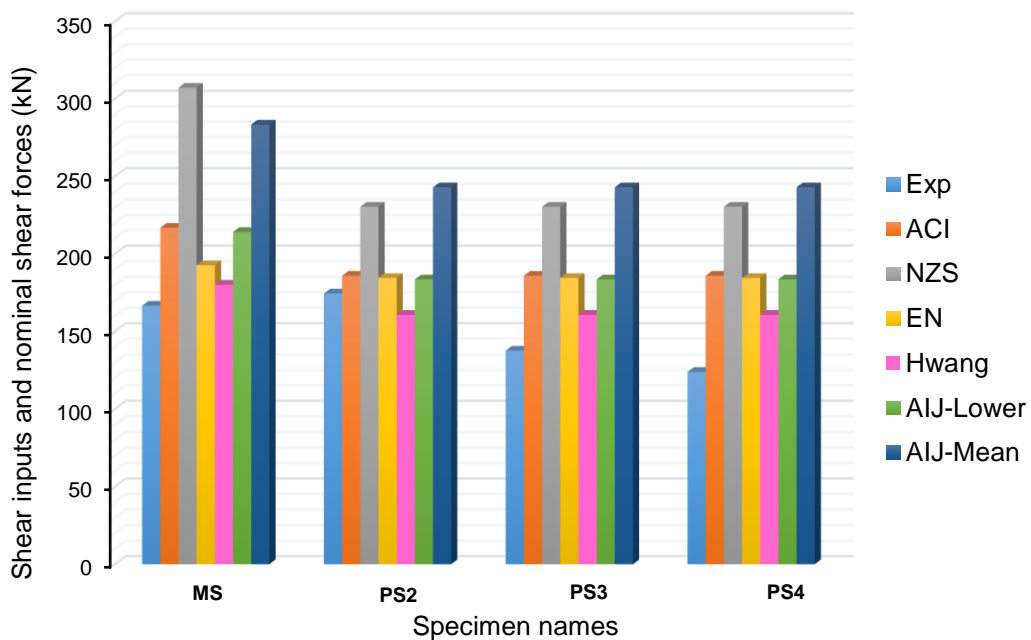


Fig. 2-23. Comparisons between the experiments and analytical results.

Table 2-5. The values of V_{jmax} from the experiment and V_n in the standards.

Name	V_{jmax} (kN)	ACI (V_n)	(%)	NZS (V_n)	(%)	EN (V_n)	(%)	Hwang (V_n)	(%)	AIJ		(%) Lower	(%) Mean
										(V_n), lower	(V_n), mean		
MS	166.6	216.9	30.2	307.2	84.4	192.7	15.7	180.1	8.1	214.1	283.4	28.5	70.1
PS2	174.5	185.9	6.5	230.4	32.0	184.5	5.7	160.7	-7.9	183.6	243.0	5.2	39.2
PS3	137.6	185.9	35.1	230.4	67.4	184.5	34.1	160.7	16.8	183.6	243.0	33.4	76.6
PS4	123.9	185.9	50.0	230.4	85.9	184.5	48.9	160.7	29.7	183.6	243.0	48.1	96.1

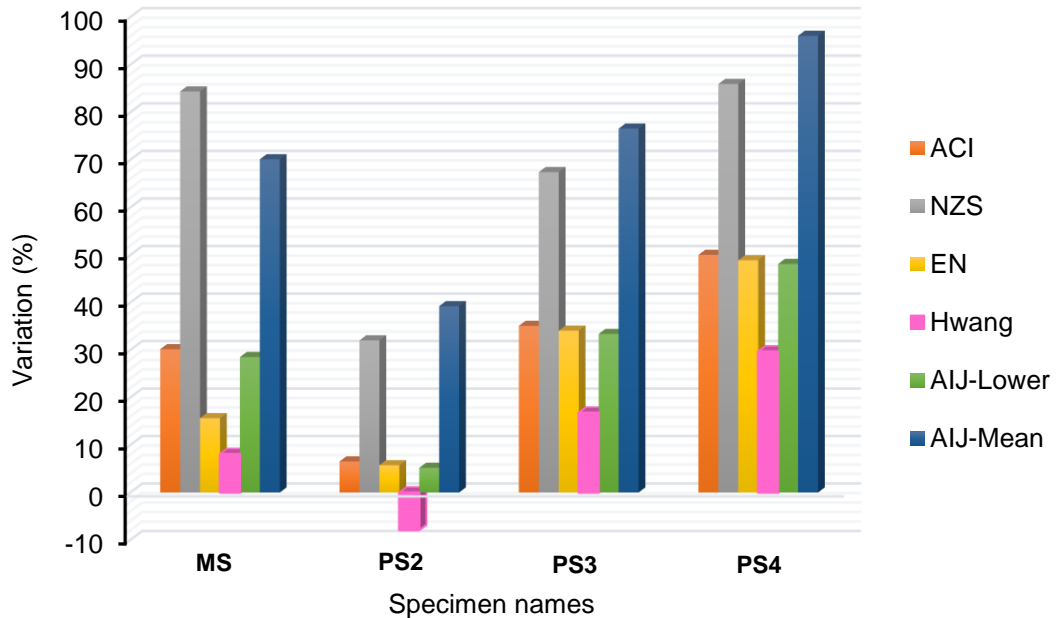


Fig. 2-24. Variations between the experiments and analytical results.

For Specimen MS, the nominal shear capacity V_n calculated by ACI 318-11 [72], NZS 3101-06 [87], BS EN 1998-1-04 [88], lower-AIJ-2010 [89], mean-AIJ-2010 [89], and Hwang and Lee [90] model was higher than V_{jmax} about 30.2%, 84.4%, 15.7%, 28.5%, 70.1% and 8.1%, respectively. For precast specimens, the nominal shear capacity V_n of Specimen PS2 estimated by the ACI 318-11 [72], BS EN 1998-1-04 [88], and lower-AIJ-2010 [89] shows nearly the same value as V_{jmax} . Meanwhile, all the standards predicted the nominal shear capacity of Specimens PS3 and PS4 with considerable variations. The lowest variation of 33.4% was for Specimen PS3 using lower-AIJ-2010 [89] while the highest variation was 96.1% when using mean-AIJ-

2010 [89] to estimate the capacity of Specimen PS4. Hwang and Lee [90] model predicts the nominal shear capacity of Specimens PS3 and PS4 with relatively smaller variation of 16.8% and 29.7%, respectively.

2.4 Summary

The proposed dry beam-column joints exhibited good performances and, therefore, can be potentially used in the prefabrication construction in both non-earthquake and earthquake-prone regions. From the experimental results and observations, the following conclusions were drawn.

1. CFRP bolts can well replace steel bolts to effectively mitigate corrosion problems.
2. The main failure occurred in the middle zone rather than at the top and bottom zones of the concrete-end-plates. This result is different from the observation reported in the previous study of Saqan [14].
3. The maximum applied load and effective stiffness in all the precast specimens were higher than those of the monolithic specimen by approximately 27-61% and 27-55%, respectively.
4. The ductility of Specimens PS3 and PS4 and MS was almost the same (2.2 vs 2.4). The ductility of Specimen PS2 was smaller than others due to a lack of confinement from steel spirals in the concrete-end-plate.
5. The overall dissipated energy of the precast specimens exceeded Specimen MS approximately by 45-75%. Drift ratio of all the precast specimens achieved 3% which satisfied the requirement of CSA A23.3-07 [17] and ASCE 41-06 [18] standards. Therefore, the proposed dry joint could be well applied in earthquake-prone regions.
6. The higher prestress level could not only improve the loading capacity but also reduce the joint openings of the precast beam-column joints.
7. The model recommended by ACI 318-11 [72], BS EN 1998-1-04 [88], lower-AIJ-2010 [89], and Hwang and Lee [90] predicted the nominal shear capacity of Specimens PS3 and PS4 with significant variations.

In conclusion, the proposed dry joint with CFRP bolts can effectively mitigate corrosion problems in the conventional dry joints but still meet the requirement for constructions in non-seismic and seismic-prone zones.

CHAPTER 3: EFFECTS OF STEEL FIBRES AND PRESTRESS LEVELS ON BEHAVIOUR OF NEWLY PROPOSED EXTERIOR DRY JOINTS USING SFRC AND CFRP BOLTS

ABSTRACT²

This chapter proposes a new type of dry exterior beam-column joints for precast moment-resisting concrete frames. This dry joint type uses steel fibre reinforced concrete (SFRC) and carbon fibre reinforced polymer (CFRP) bolts to improve the joint capacities. In addition, an analytical model to predict the load-carrying capacity of this precast joint type is also proposed. Five exterior beam-column joints were cast and tested under quasi-static cyclic loads until failure. The experimental results revealed that the use of SFRC significantly improved all the indices, including the load-carrying capacity, drift ratio, ductility, energy dissipation and stiffness. Also, the proposed joints outperformed the monolithic specimen in terms of load-carrying capacities, energy dissipation, and stiffness by 27%-61%, 45%-75%, and 27%-55%, respectively. Particularly, the drift ratio of the proposed joints reached 3.5%, which satisfies the requirements for ductile joints to be used in earthquake-prone regions according to various standards. Finally, the proposed model yielded good predictions as compared to the experimental results with minor variations of approximately 0.9%-2%. These exciting results indicate that the use of SFRC and CFRP bolts could help to avoid the challenging issue of corrosion in the conventional dry exterior joints and still ensure the sufficient requirements for reinforced concrete structures in non-seismic and seismic-prone areas.

² This work was published in **Engineering Structures** with the full bibliographic citation as follows:

Ngo TT, Pham TM, Hao H. Effects of steel fibres and prestress levels on behaviour of newly proposed exterior dry joints using SFRC and CFRP bolts. *Eng Struct* 2020;205:110083.
<https://doi.org/10.1016/j.engstruct.2019.110083>

3.1 Introduction

Beam-column joints serve as an important component of a reinforced concrete (RC) structure to guarantee the integrity and overall stability when the frame is subjected to a cyclic lateral load [1]. Under seismic loading, shear stress significantly concentrates at beam-column joints whereas in some cases transverse reinforcements are not sufficient to resist this shear stress [40, 91]. Therefore, various inclined cracks in two directions develop and cause brittle shear failure in beam-column joints. This brittle shear failure causes numerous serious consequences since it often occurs suddenly without any warnings before the total collapse of buildings [1, 45]. Various recent devastating earthquakes across the world have demonstrated this dangerous brittle failure, such as the 1995 Hyogo-ken (Japan), the 1999 Kocaeli (Turkey), and the 1999 Chi-Chi (Taiwan) earthquakes and many more. The brittle shear failure is an undesirable result of non-ductile performance, caused by either inadequate anchorage of the main reinforcing bars or a shortage of transverse reinforcements in the joint [92, 93]. Therefore, it is crucial to improve the ductility of beam-column joints.

Most of existing studies focused on investigating the structural performances of monolithic, wet or hybrid joints [7-9, 45, 54, 58, 94, 95] concerning their good performances in terms of strength, stiffness, energy dissipation capacity, and especially ductility under cyclic loadings. Nevertheless, the use of these joints has revealed some shortcomings, such as higher construction time and construction cost. Actually, most of these disadvantages could be overcome with the application of dry joints. Dry joints use mechanical connections to assemble prefabricated structural components and, thus, do not require formworks [14, 96, 97]. Also, these joints require fewer efforts on the construction quality control. Additionally, it is easier and more cost-effective to have dry joints directly recycled [13-15, 96-99]. Despite their advantages, the use of dry joints in reality is still limited due to their remaining disadvantages, such as inadequate ductility, strength, and vulnerability to corrosion damage. Among them, corrosion is the most costly issue and is the main cause for structure deterioration, i.e. it has been estimated that the average annual cost of maintaining and improving bridges in the United States of America could respectively reach \$5.8 billion and \$10.6 billion during the period of 1998 to 2017 [100]. Corrosion is more likely to occur in traditional dry precast joints since such connecting elements

as steel bolts, plates, and tendon strands are not covered and protected by concrete. Corrosion of the connecting elements might lead to serious damage or even collapse of the entire structures even though other parts of the building are still in a good condition [3, 57, 101]. More problematically, in some cases, the repairing and maintaining costs of damaged members could be twice as much as the original ones [5, 6].

To improve the performance of dry joints, Chapter 2 proposed dry joints with concrete-end-plate and CFRP bolts which showed excellent performance in all the important indices such as the load-carrying capacity, energy dissipation, ductility and stiffness compared to conventional monolithic joints. Replacing steel bolts with CFRP bolts helps to resolve the corrosion issue effectively. These promising results indicated that those proposed precast joints could be potentially applied to prefabrication constructions in non-seismic and seismic-prone areas. Also, the results showed that the main failure of this joint type was caused by inclined cracks induced by shear stresses [19]. To avoid such failure, the contemporary design standards [71, 72, 87, 88] require a high percentage of stirrups in the concrete-end-plate. These requirements could lead to steel congestion, construction difficulties, and size increase of the concrete-end-plate. Meanwhile, in order to ensure the architectural requirements, it is necessary to reduce the size of the concrete-end-plate which might cause the slip and anchorage failure of the beam's longitudinal reinforcements.

Considering the above issues, fibre reinforced concrete (FRC), as later proposed and investigated in the current chapter, might be a potential solution. FRC offers higher tensile strength, greater shear resistance, higher toughness, better bond, and greater seismic resistance than conventional concrete [40, 92, 102-107]. It is well-known that conventional concrete exhibits excellent behaviours in compression but weak performance in tension. This disadvantage could be resolved by the inclusion of suitable fibre volume to improve the pre-cracking and post-cracking performance [105-107].

Fibres are popularly used in FRC in four types, including steel fibres, glass fibres, carbon fibres, and synthetic fibres. Fibres are not only used to improve the structural strength but also to other aspects of structural performances due to their numerous benefits, including chemical resistance, corrosion resistance, and abrasion resistance.

Glass fibres have been used since the late 1960s and offered excellent engineering properties [92]. For example, these fibres exhibit high tensile strength (2-4 GPa) and elastic modulus (40-80 GPa). However, durability is a disadvantage of glass fibres because the fibres suffer a significant strength reduction when they are exposed to harsh environments. Therefore, glass fibre reinforced concrete has not been popularly applied in reality. As the second type of fibres, carbon fibres have higher tensile strength and elastic modulus than glass fibres. However, their application has still been limited because they are more expensive than other types of fibres. Meanwhile, synthetic fibres, which are produced from the textile and petrochemical industries, contribute approximately half of all fibre utility. There are various classes of synthetic fibres but nylon, acrylic, polyester, and polyolefin dominate in the market. Also, synthetic fibres have significantly different levels of tensile strength and elastic modulus, approximately 230-1100 MPa for tensile strength and 5-19 GPa for elastic modulus [108]. Besides, steel fibres have been applied in concrete since the early of the 1990s and there have been various changes in shapes until now [92]. The early steel fibres had a round, straight, and smooth form with chopped lengths. This steel fibre type has been rarely used in recent years and is almost replaced by modern steel fibres with a deformed surface of hooked ends to ensure a better anchorage in concrete. In general, steel fibres exhibit ductile stress-strain characteristics with high tensile strength (0.5-2 GPa) and elastic modulus (up to 200 GPa) [92]. Considering the comparisons of these fibre types, steel fibres were chosen for the current study.

In the literature, there have been only two experimental studies investigating the joint behaviours using the concrete-end-plate and steel bolts [13, 14]. However, steel bolts in the connections are susceptible to corrosion, thus, Chapter 2 proposed CFRP bolts to replace these steel bolts. Chapter 2 found that the inclined cracks at the middle zone of the concrete-end-plate are the main failure mode of this precast joint type. Therefore, the current chapter investigates the use of SFRC to minimize the inclined cracks on the concrete-end-plate and thus improve the load-carrying capacity, ductility, energy dissipation, stiffness and drift ratio of these joints. In addition, the current chapter also investigates the effects of the prestress levels on the bolts. Finally, since there is no analytical model for this precast joint type, this chapter also proposes an empirical model for this precast joint type so that it could be effectively applied in practice.

3.2 Experimental program

Five specimens were cast and examined under quasi-static cyclic loads until failure to evaluate effects of various parameters on their performance. The five specimens, namely M1, P2-C-SP, P3-C-NSP-F, P4-S-SP-H, and P5-S-SP, were labelled based on their characteristics. The letters “M” and “P” indicate the reference monolithic specimen and the precast specimens, respectively. The letters “C” and “S” denote the use of CFRP bolts or steel bolts. The letters “NSP”, “SP”, and “F” represent the use of no spirals, spirals, and steel fibres in the concrete-end-plate, respectively. Among the specimens, only Specimen P4-S-SP-H was prestressed at a high level of 51 kN so the letter “H” is used to distinguish this difference while the prestressing force of other specimens was approximately 6.5-10.5 kN. The 20-mm diameter bolts were used for all the precast specimens.

3.2.1 Design of the specimens

To investigate the effects of steel fibres and prestress levels on the structural response of the beam-column joints using concrete-end-plate and bolts, four precast exterior beam-column joints were designed based on previous studies [13-15, 19]. It should be noted that there were no specific standards for the precast joints using bolts and concrete-end-plates. The monolithic specimen which had similar dimensions of the precast specimens was designed in accordance with ACI 352R-02 [71] and ACI 550R-96 [70], and was served as a reference specimen. The design philosophy of strong column and weak beams was applied to all the specimens. The columns in all the specimens had the same length of 1280 mm with a square-shaped cross-section of $200 \times 200 \text{ mm}^2$. Four deformed steel bars with a diameter of 16 mm, placed at the four corners, were used as longitudinal reinforcements. Stirrups with a diameter of 10 mm were arranged with a spacing of 70 mm to resist shear forces in the columns (Fig. 3-1).

There are two components on the beams of the precast specimens, including (1) the concrete-end-plate and (2) a rectangular beam, namely Beam A. All the beams also had a square cross-section of $150 \times 150 \text{ mm}^2$ and were reinforced with 16-mm deformed bars. Additionally, the shear reinforcements of these beams, which had the same diameter of 10 mm, were also placed with a spacing of 70 mm. The size of Beam A

was $150 \times 150 \times 520 \text{ mm}^3$ while that of the concrete-end-plate was $350 \times 150 \times 200 \text{ mm}^3$ as exhibited in Fig. 3-1.

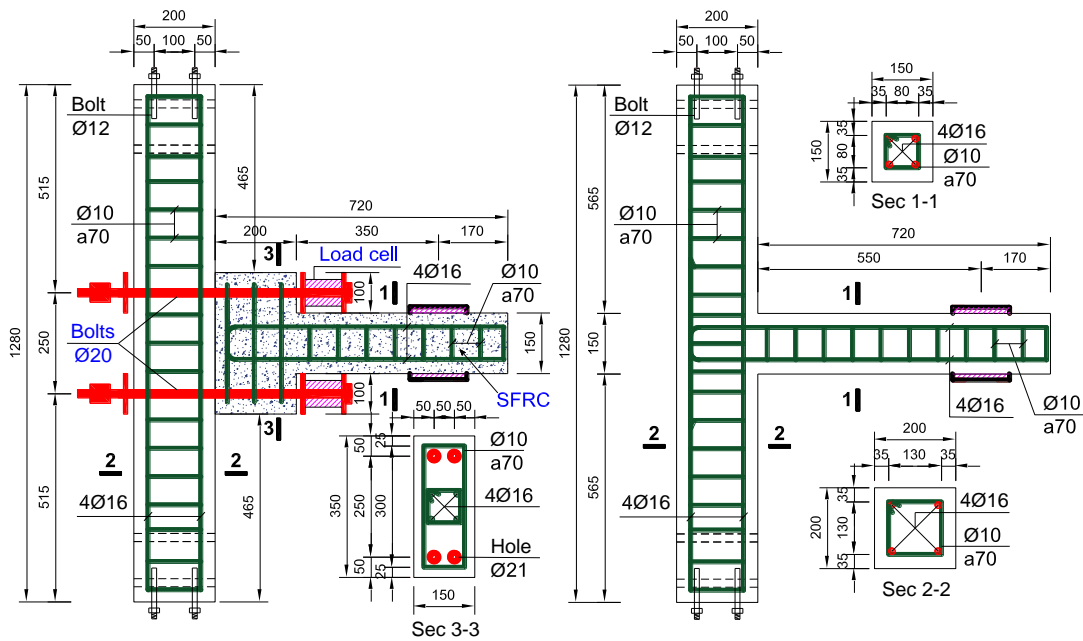


Fig. 3-1. Designs of the precast specimen (left) and monolithic specimen (right) (unit: mm).

To monitor strain of concrete inside the concrete-end-plate, 6.1-mm aluminium bars were placed in the assumed direction of the concrete strut and strain gauges were attached to these bars as shown in Fig. 3-2. In addition, to ensure the sufficient bond between the concrete and the aluminium bars, notches were created by a cutting machine. All the beams and columns had a clear concrete cover of 35 mm as per ACI 318-11 [72]. The prestress level and the tensile force in the bolts during the test are important parameters which affect the load-carrying capacity and joint opening of this kind of joint [19]. Therefore, this current study used two load cells with a capacity of 20 ton to monitor the tensile forces in the bolts during the tests as shown in Fig. 3-3.

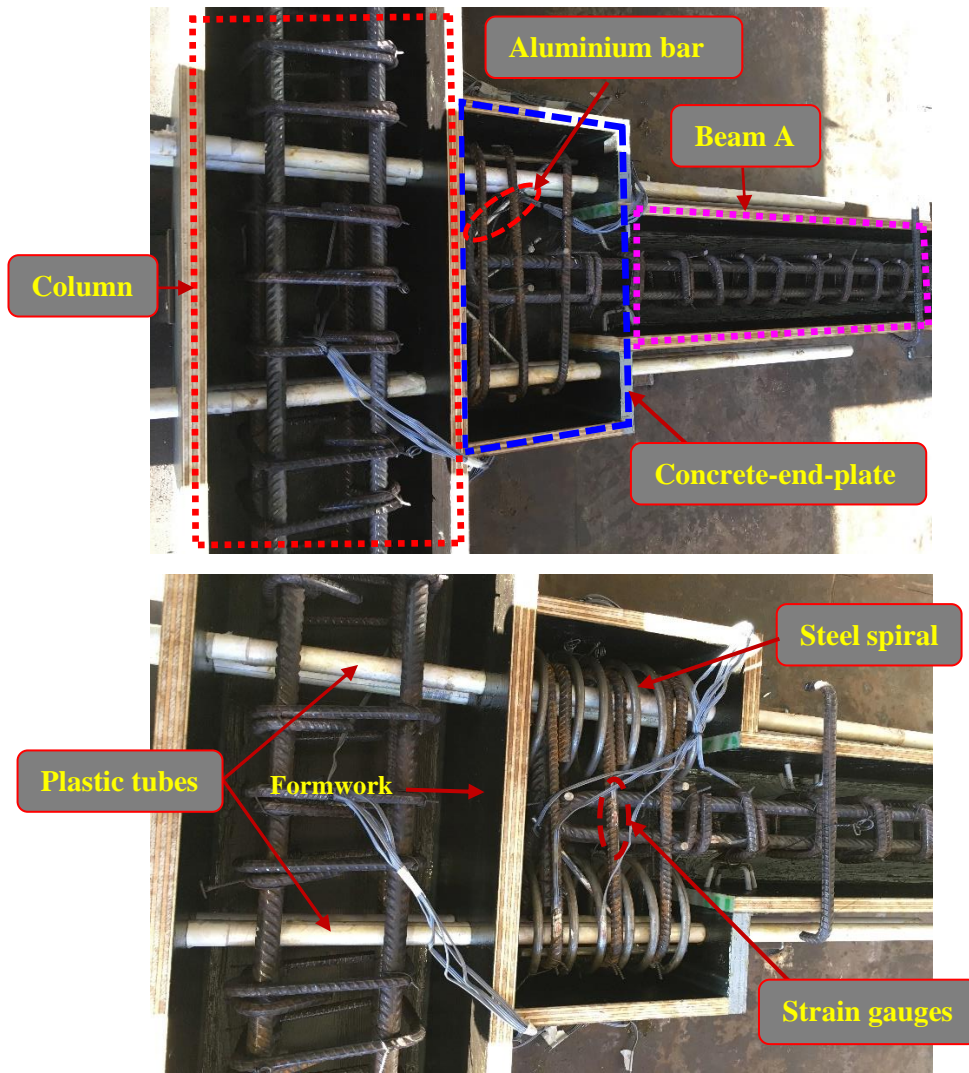


Fig. 3-2. Details of the reinforcements.

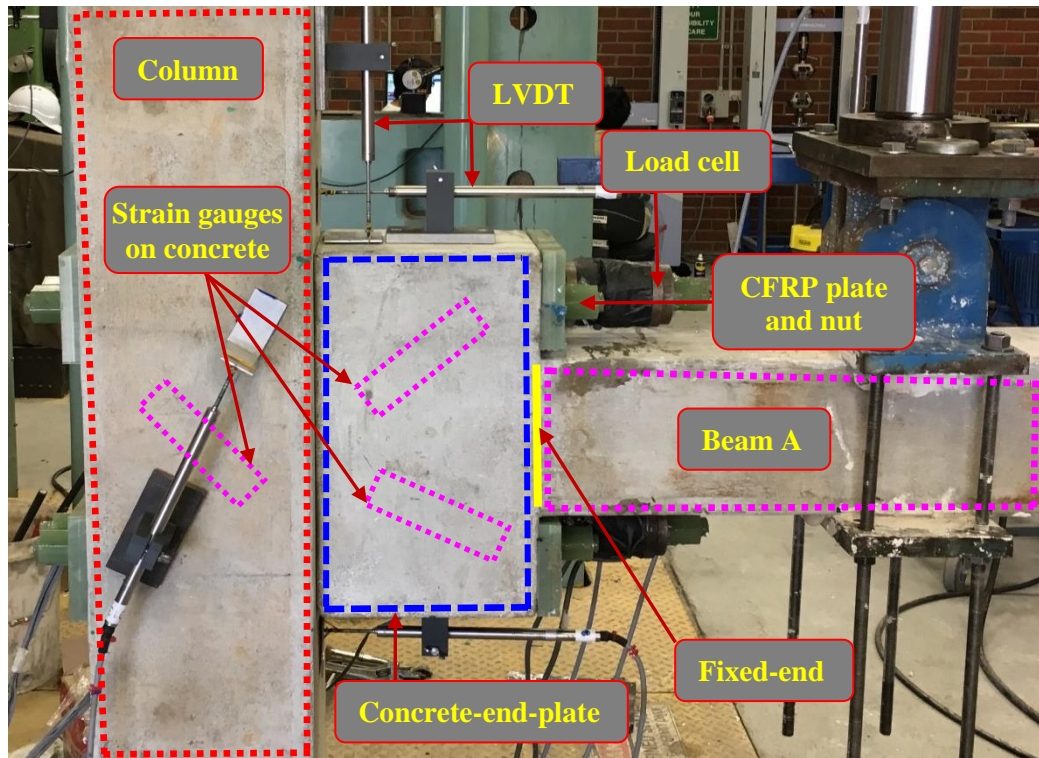


Fig. 3-3. Positions of load cells on the bolts and strain gauges on the concrete-end-plate.

3.2.2 Mechanical properties of materials

Ready-mixed concrete from local suppliers (i.e., Western Australia) was used to cast the specimens. For the beam of Specimen P3-C-NSP-F, the concrete was mixed with 1% fibre volume by a concrete-mixer in the Civil Engineering Laboratory, Curtin University. The average compressive strength (f'_c) and tensile strength (f_{ct}) on the testing day were 38.4 MPa and 3.8 MPa for conventional concrete, and 32.3 MPa and 4.3 MPa for SFRC, respectively. It is noted that Specimen P3-C-NSP-F was cast by a different concrete batch from the other four specimens. The hook-ended steel fibres were supplied by TEXO company [109]. The length and the diameter of steel fibres were 35 mm and 0.55 mm, respectively. The tensile strength, elastic modulus, and aspect ratio (l/d) were 1350 MPa, 210 GPa, and 65, respectively. Conventional steel bars of 8 mm, 10 mm, and 16 mm were used for spirals, stirrups, and longitudinal reinforcements, respectively. Bolts, nuts, and plates were produced from CFRP material and were provided by J and R Metalwork Industry Pty Ltd [76]. Other properties of these steel bars, aluminium bars, CFRP bolts, and CFRP nuts, which were provided by the manufacturers, are presented in Tables 3-1 and 3-2. Strain gauges with

the length of 60 mm and 5 mm were attached on concrete surfaces, longitudinal reinforcements, aluminium bars, and stirrups to measure their strain. Locations of these strain gauges are specified in Figs. 3-2 and 3-3.

Table 3-1. Steel reinforcements and aluminium bars properties.

Diameters	f_y	f_u	E_s	Area	Notes
(mm)	(MPa)	(MPa)	(GPa)	(mm ²)	
8	377	522	200	50	Spirals
10	560	675	200	78	Stirrups
16	597	706	200	201	Longitudinal reinforcements
6.3	110	150	69	31	Aluminium bars

Table 3-2. Details of CFRP bolts, nuts, and plates [76].

Names	Size	Tensile strength	Shear strength	Bending strength	Compressive strength	Ultimate load	Impact strength	Elastic modulus	Weight
	(mm)	(MPa)	(MPa)	(MPa)	(MPa)	(kN)	(kJ/m ²)	(GPa)	(g)
Bolts	φ20	≥ 850	≥ 160	480	760	≥ 267	185	100	376
Nuts	φ20	*	*	*	*	100	*	100	44
Plates	150×90×20	*	*	*	*	≥ 100	*	100	540

Note: * not given.

3.2.3 Test setup

The columns of the precast specimens were connected to a steel frame, followed by the setup of the beam. CFRP plates with a size of 150×90×20 mm³ were positioned into the CFRP bolts before the nuts were tightened with a torque wrench. The torsion level applied to the nuts was 80 Nm to avoid concentrated stresses around the bolts [19]. The main hydraulic jack was placed at the beam tip with a distance of 550 mm from the column surface to apply a vertical quasi-static cyclic load. Another hydraulic jack was placed on the column top to apply the vertical restraint with an axial force of 15 kN. This force was maintained as low as possible to minimize beneficial effects of axial force on the capacity of the joints [79]. The schematic setup and details are presented in Fig. 3-4. All the exterior joints were subjected to quasi-static cyclic loads

until failure and the loading history is shown in Fig. 3-5. All the testing process was conducted under displacement control at the rate of 6-9 mm/min.

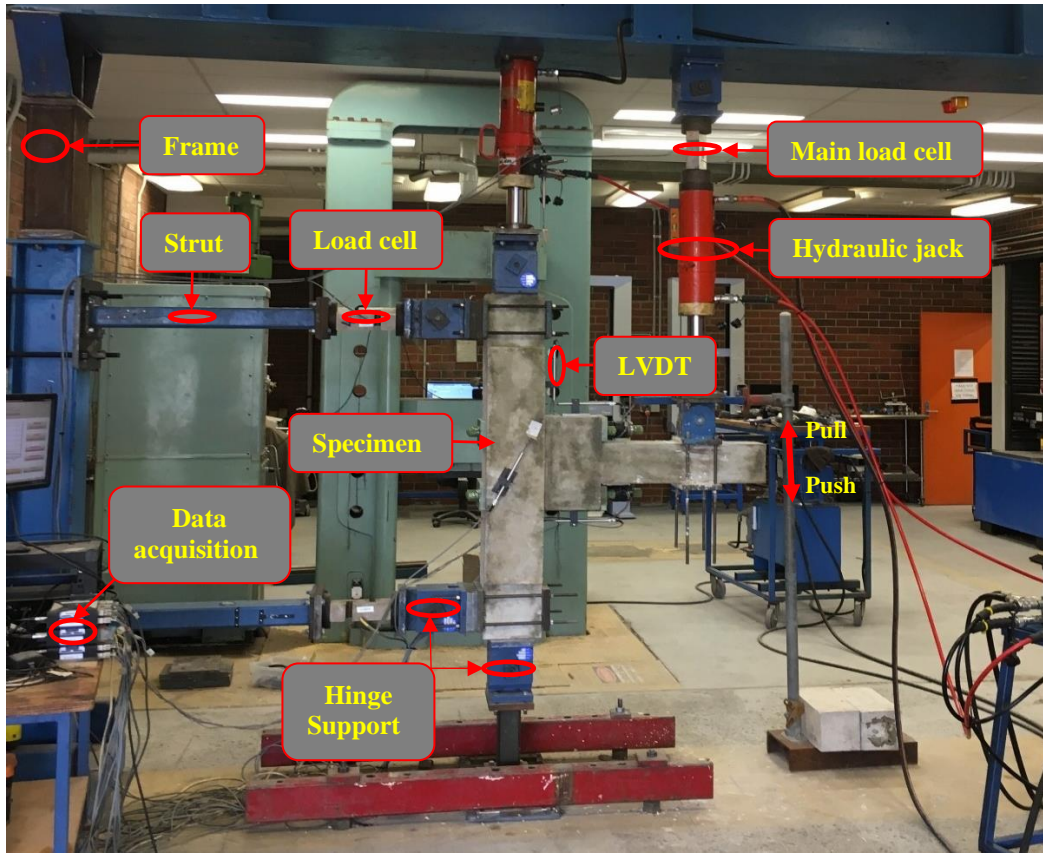


Fig. 3-4. Details of the test setup.

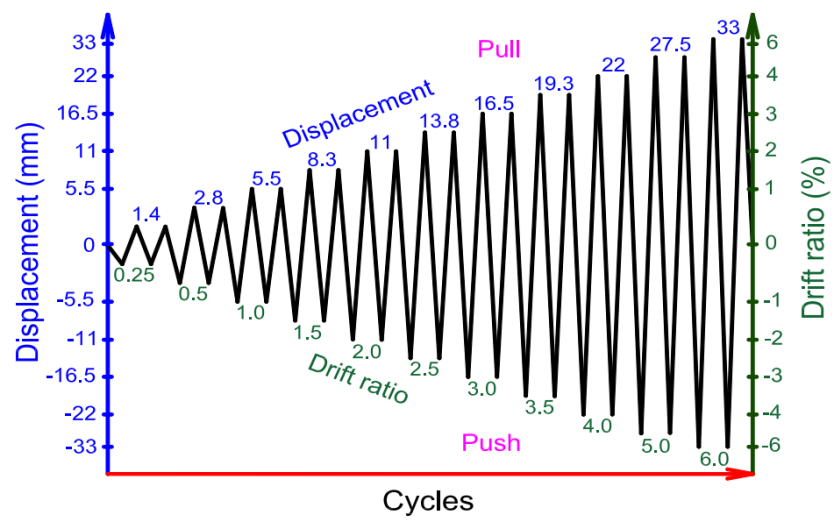


Fig. 3-5. Cyclic loading history.

3.2.4 Experimental results and discussion

3.2.4.1 Hysteretic response

The applied load versus drift ratio responses of all the specimens are presented in Figs. 3-6 and 3-7. Overall, the applied load-displacement hysteretic responses were almost symmetrical in both push and pull directions because there were the same top and bottom reinforcements in all the tested specimens. Nevertheless, after the peak loads, the hysteretic curves were asymmetrical because of large and irreversible deformation, which was also reported in the previous studies [14, 15]. The hysteresis loops of Specimens P2-C-SP, P4-S-SP-H, and P5-S-SP were quite similar to each other, with almost linear responses until 2% drift ratio and then the applied load slowly increased until achieving the peak load at 3% drift ratio. After 3% drift ratio, the applied load dropped although the displacement at the beam tip still increased. During this stage, the CFRP bolts and steel bolts did not reach the yielding points until the specimen failure while the longitudinal reinforcements still behaved linearly up to 3% drift ratio as seen in Fig. 3-8, which shows the measured strain of the reinforcements on the beams and the concrete-end-plates. The dots in this figure show their maximum strain at each cycle. Consequently, the concrete governed the main failure with various inclined cracks on the concrete-end-plate. These inclined cracks resulted in degradation in the applied load after reaching the peak load. Meanwhile, Specimen P3-C-NSP-F underwent more ductile responses than other precast specimens when reaching the peak load at the drift ratio of 3.5%. After 1.5% drift ratio, the hysteresis loop exhibited nonlinear behaviours up to the peak load. Afterwards, the applied load approximately obtained a plateau within a range of the drift ratio from 3.5% to 5.0%. This is a favourable response of an important structural member such as beam-column joints. This great improvement was due to the contribution of steel fibres inside the concrete-end-plate. Since SFRC had higher tensile strength (4.3 MPa) than conventional concrete (3.8 MPa), the inclined cracks on the concrete-end-plate, which caused the main failure of this kind of joint [19], were effectively minimized (see Fig. 3-9(P3-C-NSP-F)).

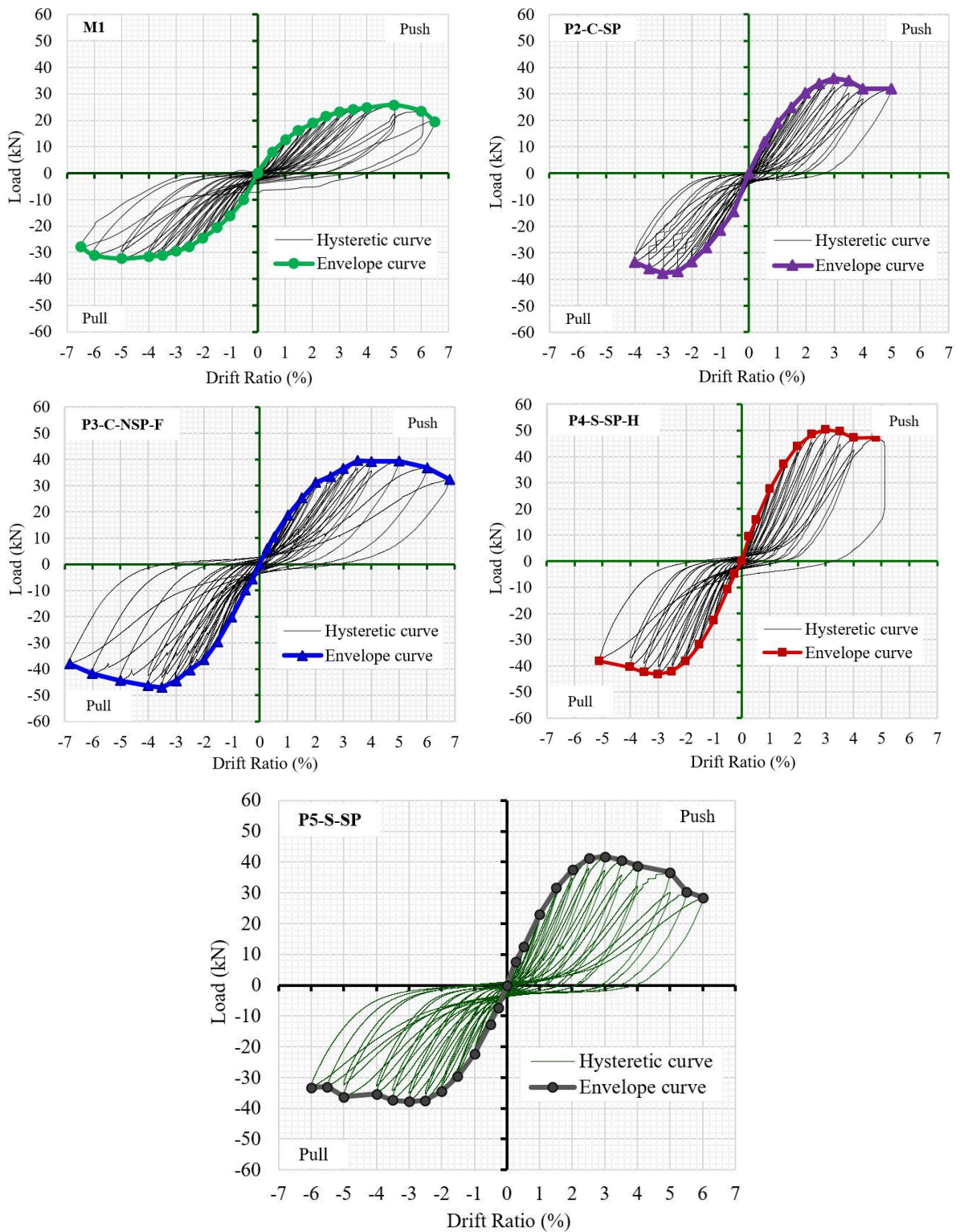


Fig. 3-6. Hysteretic load-drift ratio relationship of test specimens.

The hysteretic curves of Specimens P4-S-SP-H and P5-S-SP depict the influence of the prestress level of the bolts. These two specimens had the same design except the prestress force in Specimen P4-S-SP-H (51 kN) was higher than that of Specimen P5-S-SP (10.5 kN). The high prestress levels did not change the shape of hysteretic curves

until failure but it affected the peak loads. The maximum loads of Specimens P4-S-SP-H and P5-S-SP were 50.3 kN and 41.8 kN, respectively, which exhibits an increase of 20%. The high prestress levels in bolts improved the load-carrying capacity of this precast joint type. Interestingly, the envelope curves of all the precast specimens depict that the applied loads remained almost unchanged from 4% to 5% of the drift ratio as shown in Fig. 3-7. This phenomenon could be attributed to the yielding and strength hardening of the longitudinal reinforcements. The reinforcements started to yield at approximately 4% drift ratio and then stresses in the reinforcements still raised. This performance was a result of the fact that all the beams were designed as over reinforced. Therefore, the longitudinal reinforcements caused the plateau responses of the precast specimens from 4% and 5% drift ratio. This behaviour prevented the occurrence of brittle failure and offered necessary warnings before complete collapse of structures. This observed behaviour also shows that the use of this precast joint type may offer a safer solution as compared to other joints.

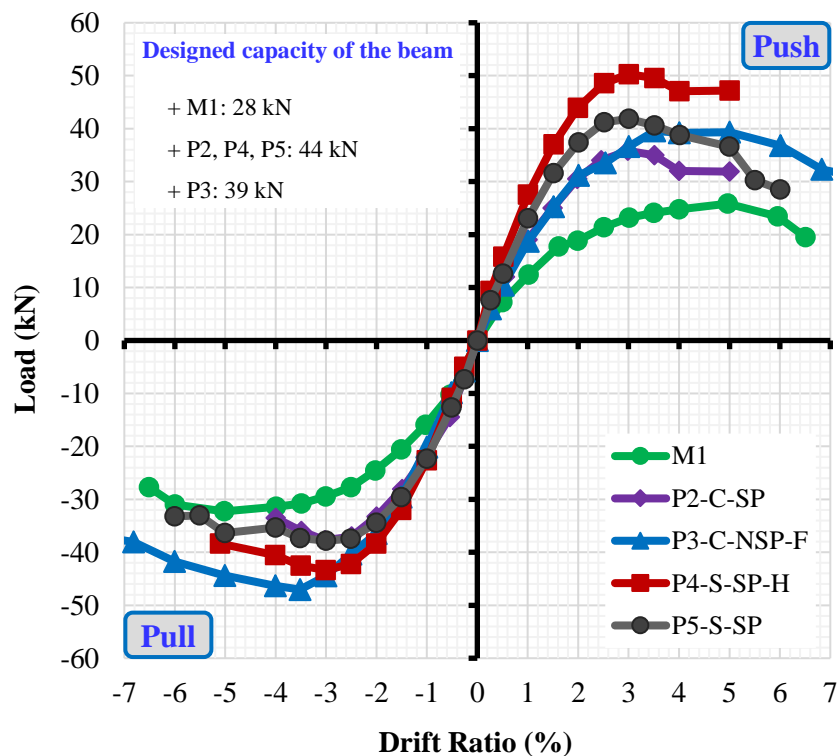


Fig. 3-7. Load-drift ratio envelopes of all the specimens.

For Specimen M1, the elastic response was observed up to drift ratio of 1%. From 1% drift ratio upwards, the number of cracks gradually increased, which signified the energy dissipation capacity of the specimen and also caused the nonlinear responses

of Specimen M1. At 2.7% drift ratio, Specimen M1 began to yield before achieving the peak load at 5% drift ratio. From 5% to 6.5% drift ratio, the applied load continuously decreased and the test stopped at 6.5% drift ratio.

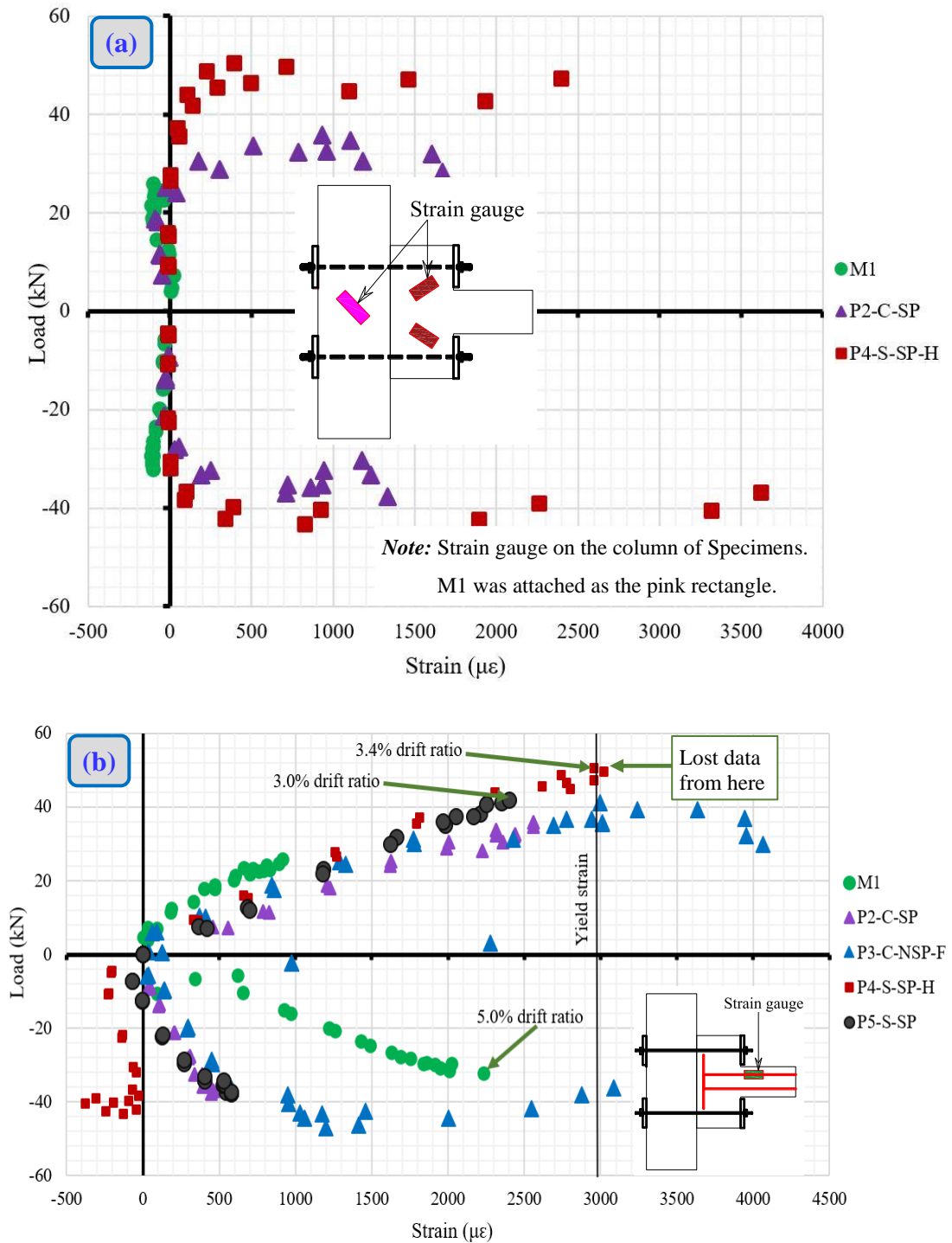


Fig. 3-8. Load versus strain of (a) the concrete-end-plate and (b) longitudinal reinforcements.

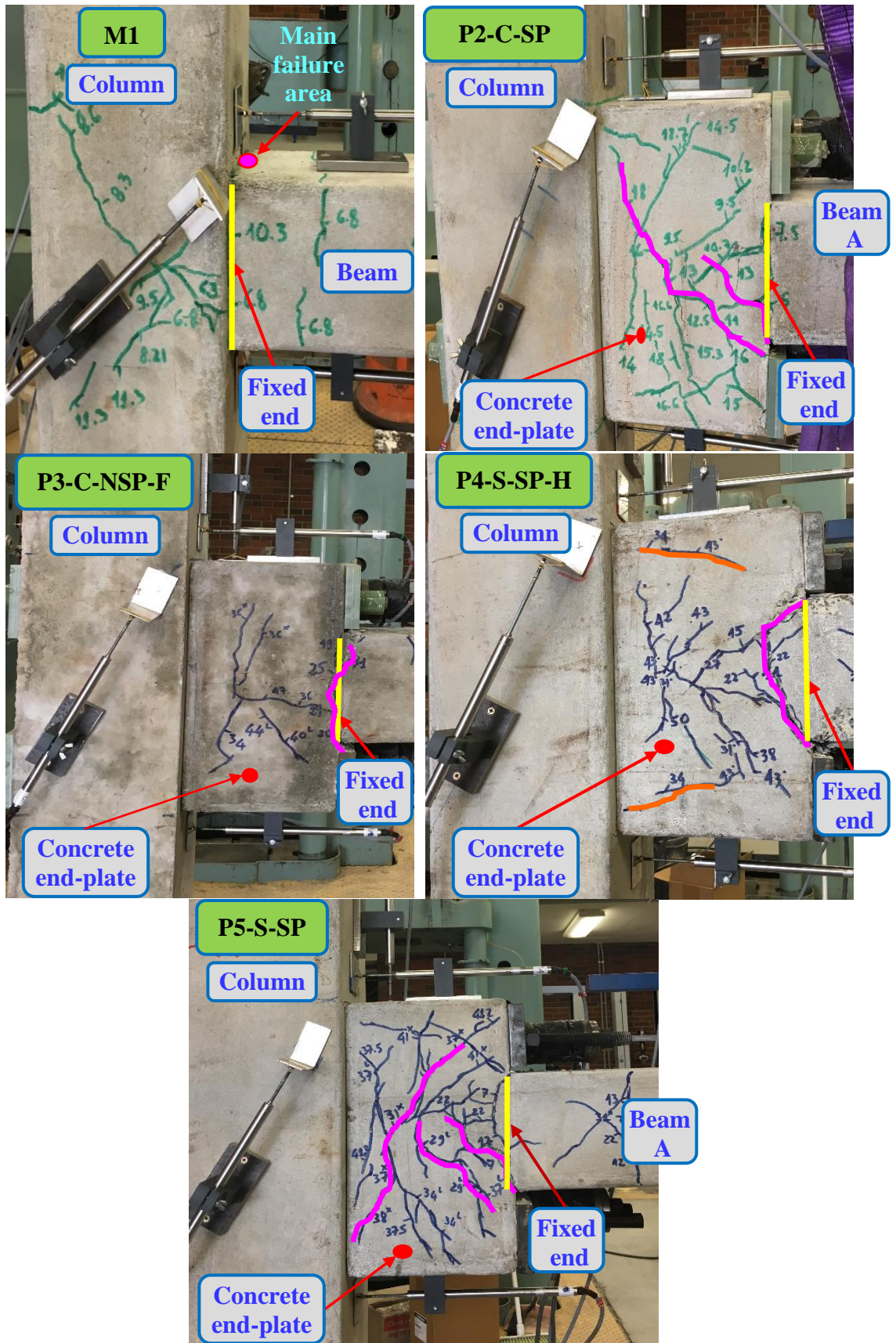


Fig. 3-9. Failure patterns.

3.2.4.2 General behaviours and failure patterns

The maximum tensile forces in the CFRP bolts and steel bolts were significantly lower than their nominal tensile strengths. For instance, the maximum tensile forces of the CFRP bolts and steel bolts in Specimens P2-C-SP and P4-S-SP-H were 34.1 and 57 kN respectively, which was approximately 34% and 40% of their ultimate tensile strength. Hence, no failure was observed in the CFRP bolts during the tests. Cracking patterns of all the tested specimens are shown in Fig. 3-9. No cracks could be found on the columns of all the precast joints while only minor cracks were observed on the column of the monolithic joint. The columns showed excellent behaviours with no failure, which makes all the specimens satisfy the requirements of the design principle of weak beams-strong columns. In addition, although this precast joint type did not have corbels or brackets to resist shear forces, the LVDT data demonstrated that there were no slips between the concrete-end-plates and column interfaces. It means that the friction between the column and the concrete-end-plate is sufficient to resist shear forces.

To further investigate the failures of all the specimens, it is necessary to estimate the load-carrying capacities of the joints, which are governed by the capacities of either the concrete-end-plate or the beam (Beam A). Assuming failure occurs at Beam A, the design load of the monolithic joint is 28 kN while all the precast beams have a design load of 44 kN, except for Specimen P3-C-NSP-F with 39 kN. The design load of Specimen P3-C-NSP-F was lower than that of other precast specimens due to its lower compressive strength ($f'_c = 32.3$ MPa for P3-C-NSP-F and $f'_c = 38.4$ MPa for other precast specimens). If the maximum load of a specimen was lower than the estimated design load of the beam, it could be concluded that this specimen failed in the joint. Otherwise, this specimen failed on the beam. Specimens P2-C-SP and P5-S-SP reached their maximum loads of 37.7kN and 41.8 kN at 3% drift ratio, respectively. These peak loads were slightly lower than the estimated design loads of the corresponding beams. Therefore, it can be concluded that the main failure of Specimen P2-C-SP and P5-S-SP occurred in the joints, specifically at the concrete-end-plates, whereas that of Specimens M1 (32.3 kN), P3-C-NSP-F (47.0 kN), and P4-S-SP-H (50.3kN) occurred on the beams at the fixed-ends as seen in Fig. 3-9. The maximum loads of these beams were higher than the estimated capacities, which could be

attributed to the variation between the actual stress and the nominal tensile strength of the longitudinal reinforcements and also the conservative design.

During seismic loadings, beam-column joints could fail as a result of shear forces or diagonal compressive forces [90, 95, 110]. Chapter 2 indicated that the main failure of the proposed precast joint was due to inclined cracks in the middle region of the concrete-end-plate. The data of strain gauges in Fig. 3-8(a) show that the compressive strain ($< 110 \mu\epsilon$) in the compressive struts of the concrete-end-plate did not reach the ultimate compressive strain of concrete, while the ultimate tensile strain ($131 \mu\epsilon$) significantly exceeded approximately > 10 times. For example, the tensile strain of concrete of Specimen P2-C-SP was $1333 \mu\epsilon$ at 3% drift ratio (see Fig. 3-8). The ultimate tensile strain of concrete was calculated according to its tensile strength (f_{ct}) and the Young's modulus. The above observations could be attributed to the effects of strut angles. Fig. 3-10 shows two assumed struts, namely QU and QK, which could appear on the concrete-end-plate. The angle of the compressive strut (QU) was only 34° which led to low compressive stress inside Strut QU. Normally, if the strut angle is greater than 45° , compressive failure may occur [14, 73]. For Strut QK, although this strut had a larger angle (50°) than that of Struts QU, it did not fail by compressive stress. The data of strain gauges in Fig. 3-11 and observations during the test exhibit that the concrete-end-plate failed by tensile cracks in the middle zone.

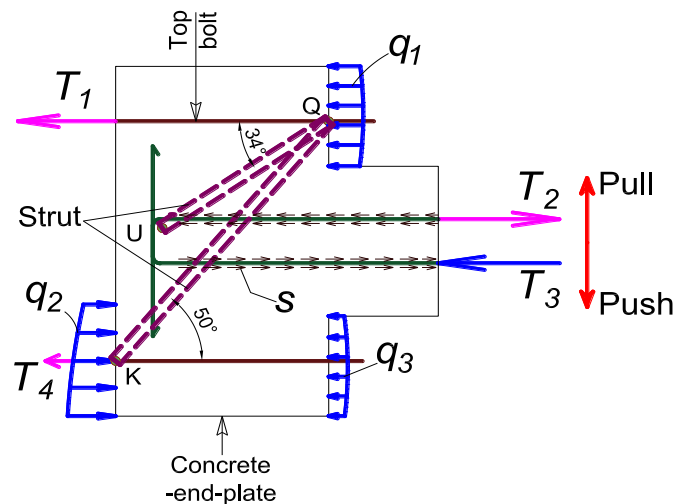


Fig. 3-10. Explaining the cause of inclined cracks.

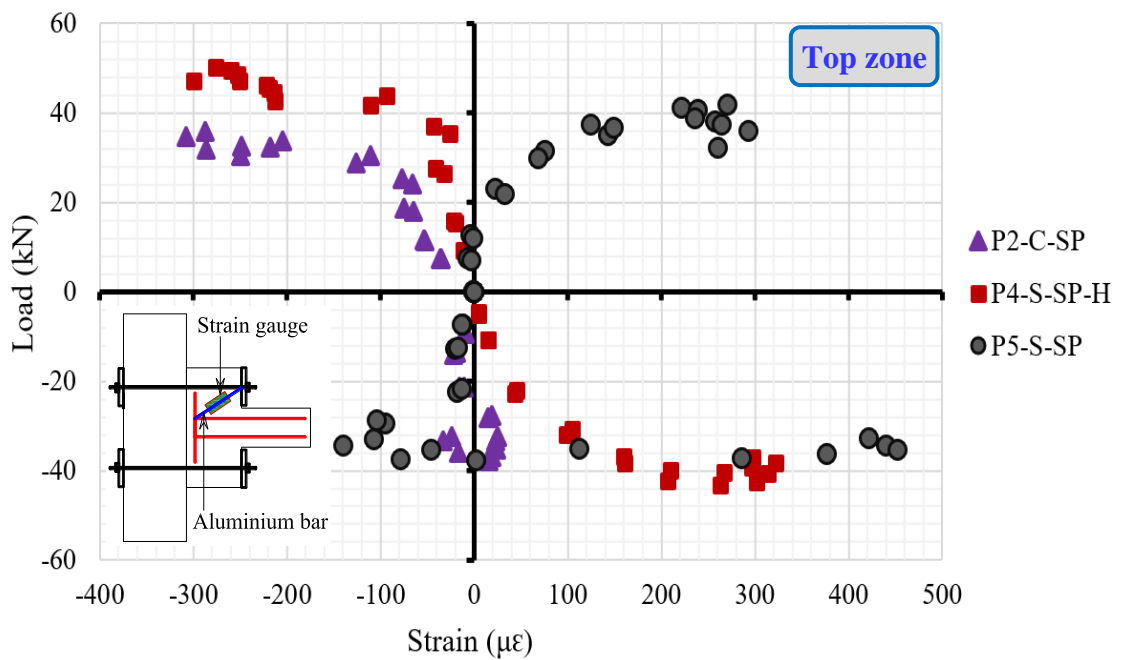
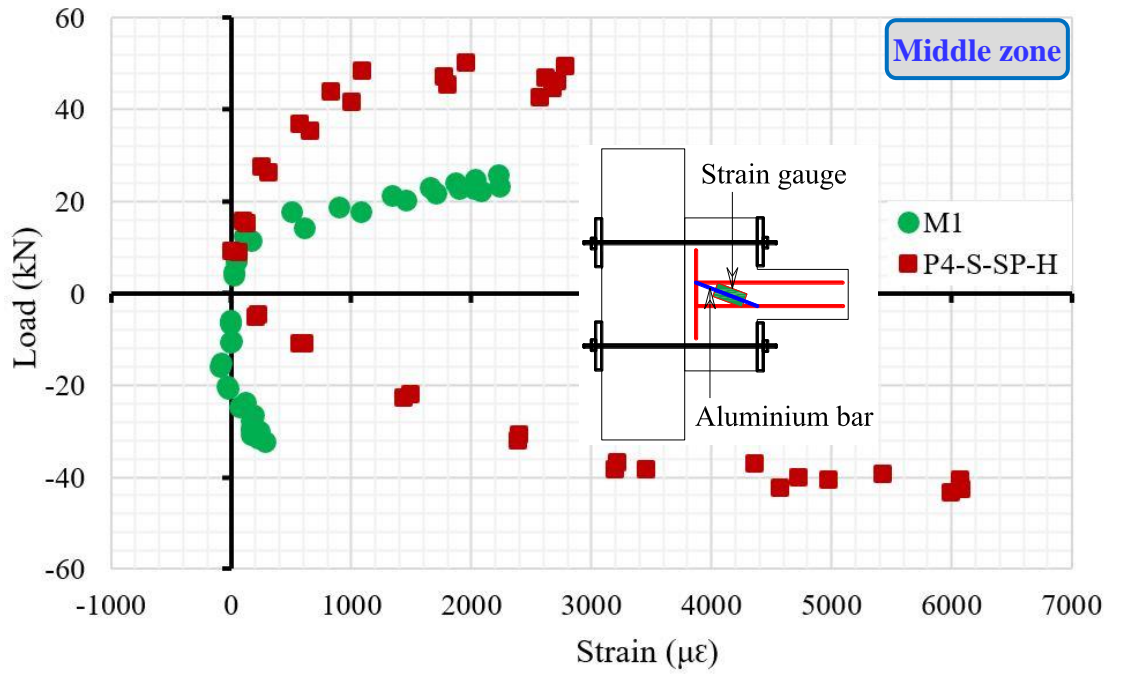


Fig. 3-11. Strain of the strain gauges on the aluminium bars.

Steel fibres were applied in this chapter to resist tensile cracks and, therefore, significantly increased the joint capacity. Fig. 3-9 demonstrates that Specimen P3-C-NSP-F had the least number of cracks among the four precast specimens. Only four minor inclined cracks were found in the concrete-end-plate at 1.8% drift ratio. The crack development could be summarized in four stages: the first-crack, main-crack, ultimate-crack and specimen failure. The initial stage was considered from the

beginning of the test to the moment when the first-crack appeared. The first-crack occurred when the tensile stress in the concrete-end-plate and Beam A overcame the tensile resistance of concrete. For the joint, its first-crack mainly depended on the concrete strength, rather than the stirrups inside the concrete-end-plate [102]. Therefore, the applied load of Specimen P3-C-NSP-F at the first-crack was greater than that of other precast specimens due to higher tensile strength (4.3 MPa) compared to that of conventional concrete (3.8 MPa). For example, the applied load of Specimen P3-C-NSP-F at the first crack increased by approximately 21% if compared to Specimen P2-C-SP. After this initial stage, the inclined crack started to develop in the concrete-end-plate which led to a strain increase in the stirrups when the applied load increased. The stage after the appearance of the first crack to the moment when the stirrups in the concrete-end-plate started to yield was so-called the main crack stage. For Specimen P3-C-NSP-F, the stirrup strain ($2233 \mu\epsilon$) at 3.5% drift ratio corresponding to the peak load did not reach the yield strain ($2800 \mu\epsilon$). This phenomenon could be explained that bridging actions of steel fibres helped to prevent the formation of the main tensile cracks on the concrete-end-plate [92, 105-107]. Therefore, the main failure position was on the beam instead of the joint, with a plastic hinge forming at the fixed-end as shown by the pink curve in Fig. 3-9(P3-C-NSP-F). After that, during the ultimate-crack stage, the applied loads increased with a limited rate until reaching the peak load. In the final stage, pulled-out fibres and spalling of concrete occurred at the fixed-end which caused the failure of Specimen P3-C-NSP-F. This final stage occurred after the specimen reached the peak load until the end of the test.

As shown in Fig. 3-9, Specimens P4-S-SP-H and P5-S-SP exhibited different failure modes and trends of the crack development while Specimens P2-C-SP and P5-S-SP behaved similarly irrespective of the bolt materials. For Specimens P2-C-SP and P5-S-SP, which had similar design except for the bolts (CFRP bolts vs steel bolts), the flexural crack initially developed at the fixed-end at $\pm 0.5\%$ drift ratio when the tensile strain of concrete at this section reached its maximum tensile strain. After this stage, the longitudinal reinforcements of Beam A started to make the main contribution to the flexural resistance. Therefore, the inclined cracks firstly propagated into the middle zone and then the top and bottom zones of the concrete-end-plate which caused the main failure for Specimens P2-C-SP and P5-S-SP. It means that the bolt material did

not affect the failure mode, indicating CFRP was successfully used to replace steel bolts. Meanwhile, Specimens P4-S-SP-H and P5-S-SP had the same design except for the only difference in the prestress levels (i.e., 51 kN for Specimen P4-S-SP-H and 10.5 kN for Specimen P5-S-SP). Specimen P5-S-SP exhibited much more number of inclined cracks in the concrete-end-plate as compared to Specimen P4-S-SP-H (see Fig. 3-9). In other words, the inclined cracks on Specimen P5-S-SP thoroughly distributed across the entire concrete-end-plate surface while Specimen P4-S-SP-H showed cracks concentrated in the middle zone, except for only one developed in the top and bottom of the concrete-end-plate after reaching the peak load of 50.3 kN at 3.0% drift ratio (see the orange curves in Fig. 3-9(P4-S-SP-H)). This difference could be attributed to the high compressive stress which was established in the top and bottom zones of the concrete-end-plate due to the high prestress level. Therefore, the tensile cracks in the top and bottom zones could only be developed when the tensile stress counteracted this compressive stress. From the above analysis, it could be concluded that the high prestress level in the bolts reduced the number of cracks in the top and bottom zones of the concrete-end-plate. In addition, the prestress level in the bolts also affected the failure mode of precast specimens because high prestress level effectively minimized the appearance of tensile cracks in the top and bottom zones of the concrete-end-plate. For instance, Specimen P4-S-SP-H failed at the fixed-end of the beam while the failure of Specimen P5-S-SP occurred in the concrete-end-plate. Therefore, the load-carrying capacity of Specimen P4-S-SP-H was significantly improved (i.e., approximately 20% in push direction compared to Specimen P5-S-SP).

The primary failure of the reference Specimen M1 occurred at the fixed-end of the beam. Minor spalling of concrete initially occurred at the fixed-end when the drift ratio reached 2%. Specimen M1 achieved its maximum capacity at 5% drift ratio. Afterwards, the failure was caused by the vertical cracks and spalling of concrete at the fixed-end of the beam.

3.2.4.3 Drift ratio and load-carrying capacities

The drift ratio is an important parameter to evaluate the joint performances under earthquake loadings. The drift ratio is defined as the ratio of vertical displacement (Δ) at the loading point of the beam to the distance ($l = 550$ mm) between the column face and the loading point, as follows:

$$R = \Delta/l \quad (3-1)$$

In most of the previous studies, the drift ratio of precast beam-column joints is usually lower than that of corresponding monolithic joints [56, 111]. The drift ratio of precast specimens usually varies from 1.5% to 3% [10, 14] whereas the requirements for structures to be applied in earthquake-prone regions are approximately 3.5% according to ACI T1.1-01 [16], 2.5% in CSA A23.3-07 [17], and 2% in ASCE 41-06 [18] to ensure the life safety. The precast joint using the concrete-end-plate and steel bolts in the previous study by Saqan [14] only reached the drift ratio of 1.5%. Meanwhile, Chapter 2 improved this kind of joint and achieved a higher drift ratio of 3%. This drift ratio satisfied the requirement of CSA A23.3-07 [17] and ASCE 41-06 [18] but still lower than the requirement of ACI T1.1-01 [16]. This issue has been resolved in the current chapter with the addition of steel fibres. The results show that the 3.5% drift ratio of the currently tested specimens satisfied the requirement of ACI T1.1-01 [16] so that the proposed joint can be effectively used in earthquake-prone regions. Table 3-3 and Fig. 3-12 show the maximum loads with the corresponding drift ratios of all the tested specimens.

Table 3-3. Details of load-carrying capacities with corresponding drift ratios.

Names	Peak load (kN)		Increase (%)		Average (kN)	Increase (%)	Drift ratio at peak load (%)	
	Push	Pull	Push	Pull			Push	Pull
M1	25.8	32.3	-	-	29.1	-	5.0	5.0
P2-C-SP	35.8	37.7	38.6	16.9	36.8	26.6	3.0	3.0
P3-C-NSP-F	39.6	47.0	53.2	45.7	43.3	49.1	3.5	3.5
P4-S-SP-H	50.3	43.3	94.7	34.3	46.8	61.2	3.0	3.0
P5-S-SP	41.8	37.8	62.0	17.1	39.8	37.1	3.0	3.0

Note: - = not applicable.

In general, the proposed dry joints showed excellent performance in terms of drift ratio and load-carrying capacity as compared to those from the previous studies [13-15]. Specimen P3-C-NSP-F with steel fibres reached 3.5% drift ratio and satisfied the requirement for use in earthquake-prone regions of the contemporary standards, namely ACI T1.1-01 [16], CSA A23.3-07 [17], and ASCE 41-06 [18]. The average peak load of Specimen P3-C-NSP-F (43.3 kN) was higher than those of Specimens

P2-C-SP (36.8 kN) and P5-S-SP (39.8 kN). In addition, the load-carrying capacity of this specimen was also 49.1% higher than that of the monolithic specimen M1. Although Specimen M1 exhibited a ductile load-displacement response with the highest drift ratio of 5%, the load-carrying capacity of this specimen was the lowest among all the tested specimens. For failure at the fixed-end, the above results might be explained that the lever arm from the fixed-end to the loading point of Specimen M1 (550 mm) was longer than that of the precast specimens (350 mm) due to the absence of the concrete-end-plate, while all the specimens had the same square cross-section of $150 \times 150 \text{ mm}^2$ at the fixed-end. Therefore, the moment at the fixed-end of Specimen M1 was approximately 57.1% higher than that of the precast specimens with the same applied load. It implies that the use of the concrete-end-plate enhances the load-carrying capacity of an exterior precast joint if the failure occurs at the beam. For the failure in the middle zone of the concrete-end-plate, the load-carrying capacity of all the precast specimens depended on the thickness and the height of the concrete-end-plate. This study purposefully modified the thickness in the previous study by Saqan [14]. Therefore, the load-carrying capacity of the precast specimens was significantly improved if compared to that of the reference specimen M1.

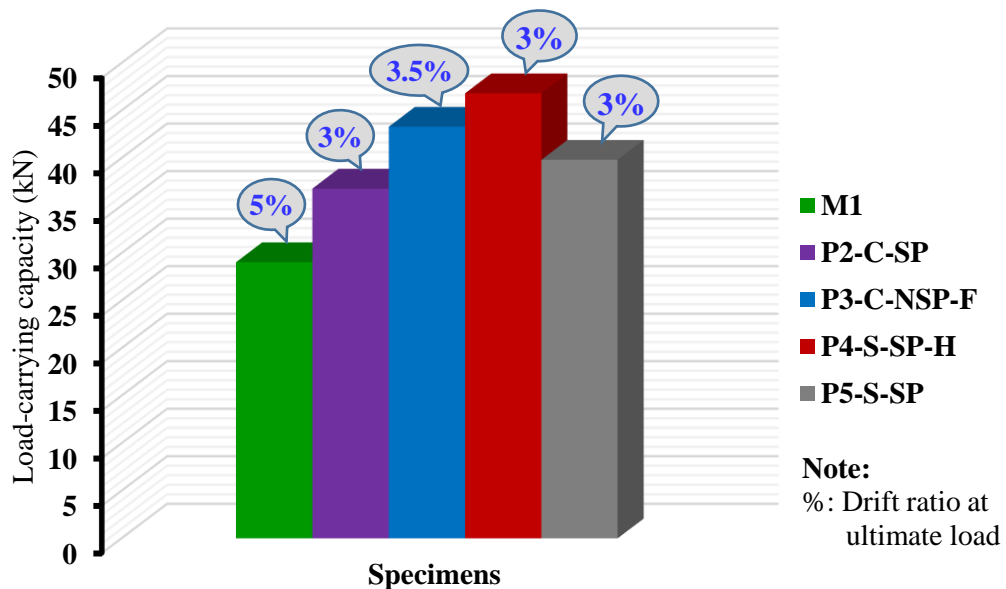


Fig. 3-22. Average load-carrying capacity and the corresponding drift ratio.

In the meantime, Chapter 2 suggested that the prestress levels affected the load-carrying capacity while the use of CFRP bolts to replace steel bolts did not

significantly change the load-carrying capacity of this precast joint type. These two main parameters are investigated in this chapter. The comparisons between the two specimens with similar design except for the prestressing force in the bolts (i.e., Specimens P4-S-SP-H and P5-S-SP) were conducted to explore the influence of the prestress levels. The prestress level of Specimen P4-S-SP-H was 51 kN whereas that of Specimen P5-S-SP was 10.5 kN. The experimental results revealed that the load-carrying capacity of Specimen P4-S-SP-H was higher (20%) than that of Specimen P5-S-SP. Therefore, it is concluded that the high prestress level improved the load-carrying capacity. For replacing steel bolts by CFRP bolts, Specimens P2-C-SP and P5-S-SP which had the same design, but different bolt material showed a similar load-carrying capacity and drift ratio of 3% (36.8 kN for Specimen P2-C-SP and 39.8 kN for Specimen P5-S-SP). Therefore, it can be concluded that steel bolts could be effectively replaced by CFRP bolts to resolve the corrosion issue without negative effects on the load capacity and the drift ratio of the joint.

3.2.4.4 Ductility of Joints

Structures are considered as ductile if they can dissipate significant energy during inelastic cyclic deformations [82]. Ductility indicates the capacity that a structure can withstand without any significant degradation in its strength during deformation. It is considered as a crucial parameter in seismic performances of a structure in order to avoid brittle failure. In this study, the ratio of the ultimate displacement (Δ_u) to displacement at the yield loads (Δ_y) is defined as the ductility of a structure, as expressed in Eq. 3-2 as follows:

$$\mu = \Delta_u / \Delta_y \quad (3-2)$$

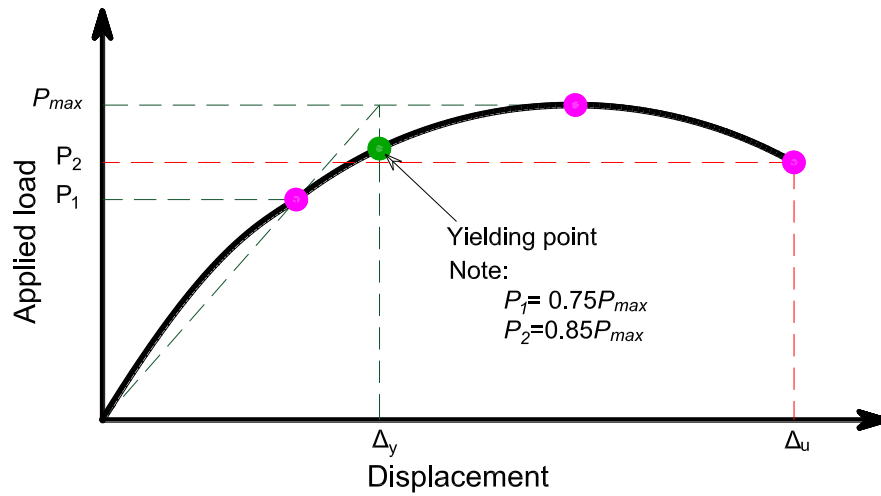
In a reinforced concrete structure, the applied load versus displacement relationship does not reveal a clear yield point due to either the nonlinear performance of materials or the onset of yield at different load levels in various parts of structures. Consequently, the definition of yielding deformation is quite subjective and thus the yield and ultimate displacement of all the tested specimens are determined as shown in Fig. 3-13.

Table 3-4. Displacement and ductility of all the tested specimens.

Names	Force	P_{max}	P_1	Δ_y	P_2	Δ_u (85%)	$\mu = \Delta_u / \Delta_y$	Average (μ)	Decrease (%)
	(Unit)	(kN)	(kN)	(mm)	(kN)	(mm)			
M1	Push	25.8	19.4	15.6	22.0	35.8	2.3	2.4	-
	Pull	32.3	24.2	14.5	27.4	35.6	2.5		
P2-C-SP	Push	35.8	26.9	12.2	32.2 ^a	27.5 ^a	2.3	2.1	-12.5
	Pull	37.7	28.3	11.1	34.0 ^a	21.5 ^a	1.9		
P3-C-NSP-F	Push	39.6	29.7	13.8	33.7	36.2	2.6	2.6	8.3
	Pull	47.0	35.3	14.0	40.0	35.0	2.5		
P4-S-SP-H	Push	50.3	37.7	11.4	45.3 ^a	26.5 ^a	2.3	2.3	-4.2
	Pull	43.3	32.5	11.4	39.0 ^a	26.3 ^a	2.3		
P5-S-SP	Push	41.8	31.4	11.0	35.5	28.0	2.5	2.8	16.6
	Pull	37.8	28.4	10.4	32.1	31.2	3.0		

Note: - = not applicable.

^a at 90% of the post-peak load.

**Fig. 3-13.** Definition of the yielding point.

Due to the limitations of the hydraulic jack, the ultimate displacements of Specimens P2-C-SP and P4-S-SP-H were stopped at 28.1 mm, which corresponded to 90% of the peak load. For other specimens, a new hydraulic jack was utilised so that the ultimate displacement could be determined at 85% peak load. The ductility of all the tested specimens is presented in Table 3-4. The results reveal that Specimen P5-S-SP exhibited the highest ductility ($\mu = 2.8$) among all the tested specimens. Specimens P3-C-NSP-F and P5-S-SP revealed higher ductility than Specimen M1 ($\mu = 2.4$), with

approximately 8.3% and 16.6% increase, respectively. Specimens P2-C-SP and P4-S-SP-H exhibited the ductility of $\mu = 2.1$ and $\mu = 2.3$, which were close to the reference specimen M1. It is noted that the applied loads of these two specimens were stopped at 90% of the peak loads. Therefore, it is expected that if the applied load continued to 85% of the peak loads, the ductilities of these specimens would be similar or even higher than that of Specimen M1. The precast specimens exhibited excellent ductility due to the beneficial influences of steel fibres and steel spirals inside the concrete-end-plate. As an evidence, the ultimate displacement of Specimen P3-C-NSP-F (36.2 mm) was 31.6% higher than that of Specimen P2-C-SP (27.5 mm) in the push direction. From the above analysis, it is clear that the addition of steel fibres into the concrete mixture could significantly enhance the ductility of the precast joint using concrete-end-plate and bolts.

3.2.4.5 Energy dissipation capacities

The energy dissipation capacity of the exterior joints is determined as the area enclosed (A_h) inside the applied load-displacement hysteretic loop in that corresponding load cycle. A beam-column joint under quasi-static cyclic loads is classified as a ductile joint if it can dissipate sufficient energy while there is no significant reduction of its strength and stiffness [56, 85]. The energy dissipation capacity versus drift ratio curves of all the specimens are shown in Fig. 3-14. As can be seen up to 1% drift ratio, similar trends and values were observed in the energy dissipation capacity of all the specimens since they behaved elastically. Nevertheless, the overall energy dissipation capacity of Specimen P3-C-NSP-F was lower than the other precast specimens from 1%-3.5% drift ratio. When this specimen reached the peak load at 3.5% drift ratio, the energy dissipation capacity dramatically increased until failure. This interesting phenomenon could be explained that steel fibres minimized the appearance of inclined cracks in the concrete-end-plate from the initial stage to 3.5% drift ratio. After this stage, the inelastic deformation and the crack width significantly increased because steel fibres were progressively pulled out from the matrix. Consequently, the toughness and dissipated energy of this specimen significantly increased. Moreover, the energy dissipated by Specimen P4-S-SP-H was approximately similar to that of Specimen P5-S-SP, indicating that the prestress level did not considerably affect the energy

dissipation capacity of the precast joints (409 kN.mm for Specimen P4-S-SP-H and 387 kN.mm for Specimen P5-S-SP at 4% drift ratio).

The energy dissipation capacity at 4% drift ratio of all the precast specimens (P2-C-SP, P3-C-NSP-F, P4-S-SP-H and P5-S-SP) was 45.1%, 65.9%, 74.5%, and 65.3% greater than that of Specimen M1, respectively, which could be mainly attributed to fatter hysteretic loops as shown in Fig. 3-6. Therefore, it could be concluded that the proposed precast specimens exhibited excellent energy dissipation capacity for earthquake loading resistance.

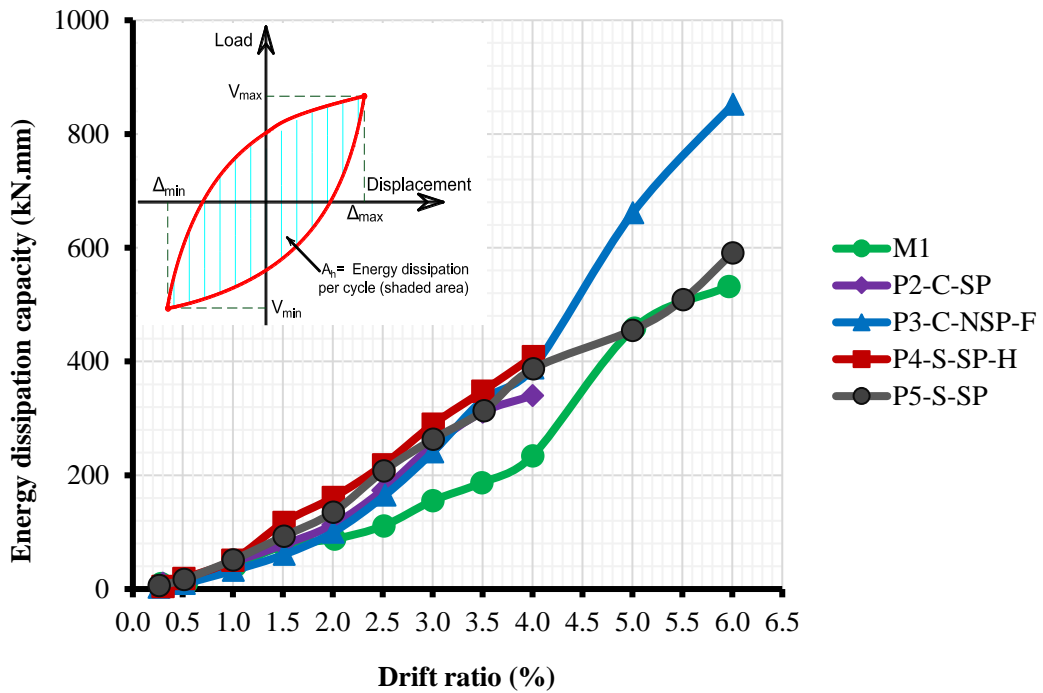


Fig. 3-14. Comparison of energy dissipation capacity.

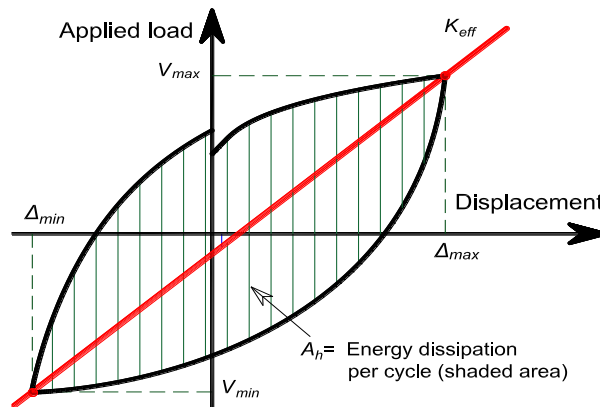


Fig. 3-15. Effective stiffness and energy dissipation under cyclic loads.

3.2.4.6 Stiffness degradation

The stiffness degradation of all the specimens under cyclic loads was evaluated in term of effective stiffness. The effective stiffness at each cycle was determined based on the slope of the line connecting the peak-to-peak loads in the positive and negative directions during the first cycle of the two reversal cycles at each drift ratio (see Fig. 3-15) [19]. In general, the effective stiffness of all the specimens was continuously decreased when the applied load increased. It is expected that the stiffness reduction only occurs when a structure has partial damage or enters the plastic stage. The envelope curves in Fig. 3-7 show almost linear responses of the specimens from the initial stage to the drift ratio of 1.5-2%. However, the stiffness reduction of these specimens occurred at quite an early stage of about 0.5% drift ratio, which can be explained by two reasons. Firstly, since the tensile cracks at fixed-end appeared quite early at 0.5% drift ratio, it means that there was minor damage at this stage. Secondly, the strain of concrete reached $30\% \epsilon_c'$ so concrete began to behave nonlinearly. Fig. 3-16 presents the stiffness degradation for all the specimens versus their drift ratios.

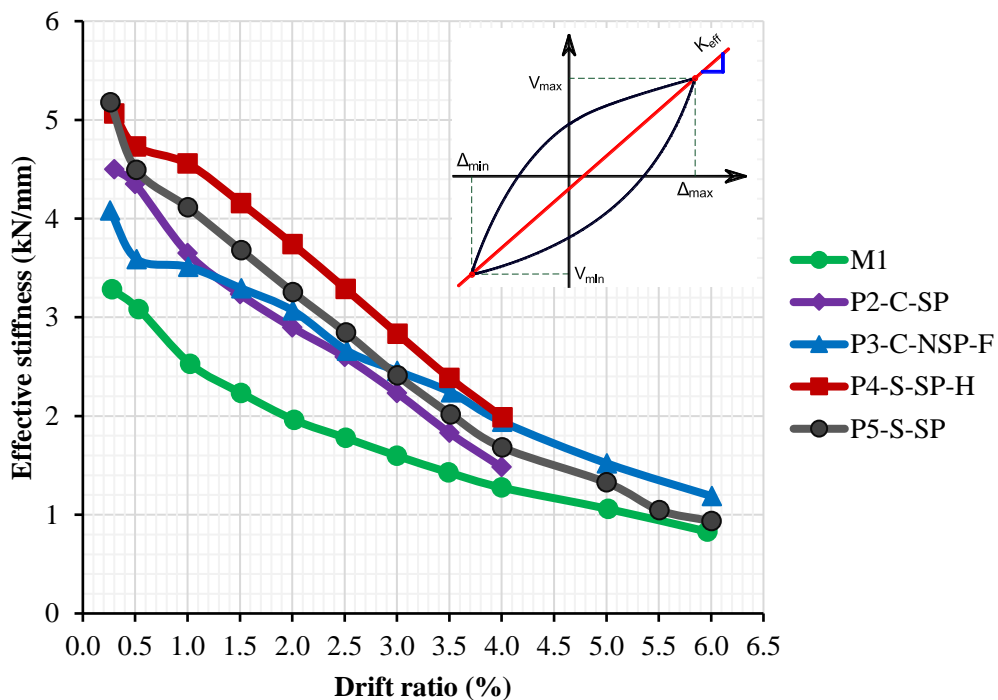


Fig. 3-16. Comparison of the effective stiffness.

Fig. 3-16 shows that the effective stiffness of all the precast specimens was greater than that of Specimen M1 until failure because the use of the concrete-end-plate

improved the stiffness of the precast specimens. It is noted that the design of the concrete-end-plate was improved in this study so that premature failure at the concrete-end-plate did not occur as observed in the previous studies [14, 19]. The stiffness of Specimen P3-C-NSP-F was approximately 26.7% higher than that of Specimen P2-C-SP at 4% drift ratio. This observation could be explained that the use of steel fibre concrete has increased the joint stiffness and minimized damage to the concrete. Moreover, the effective stiffnesses of Specimens P4-S-SP-H and P5-S-SP were almost the same, indicating that the prestress level did not significantly affect the initial stiffness (5.1 kN/mm for P4-S-SP-H and 5.2 kN/mm for P5-S-SP). This observation agrees well with findings from other studies [80, 81, 112]. Le et al. [81] also found that the prestress level showed unnoticeable influences on the initial stiffness of structures. In Fig. 3-16, the stiffness degradation curves of these two specimens from 1% to 4% drift ratio were also parallel, so the overall stiffness of this precast joint type using bolts was not significantly affected by the prestress levels. However, it is worth mentioning that these parallel curves did not occur between 0.5% and 1% drift ratio because the trend of crack development on both specimens was totally different in the initial stage as discussed in Section 3.2.4.2. Therefore, the stiffness degradation was not similar from 0.5% to 1% drift ratio. In addition, the stiffness of specimens using steel bolts (i.e., P4-S-SP-H and P5-S-SP) in the initial stages was greater than that of specimens using CFRP bolts (i.e., P2-C-SP and P3-C-NSP-F), (i.e., approximately 23.8% at 0.3% drift ratio) because steel bolts had higher elastic modulus (200 GPa) than CFRP bolts (100 GPa). Therefore, the specimens with steel bolts showed higher stiffness than the specimens with CFRP bolts.

3.3 Analytical calculations

In this section, an analytical model to estimate the load-carrying capacity of the precast beam-column joints, using concrete-end-plates and bolts, is proposed. As previously discussed in Section 3.2.4.2, there are two possible failure sections in this precast joint type, including (1) at the fixed-end and (2) in the middle zone of the concrete-end-plate. Maximum applied load (P_{max}) is the minimum applied load at the loading point of the beam when the failure occurs either at the fixed-end (P_{max1}) or the middle zone of the concrete-end-plate (P_{max2}).

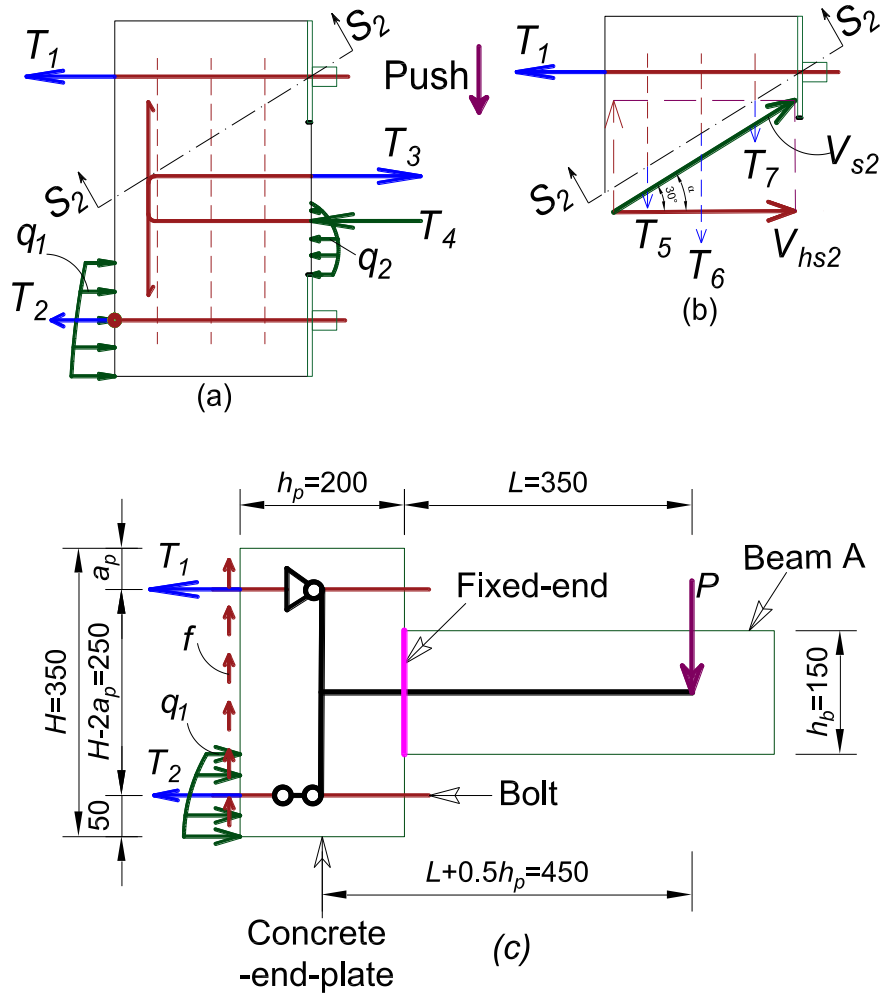


Fig. 3-17. Global equilibrium of an exterior joint.

3.3.1 Failure at fixed-end

When failure occurs at the fixed-end of the beam, P_{max1} is estimated based on the flexural capacity of the beam. This applied load is calculated with a reference to the nominal moment strength (M_{n1}) of Beam A at the fixed-end. P_{max1} can be calculated as follows:

$$P_{max1} = \frac{M_{n1}}{L_1} \quad (3-3)$$

where L_1 is the distance from the loading point to the fixed-end ($L_1 = 350$ mm in the present study).

In a general circumstance, M_{n1} of Beam A is determined with the assumption that the longitudinal reinforcements have reached a yielding point when Beam A fails.

However, all the specimens in the current study were designed as over reinforced. Therefore, M_{n1} is calculated based on the actual strain of the longitudinal reinforcements.

3.3.2 Failure in the middle zone

When the failure occurs in the middle zone of the concrete-end-plate, P_{max2} is determined based on the assumption that the stirrups have yielded. Fig. 3-17 presents the free body diagram and global equilibrium of the specimens, in which T_1 vs T_2 and T_3 are the tensile forces of the bolts and reinforcements, T_4 is the compressive forces in the reinforcements, f is the friction between two surfaces of the column and concrete-end-plate, and q_1 and q_2 are the compressive stress in concrete on the left and right of the concrete-end-plate, respectively. It is worth mentioning that the tension forces (T_1 and T_2) of the bolts are caused by two sources, including the applied load (P) and the prestressing force. As a result, T_1^a represents the tensile force caused by the applied load while T_1^b is caused by the prestressing force. From the force-equilibrium as shown in Fig. 3-17(b), the tensile force in the top bolts (T_1) could be determined as follows:

$$T_1 = T_1^a + T_1^b = V_{hs2} + \gamma P_r \quad (3-4)$$

where P_r is the prestress levels of bolts, γ refers to the prestress level loss in bolts, γ is determined from the initial prestress force (P_r) and tensile force in the bolt at 0% drift ratio immediately after the applied load has reached the peak load. All these tensile forces were taken from data of the load cells in the current study, in which $\gamma = 0.84$ is for steel bolts and $\gamma = 0.25$ for CFRP bolts, V_{hs2} is the horizontal shear force which is calculated based on the inclined shear force (V_{s2}) at Section S2-S2 (see Fig. 3-17(b)) as follows:

$$V_{s2} = V_s \sin \alpha + V_c + V_f \quad (3-5)$$

$$V_{hs2} = V_{s2} \cos \alpha \quad (3-6)$$

where $V_s = nA_v f_{yt}$ is the shear force contributed by the stirrups, n , A_v , and f_{yt} are the number of stirrup legs, cross-section area, and yield strength of the stirrups, respectively. The strain gauges attached on the stirrups inside the concrete-end-plate

show that strain of two side stirrups was significantly lower than that of the middle stirrup. For instance, the strain of the middle stirrup of Specimen P2-C-SP was 3286 $\mu\epsilon$ whereas that of side stirrups was only 155 $\mu\epsilon$ at 3% drift ratio. Therefore, only the contribution of the middle stirrup was considered to compute V_s while the contribution of the other two stirrups was ignored. For the shear force carried by the concrete, $V_c = \beta h_p b_p \sqrt{f'_c}$, $\beta = \frac{1}{6}$ is an empirically derived function whose value is adopted in this chapter based on the model of the beam in ACI 318-11 [72], h_p and b_p are the thickness and width of the concrete-end-plate. For shear force contributed by steel fibers, $V_f = 2 \frac{l_f}{d_f} v_f h_p b_p$, l_f , d_f , and v_f are the length, diameter, and volume fraction of steel fibres [102].

P_{max2} is determined from the equilibrium condition as shown in Fig. 3-17(c), as follows:

$$P_{max2} = \frac{T_1(H-2a_p)}{(L+0.5h_p)} \quad (3-7)$$

where L , a_p , h_p , and H are the length of Beam A, the distance from the extreme-top fibre of the concrete-end-plate to the centroid of the top bolts, the thickness and height of the concrete-end-plate, respectively (see Fig. 3-17(c)).

The maximum applied load (P_{max}) of this precast joint type is determined in the following equation:

$$P_{max} = \min(P_{max1}, P_{max2}) \quad (3-8)$$

To compare the results of the proposed model and those of the experiment, the maximum applied load from the experiment ($P_{exp-max}$) for each specimen is taken from the data of the main load cell which was connected to the hydraulic jack at the beam tip (see Fig. 3-4). The data of the main load cell and the load cell on bolts are shown in Figs. 3-7 and 3-18. It is noted that no data of the load cell on the top bolt of Specimen P3-C-NSP-F was recorded due to malfunction of the data acquisition system during the test. ($P_{exp-max}$) of all the precast specimens are summarized in Table 3-5. The P_{max} comparisons between the proposed model and the experimental results are

indicated in Fig. 3-19. It is noted that the analytical model was validated at the main failure positions (fixed-end or middle zones) for brevity.

Table 3-5. The comparisons of P_{max} between the experiment and analytical model.

Names	Experimental results	Theoretical results (fixed-end)			Theoretical results (middle zone)			
	$P_{exp-max}$	M_{n1}	P_{max1}	(%)	V_{hs2}	T_1	P_{max2}	(%)
	(kN)	(kN.m)	(kN)		(kN)	(kN)	(kN)	
P2-C-SP	37.7	15.7	44.7	-	64.9	66.5	37.0	-2.0
P3-C-NSP-F	47.0	16.3	46.6	-0.9	98.0	100.0	55.6	-
P4-S-SP-H	50.3	17.3	49.5	-1.6	64.9	107.7	59.9	-
P5-S-SP	41.8	14.9	42.7	-	64.9	73.8	41.0	-2.0

Note: - = not applicable.

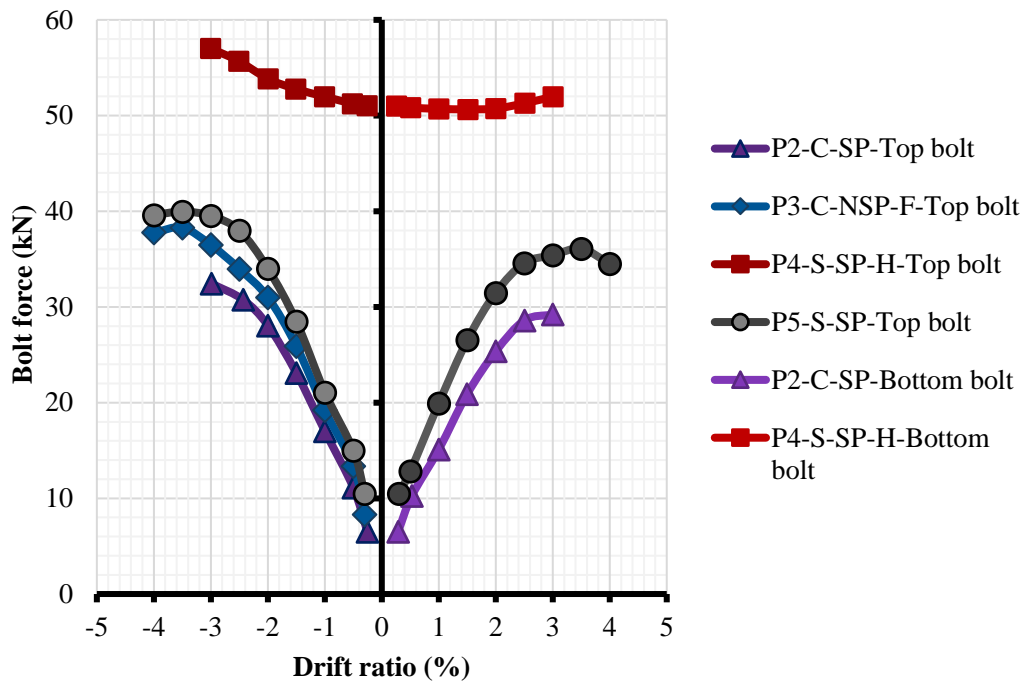


Fig. 3-18. Tensile forces of the top and bottom bolts.

As can be seen from Table 3-5 and Fig. 3-19, where the actual data from the test was used to verify the accuracy of the proposed model, the proposed model could well predict the load-carrying capacity of all the precast specimens. For the failure at the fixed-end, the variations between the experimental results and the proposed model results of Specimens P3-C-NSP-F and P4-S-SP-H were minor, only 0.9% and 1.6%,

respectively. For the failure in the middle zone, Specimens P2-C-SP and P5-S-SP had the same failure modes in the middle zones, indicating this proposed model accurately predicted the maximum applied load (P_{max}) with a low variation of 2%. The above analyses prove that the proposed model could be well applied to predict the capacity of this precast joint type.

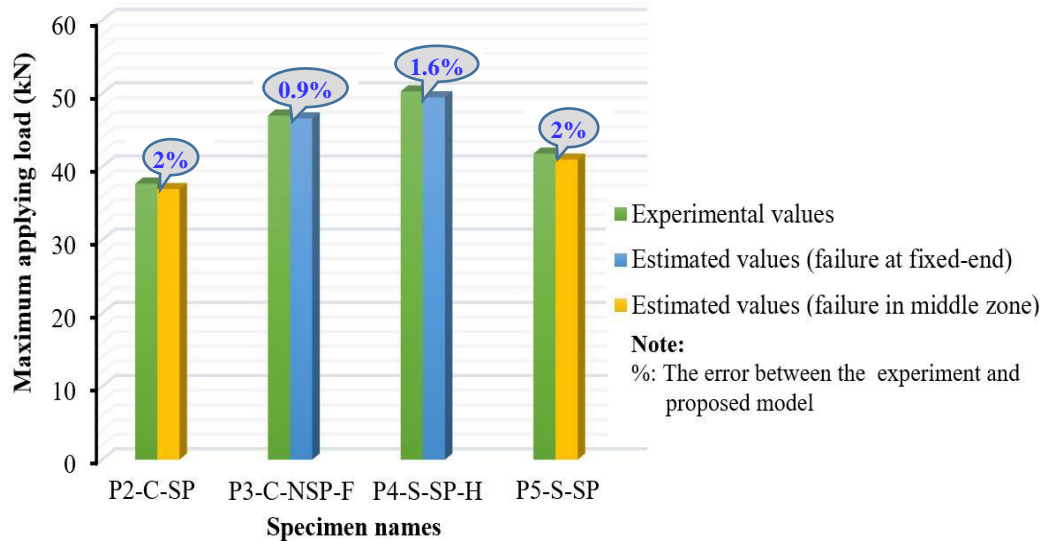


Fig. 3-19. Comparisons between the experimental and analytical results.

3.4 Summary

This chapter carried out an experimental investigation on the effects of steel fibres and prestress levels on the structural performance of the proposed dry joints. In addition, a new model to estimate the load-carrying capacity of this precast joint type was proposed. The excellent performances of all the precast specimens show that this precast joint type can be potentially utilised in both non-earthquake and earthquake-prone regions. Findings from this chapter can be summarized as follows:

1. The proposed dry joints outperformed the corresponding monolithic joint in terms of load-carrying capacities, energy dissipation, and stiffness. In addition, the proposed model could well predict the maximum applied load of all the precast specimens with minor variations ranging from 0.9% to 2%.
2. Using SFRC could significantly improve the load-carrying capacity (18%) and ductility (53%) of the proposed dry joint.

3. The average peak loads of all the precast specimens were from 27% to 61% higher than that of the monolithic specimen.
4. All the precast joints have higher effective stiffness than that of monolithic joint M1 until failure.
5. The high prestress level improved the load-carrying capacity of the precast beam-column joints but did not increase the initial stiffness.

In general, CFRP bolts could be effectively applied in dry beam-column joints using concrete-end-plates and bolts. They could effectively resolve the corrosion issue in steel bolts while still assure excellent performance under quasi-static cyclic loads.

CHAPTER 4: PERFORMANCE OF GEOPOLYMER CONCRETE IN MONOLITHIC AND NON-CORROSIVE DRY JOINTS USING CFRP BOLTS UNDER CYCLIC LOADING

ABSTRACT³

This chapter evaluates the performances of beam-column joints made of geopolymer concrete (GPC). A new dry joint type made of GPC and carbon fibre reinforced polymer (CFRP) bolts was proposed for moment-resisting concrete frames under earthquake loadings. Cyclic loading was applied to test the four specimens which were preparatorily cast by ordinary portland concrete (OPC) and GPC. Compared to monolithic joints, the proposed dry joints showed better performances in the maximum load-carrying and energy dissipation capacity. Additionally, new analytical models to design GPC monolithic and GPC precast joints are proposed. These models well predict the peak loads, main failure modes, failure positions, and horizontal shear strength with a minor variation of 1.3%. The application of GPC promises to effectively recycle a large number of industrial wastes. Furthermore, the proper design made sure the CFRP bolts survive during the test without brittle failure and shear failure. Therefore, they could be potentially applied in the proposed dry joint to well resolve the corrosive issues in conventional precast joints, as well as satisfying the requirements for construction in seismic regions.

³ This work was published in **Composite Structures** with the full bibliographic citation as follows:

Ngo TT, Tran TT, Pham TM, Hao H. Performance of geopolymer concrete in monolithic and non-corrosive dry joints using CFRP bolts under cyclic loading. *Compos Struct* 2020:113394.
<https://doi.org/10.1016/j.compstruct.2020.113394>

4.1 Introduction

One of the most challenging global issues is the alarming increase of CO₂ emission from cement manufacturing due to ever-growing demand for construction. CO₂ emission is also responsible for global warming which has negative effects on human health and our planetary ecology [22]. If no actions are taken, the amount of CO₂ emitted from the global cement industry is warned to reach 2.34 billion tons by 2050 [22, 23]. Therefore, it is urgent to investigate and introduce new “green” binders which could completely or partially replace the ordinary portland cement in the nearest future. GPC is so-called a “green” material because it uses industrial wastes (i.e., calcium fly-ash, slag, silica fume, rice-husk ash) to produce the new binder replacing ordinary portland cement [113]. Three main components in GPC include fly ash, slag, and alkaline chemicals. Fly ash is a product found in coal-fired power stations while slag is a left-over product after a targeted metal has been successfully refined out of its raw ore. If OPC is replaced by GPC, industrial wastes could be effectively recycled to produce new binders (i.e., slag and fly ash) in GPC.

GPC has been intensively researched for over 20 years. Although many different mixes have been proposed to achieve different strengths of GPC, the application of GPC in construction is still limited partially because of a lack of design guide of structures made of GPC. Most of existing studies focus on seeking the optimal mixture design and mechanical properties of GPC [114, 115]. Wang et al. [29] and Rafeet et al. [30] reported that increasing the slag/fly ash ratio could improve the mechanical properties of GPC (e.g., compressive strength, elastic modulus). Xie et al. [28] suggested that the use of GPC with a combination of 50% slag, 50% fly ash and 0.5 water/binder ratio showed good mechanical behaviours and workability. In addition, 80 °C for 12-24 hour was an optimum curing condition of GPC [29]. Therefore, various studies suggested that the use of GPC under heat-cured condition offers numerous advantages such as little drying shrinkage, low creep, high compressive strength and bond strength, and excellent resistance in acid and sulphate environments [31, 32]. Nevertheless, the mechanical properties of GPC also have some disadvantages. Among these disadvantages of reinforced-GPC structures, two unfavourable characteristics are low elastic modulus [116] and brittleness [117]. The low elastic modulus affects the stiffness degradation of structures while the ductility of the

structure could be decreased due to the brittleness of GPC. Therefore, it is necessary to improve the weaknesses of GPC toward better performances.

Despite numerous studies on the mechanical properties of GPC, the behaviours of GPC-based structures are still understudied with contrary findings reported, which limits the wide applications of GPC in construction. Several studies presented that the performances of heat-cured GPC beams and columns were almost similar to those of OPC beams and columns. Therefore, the use of current standards for OPC to design the GPC beams and columns could be accepted [33, 34]. However, some recent investigations showed that the strength of ambient cured and over reinforced GPC beams and columns was overestimated by conventional sectional analysis procedures [35, 36]. Furthermore, current studies concentrated on heat-cured GPC, which could only be applied to precast concrete structures, but difficult to cast-in-situ concrete structures. A previous study has shown that the performances of ambient and heat-cured GPC are different [31], i.e. shrinkage and brittleness. Therefore, further studies investigating the structural performances of ambient cured GPC structures are necessary for possible wide applications of GPC to both precast and monolithic structures.

Beam-column joints are a crucial member of a building under earthquake loading because it relates to the strength development of the adjacent beams and columns [19]. Numerous recent devastating earthquakes across the world showed that if beam-column joints are destroyed, the buildings collapse even though the beams and columns are still in good condition. Beam-column joints often fail by shear stress due to insufficient transverse rebars in these joint regions [40-43, 91]. In most cases, the brittle shear failure is abruptly experienced, even without any cautionary evidence about the collapse of the structures [19, 45]. This unexpected failure is attributed to non-ductile performances of structures [19]. Therefore, it is necessary to enhance the ductility of the joints under seismic loading.

The application of dry joints could resolve many disadvantages of monolithic, wet, and hybrid joints such as long construction time, high construction cost, and negative effects on the environment [14, 96]. However, dry joints with steel bolts are vulnerable to corrosion which is commonly considered as one of the priciest issues and also the critical causes for structural deterioration. In some circumstances, the costs for

maintaining and repairing deteriorated components can be incredibly greater than constructing the new ones [5, 6]. For instance, Kitane et al. [100] reported that during the period of 1998 to 2017, it cost the United States of America an annual average of \$5.8 billion to maintain bridges. This issue could be effectively resolved by using non-corrosive FRP bolts with excellent corrosion resistance. However, the application of FRP bolts in the reality of structural engineering is still limited because these bolts have relatively low shear capacity if compared to conventional steel bolts. The tensile strength of FRP bolts is higher than that of steel bolts but the shear capacity, elastic modulus, and torsion resistance of FRP bolts are lower than those of steel bolts. It is noted that FRP bolts are made of anisotropic materials and behave linear-elastic stress-strain characteristic up to failure [41]. This feature could cause brittle failure if FRP bolts govern the main failure of the beam-column joints. Some researchers [46, 118] reported, however, that specimens did not show brittle failure if FRP material did not govern the main failure of specimens.

There have been a few published studies investigating GPC monolithic joints [119-122] while there has been no research examining the performances of ambient-cured GPC precast joints under cyclic loading in the open literature. The majority of previous studies related to GPC joints were based on testing on small size samples. No analytical model or design procedure has been proposed for GPC joints. According to the above review, ductility of the joint is crucial while GPC reveals very brittle performances at the peak load. Therefore, it is necessary to investigate joint performances using GPC cured under ambient condition. This chapter aims to investigate the performances of a GPC monolithic joint and a new GPC precast joint type using CFRP bolts and concrete-end-plate (CEP). Additionally, an empirical model to calculate the maximum applied loads of the monolithic and precast joints made of GPC is proposed. In order to evaluate the effects of the GPC utility and the accuracy level of the proposed model, the behaviours and the results of the model are sequentially compared with those of the OPC control specimens. It should be noted that the performances of OPC monolithic joints have been fully investigated in many previous studies and models to design these OPC monolithic joints have been proposed in various standards [71, 87-89].

4.2 Experimental program and analytical calculations

4.2.1 Design of the experimental specimens

Two monolithic joints and two precast joints, namely specimens MO1-MG2 and PO3-PG4 were prepared and tested in the study. The letters “O” and “G” denote the use of OPC and GPC to cast these specimens. The two precast joints used CFRP bolts with a diameter of 20 mm to connect beams and columns. The CFRP bolts were applied a prestress level of approximately 6 kN. Two 20-ton load cells were used to determine these tensile forces in the bolts (see Fig. 4-1). All the monolithic joints were designed following ACI 550R-96 [70] and ACI 352R-02 [71]. The use of longitudinal rebars and stirrups was based on the requirements of ACI 318-11 [72]. The two precast joints were designed in reference to the previous studies [19, 46] since no standards are available for this precast joint type. In addition, the weak beam-strong column principle is applied to design all the specimens. Therefore, cross-sections of the columns ($200 \times 200 \text{ mm}^2$) were larger than those of the beams ($150 \times 150 \text{ mm}^2$). These cross-sections were chosen based on previous studies [46, 56, 123]. The beams of the precast joints consisted of two parts: (1) Beam A and (2) the CEP. Details of specimen dimensions and rebars can be found in Fig. 4-2.

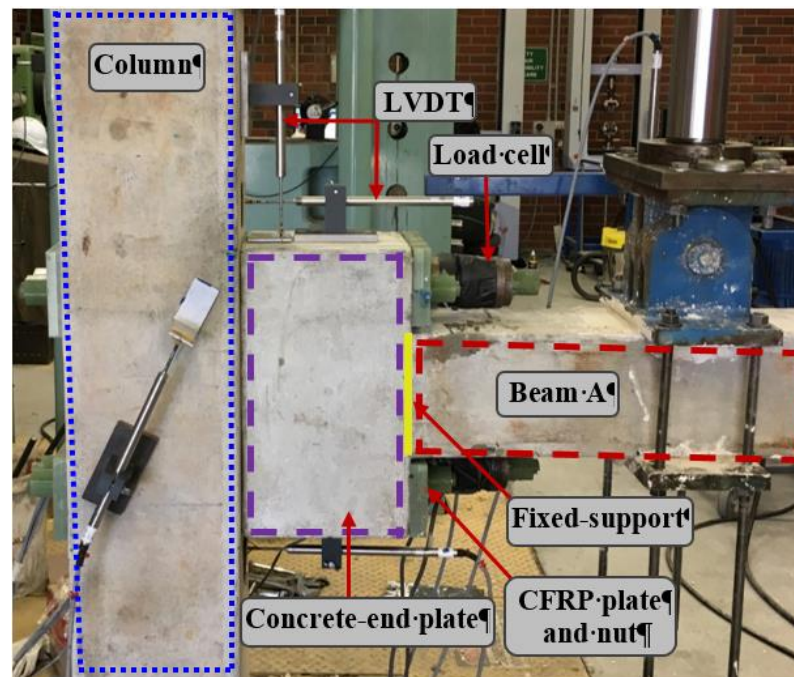


Fig. 4-1. Positions of load cells and LVDTs.

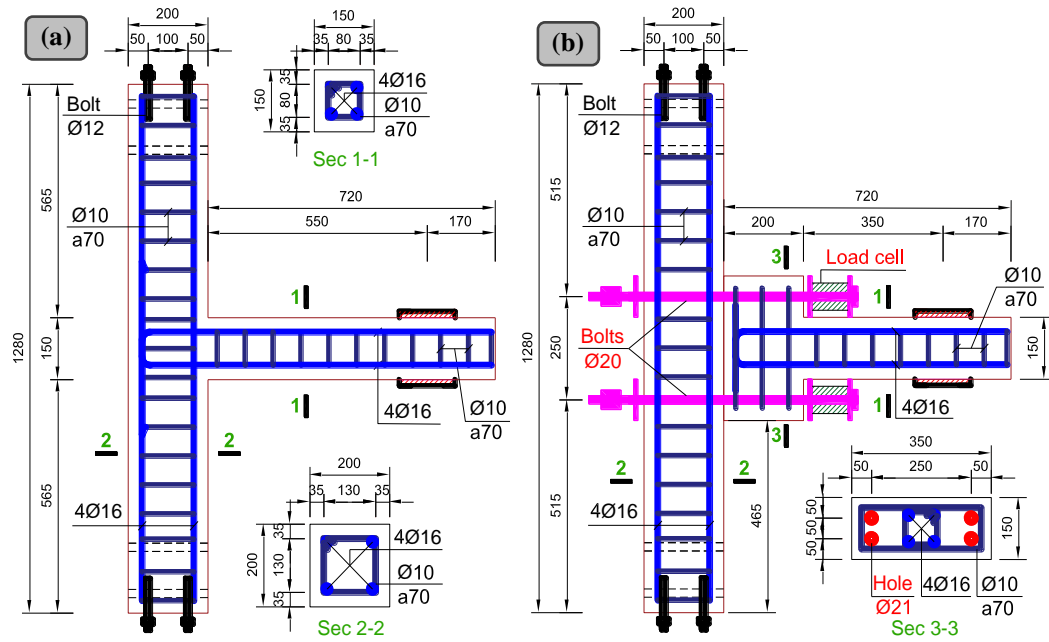


Fig. 4-2. Design of (a) monolithic joint and (b) dry joint (unit: mm).

4.2.2 Mechanical properties of materials

Table 4-1 presents the mixture proportions of 1 m³ GPC and OPC. Two specimens were cast with GPC concrete based on the mixed design of the previous study [124] as presented in Table 4-1. Low calcium fly ash (FA) and ground granulated blast furnace slag (GGBFS) were used as binder materials. Their chemical compositions are presented in Table 4-2. A mixture of 12M sodium hydroxide (NaOH) and D-grade sodium silicate (Na₂SiO₃) solution was utilized as an alkaline activator (Aa). It is noted that 480-g solid NaOH was mixed with 1-litre water to create 12M NaOH. The D-grade sodium silicate consisted of 14.7% Na₂O, 29.4% SiO₂, and 55.9% H₂O. 99% purity of solid NaOH and liquid Na₂SiO₃ were provided by Chem-supply Pty Ltd [125] and PQ-Australia Pty Ltd [126], respectively. Silica sand was used as fine aggregate. The mechanical properties of GPC and OPC were determined according to AS 1012.8.1-14 [74] and AS 1012.9.1-14 [75]. Three cylinders (200-mm height and 100-mm diameter) for compressive tests and three cylinders (300-mm height and 150-mm diameter) for splitting tensile tests were prepared for each GPC batch. The GPC mixture had low workability which needs to be improved in future work. After the casting process, plastic sheets were utilized to cover the top surface of all the specimens. Ambient curing condition was applied for all the GPC specimens until the testing day. Specimens MO1 and PO3 were respectively tested on the 28th and 29th day while two

GPC specimens were tested on the 56th day after casting. The testing-day compressive strength (f'_c) and tensile strength (f_{ct}) of GPC were 66.1 MPa and 5.5 MPa, respectively, while those of OPC were 38.4 MPa and 3.8 MPa, respectively. The mechanical properties of GPC and OPC were different due to different concrete batches. Two OPC specimens (MO1 and PO3) were cast with ready-mixed concrete from a local supplier whereas GPC specimens (MG2 and PG4) were mixed manually at a structural laboratory. This difference of the mechanical properties was also reported in some previous studies [46, 127-129]. As informed by the concrete supplier, the sizes of crushed stone aggregate and slump test results were 7 mm and 150 mm, respectively. Therefore, 7-mm crushed stone aggregates were also used in GPC batches to be compatible with OPC batches. The small aggregate was applied in this study to limit micro-crack width caused by aggregate restrained shrinkage [130]. 10-mm deformed steel bars were used for stirrups whereas the diameter of longitudinal rebars was 16 mm. The top and bottom longitudinal rebars were similarly chosen because cyclic loading was applied for these joints. CFRP bolts, nuts, and plates were supplied by a company in China [76]. As informed by the supplier, GB/T 1447-05 [77] was applied to check the mechanical properties of CFRP bolts. The number of the samples which were used for the testing was 20-30 with the length of 800-1000 mm. The properties of all the rebars and CFRP bolts provided by the manufacturer are summarized in Tables 4-3 and 4-4. The geometry and dimensions of the CFRP bolts and nuts are shown in Fig. 4-3.

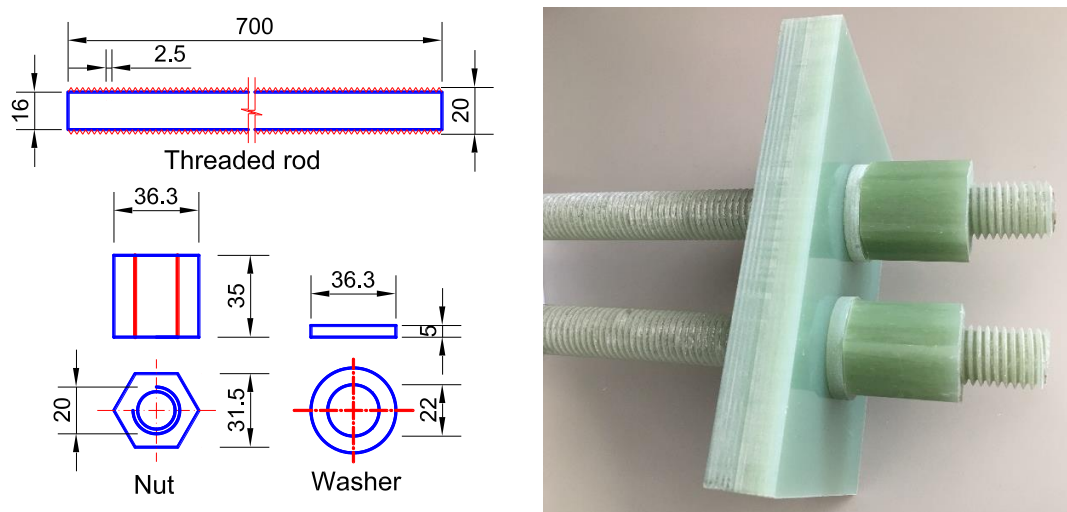


Fig. 4-3. Details of CFRP bolts (unit: mm).

Table 4-1. Mixture proportions of 1 m³ GPC and OPC.

Materials	Unit	GPC	OPC
Sand	(kg/m ³)	630	534
7-mm coarse aggregate	(kg/m ³)	1100	1100
GGBFS	(kg/m ³)	160	-
FA	(kg/m ³)	240	-
Aa/binder ratio	-	0.6	-
Na ₂ SiO ₃ solution	(kg/m ³)	172	-
12 M NaOH solution	(kg/m ³)	69	-
Na ₂ SiO ₃ /NaOH ratio	-	2.5	-
Coarse sand Gin Gin	(kg/m ³)	-	225
Cement	(kg/m ³)	-	400
Water	(L/m ³)	-	175
Plastiment BV35	(L/m ³)	-	1.6
Viscocrete 10	(L/m ³)	-	1.2
Viscoflow 15	(L/m ³)	-	1.2

Note: - = not applicable.

Table 4-2. Chemical compositions of FA and GGBFS.

Composition (wt. %)	FA	GGBFS
Fe ₂ O ₃	12.5	0.9
SiO ₂	51.1	32.5
Al ₂ O ₃	25.6	13.6
K ₂ O	0.7	0.35
CaO	4.3	41.2
MgO	1.5	5.1
MnO	0.15	0.25
Na ₂ O	0.8	0.3
P ₂ O ₅	0.9	0.03
TiO ₂	1.3	0.5
SO ₃	0.24	3.2
Others	0.46	1.12
LOI ^a	0.6	1.1

Composition (wt. %)	FA	GGBFS
------------------------	----	-------

Note: ^a Loss on ignition.

Table 4-3. Rebar properties.

Diameters (mm)	f_y (MPa)	E_s (GPa)	Area (mm ²)	Notes
8	377	200	50	Spirals
10	560	200	78	Stirrups
16	597	200	201	Longitudinal rebars

Table 4-4. Details of CFRP bolts and nuts [76].

Names	Size	Tensile strength	Shear strength	Bending strength	Compressive strength	Ultimate load	Elastic modulus
	(mm)	(MPa)	(MPa)	(MPa)	(MPa)	(kN)	(GPa)
Bolts	φ20	≥ 850	≥ 160	480	760	≥ 267	100
Nuts	φ20	-	-	-	-	100	100

Note: - = not given.

4.2.3 Test setup

Fig. 4-4 shows the typical test setup of all the specimens. As shown in this figure, vertical displacements of the top and bottom column ends were resisted by a hydraulic jack, hinge, and a strut system. This hydraulic jack applied an initial axial force of 15 kN to the column. It is noted that the applied axial force may bring beneficial effects to the joint behaviours [79] which, however, were not investigated in this chapter. The load was applied on the beam tip under manual displacement control by a 500-kN hydraulic jack with the level of 6-9 mm/min based on ACI 374.1-05 [131]. Fig. 4-5 shows the incremental cyclic load history. Two fully reserved cycles were applied at each drift ratio (DR) with an initial ratio of 0.25% to ensure that all the specimens showed linear elastic responses in this initial stage. For the precast specimens, the columns were the first to be set up on the reaction frame. Then, the beams were connected to the columns by four CFRP bolts with a diameter of 20 mm. The four holes on the beams and columns were created by four plastic tubes with the outside diameter of 21 mm. These plastic tubes were embedded into formworks and steel cages

before the concrete casting and were removed one day after the casting. In order to easily remove these plastic tubes, a cutting line was created on each tube with an electric hand cutting machine. Outside tubes were also covered by cling wrap and oil. All CFRP bolts were applied a prestress level of 6.5 kN for Specimen PO3 and 5.3 kN for Specimen PG4.

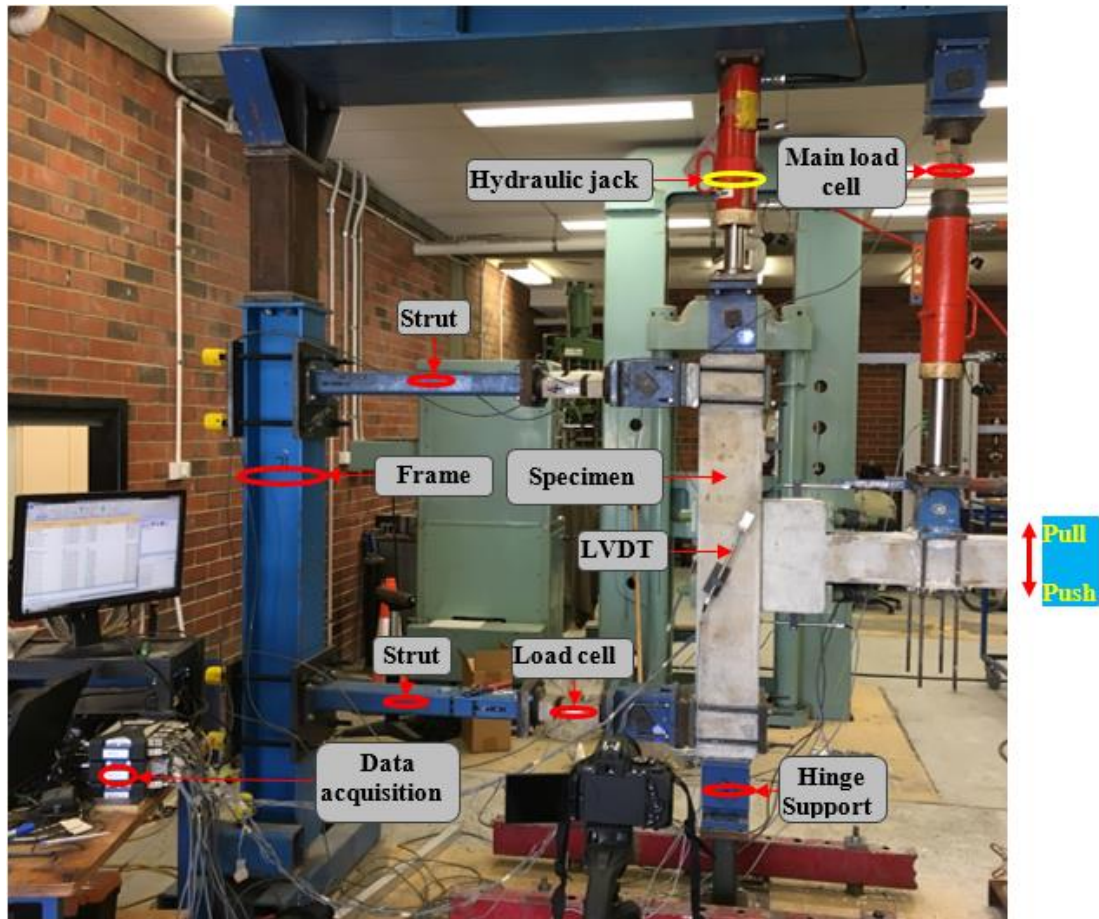


Fig. 4-4. Details of the test setup.

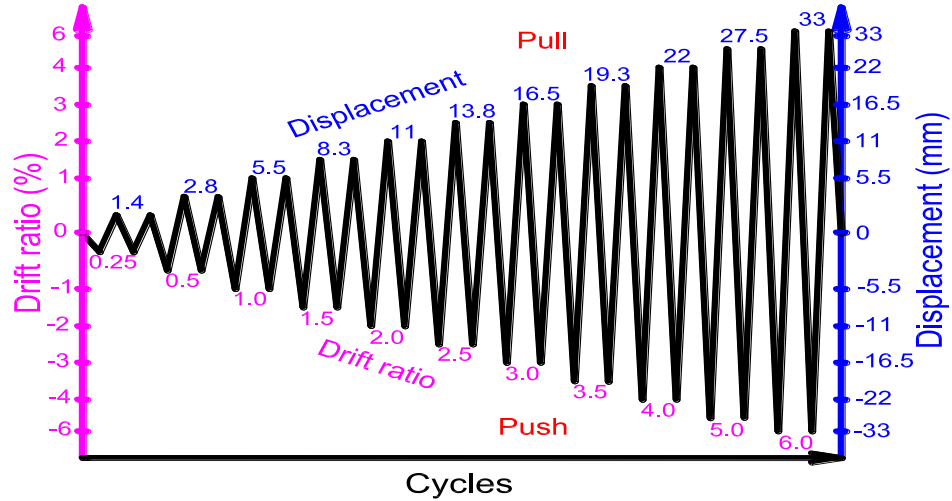


Fig. 4-5. Cyclic loading scheme.

4.2.4 Analytical model to estimate the maximum applied loads and the main failure position

In order to apply these GPC monolithic and GPC precast joints into reality, it is necessary to propose a model for designers to estimate the load-carrying capacity or the horizontal shear resistance (V_{jh}) in the middle zone of the joints. Based on this model, the main failure mode and failure position could be also determined. This section adopts the model proposed by Chapter 3 with some modifications for the GPC specimens. The results of the proposed model are compared to the experimental results of these current and previous studies. This kind of dry joints could fail at the fixed-supports and the joint areas. Therefore, the load-carrying capacity (P_{max}) is the minimum of applied load (P_{max1}) and (P_{max2}) corresponding to the failure occurrence at these two locations. It is noteworthy that two assumptions were adopted to determine P_{max2} of the precast joints: (1) Only the middle stirrup inside CEP mainly resisted the shear force in the joint area [46], and (2) The middle stirrup and longitudinal rebar yielded at the maximum applied load.

4.2.4.1 Failure at the fixed-support

P_{max1} was calculated following the nominal moment strength (M_{n1}) of beams. The following formula was used to calculate P_{max1} :

$$P_{max1} = \frac{M_{n1}}{L_1} \quad (4-1)$$

where L_I is the length of cantilever beams (L_I is 550 and 350 mm for monolithic and precast specimens, respectively).

For Specimens MG2 and PG4, previous studies showed that current standards and available models of OPC beams can be applied to design GPC beams with high accuracy, however, some modifications are needed if the beam is over reinforced [36]. In reality, the cross-sections of beams need to be reduced to ensure requirements of architecture so the beams could be designed with over reinforced. Most of the previous studies have ignored this issue [132, 133]. In the current study, the specimens were designed over reinforced which ensures the practicality of the results. Therefore, the use of existing standards to calculate M_{n1} requires some modification in k_3 of the rectangular stress-block parameters [36]. In this study, M_{n1} of OPC specimens was determined based on ACI 318-11 [72] while M_{n1} of GPC specimens was calculated based on the study by Tran et al. [36] in which the value of k_3 was changed from 0.9 to 0.7. M_{n1} of all the specimens were calculated by using the nominal yield strength of rebars.

4.2.4.2 Failure in the middle zone

For monolithic specimens, P_{max2} was determined based on the nominal shear strength (V_{ACI}) recommended by ACI 318-11 [72] as follows:

$$V_{ACI} = \gamma \sqrt{f'_c} A_j \quad (4-2)$$

where γ depends on the effects of confinement in a joint, $\gamma = 1.7$, $\gamma = 1.2$, and $\gamma = 1.0$ if beams are confined at all four faces, two or three faces, and other cases of joint, respectively; the compressive strength of concrete is denoted as f'_c , A_j is an effective joint area. If h_{col} and b_j represent the effective joint depth and width, respectively, and b_c and b_b denote the width of the column and beam (Fig. 4-6), respectively, it has

$$A_j = b_j h_{col}, b_j = \min\{b_b + 2x, b_b + h_{col}\} \text{ if } b_c \geq b_b, b_j = b_c \text{ if } b_c < b_b \quad (4-3)$$

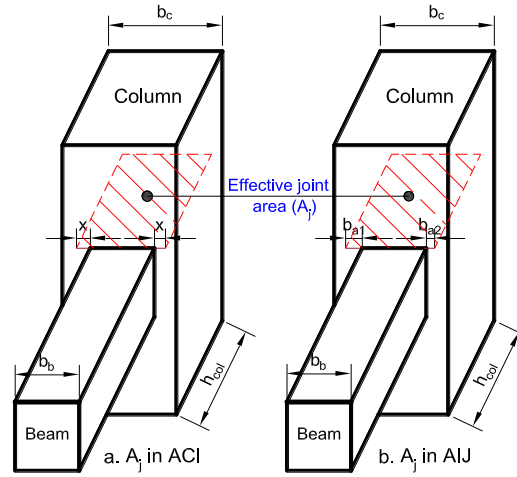


Fig. 4-6. Definition of the effective joint area.

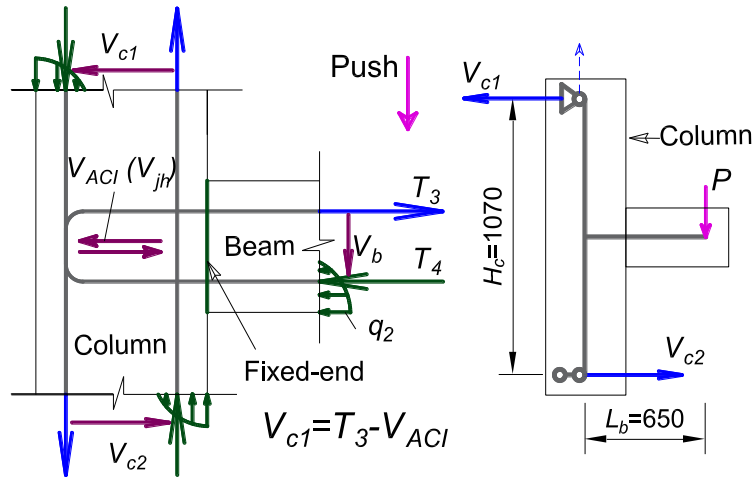


Fig. 4-7. Global equilibrium of the monolithic joint.

As shown in Fig. 4-7, P_{max2} of the monolithic specimens is determined as follows:

$$V_{c1} = T_3 - V_{ACI} \quad (4-4)$$

$$P_{max2} = \frac{V_{c1}H_c}{L_b} \quad (4-5)$$

where V_{c1} , T_3 , H_c , and L_b are the shear force at column top, the tensile forces of the rebars, the height of the column, and the distance from the loading point to the centroid of the column, respectively.

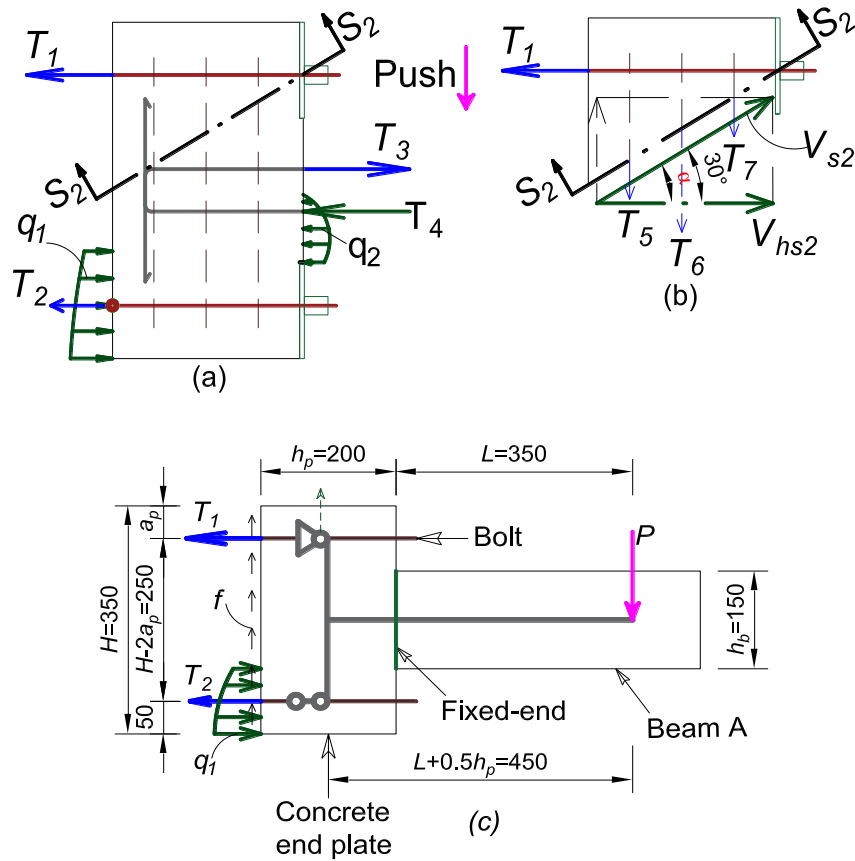


Fig. 4-8. Global equilibrium of the proposed precast joint.

For the precast specimens, stirrups were assumed to yield for calculating P_{max2} . Fig. 4-8(b) shows the free body diagram of the tested specimens. The tensile force in the top bolts (T_1) is expressed as follows:

$$T_1 = T_1^a + T_1^b = V_{hs2} + \gamma_r P_r \quad (4-6)$$

where P_r and γ_r are the initial prestress forces and the prestress rate lost in the bolts (i.e. γ_r is 0.25 and 0.84 for CFRP bolts and steel bolts, respectively [46]). It is noticeable that the tensile forces (T_1 and T_2) in the bolts consist of two components (i.e., T_1 including T_1^a and T_1^b) caused by the applied load and prestress force, respectively. At Section S_2 - S_2 , the horizontal shear force (V_{hs2}) is determined as follows:

$$V_{s2} = V_s \sin \alpha + V_c \quad (4-7)$$

$$V_{hs2} = V_{s2} \cos \alpha \quad (4-8)$$

where $V_s = nA_v f_{yt}$ refers to the shear resistance of the stirrups, n is the number of legs of stirrups, and f_{yt} and A_v are respectively the yield strength and cross-sectional area of stirrups. According to the previous study [46], only the middle stirrup inside CEP mainly resisted the shear force. Therefore, the middle stirrup was considered to determine V_s . For the shear resistance of the OPC, $V_c = \beta h_p b_p \sqrt{f'_c}$, $\beta = \frac{1}{6}$ is adopted [72], b_p and h_p denote the width and thickness of CEP. For the shear resistance of the GPC, $\beta = 0.29$ is adopted to determine V_c based on the upper value of the shear strength in ACI 318-11 [72].

Fig. 4-8(c) shows the free body diagram of the precast beam. P_{max2} is calculated as follows:

$$P_{max2} = \frac{T_1(H-2a_p)}{(L+0.5h_p)} \quad (4-9)$$

where L is the distance from the fixed-support to the loading point, a_p refers to the distance between the centroid of the top bolts and the extreme-top fibre of the CEP, H and h_p denote the height and thickness of the joint area, respectively.

The maximum applied load (P_{max}) of both joint types (i.e., monolithic and precast joint) is determined as follows:

$$P_{max} = \min(P_{max1}, P_{max2}) \quad (4-10)$$

For the horizontal shear resistance (V_{jh}) in the middle zone of the precast specimens. V_{jh} of the proposed model is determined based on the tensile forces in the bolts (T_1) and in the longitudinal rebars (T_3). T_1 was calculated by Eq. 4-6 whereas T_3 is calculated from a bending moment (M) when P_{max2} was determined by using Eq. 4-9. Therefore, V_{jh} can be determined as follows:

$$V_{jh} = T_1 - T_3 \quad (4-11)$$

This study also adopts the experiment results of Chapter 3 and Saqan [14] to evaluate the accuracy of the proposed models. The maximum applied loads ($P_{exp-max}$) of all the tested specimens were taken from experimental results. Specimens PO3, P5-S-SP, and DB-TC failed in the joint area. Therefore, V_{jh} of these specimens is determined by

Eq. (4-11), in which T_3 is calculated from the nominal yield strength of the longitudinal rebars. The main parameters are summarized in Table 4-5.

As can be observed from Table 4-5, the proposed model predicts that Specimen PO3, P5-S-SP, and DB-TC experienced the main failure in the joint areas whereas other specimens failed at the fixed-support. The variations of P_{max1} between the proposed model and the experiment results are from 10% to 32%. Specimen MG2 presents the highest variation of 32%. This high variation could be attributed to the inaccuracy in estimating the moment capacity of the GPC beam. It should be noted that no standards have been introduced to accurately estimate the nominal moment strength of GPC beams yet. Therefore, this chapter adopted a model proposed by Tran et al. [36], which modified the stress block parameters for use in GPC beams based on analytical derivations and limited testing data. The accuracy and the applicability of the proposed model by Tran et al. [36] need to be studied further since the beam moment strength depends on many parameters which are most likely nonlinear intercorrelated. The model proposed based on limited testing data and analytical derivations with an ideal assumption of beam conditions does not necessarily cover the beam conditions in this chapter. On the other hand, P_{max1} of Specimens MO1, MG2, PG4, and P4-S-SP-H were lower than the $P_{exp-max}$, indicating reasonable safety margin for the joints.

Concerning the failure in the joint areas, the maximum applied loads were well predicted by the proposed model with a variation between 2 and 26%. Also, the variations of the horizontal shear strength in Specimens PO3 and P5-S-SP were 26% and 46%, respectively. Specimens PO3 and P5-S-SP were over reinforced. The nominal yield strength of the rebars was adopted to calculate T_3 . As a result, the high variation of the horizontal shear strength was attributed to this assumption. For example, only 1.3% variation of the horizontal shear strength in Specimen PO3 is observed if the actual strain of the rebars is adopted to calculate T_3 . In addition, the variation of the horizontal shear strength between ACI 318-11 [72] and the experiment reached approximately 35% in Specimen PO3. This high variation is understandable because ACI 318-11 [72] model is meant for monolithic joints, not for precast joints with the CEP and bolts as in the current study.

Table 4-5. The comparisons between the experimental and theoretical results of P_{max} and V_{jh} .

Names	Experimental results		Theoretical results (fixed-support)				Theoretical results (middle zone)					
	$P_{exp-max}$	V_{jmax}	M_{nl}	P_{max1}		V_{ACI}	$V_{c1}; T_1$	V_{hs2}	P_{max2}		V_{jh}	
	(kN)	(kN)	(kN.m)	(kN)	(%)	(kN)	(kN)	(kN)	(kN)	(%)	(kN)	(%)
MO1	32.3	-	15.4	28.0	-13.3	216.9	23.2 ^a	-	38.2	-	-	-
MG2	46.2	-	17.2	31.3	-32.3	284.6	44.4 ^a	-	73.2	-	-	-
PO3	37.7	137.6	15.4	44.0	-	185.9	66.5 ^b	64.9	37.0	-2	173.6	26
PG4	54.6	-	17.2	49.1	-10.0	-	100.7 ^b	99.3	55.9	-	-	-
Chapter 3 [46]												
P4-S-SP-H	50.3	-	17.3	49.4	-1.7	185.9	107.7 ^b	64.9	59.9	-	-	-
P5-S-Sp	41.8	114.1	14.9	42.6	-	185.9	73.76 ^b	64.9	41.0	-2	166.4	46
Saqan [14]												
DB-TC	499	*	337.8	422.3	-	-	708.3	271.5	367.1	26	*	*

Note: - = not applicable.

* = lack of data.

^aValue of V_{c1} .

^bValue of T_1 .

4.2.5 Experimental results and discussion

4.2.5.1 General behaviours and failure patterns

All the specimens were tested under cyclic loading. CFRP bolts and the longitudinal rebars remained in a linear elastic range up to the maximum applied loads. No failure occurred in either the CFRP bolts or longitudinal rebars. For example, the maximum tensile strength of the CFRP bolts in Specimens PO3 and PG4 was 32 kN and 45 kN, which accounted for 32% and 45% of their ultimate tensile strength (100 kN), respectively. The main failure of all the tested specimens was governed by concrete as also reported in the previous studies [19, 46]. This design ensured that the application of CFRP material did not cause the brittle failure in this precast joint type. Fig. 4-9 shows the failure modes of all the specimens. All the columns of the precast specimens were designed with higher capacity compared to the beams. There was no failure on the columns of the precast specimens while some minor inclined cracks were observed on the columns of the monolithic specimens. This design ensured that all the joints satisfied the requirements of the weak beam-strong columns for the reinforced-concrete structures under earthquake loading. Fig. 4-10 shows that strain in

longitudinal rebars of the beams was considerably higher than that of the columns. For instance, in Specimen PO3, the maximum strain in the longitudinal rebars of the beam was 2559 $\mu\epsilon$ whereas that of the column was only 619 $\mu\epsilon$. In addition, slips between the column and CEP were not recorded by LVDT (linear variable differential transformer) during the test due to high friction between their two interfaces. Therefore, shear stress did not cause failure in CFRP bolts during the tests.

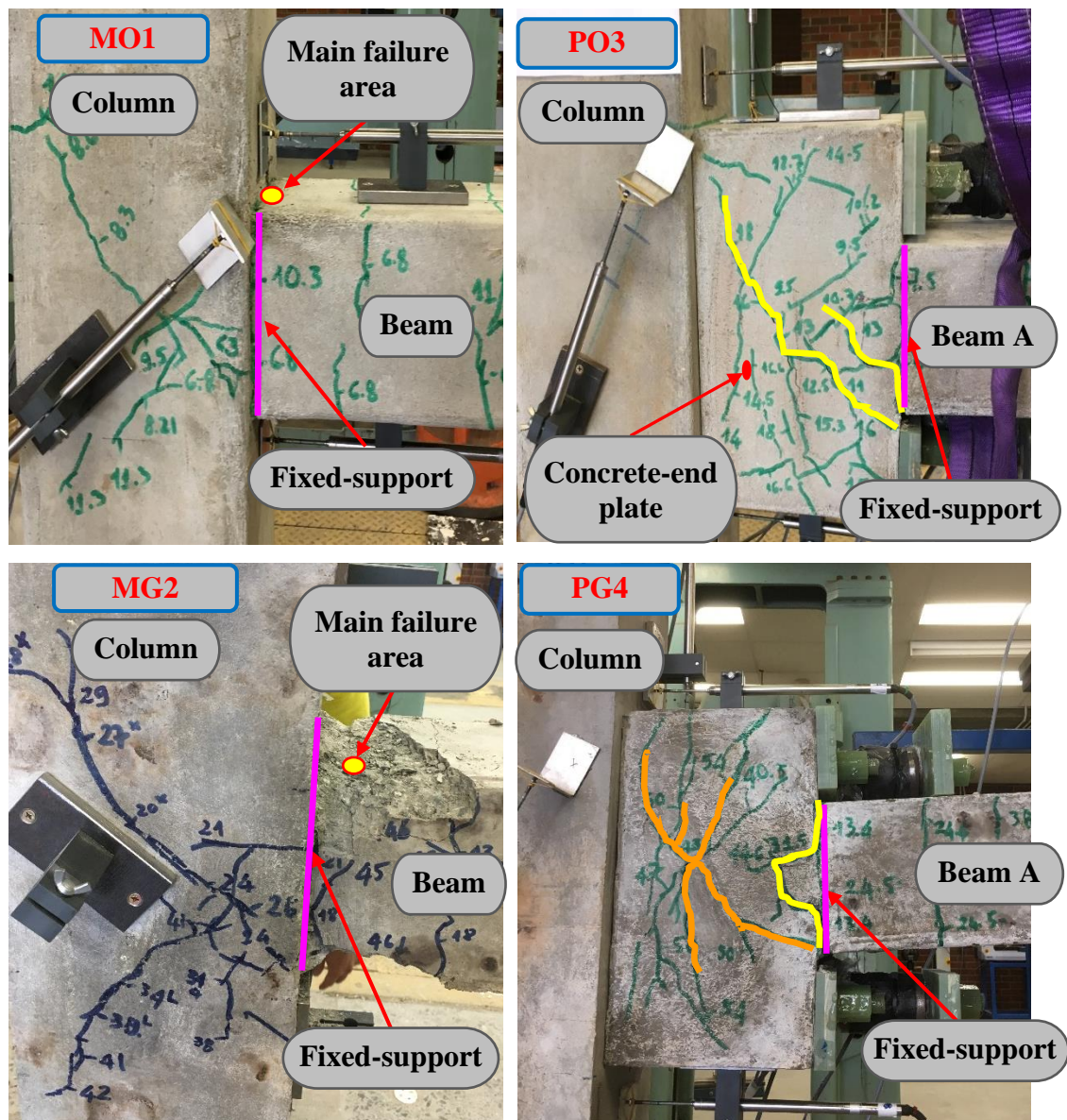


Fig. 4-9. Crack patterns.

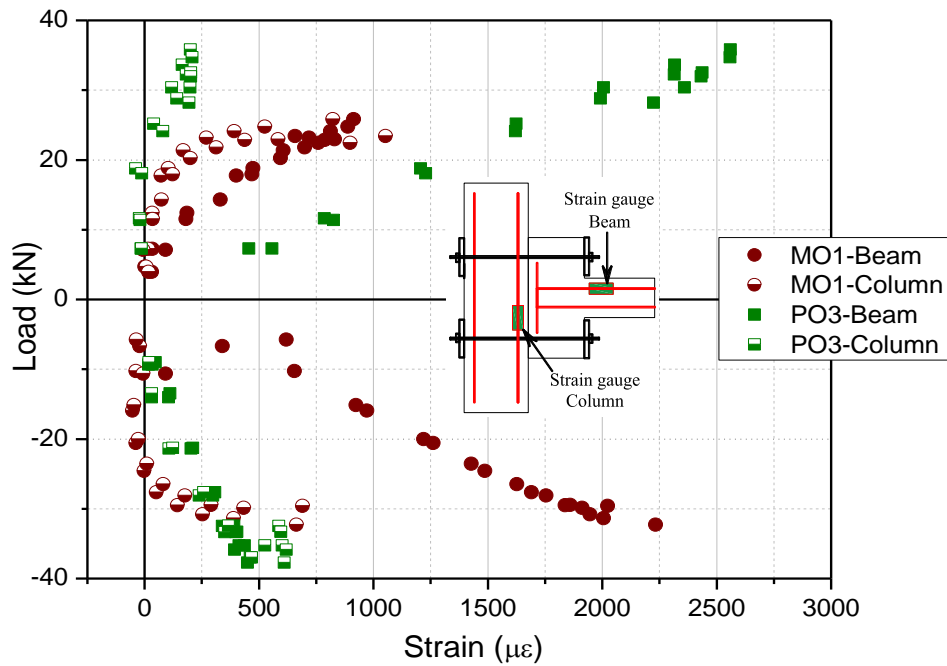


Fig. 4-10. Data of strain gauges on longitudinal rebars of beams and columns.

As can be seen in Fig. 4-9, Specimens MO1 and MG2 exhibited similar failure patterns and trends of crack development whereas two precast specimens showed different failure modes and failure positions. Except for the concrete, two monolithic specimens were designed similarly. Specimen MO1 was cast by OPC while GPC was used to cast Specimen MG2. The vertical flexural cracks appeared initially at $\pm 0.5\%$ DR when the tensile strain of concrete at the beam soffit reached its nominal tensile strain. It is noted that cracks on Specimen MG2 developed later than those on Specimen MO1 at the same DR (see Fig. 4-11). For example, the inclined cracks on Specimen MO1 propagated into the joint at 1% DR whereas there were only flexural cracks appearing on the beam of Specimen MG2 at the same DR. This phenomenon could be attributed to the different tensile strengths of concrete. The tensile strength of GPC (5.5 MPa) was higher than that of OPC (3.8 MPa). Therefore, the tensile cracks and shear cracks developed in Specimen MG2 more slowly than those in MO1. After 1% DR, the inclined cracks rapidly spread into the joint region when the longitudinal rebars mainly contributed to resist the bending moment of the beam. The inclined cracks on both the monolithic specimens initially concentrated in the middle joint area and then these inclined cracks propagated to two corners of the column. In addition, minor concrete

crushing appeared at the fixed-support at 2% DR for Specimen MO1 and 2.5% DR for Specimen MG2. Specimen MO1 reached the maximum applied load at 5% DR while that of Specimen MG2 was 4%. The different results are attributed to the brittleness of GPC at the peak load. Therefore, although cracks occurred later, the applied load decreased immediately when Specimen MG2 reached the maximum applied load. Figs. 4-9(MO1) and 4-9(MG2) show that both the monolithic specimens failed due to the crushing of concrete and vertical cracks at the fixed-support of the beams.

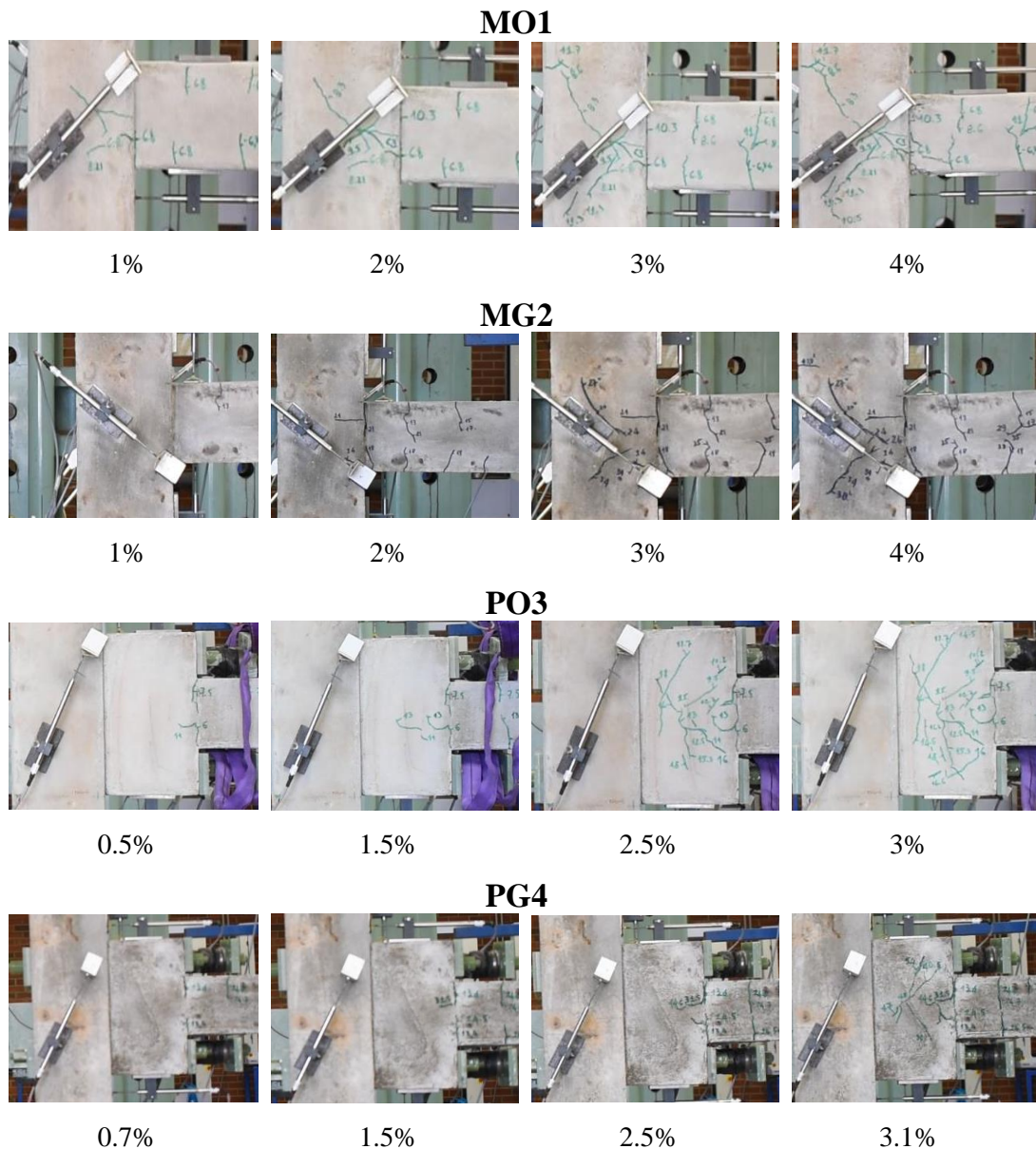


Fig. 4-11. Progressive development of cracks.

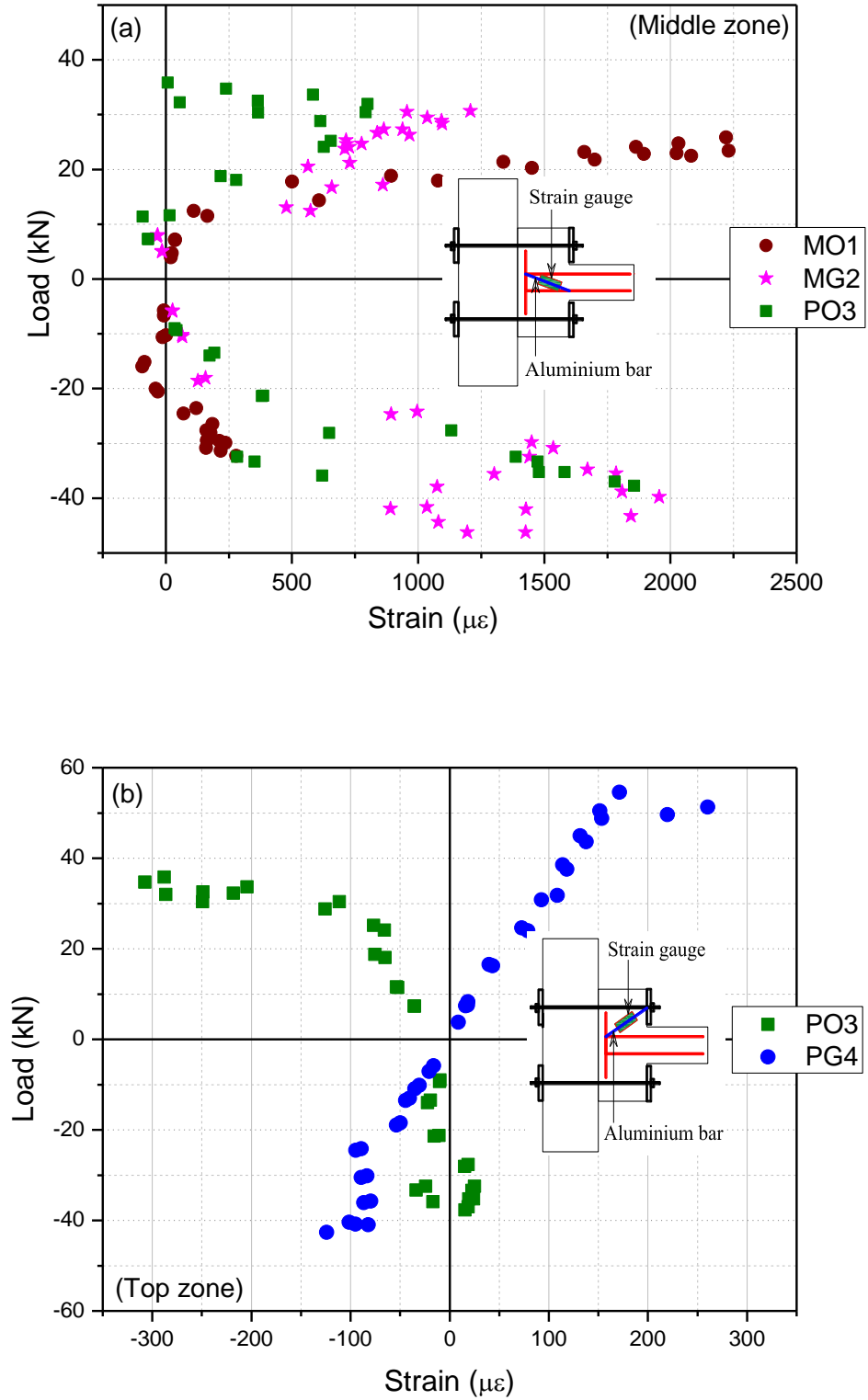


Fig. 4-12. Strain of aluminium bars embedded inside of concrete to measure concrete strain.

According to the previous studies [9, 14, 67, 90], beam-column joints could fail due to either diagonal compressive forces or shear forces. However, data of the strain gauges attached on aluminium bars to measure concrete strain (see Figs. 4-12 and 4-13) show that the main failure of these dry joints was a result of the tensile cracks and shear cracks in the joint areas. Therefore, the use of spirals in the top and bottom zones (see Fig. 4-13) did not improve the peak loads compared to Specimen without spirals. Concerning the analysis in Section 4.2.4.2, increasing the diameter of the middle stirrups inside the CEP is a promising solution to enhance the performance of these dry joints. Both precast joints exhibited different failure modes as shown in Fig. 4-9. Specimen PO3 failed in the middle zone of CEP whereas Specimen PG4 failed at the fixed-support. Flexural cracks also occurred quite early at 0.5% DR because concrete tensile strain at the fixed-support exceeded its limit. Following this stage, the longitudinal rebars of the beam mainly resisted the bending moment. Therefore, tensile cracks spread into the middle area of the CEP. Numerous inclined cracks formed in the CEP from 0.5% to 3% DR as shown in Fig. 4-11(PO3). Two yellow cracks with a width of 1.5 mm caused the main failure of this specimen (see Fig. 4-9(PO3)). In addition, the appearance of cracks on the precast GPC specimen (PG4) also took longer than that on the precast OPC specimen (PO3). It indicates the tensile strength of concrete significantly affected the joint behaviours. Fig. 4-11(PG4) shows that only four minor cracks appeared on the CEP of Specimen PG4 at the peak load while various inclined cracks were distributed over the entire surface of CEP in Specimen PO3. This different failure mode could be attributed to the higher tensile strength (5.5 MPa) and brittleness of GPC as compared to OPC (3.8 MPa). The high tensile strength of GPC concrete minimized the tensile crack development in the CEP of Specimens PG4. Therefore, the main failure mode was changed from the joint to the beam at the fixed-support as shown by the yellow curve in Fig. 4-9(PG4). After reaching the peak load, the inclined cracks continued to develop on the CEP surface of specimen PG4 until the end of the test. This performance is attributed to the strength hardening of longitudinal rebars. Therefore, the tensile stress in the longitudinal rebars still increased after achieving the maximum applied load. Furthermore, if the precast joints with OPC and GPC had the same compressive and tensile strength, no significant difference could be observed between the failure mode and failure position of the two joints. Both precast joints might fail at the joint areas because tensile and shear cracks governed the main failure mode of these specimens. However, more brittle failure with

more inclined cracks could occur on the CEP of the precast specimen with GPC (PG4), compared to Specimen PO3 due to the brittle characteristic of GPC material [117].

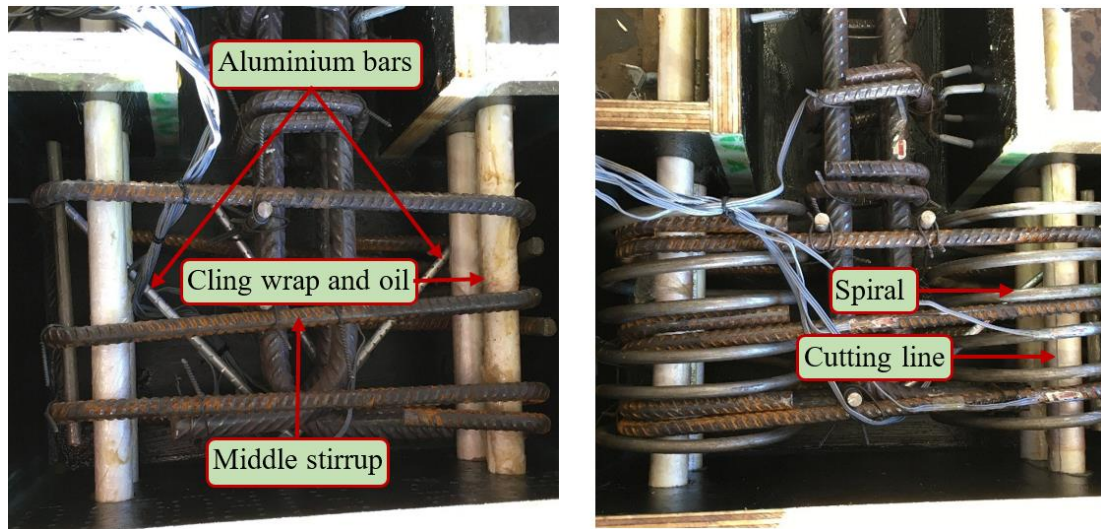


Fig. 4-13. Arrangement of rebars in the concrete-end-plate.

4.2.5.2 Hysteretic performance and energy dissipation capacity

Hysteretic response and energy dissipation capacity are the crucial characteristics to evaluate the performances of beam-column joints under seismic loads. A beam-column joint is considered having excellent energy dissipation capacity if the joint shows ductile behaviours without a considerable reduction of the effective stiffness and strength. The energy dissipation is calculated by the enclosed area (E_h) inside the hysteretic loop of each cycle [19]. The hysteretic responses and the energy dissipation capacities of all the specimens are shown in Figs. 4-14 and 4-15. Up to 1% DR, the energy dissipation capacity of all the specimens showed a similar trend and values since the response remains primarily in the elastic range. In general, the shape of the hysteresis loops of Specimens MO1 and MG2 was similar to each other while the two precast specimens revealed different hysteretic performances with less pinching observed in Specimen PG4 as compared to Specimen PO3. It should be noted that the pinching is associated with the considerable variations in the area of hysteresis loops. This observation could be explained that Specimen PG4 experienced fewer cracks than Specimen PO3 at the same DRs as shown in Fig. 4-11. As previously mentioned, the tensile strength of concrete considerably affects the crack development of these precast joints. Consequently, the use of high tensile strength concretes in Specimen PG4 limited the appearance and development of tensile cracks on the CEP. However,

overall energy dissipation of Specimen PO3 was lower than that of Specimen PG4 from 1% to 3% DR because the applied load per cycle of Specimen PO3 was lower than that of Specimen PG4. Therefore, the enclosed area (E_h) inside the hysteretic loop of each cycle of Specimen PO3 was lower than that of Specimen PG4. After reaching the maximum applied load at 3% DR, the failure modes of the two precast specimens were different. Specimen PO3 failed at the joint area whereas Specimen PG4 failed in the beam at the fixed-support. Wider flexural cracks were observed at the fixed-support of Specimen PG4, compared to the inclined cracks on CEP of Specimen PO3. Consequently, these wider flexural cracks combined with higher impact forces causing a sharp increase of energy dissipation of Specimen PG4 as compared to that of Specimen PG3.

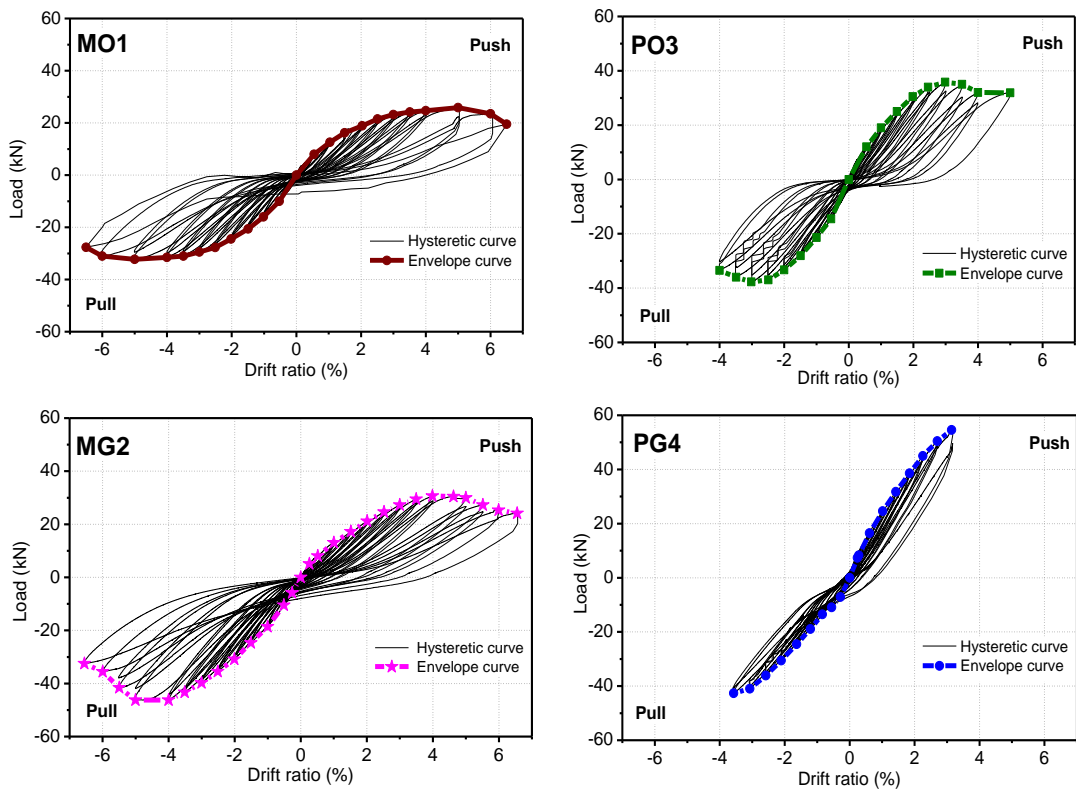


Fig. 4-14. Comparison of hysteretic load-drift ratio responses.

Meanwhile, the monolithic joints revealed linear responses from the beginning of the test to 1% DR because most of the materials remained in the elastic range in the initial stage. Therefore, less energy was dissipated in the early stage since only few minor cracks were formed. After 1% DR, the cracks on the beam and in the joint zone gradually developed causing the increase of the pinching on the hysteretic loop. Up to

3.5% DR, the energy dissipation of Specimens MO1 and MG2 was quite similar (see Fig. 4-15). However, when the DR increased from 3.5% to 6%, the energy dissipation of MO1 had a tendency to overcome that of MG2. This observation could be explained that the compressive and tensile strengths of GPC were higher than those of OPC. Therefore, the development of vertical cracks and crushing concrete at the fixed-support were minimized on Specimen MG2. More cracks on Specimen MO1 means it absorbed more energy than its counterpart.

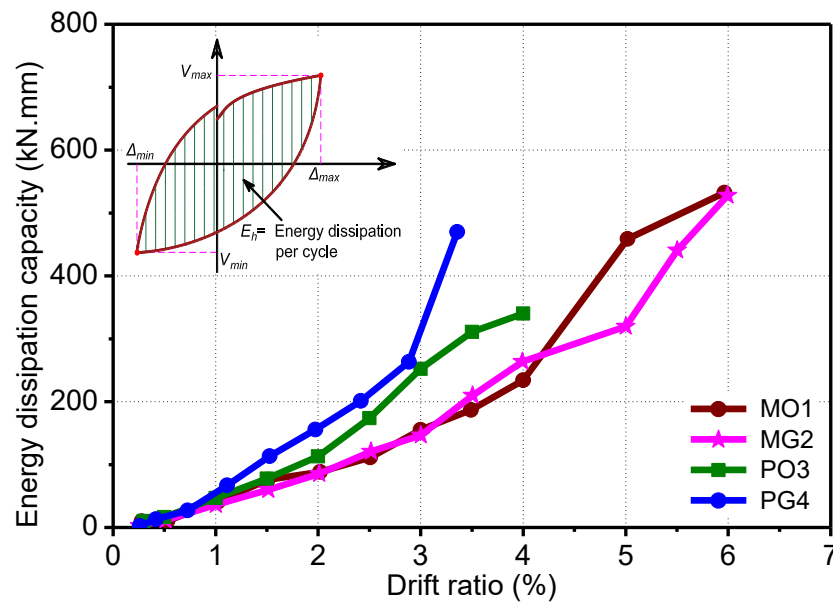


Fig. 4-15. Comparison of energy dissipation capacity.

As shown in Fig. 4-15, the energy dissipation of the dry joints (PO3 and PG4) was greater than that of the monolithic joint (MO1 and MG2) from 1% DR till the end of the test. For instance, the energy dissipation of Specimen PO3 was higher than that of Specimen MO1, approximately 62% at 3% DR. Fatter hysteretic loops of the dry joints, compared to the monolithic joints, caused the difference of energy dissipation between the two joint types. The above results proved that the proposed dry joints could be effectively applied in earthquake-prone regions.

4.2.5.3 Envelope curves and maximum applied loads corresponding to DR

The envelope diagrams of the tested specimens were indicated in Fig. 4-16. It is noted that the envelope curve of Specimen PG4 is only up to 3.1% DR in push (+) direction and 3.5% in pull (-) direction because no data were recorded after achieving the peak

load due to malfunction of the testing system. Overall, all the envelope curves in Fig. 4-16 were almost symmetrical in the push and pull directions due to the similar design of the top and bottom longitudinal rebars of the beams. However, the load-carrying capacity in the first direction of each cycle was slightly higher than that in the second direction. This phenomenon is attributed to the slight reduction of the applied load in the second direction due to damages in the specimens induced by the first cycle.

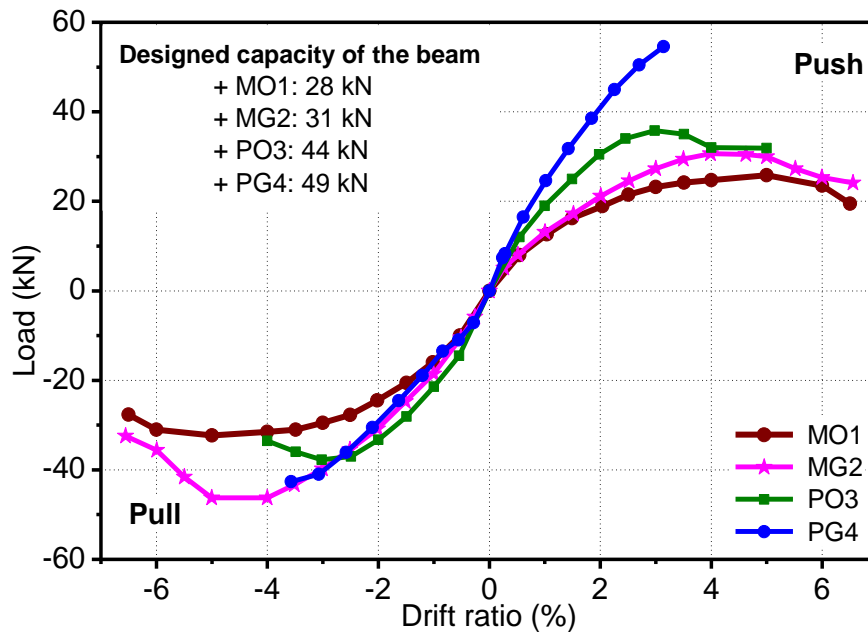


Fig. 4-16. Load-drift ratio envelope curves.

Two OPC Specimens (MO1 and PO3) had the same design with their counterparts GPC specimens (MG2 and PG4), respectively, except concrete. It is because the performances of GPC were the main parameter to be investigated in this chapter. The use of high strength GPC did not affect the shape of the envelope curve but affect the load-carrying capacity as shown in Fig. 4-16. For instance, Specimen PG4 achieved 54.6 kN at the peak load whereas the peak load of Specimen PO3 was 37.7 kN. This different load-carrying capacity was attributed to the different tensile and compressive strength of the two kinds of concrete. High tensile and compressive strengths of the GPC specimens improved the tensile crack resistance in the middle joint and the crushing of concrete at the fixed-support. Meanwhile, after reaching the peak load from 4% to 5% DR for Specimens MO1 and MG2, the applied load of these two specimens reached its plateau. The yielding and strength hardening of the rebars led to

this favourable response which prevented the brittle failure of the beam-column joint and offered essential warnings before the joint could completely fail [46].

Table 4-6 summarizes the maximum applied loads with the specimens' DRs. In order to evaluate the ductility of the joint response, the DR is commonly utilized to compare between different beam-column joint types. The DR (R) is determined as follows:

$$R = D/l \quad (4-12)$$

where D and l are the vertical displacement and the beam length (l is 550 mm in this study).

Table 4-6. Maximum applied loads with corresponding DRs.

Names	Peak load (kN)		Increase (%)		Average (kN)	Increase (%)	DR at peak load (%)	
	Positive	Negative	Positive	Negative			Positive	Negative
MO1	25.8	32.3	-	-	29.1	-	5.0	5.0
MG2	30.7	46.2	18.7	43.3	38.4	32.3	4.0	4.0
PO3	35.8	37.7	38.6	16.9	36.8	26.6	3.0	3.0
PG4	54.6	42.7	111.2	32.2	48.6	67.3	3.1	3.6

Note: - = not applicable.

DR of the precast specimens is often lower than that of the monolithic specimens due to the discontinuity of the longitudinal rebars or the concrete between the beams and columns. For example, the DR of the monolithic joints usually achieves about 3% to 5% [129, 134] while precast joints only reach between 1.5% to 3% DR [10, 14]. This result explains why precast joints have not been popularly applied in earthquake-prone regions. In addition, standards require different DRs to be achieved for ductile moment-resisting frames. For instance, 2% DR is a requirement of ASCE 41-06 [18] while the requirement of CSA A23.3-07 [17] for structures built in seismic regions is 2.5% DR. The two precast specimens (PO3 and PG4) reached 3% DR while DR of the two monolithic specimens, namely MO1 and MG2, were 5% and 4%, respectively. Therefore, all the specimens using OPC and GPC could be effectively applied in seismic regions. It is noted that the DR of Specimen MG2 was lower than that of Specimen MO1, although they had the same design except the different properties of the concrete. This observation could be explained by two reasons: (1) GPC demonstrated very brittle failure at the maximum applied load owing to the material

characteristics. (2) Specimen MG2 was cast by a high strength GPC (66.1 MPa). The brittle behaviours resulted in a low DR of Specimen MG2 as compared to Specimen MO1 (38.4 MPa) because concrete governed the main failure of the specimens.

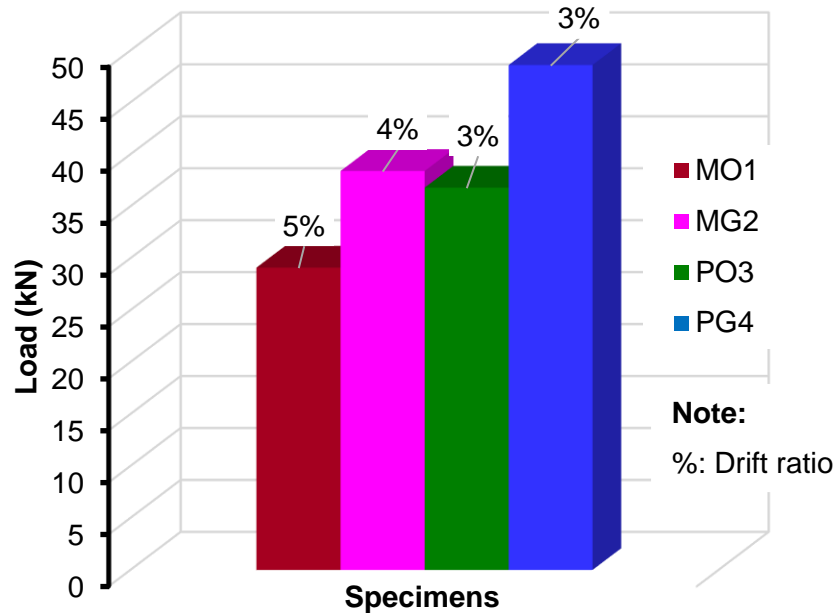


Fig. 4-37. Comparison of average load-carrying capacity and drift ratio.

Fig. 4-17 shows the maximum-load comparisons of the specimens. Overall, the proposed precast joints exhibited promising performances in DR and the maximum applied loads, compared to those of the existing research [13-15]. The peak loads of the two precast joints (PO3 and PG4) were higher than both of the monolithic joints (MO1 and MG2), by approximately 26.6%. This excellent result might be attributed to the effects of the CEP. For failure at the fixed-support, the 550-mm cantilever beam of monolithic joints was longer than that of the precast joints (350 mm) whereas these beams had the identical cross-sections. Consequently, when the same load was applied, the bending moment at the fixed-support of monolithic joints was greater than that of the precast joints by approximately 57%. Therefore, it suggests that the utility of the CEP improves the maximum loads of these precast joints. For the failure in the joint areas, the maximum applied loads of the dry joints were determined by the height and thickness of the CEP. This study intentionally adjusted the thickness reported in the previous study [14]. As a result, the maximum applied loads of the precast joints dramatically enhanced when compared to those of the control monolithic joints. In

addition, the peak load comparisons between the OPC group (MO1 and PO3) and the GPC group (MG2 and PG4) show that the peak load of the GPC group was 32% higher than that of the OPC group because the compressive strength (66.1 MPa) and the tensile strength (5.5 MPa) of the GPC group were higher than the compressive strength (38.4 MPa) and the tensile strength (3.8 MPa) of the OPC group. Therefore, it can be concluded that GPC could effectively replace OPC and meet performance requirements.

4.2.5.4 Ductility of joints

Ductility and drift ratio are two main parameters to evaluate the load-carrying capacity of structures without any considerable strength reductions. In this study, the ductility of beam-column joints is determined by the following equation [46, 82]:

$$\mu = \frac{\Delta_u}{\Delta_y} \quad (4-13)$$

where Δ_u and Δ_y denote the ultimate and yield displacements of the joints at the ultimate and yielding load, respectively. The ultimate displacements of Specimens PO3 and PG4 were monitored at 90% post-maximum load and at the maximum load, respectively because of the limitation of equipment. Meantime, the ultimate displacements of the two monolithic joints were determined at 85% of the post-maximum load because the new equipment was used to replace the old one. For the yield displacement, there are numerous methods to determine this parameter. Fig. 4-18 shows the adopted method to define the ultimate and yield displacement of all the tested specimens.

Table 4-7. Ductility of tested specimens.

Names	Force	Q_{max}	Q_1	Δ_y	Q_2	Δ_u (85%)	$\mu = \Delta_u / \Delta_y$	Average (μ)	Decrease (%)
	Units	(kN)	(kN)	(mm)	(kN)	(mm)			
MO1	Positive	25.8	19.4	15.6	22.0	35.8	2.3	2.4	-
	Negative	32.3	24.2	14.5	27.4	35.6	2.5		
MG2	Positive	30.7	23.0	16.7	26.1	31.9	1.9	1.8	-22.9
	Negative	46.2	34.7	17.8	39.3	31.3	1.8		
PO3	Positive	35.8	26.9	12.2	32.2 ^c	27.5 ^c	2.3	2.1	-11.6
	Negative	37.7	28.3	11.1	34.0 ^c	21.5 ^c	1.9		
PG4	Positive	54.6	41.0	14.6	54.6 ^d	17.3 ^d	1.2	1.2	-50.0
	Negative	42.7	32.0	16.3	42.7 ^d	19.6 ^d	1.2		

Note: - = not applicable.

^cAt 90% of the post-maximum applied load.

^dAt the maximum applied load.

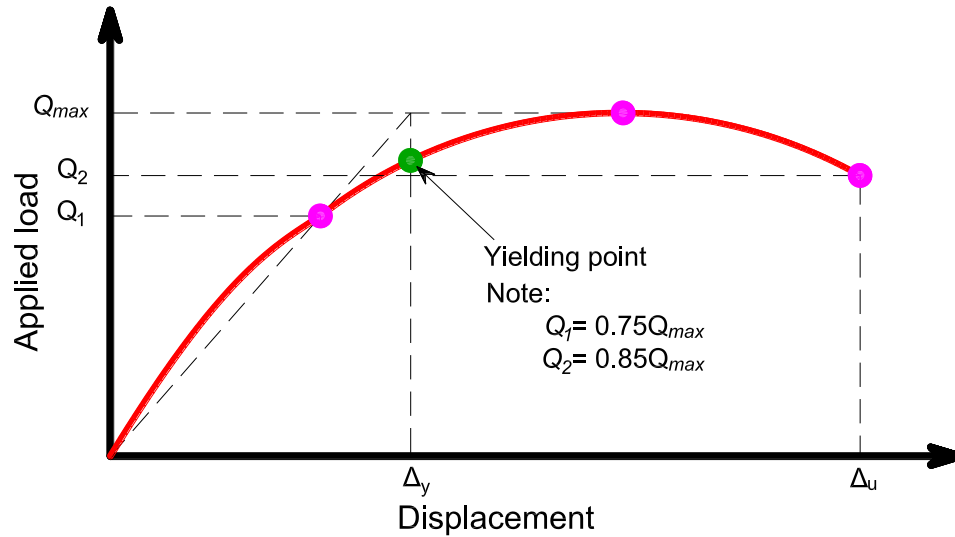


Fig. 4-18. Method to determine the yielding point and failure point.

All the specimens were designed so that concrete governs the failure modes such as concrete crushing, tensile cracks or shear cracks. As a result, the ductility of the specimen was governed by concrete rather than the CFRP bolts. The ductility comparisons of all the specimens are presented in Table 4-7. Specimen MO1 showed the highest ductility ($\mu = 2.4$) among the four specimens while the ductility of Specimens MG2, PO3, and PG4 was approximately 23%, 12%, and 50% lower than that of Specimen MO1, respectively. The ductility comparisons of the monolithic group and precast group present that the GPC specimens revealed lower ductility than the corresponding OPC specimens. For example, Specimens MO1 and MG2 had the same design. Also, the ultimate displacements of these two specimens were determined at the same 85% of the post-peak load. Nevertheless, the ductility of Specimen MG2 ($\mu = 1.8$) was lower than that of Specimen MO1 ($\mu = 2.4$). This reduction in the ductility of the GPC joint is attributed to the brittleness of high strength GPC. Meanwhile, the ductility of Specimen PO3 ($\mu = 2.1$) was quite close to that of the reference Specimen MO1 ($\mu = 2.4$). It is noted that the ultimate displacement of Specimens PO3 was determined at 90% of the post-peak loads while that of Specimen MO1 was 85% of the post-peak load. Therefore, it is expected that if the ultimate

displacements of both specimens were monitored at the same 85% of the post-maximum loads, the ductility of Specimen PO3 might be similar or even greater than that of Specimen MO1. From the above analysis, the ductility of the specimens using the high strength of GPC should be improved in future research even though the current design still satisfies the requirements for the earthquake-prone region. Adding fibres in the mixture of the high strength GPC might be a potential solution to be considered for further investigations.

4.2.5.5 Effects of CFRP bolts on joint opening and stiffness

This study used two LVDTs to measure the joint opening of all the precast joints, as shown in Fig. 4-1. These LVDTs were set up in the horizontal direction on the top and bottom surfaces of the CEP. During the serviceability condition, the joint opening in precast beam-column joints is expected to close. However, when the applied load exceeds the serviceability condition (i.e., approximately 60-70% of the ultimate load [135]), the joint might open and then close after the load decreases. Joint openings of Specimens PO3 and PG4, which were measured by LVDT at the serviceability loads and maximum load, were around 0 mm and 1.6 mm, respectively. The marginal joint opening was attributed to the effects of low prestress levels in the bolts. The CFRP bolts were applied a prestress level of about 6 kN, as shown in Fig. 4-19. The torsion resistance of CFRP bolts was quite low so they were not prestressed to a high level. A high prestress level on CFRP bolts might lead to premature damage of the bolts. It is suggested that the CFRP bolts need to be prestressed to a higher level to minimize the joint opening. To resolve this issue, a new FRP bolts type and a new method to apply high prestress levels for FRP bolts are proposed and will be represented in another study.

The application of CFRP bolts in this precast joint type could also lead to lower stiffness during the initial stages (i.e., approximately 24%) compared to precast specimens with steel bolts [46]. This behaviour was attributed to the effects of elastic modulus than the prestress level on the bolts [46]. The elastic modulus of CFRP bolts (100 GPa) was lower than that of steel bolts (200 GPa). Therefore, the stiffness of the specimens with CFRP bolts was lower than that of the specimens with steel bolts. High prestress levels in bolts only result in a minor effect on the stiffness which was also reported in some other studies [80, 112]. In addition, the use of CFRP bolts to replace

steel bolts in the proposed dry joints minimized a residual joint opening after resisting intensive load due to the linear behaviour of CFRP material.

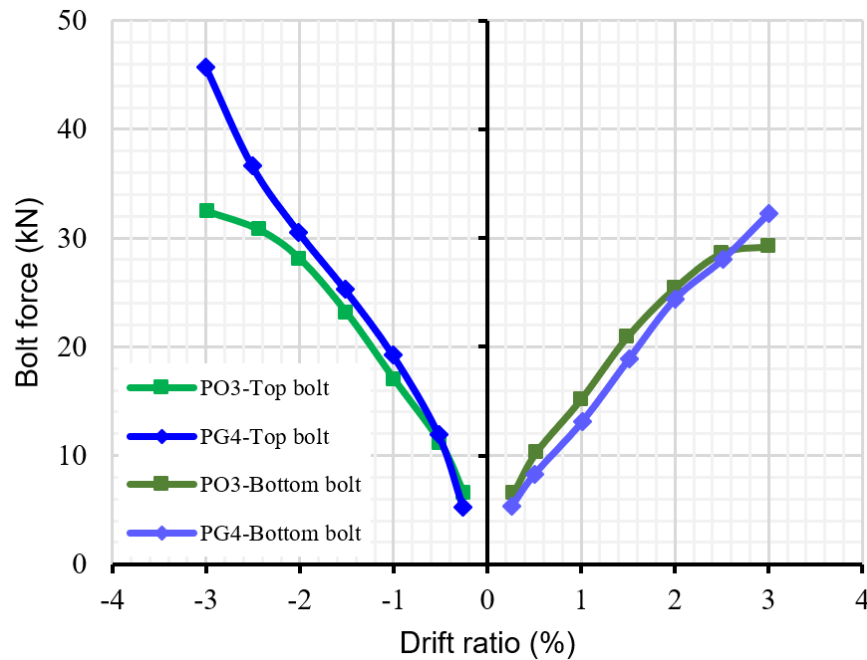


Fig. 4-19. Tensile forces of CFRP bolts.

4.2.6 Verification of predicted results

The results of the analytical model are verified with the experimental data in this section, including (1) the failure mode and (2) the maximum applied load. For the failure modes, it can be seen that there was a good correlation between the experimental observations and predictions of the proposed analytical model in Section 4.2.4. For instance, the proposed analytical model predicted that only Specimen PO3 could fail at the joint area while the other three specimens (MO1, MG2, and PG4) might fail in the beam at the fixed-support. This prediction coincided with the failure modes and failure position of all the specimens in the tests, as shown in Fig. 4-9 and Table 4-5.

Concerning the failure at the fixed-support, the proposed analytical model well predicted the maximum applied load of OPC Specimen MO1 with a variation of approximately 13% while the higher variation of 32% was observed on GPC Specimen MG2 due to the inaccuracy in estimating the moment capacity of the GPC beam (see more details in Section 4.2.4.2). For the failure at the joint area, the variation of the maximum applied load among analytical predictions and experimental tests was

around 2-26% whereas only 1.3% variation of the horizontal shear strength was observed if the actual strain of the longitudinal rebars was adopted to determine T3. The above results proved that the proposed analytical model can predict the failure modes, peak load, and horizontal shear strength of the specimens. However, to improve the reliability of the proposed analytical model, it is necessary to use the numerical simulation to study some parameters which are too complicated to measure during experimental tests such as shear stress in CFRP bolts and the validity of the two assumptions in this analytical model. The proposed analytical model in this chapter can successfully offer the foundation for further studies.

4.3 Summary

This chapter conducted an experimental investigation on the structural performances of the ambient-cured GPC monolithic joints and the newly proposed dry joint using GPC and CFRP bolts under cyclic loading. A new analytical model to design GPC monolithic and GPC precast joints was also proposed. The results showed that GPC precast joint offered various advantages in terms of the load-carrying capacity and energy dissipation, compared to the monolithic joint. Nevertheless, GPC joints also revealed a reduction in the ductility due to the brittle characteristic of GPC material. The following key points are drawn from the experimental results and theoretical predictions:

1. The proposed analytical model could well predict the main failure modes, failure positions, and failure load of both the monolithic and precast joints made of OPC and GPC. The analytical model predicted the horizontal shear strength of the precast specimen with a low variation of 1.3% while this variation of ACI 318-11 [72] model was 35%.
2. The crack development and failure mode of both OPC and GPC joints were similar. The tensile strength of concretes significantly affected several crucial parameters of the beam-column joints such as failure mode, load-carrying capacity, and energy dissipation.
3. The ductility of both GPC monolithic and GPC precast joints was lower than their counterparts OPC joints by approximately 22.9-42.8%. The GPC specimens showed brittle failure at the peak load.

4. Drift ratio of all the specimens was higher than 2.5%, which satisfied the requirements of ASCE 41-06 [18] and CSA A23.3-07 [17] standards for structures in seismic regions.
5. Both the GPC monolithic and GPC precast joints showed promising results in the indices of the peak load and energy dissipation compared to the corresponding OPC monolithic and OPC precast joints, respectively.
6. The application of CFRP bolts in the precast joints could minimize the residual joint opening after resisting intensive load. However, it showed an approximately 24% lower stiffness during the initial stages in the tests, compared to the precast specimens with steel bolts due to the lower elastic modulus of CFRP than steel.
7. CFRP bolts could replace steel bolts in the proposed dry joints to resolve corrosion problem while they still meet the design requirements of shear resistance and ductility for the dry joints.

In conclusion, this chapter suggests potential solutions for three main problems in the construction sector. Firstly, GPC could effectively replace OPC to reduce environmental pollution owing to reuse of industrial wastes. Secondly, the corrosion of the connecting elements in the conventional dry joints could be effectively mitigated by the application of CFRP bolts and plates. Finally, the new proposed dry joint type met the requirements for application in the earthquake-prone regions.

CHAPTER 5: EXPERIMENT AND NUMERICAL STUDY ON NEWLY PROPOSED DRY AND HYBRID CONCRETE JOINTS WITH GFRP BOLTS AND GFRP REINFORCEMENTS UNDER CYCLIC LOADING

ABSTRACT⁴

This chapter proposes a new hybrid concrete joint using glass fibre reinforced polymer (GFRP) bolts and reinforcements to replace steel bolts and reinforcements for corrosion damage mitigation. The experimental results indicated that the proposed hybrid concrete joints satisfy the seismic-resistant design requirements with respect to the ductility and energy dissipation of ASCE 41-06 [18] and CSA A23.3-07 [17] standards. The energy dissipation of the hybrid concrete joint was approximately 57% higher than the reference monolithic joint. In addition, the application of GFRP bolts and reinforcements not only avoided brittle failure during the test but also showed excellent behaviours in terms of the drift ratio, ductility, and energy dissipation. Numerical simulation using ABAQUS software was also carried out, which successfully captured the failure modes, drift ratios, and peak loads of the dry, hybrid, and monolithic joints. The numerical results proved that the common assumptions which were adopted in the proposed models in Chapters 3 and 4 [24, 46] were reliable to predict the peak loads. The ratio of the thickness of the concrete-end-plate (CEP) over the height of the beam of 1.3 was the optimal value and it can be used in CEP design of the dry joint. Finally, the developed three-dimensional finite element (3D-FE) model verified with the testing data can be confidently applied in future studies to investigate the seismic performances of the dry, hybrid, and monolithic beam-column joints using GFRP reinforcements and bolts.

⁴ This work was under review with the full bibliographic citation as follows:

<p>Ngo TT, Pham TM, Hao H, Chen W, Ha NS. Experiment and numerical study on newly proposed dry and hybrid concrete joints with GFRP bolts and GFRP reinforcements under cyclic loading. (<i>Responding to reviewers' comments</i>).</p>
--

5.1 Introduction

Beam-column joints are important components in a building since they connect beams to columns and transmit forces between these components. It was observed in many earthquakes that failures of the beam-column joints could cause collapse of the building while no damage was observed on the beams and columns [19, 38, 39]. To resolve this issue, a design method that shifts the failure from the beam-column joints to the beam-ends has been proposed in previous studies. This method helps to increase the ductility and energy dissipation (ED) and avoid brittle failure of buildings under earthquake loading [19, 39, 46]. Numerous studies [24, 39, 46, 136] indicated that to ensure the plastic hinges only occur at the beam-end, the beam-column joints need to be sufficiently strong to resist the shear failure within the joint area. Therefore, it is critical to increase the shear resistance of the joint to resist seismic loadings.

In practice, there are generally two kinds of beam-column joints, i.e., monolithic and precast joints. For precast joints, they can be classified into three groups including wet, dry, and hybrid joints. Nowadays, the dry and hybrid joints have been increasingly applied in many constructions considering their various advantages such as shorter construction time, reduced construction cost, easier replacement of damaged components, more convenient application of new materials and technologies (e.g., 3D printing, geopolymers, ultra-high performance concrete and fibre-reinforced concrete). For dry joints, beams and columns are erected in a construction site without the requirements of formworks. For hybrid and wet joints, although beams and columns are also placed in required positions using a crane, concrete needs to be filled into gaps during the construction period. Accordingly, formwork is still required during the concrete filling process for wet joints but not hybrid joints.

Monolithic and wet joints are more commonly used because they have been more intensively studied and show promising performances in the critical indices such as drift ratio (DR), ductility, ED and load-carrying capacity. The application of the hybrid and dry joints has been avoided in the seismic-prone areas owing to the lack of appropriate hybrid and dry joint types with sufficient strength and limited knowledge about their behaviours under earthquake loading. To resolve these drawbacks, many studies have been conducted to address this issue. Chapter 2 proposed a new dry joint using CFRP bolts and concrete-end-plate (CEP). The proposed dry joints showed

higher values in terms of the peak load (27-61%), effective stiffness (27-55%), and ED (45-75%), compared to those of the corresponding monolithic joint. All the precast joints in the latter study reached 3% drift ratio (DR) which satisfied the requirements of ASCE 41-06 [18] and CSA A23.3-07 [17] for applying in seismic-prone regions. In addition, an analytical model was proposed to predict the load-carrying capacity in Chapters 3 and 4 [24, 46]. The variation between the experiment and the proposed analytical model was less than 2% [46]. However, the bulky appearance of the CEP was a disadvantage of this dry joint which needs further improvement. Alver et al. [137] and Jin et al. [10] investigated another dry joint using steel tendons to connect beams and columns. These studies indicated that the shear failure primarily governed the failure modes of the dry joint. Comparing to the dry joint using CFRP bolts and CEP [24, 44], the dry joints using steel tendons face more challenges in erecting and replacing damaged components because the steel tendons need to go through beams and columns. On the other hand, numerical studies on the dry and hybrid joints under cyclic loading are very limited, most of previous studies were based on experimental tests [85, 138-141]. The tests, however, can only provide limited measurements of the joint's performance while some critical parameters could not be observed, e.g., stress distribution in concrete and complex stress states within the joint region.

Numerical simulation using three-dimensional finite element (3D-FE) model was applied in various studies to investigate the structural performances. The application of numerical simulation can reduce the experimental costs and time for manufacturing and testing specimens. There are some software packages which can be used to simulate the behaviours of structures under static and dynamic loading, including ANSYS, DIANA, and ABAQUS. Nevertheless, previous numerical studies showed considerable variations between experimental and numerical results. Kaya and Arslan [94] used ANSYS to simulate the post-tensioned precast beam-column joints using steel tendons under various prestress levels. A large difference in stiffness between experiment and numerical simulation was observed in the study. Also, the hysteretic curves of the numerical simulation were not presented in the previous study [94]. Alaei and Li [142] used DIANA to investigate structural responses of monolithic joints using high-strength concrete and high-strength reinforcements. The 3D-FE model well captured the envelope curves and predicted the peak loads. However, a high variation of the hysteretic curve obtained from the experiment and numerical simulation was

also recorded. In other studies [143, 144], DIANA was utilized to examine the effects of the axial loads and the thickness of steel plates in hybrid steel-concrete joints. These studies found that applying the axial force up to $(\frac{N}{A_c f'_c}) = 0.3$ could improve the joint performances in term of the peak load. However, when increasing axial load with the value of $(\frac{N}{A_c f'_c}) > 0.3$, negative effects were observed in the joint's behaviours. Moreover, the thickness of the steel plate significantly affected the displacement and ED of this hybrid joint, and 14-mm thickness of the steel plate was found as an optimal design for the investigated joints.

Mosallam et al. [39] utilised ABAQUS to investigate the retrofitted monolithic beam-column joints with FRP laminates. Higher stiffness and peak load were observed for the numerical simulation results, compared to the corresponding experimental results. For instance, the variation of the peak loads in [39] was in a range of 9-32%. Le et al. [81] conducted a parametric study on precast segmental beams using ABAQUS to investigate the effects of prestressing levels on the beam performances. The numerical results indicated that the prestressing levels governed the failure patterns, peak load, and ductility. For instance, higher prestress forces could increase the peak load of the precast segmental beams by approximately 20-22%. Moreover, a significant variation of the initial stiffness between the numerical simulation and experiment was reported. The above studies suggest that achieving a good agreement between the numerical simulation and experiment results, especially the hysteretic curves under cyclic loading is challenging. This issue is attributed to a lack of material models which could well simulate material performance under different loading conditions. For example, the concrete damaged plasticity model in ABAQUS could not well capture the shear and tensile failures of reinforced-concrete structures under cyclic loading [145, 146]. Therefore, in many previous studies, only monotonic loading was considered to get the load-displacement relationship, instead of modelling the performance under cyclic loading in using ABAQUS [7, 147, 148]. In addition, running a simulation of the beam-column joints under cyclic loading requires a high computational cost compared to monotonic loading.

There are four innovations in this chapter, compared to previous studies [19, 24, 46]. (1) A new hybrid joint was proposed to resolve a disadvantage related to the bulky appearance of the dry joint with the CEP. Together with the dry joint proposed in the

previous studies [19, 24, 46], this new hybrid joint offers a new option of consideration to engineers in designing precast joints. (2) GFRP reinforcements and bolts were used to replace steel reinforcements and bolts for effective mitigation of the corrosion problem of precast joints. It is noted that there have been no studies of the performances of precast joints with GFRP reinforcements and bolts under cyclic loading in open literature yet. (3) Numerical model was build using ABAQUS to investigate the structural responses of the dry and hybrid joints with CEP and bolts under both cyclic and monotonic loads. Based on the numerical simulation, some parameters (e.g. shear stress distribution in the concrete of CEP and principal stress flow), which could not be straightforwardly measured in the experiment, will be discussed in this chapter. In addition, the assumptions in the previously proposed model to predict the load-carrying capacity in Chapters 3 and 4 [24, 46] were validated, based on the numerical simulation results. (4) The CEP thickness in both the dry and hybrid joints is the critical parameter of these joints and thus the effects of the CEP thickness were examined by using experimental and numerical results.

5.2 Experimental program

This chapter investigates the performances of a newly proposed hybrid joint using GFRP bolts, GFRP reinforcements, and concrete-end-plate (CEP). The thickness of the CEP, which is the critical parameter, was varied to examine its influence on the joints' performance. Six specimens, including two monolithic joints (M1-SR and M2-GR) as references, two-hybrid joints (H3-GR-T200 and H4-GR-T100), and two dry joints (D5-SR-S-T200 and D6-GR-S-T100), were cast and tested under cyclic loading. The letters "M", "H", and "D" indicate the monolithic, hybrid and dry joints, respectively. "GR" denotes GFRP reinforcements whereas "SR" denotes steel reinforcements. "T100" and "T200" represent the thickness of CEP of 100 and 200 mm, respectively. It is noted that both the dry joints used steel bolts to connect the beam and column so the letter "S" indicates steel bolts. The information of all the specimens is summarized in Table 5-1. Details of the specimen dimensions, test setups, and material properties are presented in the subsequent sections.

Table 5-1. Specimen design.

Names	Joint Types	Reinforcements	Bolts	CEP thickness (mm)	CEP cross-section (mm ²)
M1-SR	Monolithic	Steel	-	-	-
M2-GR	Monolithic	GFRP	-	-	-
H3-GR-T200	Hybrid	GFRP	GFRP	200	200×250
H4-GR-T100	Hybrid	GFRP	GFRP	100	200×250
D5-SR-S-T200	Dry	Steel	Steel	200	150×350
D6-GR-S-T100	Dry	GFRP	Steel	100	200×350

Note: - = not applicable.

5.2.1 Details of beam-column joints

Details of the dimensions and shapes of the monolithic joints and hybrid joints are illustrated in Figs. 5-1 and 5-2. It should be noted that in the design and preparation of the specimens for testing, the experiences gained in the previous studies [19, 46], as well as in the process of the current study, were taken into consideration. Some improvements on the hybrid and dry joints were made to further ease the assembly process of beams and columns. Therefore, the dimensions of the six tested specimens were not exactly the same, and hence the results among the specimens might not be directly comparable, but indicative only and can be used to verify the numerical models. The beam width of Specimens H3-GR-T200, H4-GR-T100, and D6-GR-S-T100 were 200 mm. To ensure fair comparisons between the hybrid/dry joints and the monolithic joint, the beam width of the monolithic specimen M2-GR was also increased up to 200 mm. The beam cross-sections of Specimen M2-GR, H3-GR-T200, H4-GR-T100, and D6-GR-S-T100 were 150-mm height and 200-mm width whereas those of Specimens M1-SR and D5-SR-S-T200 were 150 and 150 mm, respectively. The beam length of all the specimens was 820 mm. The beam of the hybrid and dry joints was divided into two parts, including Beam A and the CEP (see Fig. 5-3). The cross-section of the CEP of hybrid and dry joints was different. The CEP cross-section of hybrid joints was 200-mm width and 250-mm height, whereas that of dry joints was 200/150-mm width and 350-mm height. In addition, due to the requirements for accommodating both bolts and nuts, the cross-section of CEP was larger than that of Beam A. As the primary parameter in this chapter, the thickness of CEP varied from

100 mm (Specimens H4-GR-T100, D6-GR-S-T100) to 200 mm (Specimens H3-GR-T200, D5-SR-S-T200) to investigate its effect on the performance. The dimensions of the column remained unchanged in all the specimens with 200-mm square cross-section and 1280-mm length. The diameter of the GFRP longitudinal rebars and GFRP stirrups was 17.1 mm and 10.5 mm, respectively. For convenience, GFRP spiral stirrups were applied in both the beam and column with the same spacing of 35 mm, as shown in Fig. 5-1.

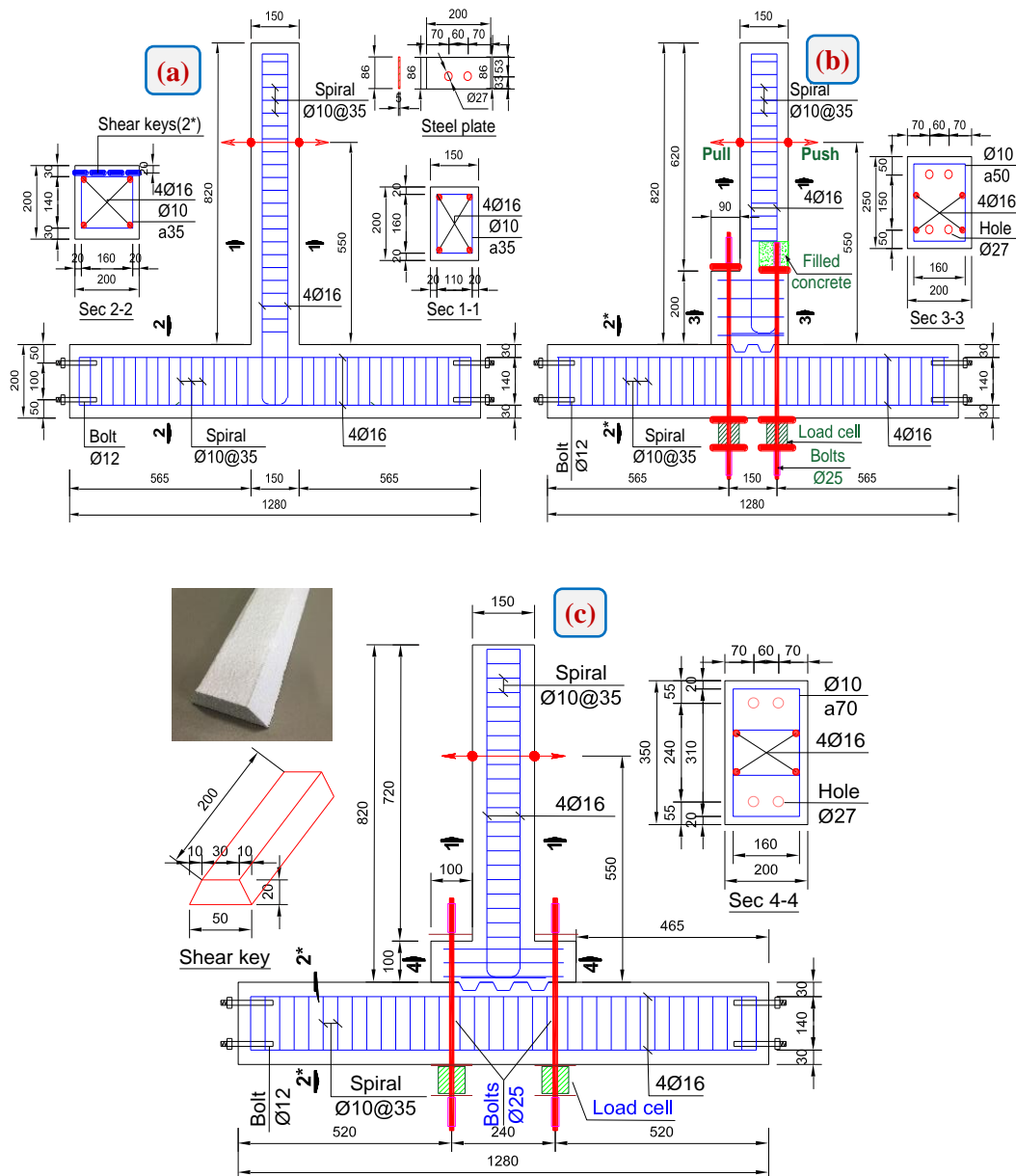


Fig. 5-1. Dimensions of the monolithic joint (a), hybrid joint (b), and dry joint (c) (unit: mm).

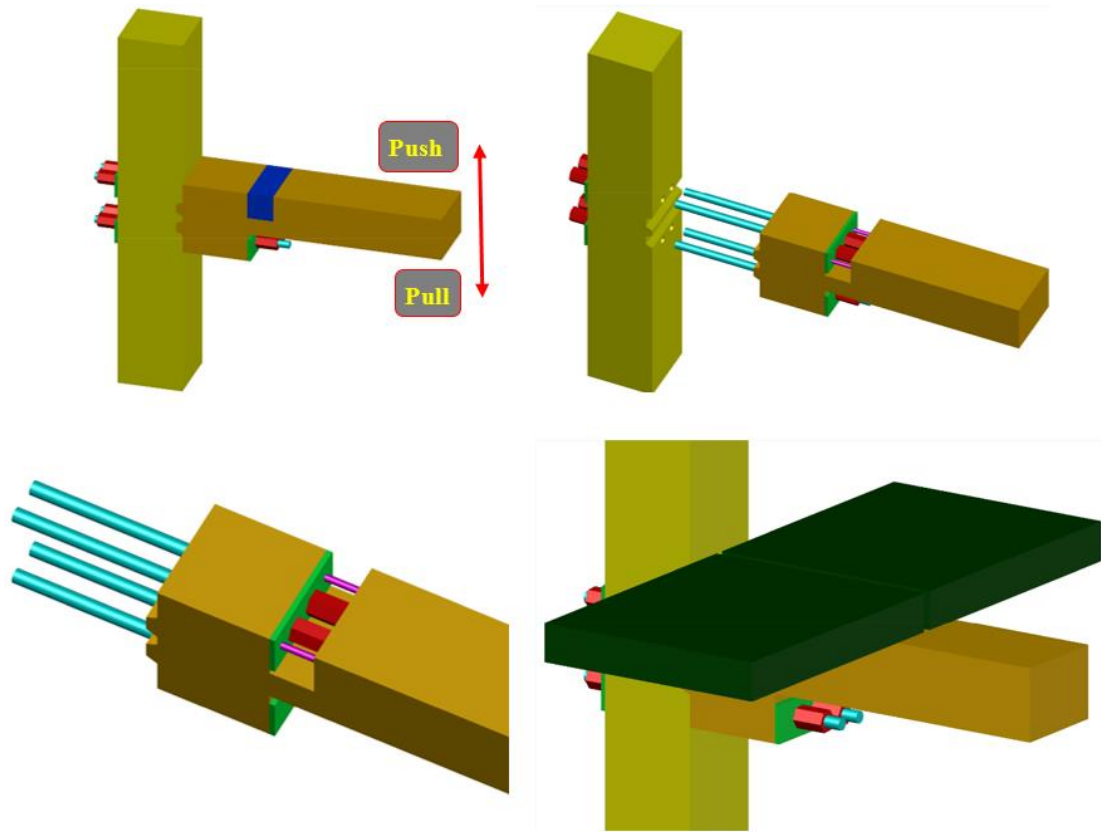


Fig. 5-2. 3D-views of the newly proposed hybrid joint.

Fig. 5-3 shows a typical view of GFRP cages, formworks, and shear keys. High strength concrete was filled into the green gap (see Fig. 5-3) after applying prestress forces to the GFRP bolts. 4 GFRP bolts with the diameter of 25 mm was applied a high prestress force up to 35 kN by the use of a hydraulic jack, chair, and spanner [2]. This new method of being able to apply high prestress force to FRP bolts was described in [2], which effectively resolved the limitations in the previous studies [19, 44] of not being able to apply large prestress force to FRP bolts owing to the weak shear strength of FRP material [19, 24, 46] (see Fig. 5-4). The conventional method of using a torch wrench to apply the prestress force to CFRP bolts caused local damage at the nut location. As a result, only 6.5-10.5 kN of the prestress force was applied to CFRP bolts due to the low torsion resistance of the bolts in the previous studies [19, 24, 46].

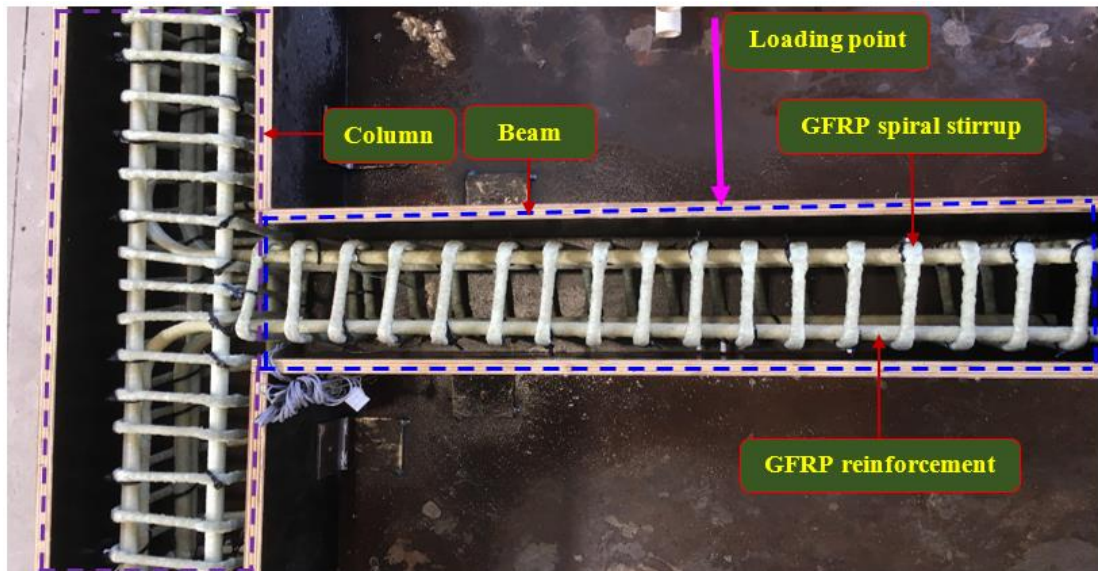
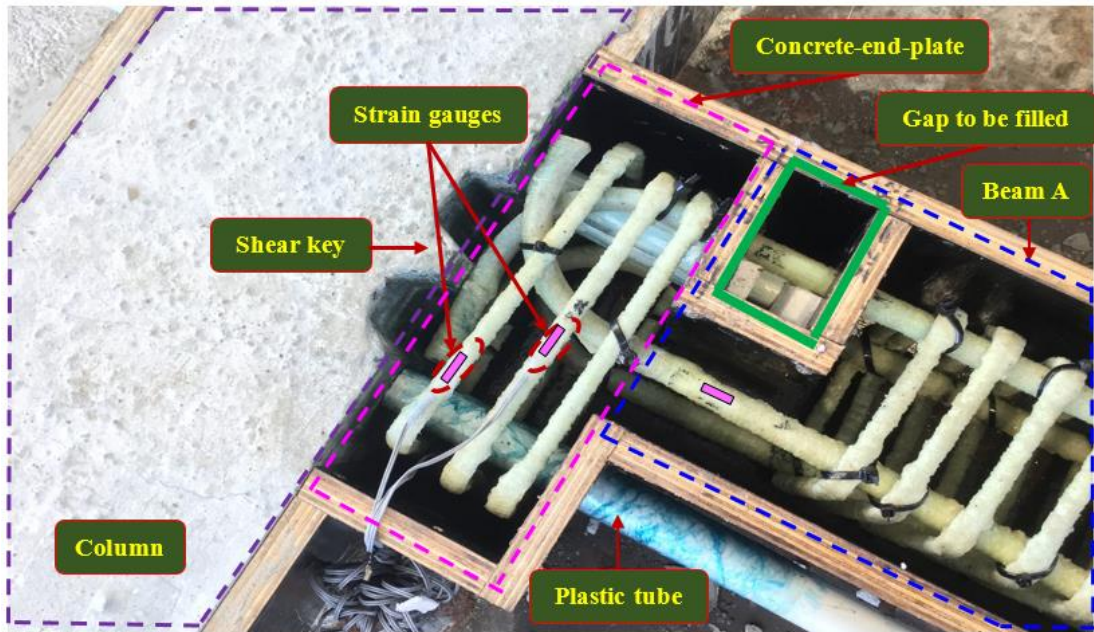


Fig. 5-3. Details of reinforcements, shear keys, and formworks.

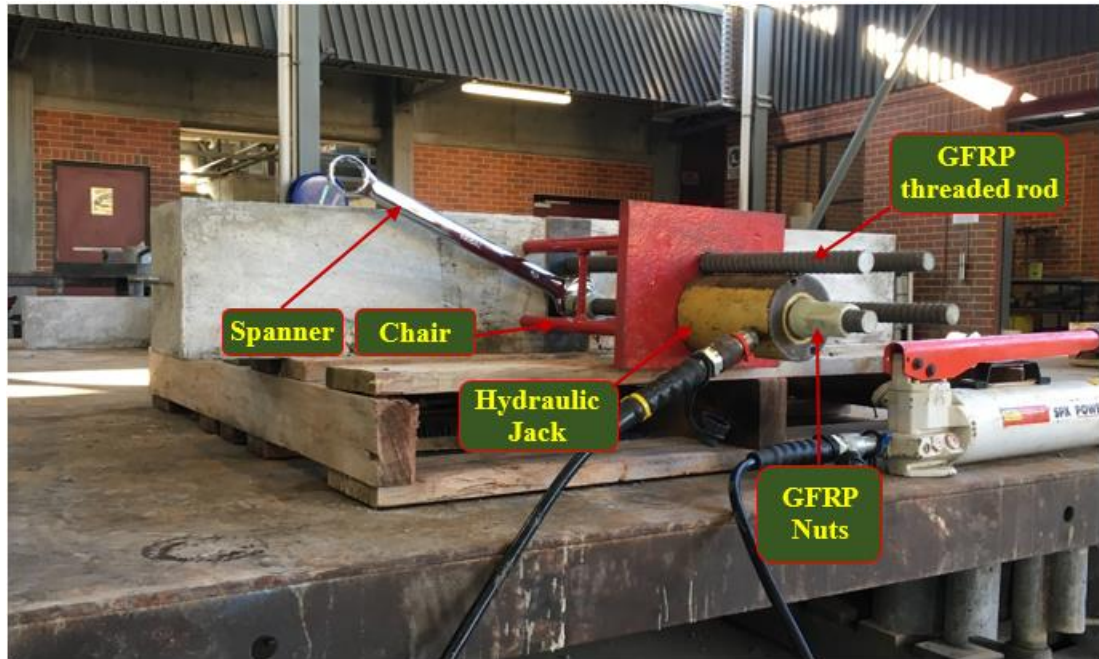


Fig. 5-4. Setup for applying prestress to GFRP bolts.

5.2.2 Test setups

Fig. 5-5 shows a typical test setup of the hybrid joints. Before testing, a prestress force of 35 kN was applied to each GFRP bolt. This value was higher than the prestress force in CFRP bolts (4.1-6.5 kN) in the previous chapters. A higher prestress level may result in an increase in the maximum applied load, as concluded in Chapter 2. A 500-kN hydraulic jack was used to apply the cyclic load at the loading point, 550 mm from the column surface. Another hydraulic jack was placed on the column top to apply 65 kN ($\approx 0.03 A_c f_c$) axial force on the column (see Fig. 5-5). This axial force was maintained as low as possible to simulate the most unfavourable case of joint behaviours. The loading history (see Fig. 5-6) was based on ACI T1.1-01 [16] standard and the previous studies [19, 46]. Displacement control at the level of 6–9 mm/min was used in the tests.

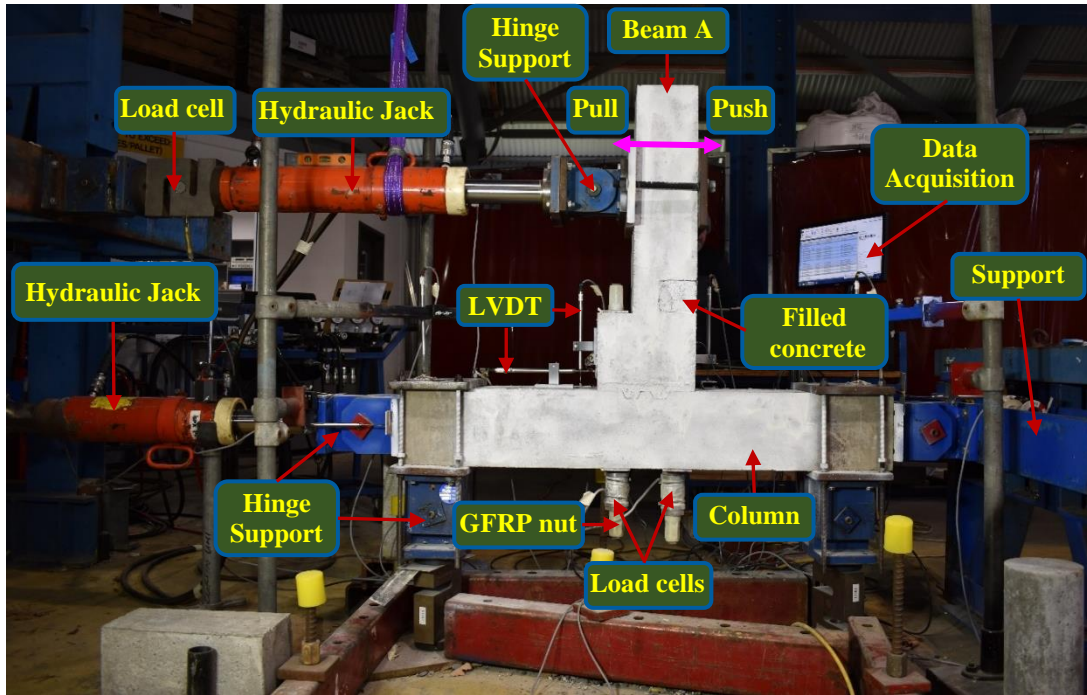


Fig 5-5. Typical test setup of hybrid joints.

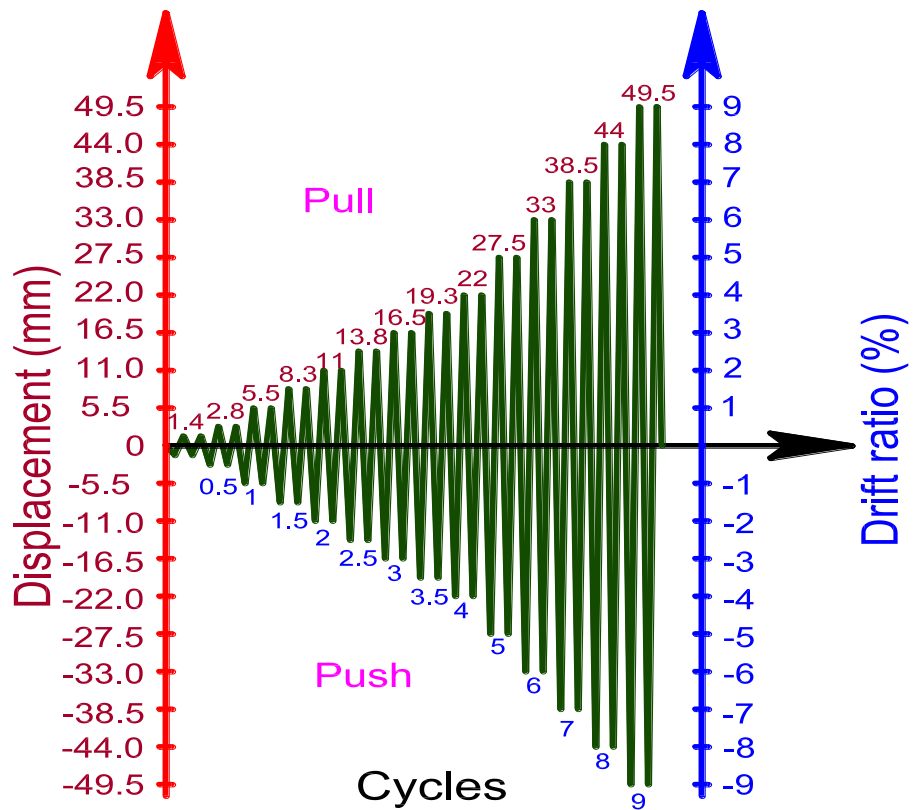


Fig 5-6. Loading history.

5.2.3 Material properties

Ready-mixed concrete from Boral Pty Ltd [149] was used to cast all the specimens in this chapter (see the mixture in Table 5-2). The concrete properties were determined according to AS 1012.8.1-14 [74] and AS 1012.9.1-14 [75] standards. Due to different concrete batches, the testing-day compressive strength (f'_c) and tensile strength (f_{ct}) of group 1 (M1-NF, D5-SR-S-T200 and D6-GR-S-T100) were 38.5 MPa and 3.8 MPa, respectively whereas those of group 2 (M2-GR, H3-GR-T200, and H4-GR-T100) were 59 MPa and 4.2 MPa, respectively. The mixture of the high strength concrete with the compressive strength of 75 MPa used to fill the gap in hybrid joints as shown in Fig. 5-3 is presented in Table 5-2. GFRP bolts and nuts were supplied by Bluey Pty Ltd [150]. The nominal tensile force of threaded rods (350 kN) was significantly higher than the failure force of the nuts (70 kN). Therefore, the capacity of the whole bolts was governed by the capacity of nuts. The mechanical properties of GFRP bolts are presented in Table 5-3. The mechanical properties of GFRP reinforcements, which were sponsored by Pultrall Inc [151], are summarized in Table 5-4.

Table 5-2. Mixture proportions of 1 m³ plain concrete [149] and filled concrete.

Materials	Unit	Ready-mixed concrete	Filled concrete
Sand	(kg/m ³)	534	1051
7-mm coarse aggregate	(kg/m ³)	1100	-
Coarse sand Gin Gin	(kg/m ³)	225	-
Cement	(kg/m ³)	400	995
Water	(L/m ³)	175	180
Plastiment BV35	(L/m ³)	1.6	-
Viscocrete 10	(L/m ³)	1.2	-
Viscoflow 15	(L/m ³)	1.2	-
Silica fume	(kg/m ³)	-	238
Superplasticizer	(kg/m ³)	-	67
Steel fibre (35 mm)	(%)	-	2

Note: - = not applicable.

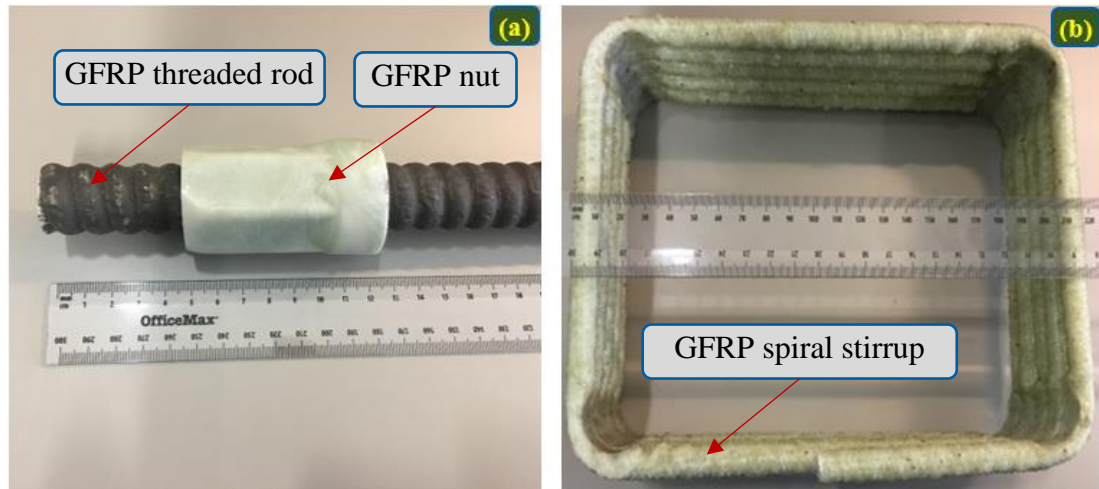


Fig. 5-7. Details of (a) GFRP bolts and (b) GFRP spiral stirrups.

Table 5-3. Properties of GFRP bolts and nuts [150].

Names	Nominal diameter (mm)	Nominal cross-section area (mm ²)	Shear @90° (kN)	Shear @50° (kN)	Ultimate load (kN)	Elastic modulus (GPa)	Weight (kg/m)
Bolt	25	346	170	345	≥ 350	60	0.9
Nut	25	-	-	-	70	60	-

Note: - = not applicable.

Table 5-4. Mechanical properties of GFRP reinforcements [151].

Nominal diameter (mm)	F_u (kN)	f_u (MPa)	F'_u (kN)	f'_u (MPa)	Q_{sh} (kN)	F_{sh} (MPa)	E_s (GPa)	Area (mm ²)	Notes
10.5	89.7	1259.2	42.3	593	33.6	235.8	54	87	Stirrups
17.1	268.9	1358.3	132.4	668.8	82.5	208.5	54	230	Longitudinal reinforcements

Note: F_u and f_u = Load at the break and tensile strength of the straight portion.

F'_u and f'_u = Load at the break and tensile strength of the bent portion.

Q_{sh} and f_{sh} = Load at the break and transverse shear strength.

E_s = Elastic modulus.

5.3 Experimental results and discussion

5.3.1 Global performances and failure modes

In the beam-column joints, there were three possible failure positions including the joint area, fixed-end of the beam, and a combination of the joint area and fixed-end. Either shear failure or compressive strut failure mainly governed the failure patterns in the joint area while flexural cracks and concrete crushing dominated failure modes at the fixed-end [24]. Fig. 5-8 shows the failure modes of all the specimens tested in this chapter. The shear keys were utilized at the interface between the columns and CEPs of the precast joints (excepting Specimen D5-SR-S-T200) to resist the shear forces. Therefore, no-slip between the column and CEP was observed during the tests. Meanwhile, despite no shear keys on Specimen D5-SR-S-T200, no-slip was recorded on this specimen either because the friction between the column and CEP surfaces was sufficient to resist the shear force. Although the maximum tensile forces in GFRP bolts almost reached their nominal capacity of the GFRP nuts (see Table 5-3), no failure was observed on GFRP nuts. For instance, the maximum tensile forces of GFRP bolts of Specimen H3-GR-T200 was 69 kN which almost reached the nominal capacity of the GFRP nuts (70 kN). After testing, all GFRP nuts were carefully checked and showed good conditions without damage. Fig. 5-9 shows strain of longitudinal reinforcements and middle stirrups in the CEP. The strain of steel and GFRP reinforcements at the peak load was lower than the yield strain ($2,985 \mu\epsilon$) and the nominal strain at the break strength ($25,238 \mu\epsilon$), respectively. For instance, strain of the longitudinal reinforcements of Specimens M1-SR, M2-GR and D6-GR-S-T100 was $2,233 \mu\epsilon$, $9,666 \mu\epsilon$, and $3,994 \mu\epsilon$, respectively. The above results proved that steel and GFRP reinforcements did not govern the main failure of the specimens so concrete dominated the main failure of the specimens. These results indicate that the structures using GFRP materials satisfy the design requirements for not suffering brittle failure. On the other hand, strain of the longitudinal reinforcements of Specimen M2-GR was around four times higher than that of Specimen M1-SR at the peak load. Lower elastic modulus of GFRP reinforcements (54 GPa), compared to that of steel reinforcement (200 GPa) caused the above difference. The lower modulus of GFRP also led to a higher DR of the specimens using GFRP reinforcements. More discussions about DR will be given in the subsequent section.

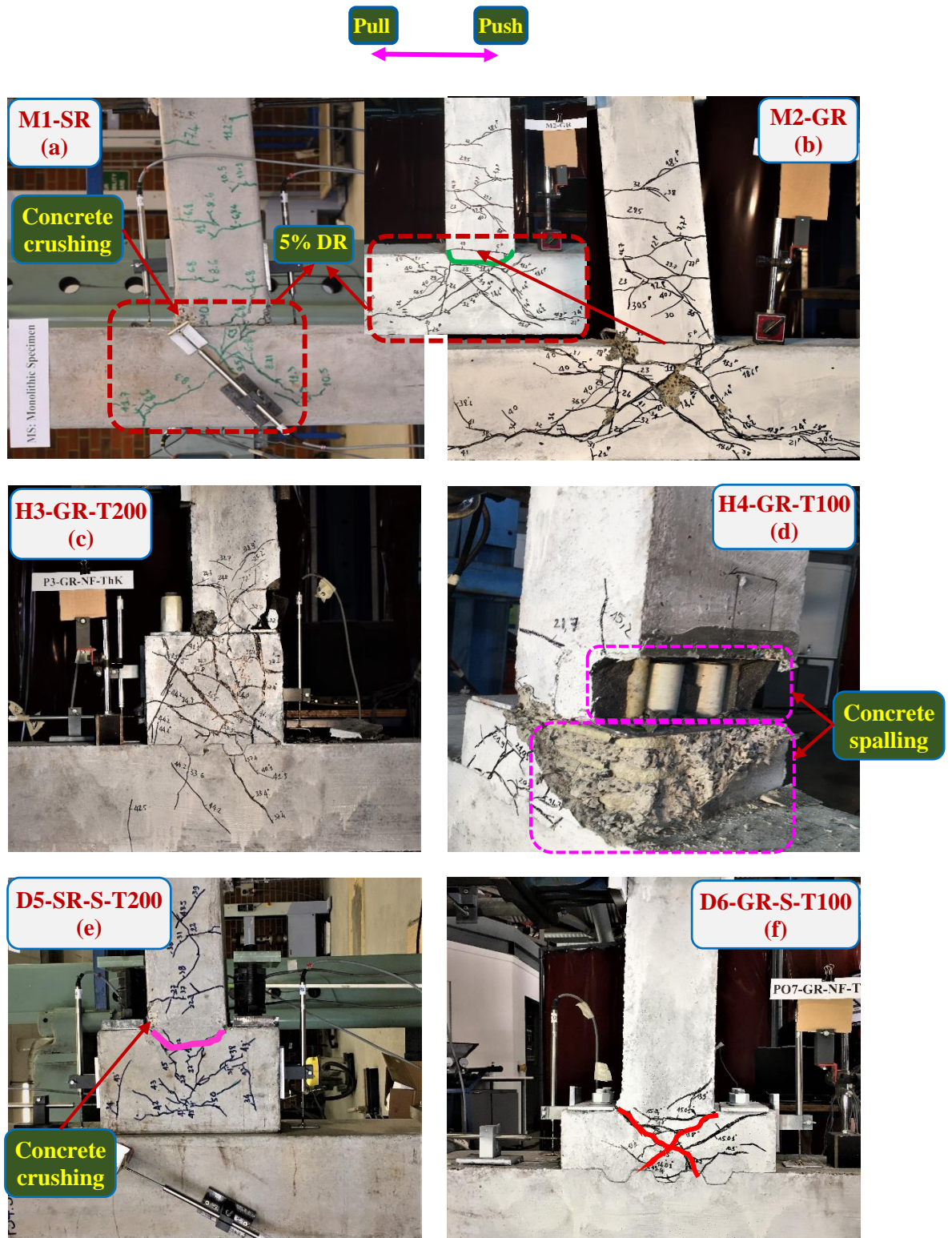


Fig. 5-8. Failure modes.

To evaluate if the specimens failed in the beam or the joint area, it is necessary to estimate the capacity of the beam, together with the observation during the test. This study adopted ACI 318-11 [72] to estimate the loading capacity of the beams with steel

reinforcements and ACI 440.1R-15 [152] for that of beams with GFRP reinforcements. The calculations showed that the design capacities of the beams of Specimens M1-SR, M2-GR, D5-SR-S-T200, and D6-GR-S-T100 were 28, 32.9, 44, and 33.2 kN, respectively. The loading capacity of the beam of Specimen M2-GR was higher than that of Specimen M1-SR due to higher concrete compressive strength and larger beam width. The concrete compressive strength and beam width of Specimen M2-GR were 59 MPa and 200 mm, respectively, whereas those of M1-SR were 38.5 MPa and 150 mm, respectively. The loading capacity of Specimens H3-GR-T200 and H4-GR-T100 was 50 kN and 39.7 kN, respectively. It is noted that the actual applied loads on the beam of the specimens with hybrid joints were lower than the respective loading capacity due to the spalling failure of the filled concrete block due to poor bonding between the filled higher strength concrete and the normal concrete of the beam. Based on the above-estimated loading capacity, if the applied peak loads to the specimens were lower than the loading capacity of the beams, the failure of these specimens was governed by other parts, i.e. joint area. Otherwise, these specimens might fail in the beam of the specimens with the monolithic or dry joints or a combined failure in both the beam and joint of the specimens with the hybrid joint. From the observation during the tests and the comparisons between the design loading capacities and the applied peak loads in the tests, it could be concluded that Specimens M1-SR and D5-SR-S-T200 failed in the beam at the fixed-end while the primary failure of Specimen D6-GR-S-T100 occurred in the joint area. The combined beam and joint failure was observed on Specimens M2-GR, H3-GR-T200, and H4-GR-T100 due to large displacement and low bonding between old and new concrete at the filled slot of the hybrid joint.

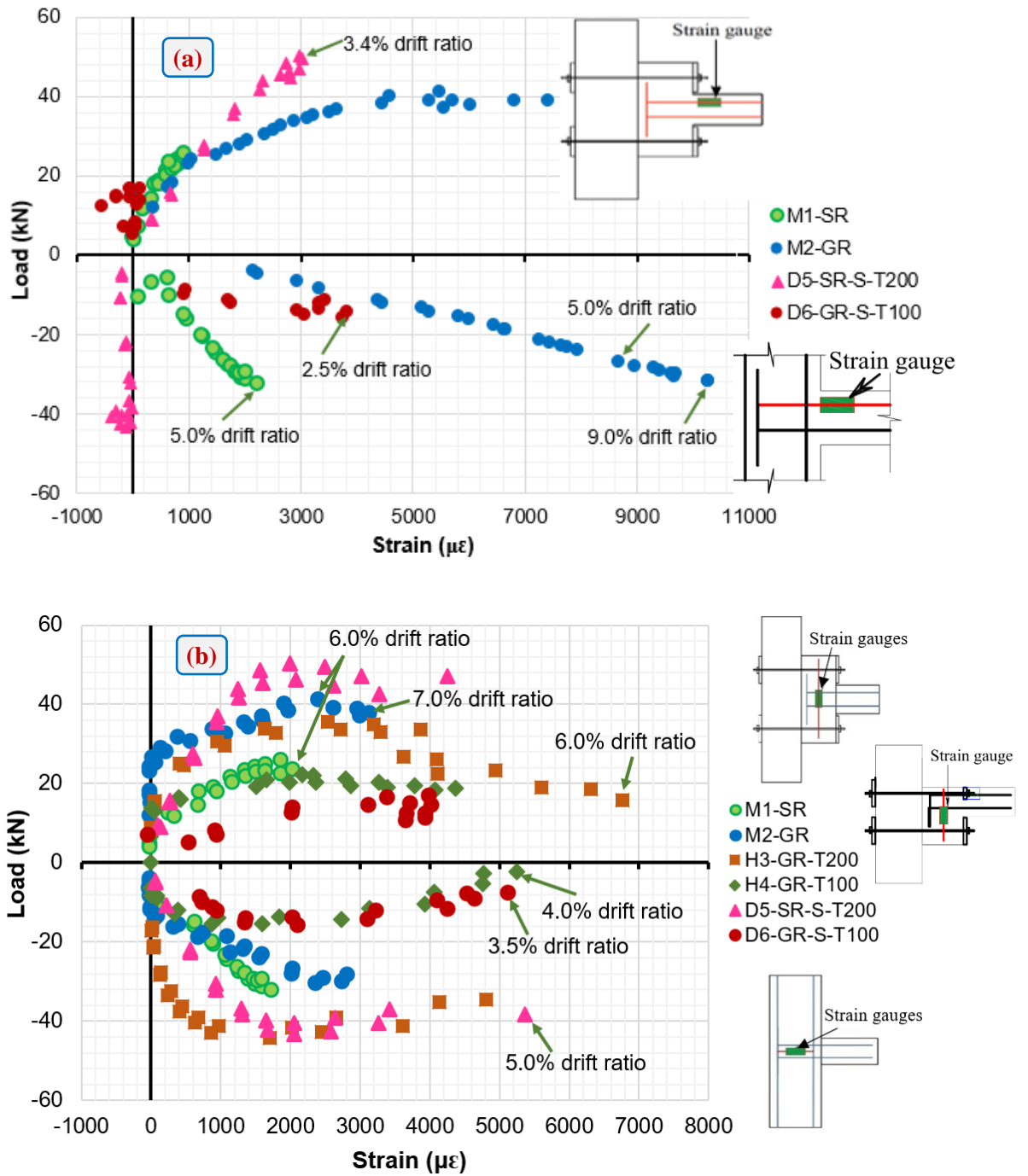


Fig. 5-9. Data of strain gauges attached on (a) longitudinal reinforcements and (b) stirrups at middle joints.

To evaluate the failure modes of the specimens using steel and GFRP reinforcements, a comparison was conducted between Specimens M1-SR and M2-GR. In general, the failure modes of these specimens were similar at the same DR. Flexural cracks occurred quite early at the fixed-end of the beam when the beam soffit was in tension at 0.3-0.5% DR. Afterwards, the flexural cracks extended to the loading point at 100

and 200 mm from the fixed-end. After 1% DR the inclined cracks tended to propagate to the joint area. However, there were three different types of failure modes in these two specimens. (1) Although the trend of the inclined cracks in the joint area was similar, more inclined cracks were observed in the joint area of Specimen M2-GR, compared to Specimens M1-SR. It is attributed to the displacement applied during the tests. The beam width of Specimens M2-GR (200 mm) was larger than that of Specimen M1-SR (100 mm). As a result, it required a larger force to deform the beam of Specimen M2-GR than that of Specimen M1-SR and, therefore, caused more cracks in the joint area of Specimens M2-GR at the same drift ratio of Specimen M1-SR, as shown in Figs. 5-8(a) and 5-8(b) at 5% DR. (2) Crushing of concrete was observed in Specimen M1-SR at 2% DR whereas no crushing of concrete appeared on Specimen M2-GR until 5% DR. This different performance was attributed to the different concrete compressive strength of these specimens. Higher concrete compressive strength of Specimen M2-GR (59 MPa) well resisted the compressive stress in concrete, compared to Specimen M1-SR (38.5 MPa). (3) Especially, more severe damage was observed on Specimen M2-GR after test, compared to Specimen M1-SR. It is because the elastic modulus of GFRP reinforcements (54 GPa) was lower than that of steel reinforcements (200 GPa). The lower elastic modulus caused higher elongation of GFRP reinforcements, compared to steel reinforcements. For instance, at the same 5% DR, strain of the longitudinal GFRP reinforcements ($8,685 \mu\epsilon$) was 3.9 times higher than that of the longitudinal steel reinforcements ($2,233 \mu\epsilon$), see Fig. 5-9(a). At the end of the tests, Specimen M2-GR showed larger displacement (10.5% DR), compared to Specimen M1-SR (6.5% DR). Larger displacement caused more severe damage in the joint area and concrete crushing at the fixed-end of Specimen M2-GR.

Figs. 5-8(c) and 5-8(d) illustrate the main failure modes of the two-hybrid joints (H3-GR-T200 and H4-GR-T100) with different thicknesses of the CEP (200 vs 100 mm). In general, the failure positions of these two specimens were similar that both the specimens failed at the fixed-end and in the joint area. Although the beams of these two specimens did not reach their loading capacity (50 kN for Specimens H3-GR-T200 and 39.7 kN for H4-GR-T100), severe damage and concrete spalling were observed at the fixed-end and in the joint area of these two specimens, as shown in Figs. 5-8(c) and 5-8(d). It is attributed to the low bonding strength between old and

new concrete surfaces. This low bonding caused initial cracks around the filled concrete block at a low DR of 0.5-1% in the pull direction and led to damage of the filled concrete block in the push direction. Consequently, the cross-section of the beam reduced and caused more severe damage at the fixed-end. At the first cycle of 1% DR, the inclined cracks started at the fixed-end and propagated to the middle zone of the CEP. Tensile and shear cracks governed the main failure of these two specimens. Therefore, strain of middle stirrups in the joint area was relatively high. For example, the strain of Specimen H3-GR-T200 at the peak load (2.5% and 3.5% DR) was 2,723 and 3,866 $\mu\epsilon$, respectively (see Fig. 5-9(b)). It is noted that the inclined cracks were only observed on the column of Specimen H3-GR-T200 from 1.5% DR while no cracks appeared on the column of Specimen H4-GR-T100 and other precast joints. The application of the shear key helped to transfer the shear force into the column and induced inclined cracks in the column of Specimen H3-GR-T200. As a result, the inclined cracks were generated on the column of Specimen H3-GR-T200 only. For Specimens H4-GR-T100 and D6-GR-S-T100, although shear keys were also applied on these specimens, no inclined cracks were observed on the column due to weak shear resistance at CEP with a thin thickness of 100 mm. Therefore, for Specimens H4-GR-T100 and D6-GR-S-T100, the CEP reached their ultimate shear capacity before the column. Lower shear resistance of the CEP of Specimen H4-GR-T100, compared to Specimen H3-GR-T200 also caused more severe damage to the CEP of Specimen H4-GR-T100, as shown in Figs. 5-8(c) and 5-8(d). In general, the failure of Specimens H3-GR-T200 and H4-GR-T100 was governed by the CEP.

Figs. 5-8(e) and 5-8(f) show a comparison of failure modes between two dry joints with different thicknesses of the CEP (100 vs 200 mm). In general, the failure modes of the two specimens were different. Specimen D5-SR-S-T200 failed at the fixed end of the beam whereas Specimen D6-GR-S-T100 failed in the joint area. The flexural cracks (see the pink curve in Fig. 5-8(e)) and crushing of concrete at the fixed-end mainly governed the main failure modes of Specimen D5-SR-S-T200 due to greater shear resistance of the CEP. Therefore, in the dry joint with the CEP thickness of 200 mm, the ultimate bending capacity of the beam was reached before the shear capacity of CEP. For Specimen D6-GR-S-T100, due to a reduction of the CEP thickness from 200 mm to 100 mm, the shear resistance of the CEP of Specimen D6-GR-S-T100 was significantly reduced. Consequently, various inclined cracks were generated in the

middle zone of the CEP (see the red curves in Fig. 5-8(f)). The inclined cracks of these two dry joints only concentrated in the middle zone of the CEP due to higher shear stress concentrated in the middle zone, compared to the right and left zone of the CEP. High prestress force in the bolts increased the confined capacity of concrete in the right and left zone of CEP [19, 46]. Therefore, fewer cracks were observed in these zones. This finding will be validated in the next section using numerical simulation with ABAQUS. Finally, almost no cracks on the beam of Specimen D6-GR-S-T100 while some flexural cracks appeared on Beam A from the fixed-end to the loading point of Specimens D5-SR-S-T200. It is because Specimen D6-GR-S-T100 failed very early before Beam A reached its ultimate bending capacity. The above results indicated that reducing the CEP thickness changed the failure mode from the beam to the joint area.

5.3.2 Hysteretic responses

Both the hysteretic and envelope curves of the monolithic and dry joints were approximately symmetrical in the push and pull directions (see Figs. 5-10 and 5-11) due to the identical longitudinal reinforcements. However, those of the hybrid joints (H3-GR-T200 and H4-GR-T100) were asymmetrical in these directions owing to the asymmetric designs of the CEP (see Figs. 5-1 and 5-2). The hybrid joints showed ductile performance in the pull direction while the applied load quickly reduced in the push direction after reaching the peak load. For instance, at 4% DR, Specimen H4-GR-T100 retained 85% of the post-peak load in the pull direction while it completely failed (almost zero applied load) in the push direction. This phenomenon is attributed to (1) the gaps on the beams owing to the spalling failure of concrete filling the slot of the hybrid joints as discussed above, and (2) the effect of the CEP thickness. The longitudinal reinforcements well resisted the tensile stress in the beam in the pull direction. Meanwhile, the filled concrete block was damaged in the push direction due to the low bonding between old and new concrete surfaces. In addition, reducing the CEP thickness caused severe damage in the joint area which mainly affected the loading capacity in the push direction, as shown in Fig. 5-8(d). The above two reasons led to significantly different loading capacity in the two directions. Fortunately, the hybrid joints indicated greater performances in the pull direction (primary loading direction in the real joint application), compared to the push direction. Therefore, this newly proposed hybrid joint could be effectively applied to structures in seismic-prone

areas to reduce construction cost. For high seismic-prone areas, the bonding between old and new concrete surfaces needs to be improved and further studies are deemed necessary.

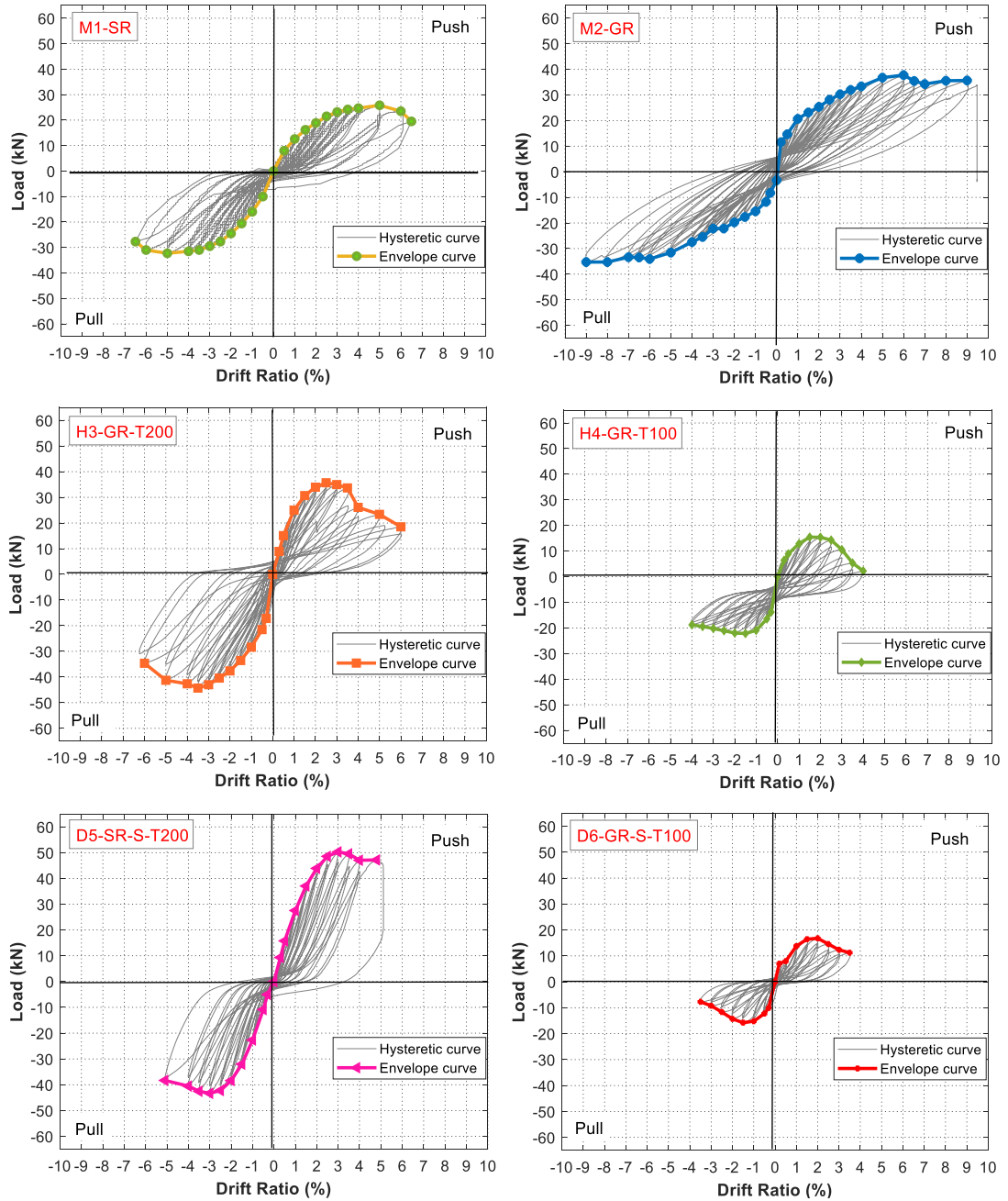


Fig. 5-10. Hysteretic responses of all the specimens.

The hysteretic curves of Specimens M1-SR and M2-GR in Fig. 5-10 indicate typical different behaviours of the specimens using the steel and GFRP reinforcements. Due to linear behaviours up to rupture of the GFRP reinforcements, smaller residual displacement (2.8 mm) was recorded in Specimen M2-GR, compared to Specimen M1

(13.8 mm) at the same 5% DR. The beams of the specimens using GFRP reinforcements could return back to its original position after unloading. It means the application of GFRP reinforcements did not induce brittle failure of the tested beam-column joints in the testing range in this chapter while the great centring capability was observed on specimens using GFRP reinforcements. This observation was also reported in another study under impact loading [2]. Yielding of steel reinforcements induced larger residual displacements for Specimen M1-SR. It is noted that concrete should govern the main failure modes in all specimens using GFRP reinforcements to avoid brittle failures. This principle should be applied in designs of the beam-column joints using GFRP materials.

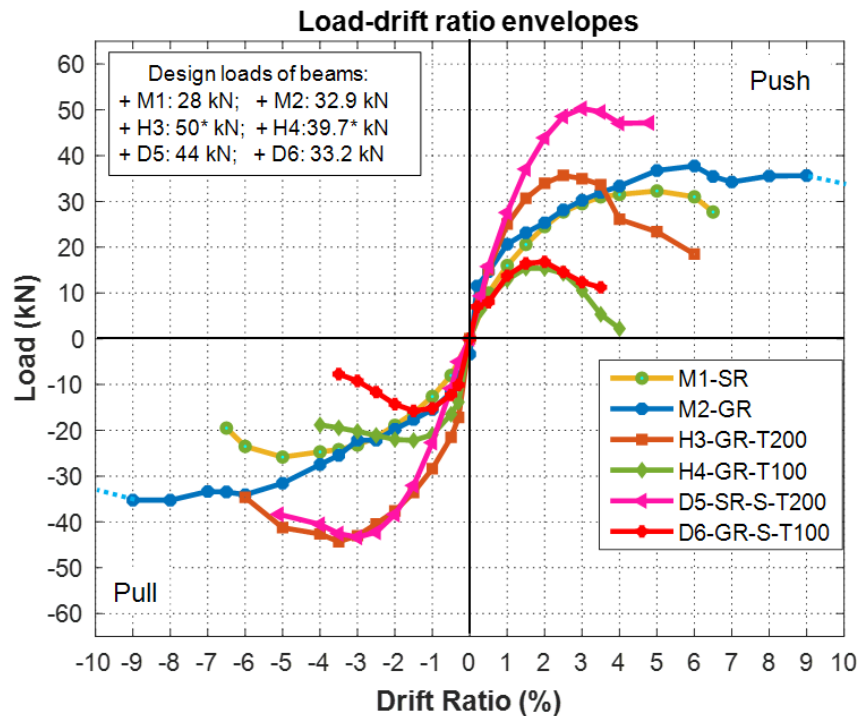


Fig. 5-11. Envelope curves of the tested specimens.

Note: * = estimated value based on the beam without gap.

5.3.3 Energy dissipation capacity

Energy dissipation (ED) is an important parameter to evaluate the performance of a structure under earthquake loading. The beam-column joints are considered to have good performances under seismic loading if they can dissipate sufficient energy while retaining their stiffness and loading capacity. The ED of the beam-column joint under cyclic loading is determined based on the area enclosed inside the hysteretic loop in

the first of every two cycles. As depicted in Fig. 5-12, the ED of all the specimens was analogous up to 1% DR owing to the elastic performance in the initial stage. After that the ED of the specimens was different. In general, the ED of the dry and hybrid joints (H3-GR-T200 and D5-SR-S-T200) was greater than that of the corresponding monolithic joints (M1-SR, M2-GR). For instance, the ED of the precast joints (hybrid and dry joints) was approximately 57-74% higher than that of the monolithic joints at 4% DR. It means the proposed dry and hybrid joints showed excellent ED under seismic loading and therefore are superior for applications in structures in seismic-prone areas. There are two possible reasons to explain this promising result. (1) Under cyclic loading, the joint opening was observed in the precast joints at the excessive load and the joint closed after unloading due to the prestress forces and linear performance of the bolts. This behaviour led to better ED in the precast joints due to friction between interfaces and damping of material, as compared to the monolithic joints in which ED depends mainly on plastic deformation and damage of structural materials. (2) Given the same drift ratio, precast joints have higher loading capacity in each cycle, compared to the monolithic joints, which led to greater ED. Therefore, the above results suggest that the precast joints could well replace the monolithic joints in seismic-prone areas.

To further evaluate whether the application of GFRP reinforcements affected the ED of beam-column joints, a comparison was conducted between Specimen M1-SR using steel reinforcements and Specimen M2-GR using GFRP reinforcements (see Fig. 5-12). In general, the ED of the both specimens was analogous while marginal higher ED was observed in Specimen M2-GR, as compared to Specimen M1-SR from 1.5% DR to 4.5% DR. This positive result is attributed to fat hysteretic loops and higher applied load in Specimen M2-GR using GFRP reinforcements. Although GFRP reinforcements showed linear performances up to rupture, fat hysteretic loops were observed on Specimen M2-GR because GFRP reinforcements have lower stiffness compared to the steel reinforcements, therefore likely led to more concrete damage although the concrete strength of M2-GR was higher than that of M1-SR. In addition, GFRP reinforcements in this chapter were designed to avoid rupture failure during the test and concrete governed the main failure modes of the specimens, as illustrated in Section 5.3.1. The applied load of Specimen M2-GR was higher than that of Specimen M1-SR due to the linear behaviour and higher strength of GFRP reinforcements than

steel reinforcements, as well as the higher concrete compressive strength and larger beam width. The loading capacity of M1-SR would not substantially increase after the steel yield. Nonetheless, the current comparison may not be valid if the concrete strength and beam size of M1-SR and M2-GR were the same, i.e., steel reinforcement might lead to more ED because of steel yielding. Nonetheless, these results indicate that the application of GFRP reinforcements can meet the ED requirements of beam-column joints under seismic loading.

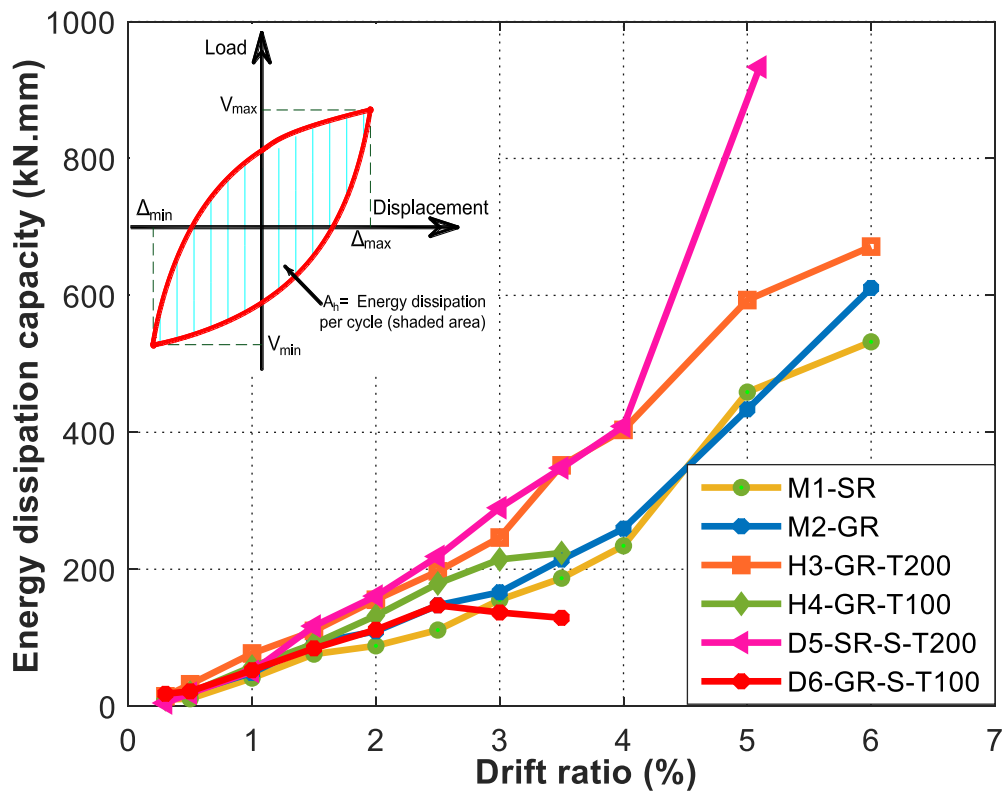


Fig. 5-12. Energy dissipation of all the specimens.

5.3.4 Drift ratio and maximum applied loads

Drift ratio is a crucial parameter to evaluate the ductility of structures under earthquake loading. This parameter is determined based on the ratio of beam displacement at the loading point (Δ) and the beam length from the column surface to the loading point ($l=550$ mm), as denoted below:

$$R = \Delta / l \quad (5-1)$$

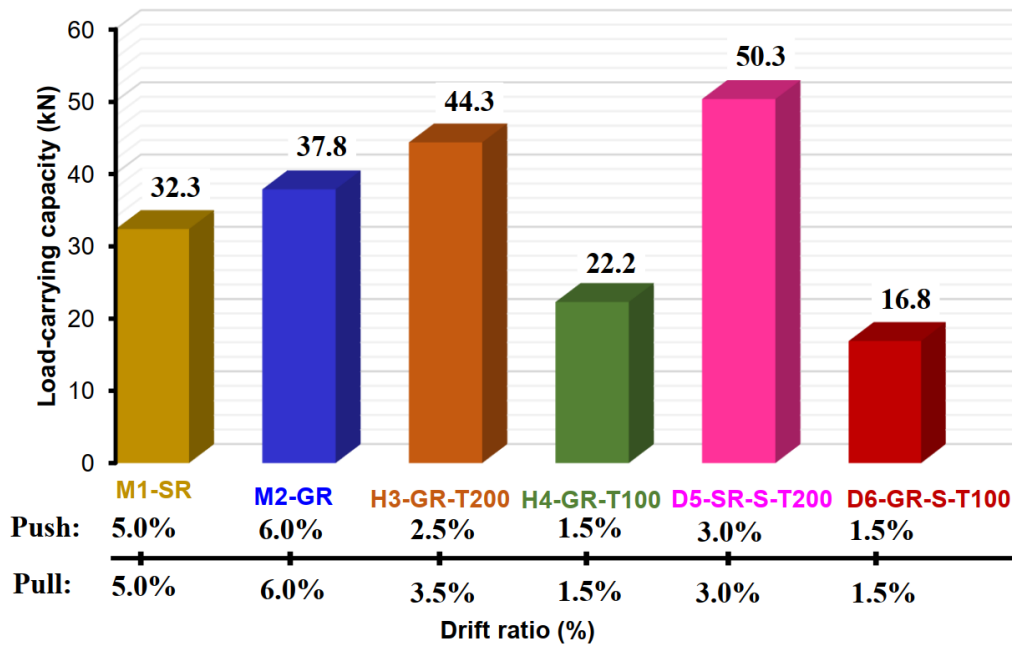


Fig. 5-13. Comparison of peak load and drift ratio.

A comparison of the peak loads and the corresponding DRs is presented in Fig 5-13. In general, the application of GFRP reinforcements illustrated good performances in terms of the peak load and DR, compared to the corresponding steel reinforcements. Specimen M2-GR reached 6% DR which was higher than that of Specimen M1-SR (5%). This DR well exceeds the requirements of many standards for structures built in the seismic-prone regions, such as ACI T1.1-01 [16] (3.5%), CSA A23.3-07 [17] (2.5%), and ASCE 41-06 [18] (2%). Lower elastic modulus and higher rupture strength of GFRP reinforcements resulted in better DR of Specimen M2-GR, compared to Specimen M1-SR using steel reinforcements. In addition, although GFRP reinforcements had lower elastic modulus as compared to steel reinforcements, the higher peak load was recorded on Specimen M2-GR. There are three reasons to explain this result. (1) The concrete compressive strength of Specimen M2-GR (59 MPa) was higher than that of Specimen M1-SR (38.5 MPa). (2) The beam width of Specimen M2-GR was 200 mm, while that of M1-SR was 150 mm. (3) GFRP reinforcements did not rupture in the tests due to its high strength. Therefore, their resistance increases linearly with the DR and applied load, whereas the loading resistance from steel reinforcements would not increase once they yield. In general, the results above demonstrate that the application of GFRP reinforcements did not cause brittle failure, thus they could be potentially applied in seismic-prone regions.

The hybrid joint shows sufficient loading capacity and DR, compared to the monolithic and dry joints. As shown in Fig. 5-13, the peak load of Specimen H3-GR-T200 (44.3 kN) was approximately 17% higher than that of Specimen M2-GR (37.8 kN). These specimens had the same cross-section and reinforcements on the column and Beam A. However, the cross-section of the CEP ($200 \times 250 \text{ mm}^2$) on Specimen H3-GR-T200 was larger than that of the beam ($200 \times 150 \text{ mm}^2$) of Specimen M2-GR. Therefore, the peak load of Specimen H3-GR-T200 was greater than that of Specimen M2-GR. However, the peak load of Specimen H3-GR-T200 was lower than that with the dry joint D5-SR-S-T200 due to lower prestress forces in the bolts [46] and failure of the filled concrete block (see Sections 5.3.1 and 5.3.2).

As can be seen that the CEP thickness in both hybrid and dry joints significantly affected the loading capacity and DR. For instance, when the thickness of the CEP reduced from 200 mm to 100 mm, the peak load decreased, approximately two times and three times in the hybrid and dry joints, respectively. In addition, the DRs in the push (2.5% DR) and pull (3.5% DR) directions of Specimen H3-GR-T200 were different while those of Specimen H4-GR-T100 were 1.5% DR in both directions. Reducing the CEP thickness in Specimen H4-GR-T100 caused more severe damage to the CEP, whereas the damage of Specimens H3-GR-T200 was governed by the debond failure of the infilled concrete block from the beam which therefore resulted in the unsymmetric push and pull loading capacities (see Figs. 5-8(c) and 5-8(d)). As a result, damage in the CEP led to the reduction of the peak load and DR of Specimen H4-GR-T100. For Specimen H3-GR-T200, a combination of damage at the CEP and infilled concrete block led to the reduction of the peak load. A higher DR was observed in the pull direction (3.5% DR) as compared to that in the push direction (2.5% DR). These DRs satisfied the requirements of CSA A23.3-07 [17] (2.5%) and ASCE 41-06 [18] (2%). Therefore, this hybrid joint is a good candidate for use in seismic-prone regions.

For dry joints, reducing the CEP thickness to 100 mm on Specimen D6-GR-S-T100 led to a reduction of DR from 3% DR to 1.5% DR. This value (1.5% DR) was consistent with the DR of the previous study by Saqan [14] who reported that this dry joint type showed poor results and it could not be applied in practice. As an effort in improving the performance, this chapter and the previous studies [2, 19, 24, 46] revised

the design of this dry joint using FRP bolts, fibres, and geopolymer concrete under cyclic and impact loading so that it could be well applied in practice. In general, the CEP thickness is one of the critical parameters that govern the DR and loading capacity of the joints and thus it is intensively investigated in the next section (Section 5.4.2) for better understanding and optimal design.

5.4. Numerical simulation with ABAQUS software

ABAQUS software was used to build 3D finite element models of the precast beam-column joints connected with GFRP or steel bolts, and GFRP reinforcements. The experimental results of Specimens M2-GR, H4-GR-T100, and D6-GR-S-T100, were used to validate the numerical model. After validating the model, an intensive parametric study was conducted to examine the assumptions used in the analytical model of the dry joints in Chapters 3 and 4 [24, 46]. For instance, shear stress primarily concentrated in the middle zone of the CEP and shear failures governed the main failure modes of the dry joints. Also, the effects of the CEP thickness on the dry joints will be investigated in this section. The influence of the CEP thickness on the hybrid joints is relatively similar to that of the dry joints so that it is not presented in this chapter for brevity.

5.4.1 Description of the finite element model

The element types, material models, mesh sizes, and contact types will be briefly presented in this section. To reduce the computational cost, the beam-column joints were built symmetrically, as shown in Fig. 5-14.

5.4.1.1 Concrete material model

Concrete of the beam-column joints was modelled by eight-node linear brick elements (C3D8). The main failure modes occurred at the joint area and fixed-end (see Fig. 5-8) so a fine mesh with a size of 20 mm was applied in these areas. Meanwhile, a coarse mesh with the size of 40 mm was used for other areas (see Fig. 5-14). It is noted that these mesh sizes were determined based on mesh convergence tests.

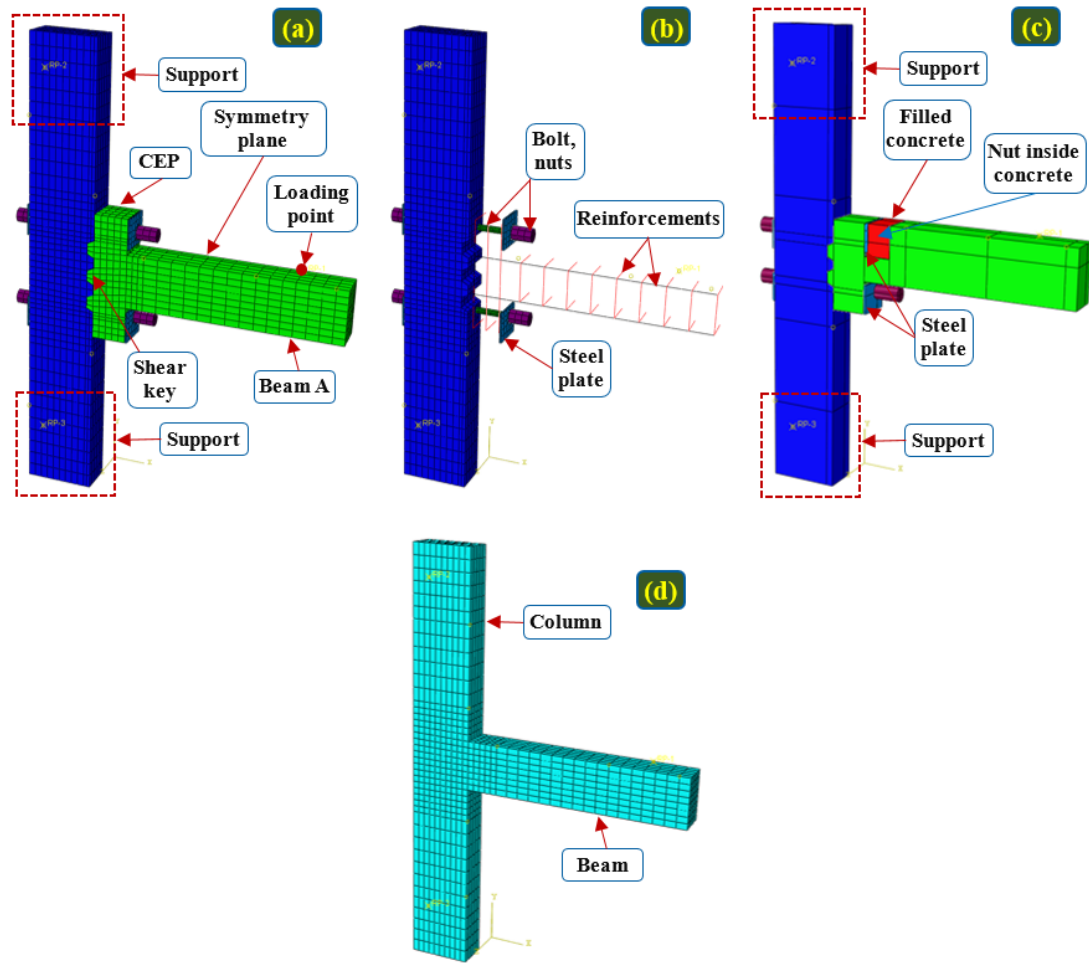


Fig. 5-14. Main components of the dry and hybrid joints; (a & b) dry joint, (c) hybrid joint, (d) monolithic joint.

There are three popular concrete models in ABAQUS including the brittle cracking model, smeared crack model, and concrete damage plasticity model (CDP) [153]. The brittle cracking model and smeared crack model are usually applied for brittle materials (e.g., brittle rocks and plain concrete) under monotonic loading [146] while CDP has been popularly adopted in simulating reinforced-concrete structures under both monotonic and cyclic loading [154]. CDP can well reflect the behaviours of specimens which is governed by concrete with compression failure under cyclic loading. For shear and tensile failures, the application of CDP to simulate the inelastic behaviours of specimens exhibited many limitations [145, 146]. Hence, this chapter adopts the newly developed softened damage-plasticity model by Feng et al. [145] and Feng et al. [155] to simulate behaviours of the reinforced-concrete joints under cyclic loading. The comparison of plain concrete and reinforced concrete under un-softening and softening effects was respectively illustrated in Fig. 5-15.

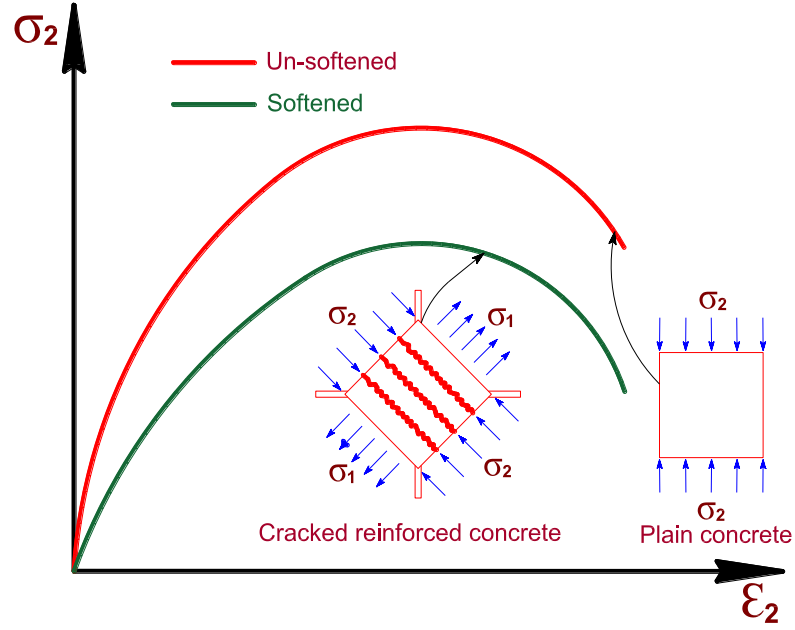


Fig. 5-15. The effects of compression-softening on reinforced concrete [55].

For brevity, hereafter the concrete material model with the softening effects is briefly introduced. The constitutive relation was represented as:

$$\sigma = (I - D^S); E_0; (\epsilon - \epsilon^p) \quad (5-2)$$

where σ , I , D^S , and E_0 denoted the Cauchy stress tensor, identity tensor, fourth-order damage tensor corresponding to compression-softening, and fourth-order elastic modulus tensor, respectively; ϵ is the strain tensor including two components (elastic part ϵ^e and plastic part ϵ^p); the damage tensor (D^S) is determined as follows:

$$D^S = d^+ P^+ + d^{S-} P^- \quad (5-3)$$

$$d^{S-} = 1 - \beta(1 - d^-) \quad (5-4)$$

where P^+ and P^- are the projection tensors; d^+ and d^- indicate the two damage variables of concrete corresponding tensile and compressive performances; β denotes the softening coefficient and is calculated as follows.

$$\beta = \frac{1}{\sqrt{1+400\epsilon^e q^+}} \quad (5-5)$$

It is noted that the softening coefficient is identified based on the tensile energy equivalent strain rather than the principal tensile strain. This model provides more

convenience in calculations under complex multi-axial stress state and accounts for the accumulated influence of compression-softening under reverse loading.

Moreover, the energy equivalence is proposed by Li and Ren [156] as follows:

$$\bar{\epsilon}^{eq+} = \sqrt{\frac{2Y^+}{E_0}}, \bar{\epsilon}^{eq-} = \frac{1}{E_0(1-\alpha)} \sqrt{\frac{Y^-}{b_0}} \quad (5-6)$$

where α and b_0 depend on the material properties; E_0 is the initial elastic modulus [157]; Y^\pm are the damage release rates and are determined as bellow:

$$Y^+ = \frac{1}{2}(\bar{\sigma}^+ : E_0^{-1} : \bar{\sigma}), Y^- = b_0(\alpha \bar{I}_1^- + \sqrt{3\bar{J}_2^-})^2 \quad (5-7)$$

where \bar{I}_1^- and \bar{J}_2^- are the first invariant of the compressive effective stress $\bar{\sigma}^-$ and the second invariant of the deviator of the compressive effective stress $\bar{\sigma}^-$, respectively [146].

The uniaxial damage evolution functions are determined as follows [155, 158]:

$$d^\pm = \begin{cases} 1 - \frac{\rho^\pm n^\pm}{n^\pm - 1 + (x^\pm)^{n^\pm}} & x^\pm \leq 1 \\ 1 - \frac{\rho^\pm}{\alpha^\pm (x^\pm - 1)^2 + x^\pm} & x^\pm > 1 \end{cases} \quad (5-8)$$

$$x^\pm = \frac{\bar{\epsilon}^{eq\pm}}{\epsilon_c^\pm}, \rho^\pm = \frac{f_c^\pm}{E_0 \epsilon_c^\pm}, n^\pm = \frac{1}{1 - \rho^\pm} \quad (5-9)$$

where f_c^\pm and ϵ_c^\pm are the tensile/compressive maximum strength and the corresponding strain; α^\pm indicates the descending parameters that govern the shape of the descending part of the stress-strain curves [55].

Moreover, ϵ^p is calculated to improve the numerical efficiency of the model, based on the empirical model by Faria et al. [159] and the modified model by Wu [160].

$$\dot{\epsilon}^p = b^p \bar{\sigma} \quad (5-10)$$

$$b^p = \xi^p E_0 H(\dot{d}^-) \frac{\langle \epsilon^e : \dot{\epsilon} \rangle}{\bar{\sigma} : \bar{\sigma}} \geq 0 \quad (5-11)$$

The plastic coefficient which dominates plastic strain level is denoted by ξ^p . The tensile plastic strain is neglected due to its insignificant effects on the whole structural

performance. It is noted that the above model of concrete was implemented into ABAQUS through user-defined subroutine UMAT.

5.4.1.2 Steel and FRP material models

The GFRP longitudinal reinforcements and stirrups were modelled by truss elements (T3D2) while C3D8 was used to model the bolts and steel plates. After conducting the mesh convergence tests, the 20-mm mesh size was applied for these elements. Material properties of GFRP bolts and GFRP reinforcements are presented in Tables 5-3 and 5-4. The anisotropic elastic material model was applied for all GFRP bolts and GFRP reinforcements in this chapter owing to the linear performance of GFRP material till failure. For steel bolts and steel plates, the elastoplastic stress-strain material model was used [81].

5.4.1.3 Contact mechanism

All the reinforcements were embedded inside the concrete. The surface-to-surface contact was applied between two shear key surfaces of the beam and column with a friction coefficient of 0.7 [81]. The spacing between the bolts and the holes on the beams and columns of dry and hybrid joints was respectively 4 mm and 1.5 mm so the unbonded contact was adopted. Zero friction was assumed in unbonded contact to define the tangential behaviour between the bolts and the holes [81]. Tie constraint contact was applied between steel plate and CEP/column surfaces and between nut and steel plate surfaces. Also, the tie constraint contact was adopted between the filled concrete and old concrete/steel plate surfaces.

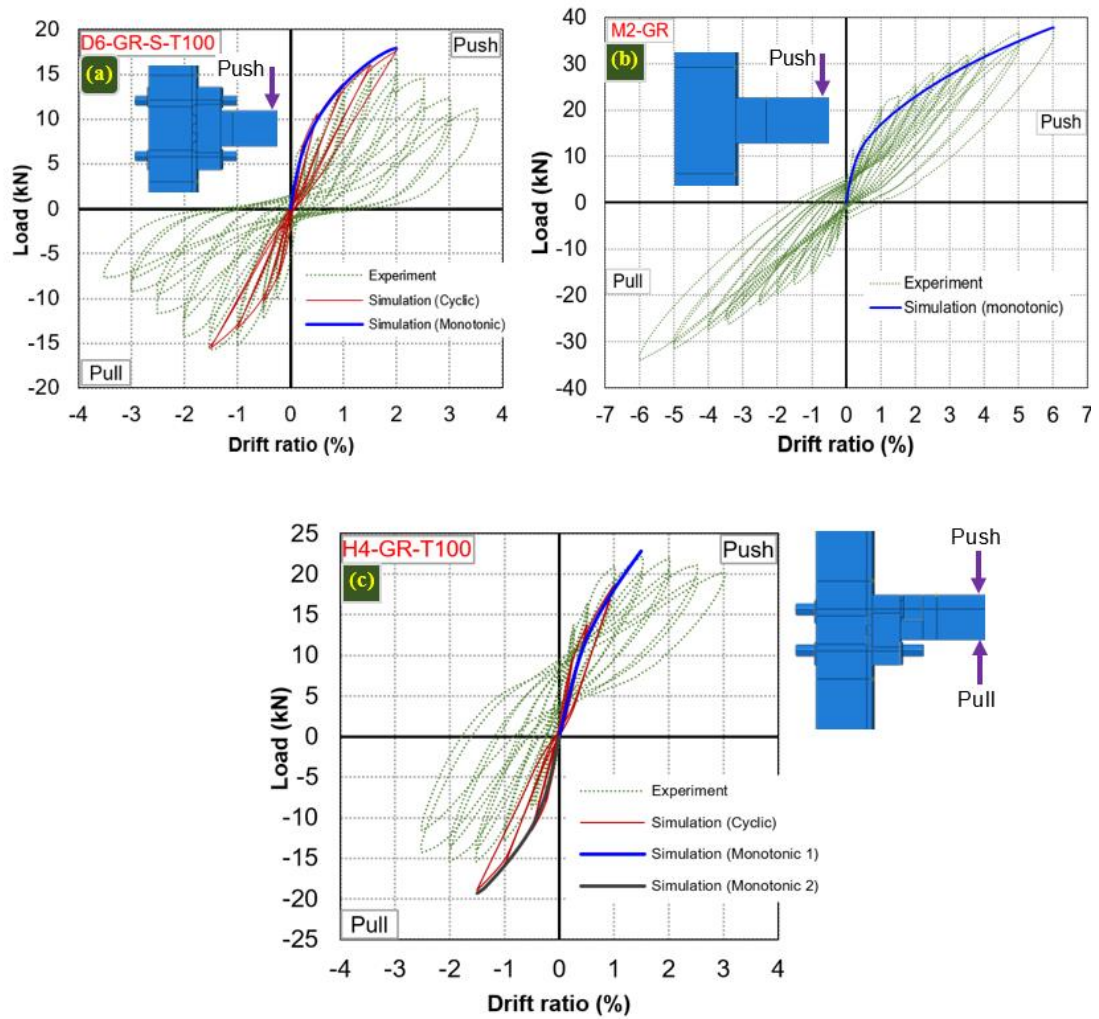
5.4.1.4 Model validation and discussions

Using ABAQUS to simulate the performance of reinforced-concrete structures with shear and tensile failures under cyclic loading is challenging due to the limitation of the concrete model as reported in the previous studies [145, 146]. Hence, only the loading-displacement relationship under the monotonic loading was simulated instead of the cyclic loading in previous studies [7, 147, 148]. This chapter shows an improvement compared to the previous studies [7, 147, 148] because the performances of the dry and hybrid joints under cyclic loading could be well simulated till the peak loads. However, inconsistent numerical results under cyclic loading conditions in the

post-peak region were observed owing primarily to the incapability of the material model to properly represent the post-failure performance of the concrete material under complex stress states induced by combined bending moment and shear force. Owing to this limitation, and also because the stress distribution and damage of materials up to the peak loads are the primary concern in the analysis and design of a beam-column joint, and also the primary focus of this investigation, in this chapter, like in the previous studies [7, 147, 148], simulation of the structural performance under monotonic loading is also carried out to obtain the loading-displacement envelope. Hence, this chapter uses both hysteretic curves under cyclic loading up to the peak load and envelope curves under monotonic loading to validate the accuracy of the numerical simulation results. Afterwards, only the numerical simulation under monotonic loading, which was computationally a lot more efficient compared to simulations under cyclic loading, was applied to conduct parametric investigations. The values of the ductility, DR, and loading capacity of the proposed dry and hybrid joints could be used to evaluate the performance of these joints when applying in seismic-prone areas. The ED derived from the results of the numerical simulation depends on the concrete constitute model and its ability to represent concrete material behaviour in the post-failure region under complex stress states, which is a good topic for future studies.

The numerical model was validated with the experimental results in terms of hysteretic loops, envelope curves, and failure modes, as shown in Figs. 5-16 and 5-17. Only the first cycle of each DR level (2 cycles in the experiment) was applied in the numerical simulation to reduce the simulation time. The envelope curve of Specimen H4-GR-T100 was plotted in both push and pull directions due to the asymmetric design of this specimen. In general, the numerical simulation well captured the peak loads, DR, and the stiffness of the monolithic and dry joints. The differences in numerical results and experimental peak loads ranged between 4.1% and 6.7%. For example, the experimental peak load of Specimen D6-GR-S-T100 was 16.8 kN while the corresponding numerical result under cyclic and monotonic loading was 17.5 kN and 17.9 kN, respectively. However, the unloading curves of the numerical simulation do not match well with the experimental results, as shown in the red curve of Fig. 5-16 (a). This limitation is attributed to the concrete model as discussed above. Multiple cycles were applied in each level of DR in the experimental test while only one cycle

at each DR was carried out in the numerical simulation to save computation time as also adopted in a previous study [55]. This difference might further contribute to the variation between the numerical and experimental results. This limitation was also reported in previous studies [146, 161] and thus improving the concrete model that takes into consideration the load-path effect is deemed necessary, particularly for unloading curves.

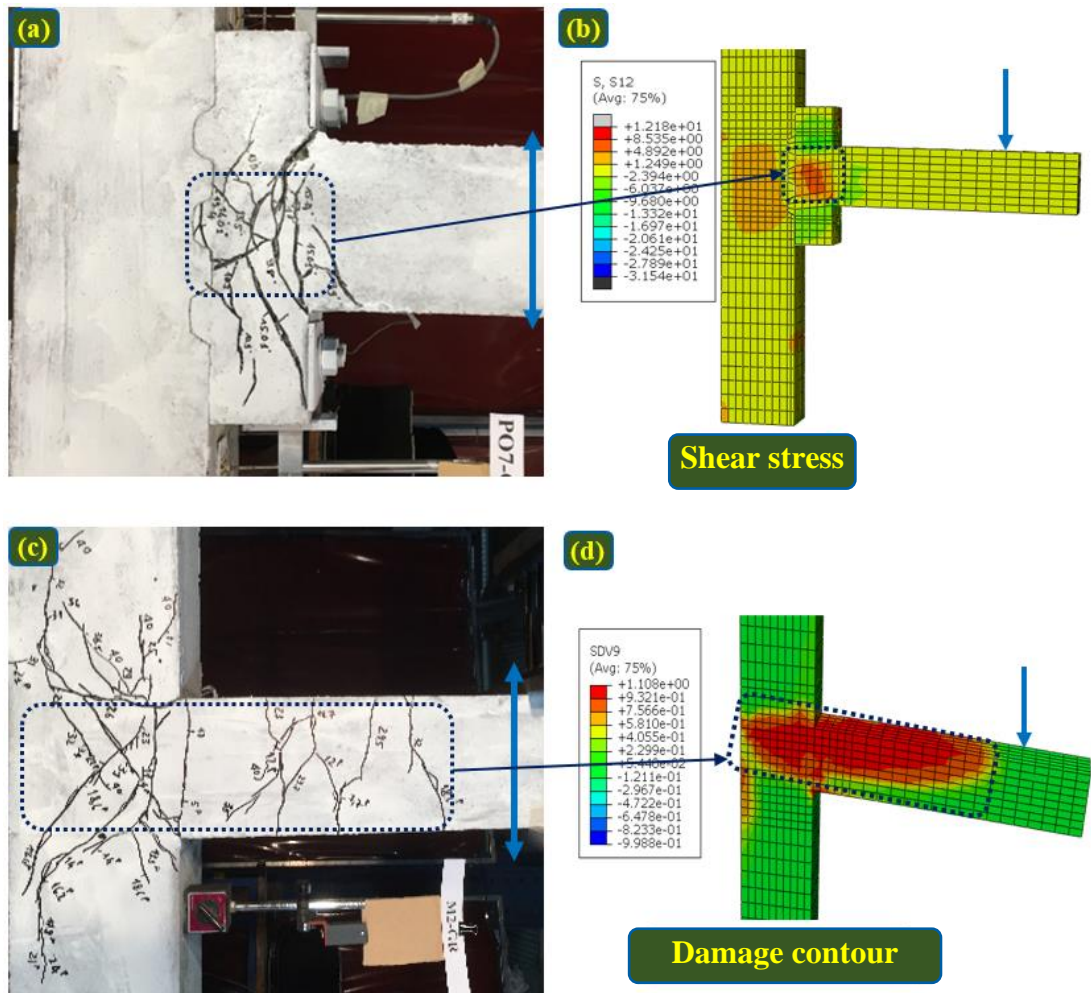


Note: Monotonic 1 and monotonic 2 are plotted in the push and pull directions, respectively.

Fig. 5-16. Comparison of hysteretic and envelope curves between experiment and numerical simulation results.

Although the numerical model successfully predicted the peak load in the push direction of the hybrid joint, a higher variation (approximately 24%) was observed in the pull direction, as shown in Fig. 5-16(c). This result is attributed to the contact between the old and new concrete surfaces used in the numerical simulation model.

This chapter adopted the tie constraint contact to simulate the contact between the old and new concrete surfaces, which did not well reflect the real contact as observed in the test. Unfortunately, no information regarding the mechanical properties of such contact is available in the literature. The contact between old and new concrete of different strengths needs to be improved in further studies. In addition, the simulations of hysteretic curves of Specimens D6-GR-S-T100 and H4-GR-T100 were stopped at the peak load with 2% and 1.5% DR, respectively, as shown in Figs. 5-16(a) and 5-16(c) because running the full hysteretic curves was computationally very intensive, and also because of the limitation of the current concrete material model which does not necessarily yield good post-failure representations as discussed above.



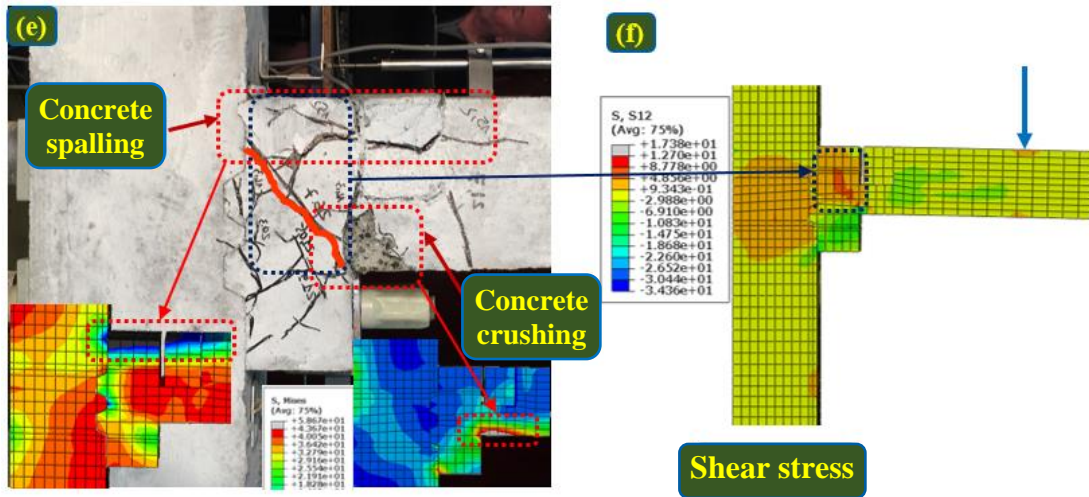


Fig. 5-17. Comparison of failure modes between experiment and numerical simulation of Specimens D6-GR-S-T100 (a-b), M2-GR (c-d), and H4-GR-T100 (e-f) at the peak load.

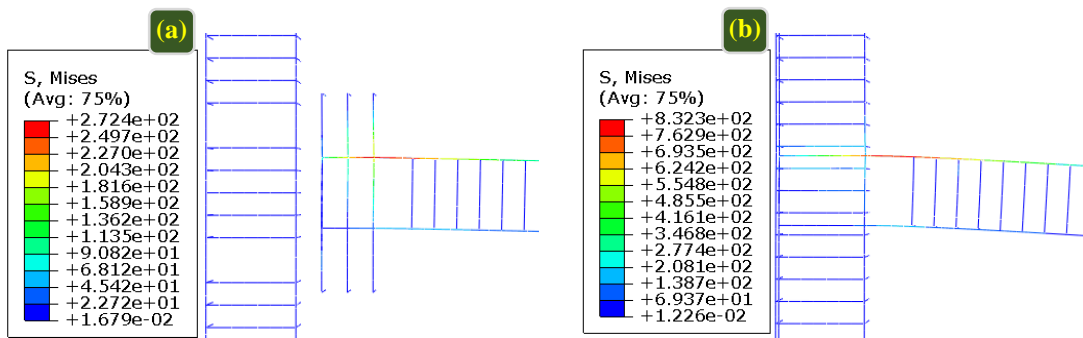


Fig. 5-18. Tensile stress in GFRP reinforcements: (a) dry joint and (b) monolithic joint.

It can be seen in Figs. 5-17(a) and 5-17(b) that the numerical model successfully captured the failure patterns of the dry joint D6-GR-S-T100. In the experimental results, the cracks mainly developed in the middle joint of the CEP while there were no visible cracks at the top and bottom zones. The data of strain gauges in the previous studies [19, 46] illustrated that shear and tensile cracks governed the main failure of this type of dry joint. This finding was consistent with the data from the numerical model, as shown in Fig. 5-17(b). It can be seen from the numerical results that shear stress firstly occurred in the middle zone of the CEP and then they extended. The tensile stress of GFRP stirrups and longitudinal reinforcements did not reach their nominal tensile strength (approximately 1,259 MPa), as shown in Fig. 5-18(a). It means the shear failure of concrete in the middle zone of CEP governed the main

failure of the dry joint (D6-GR-S-T100). This result is different from the findings of the previous studies [13, 14] which adopted the model of the monolithic joint for the precast joint and concluded that the strut-tie failure governed the main failure of this type of dry joint.

For the monolithic specimen, the damage contours of the numerical model also well predicted the failure modes of the monolithic specimen (M2-GR), as shown in Figs. 5-17(c) and 5-17(d). More severe damage was observed in the joint area and at the fixed-end of the beam due to the shear stress and the bending stress/concrete crushing, respectively. In addition, since the tensile stress of the GFRP reinforcements in the specimens did not reach their nominal tensile strength (see Fig. 5-18(b)), concrete governed the main failure modes of both the monolithic and dry joints.

Similar to the dry and monolithic joints, the concrete failure is the primary failure mode of the hybrid joints. The numerical model also successfully captured the failure patterns of Specimen H4-GR-T100, as shown in Figs. 5-17(e) and 5-17(f). The inclined cracks appeared in the joint area due to the shear stress as illustrated in Fig. 5-17(f). In addition, the numerical results indicated that the concentrated compressive stress caused the concrete crushing at the fix-end and the concrete spalling at the bottom zone of the CEP (see Fig. 5-17(e)). For instance, the maximum compressive stress of concrete at the fixed-end was 58.8 MPa which reached the compressive strength of concrete (59 MPa). The results of numerical simulations are consistent with the observed failures of the hybrid joint in Section 5.3.1.

5.4.2 Effect of concrete-end-plate thickness

The above comparisons between experiment and numerical simulation results have proven the reliability of the numerical model and thus it is used to examine the effects of the CEP thickness on the structural behaviour. The model of Specimen D6-GR-S-T100 was used as a reference dry beam-column joint. Numerical models of six specimens which had a similar design but different CEP thicknesses were built based on the model of the reference specimen. The thickness of the CEP was chosen based on the height of the beam section. The numerical model of the tested specimen D6-GR-S-T100 was named as D7-T100, and the new numerical models with other CEP thicknesses were named accordingly as detailed in Table 5-5.

Table 5-5. Description of specimens built on ABAQUS.

Name	Thickness (mm)	CEP/Beam	Reinforcements	Bolts	Axial forces (kN)	Prestress forces (kN)
D7-T100	100	0.7	GFRP	Steel	65	35
D8-T150	150	1	GFRP	Steel	65	35
D9-T200	200	1.3	GFRP	Steel	65	35
D10-T250	250	1.7	GFRP	Steel	65	35
D11-T300	300	2	GFRP	Steel	65	35
D12-T350	350	2.3	GFRP	Steel	65	35

Note: D7-T100 is the numerical model of D6-GR-S-T100.

5.4.2.1 Failure modes

Fig. 5-19 shows the shear stress distribution of the dry joints with different CEP thicknesses. Only the failure modes of Specimens D7-T100, D9-T200, D11-T300, and D12-T350 were representatively shown in this figure for brevity, as shown in Fig. 5-19. In general, the failure mode of the dry joint was shifted from the CEP area (Specimen D7-T100) to the beam at the fixed-end (Specimen D9-T200) when increasing the CEP thickness. However, if the CEP thickness was further increased, the failure model changed again from the beam to the column (Specimen D11-T300). For example, the shear failure in the middle zone of the CEP was the primary failure modes of Specimen D7-100 (see Fig. 5-19). When the CEP thickness increased from 100 to 200 mm, the shear stress in the middle zone of Specimen D9-T200 was reduced as compared to Specimen D7-T100 due to increasing the thickness of this section. The flexural failure and concrete crushing at the fixed-end of the beam became the primary failure modes of Specimen D9-T200. This result was consistent with the failure mode of Specimen PS4 reported in the previous study [19]. When the CEP thickness was 300 mm or more, the failure shifted to the column. As can be seen clearly in Figs. 5-19(D11-T300) and 5-19(D12-T350), higher shear stress was observed on the column, compared to the CEP. This shear stress caused severe damage on the column while almost no shear damage was recorded on the CEP. It means that if the CEP thickness was sufficiently large, compared to the section's height of the beam and the column, the design principle of the strong column-weak beam may not be satisfied. Therefore, the CEP thickness needs to be carefully chosen in the design process to avoid making the column the weaker component in the structure.

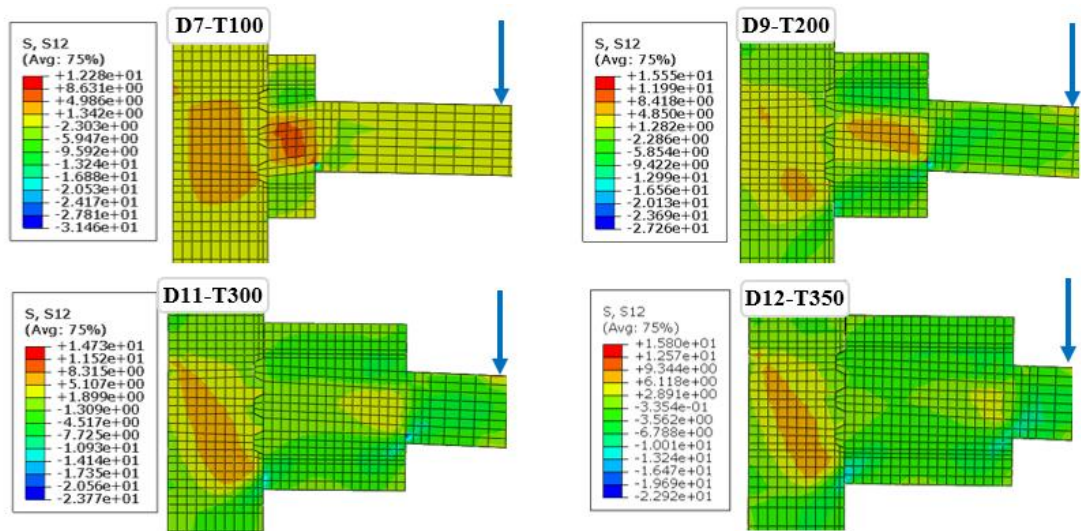


Fig. 5-19. Shear stress distribution on dry joints with different CEP thickness.

Fig. 5-20 illustrates the principal compressive stress flow of the typical specimens. The distribution of all compressive, tensile and shear stresses in the CEP of the dry joint was very complicated. Fig. 5-20 only shows stress flow of the compressive stress for demonstration. The compressive stress in the middle zone of the CEP was quite small which did not reach the compressive strength of concrete. Therefore, there was no compressive strut failure as suggested in the previous studies [13, 14]. For instance, the maximum compressive stress of concrete in the middle zone of Specimens D7-100 and D9-200 was 16 MPa and 19 MPa (see Figs. 5-20(D7-T100) and 5-20(D9-T200)), respectively which is significantly lower than the compressive strength of concrete (38.5 MPa). Hence, the compression strut failure did not occur in these specimens. In addition, high compressive stress was observed in the top and bottom zone of the CEP due to the effect of the prestress forces of the bolts. Steel spirals were utilized in these locations in the previous study [19] but the capacities of the dry joint were not improved because the failure was not governed by compressive concrete at these regions either. The compressive stress in the top and bottom zones of CEP (e.g., 26 MPa in Specimen D9-T200) was lower than the nominal compressive strength of concrete. This finding explains why steel spirals were not useful in this case. For the compressive stress flow on the column of dry joints, the stress distribution was observed as in the joint area of the monolithic joint. A compressive strut was generated in the column of the dry joint due to the compressive forces at the anchor of the bolts and at the bottom left of CEP, as illustrated in Fig. 5-20. Interestingly, when the CEP

thickness reached 300 mm, the direction of stress flow altered with no compressive strut in the middle zone of CEP due to changing the failure mode from the beam to the column.

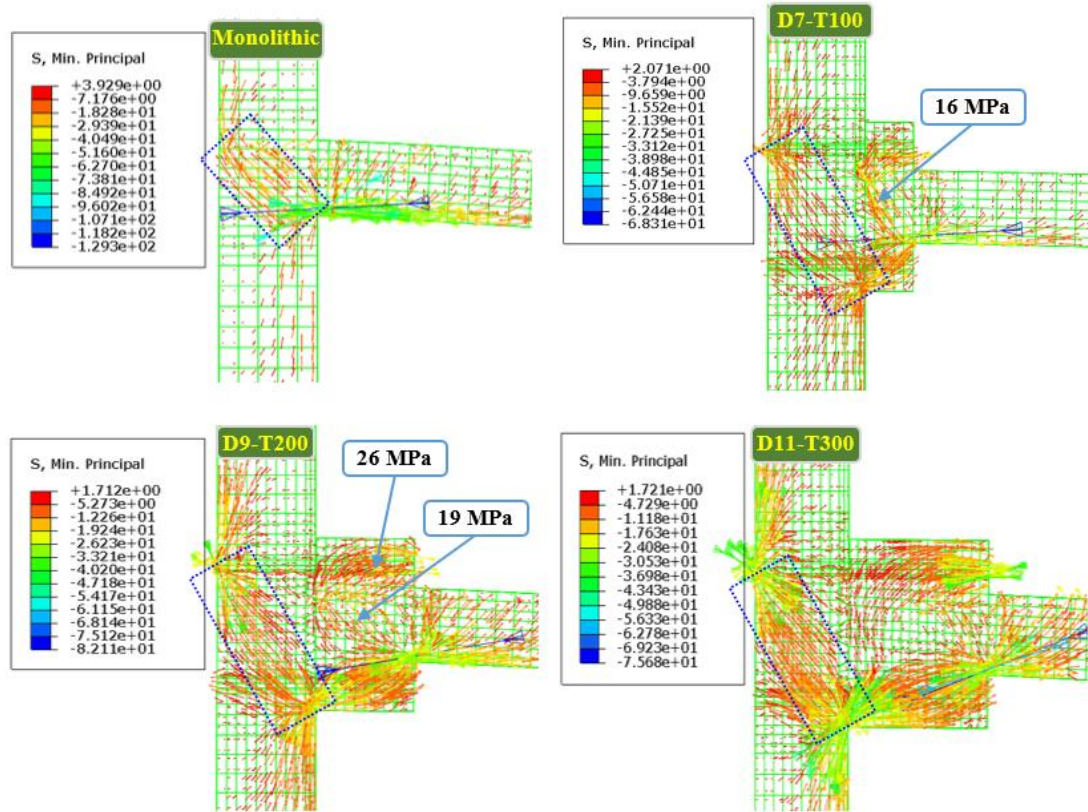


Fig. 5-20. Principal compressive stress flow.

5.4.2.2 Peak load and drift ratio

The CEP thickness significantly affects both the peak load and DR (see Fig. 5-21). As mentioned in the introduction section, this dry joint was proposed based on the previous study of Saqan [14] who reported that its DR and energy absorption were inadequate. The 1.5% maximum DR value recorded in the previous study [14] was consistent with DR of Specimen D6-GR-S-T100 in the pull direction. In the first stage of our project, the CEP thickness was intentionally increased up to 200 mm, which was thicker than the CEP thickness of Specimen DB-TC in Saqan [14]. As a result, the maximum DR increased from 1.5% to 3.0% as reported in the authors' previous studies [19, 46, 141], which satisfied the requirements of many standards (e.g., CSA A23.3-07 [17] (2.5%) and ASCE 41-06 [18] (2%)) for using in seismic-prone areas. The DR of Specimen D9-T200 (3.5%) in the numerical simulation was slightly higher than the

result of the previous studies (3%) [19, 44] because GFRP reinforcements were used to replace steel reinforcements which led to an increase of the DR, as explained in the monolithic specimen of the above section (Section 5.3.4).

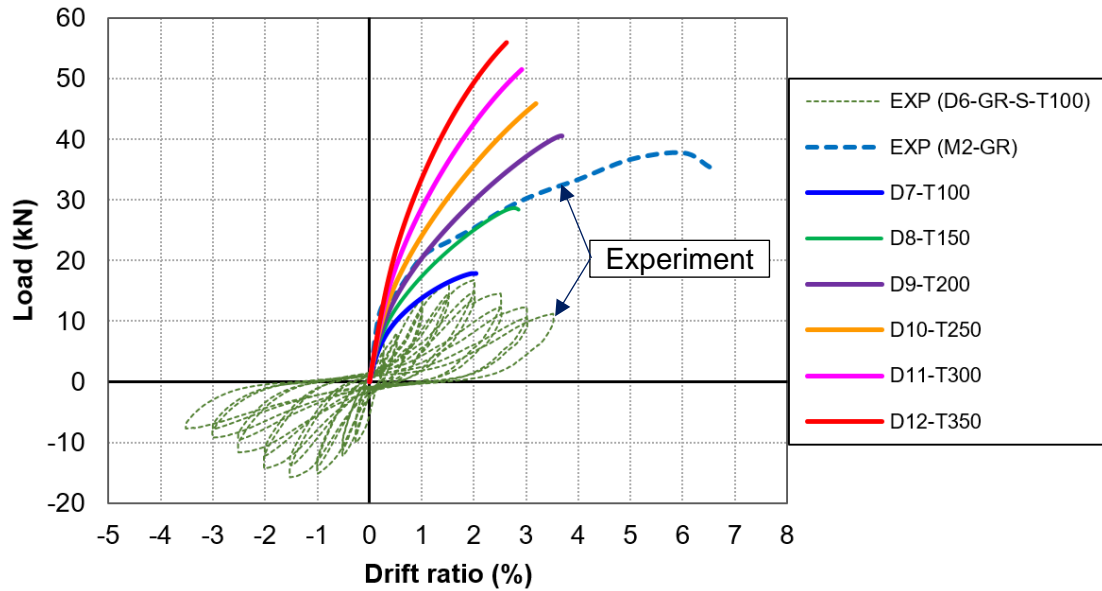


Fig. 5-21. Comparison of the peak load and drift ratio.

As mentioned in the previous section, increasing the thickness of the CEP results in improved performance of the precast joint, but further increasing the CEP thickness may lead to an adverse effect. As indicated in Fig. 5-21, there was an optimal value of the CEP thickness of approximately 200 mm. Based on the numerical results, the ratio of CEP/Beam= 1.3 (200-mm CEP thickness) was the optimal value of the dry joint in this chapter. For instance, Specimen D9-T200 reached 3.5% DR while increasing the CEP thickness up to 250, 300, and 350 mm caused a reduction of DR to 3.2%, 2.9%, and 2.6%, respectively. This reduction is attributed to changing of the failure modes from the joint and the beam to the column because the CEP made the beam and joint strong. The peak loads of the precast joints increased with the CEP thickness. For example, when the CEP thickness was increased from 100 mm to 150, 200, 250, 300, and 350 mm, the peak load also steadily increased from 17.8 kN to 28.5, 40.3, 45.7, 51.1, and 55.3 kN, respectively. Meanwhile, both the peak load and ductility need to be considered in the structural design under seismic loading. If a structure achieves a very high peak load but shows a brittle failure, it is not suitable for use in seismic-prone regions. Based on this perspective, the dry joint with the 200-mm CEP thickness was the best option in this chapter because it achieved the highest DR, compared to

other dry joints. Moreover, the peak load of Specimen D9-T200 (40.3 kN) was higher than that of the corresponding monolithic joint M2-GR (37.8 kN) as shown in Fig. 5-21. Therefore, the thickness ratio of CEP/Beam= 1.3 could be considered in the design of this dry joint type. More studies are deemed necessary to enhance the understanding and further confirm this suggestion.

5.5 Summary

A new kind of hybrid joint was proposed in this chapter to improve the design of the dry beam-column joint with a bulky CEP. The performances of the hybrid and dry joints were experimentally and numerically investigated. The main findings can be summarised as follows:

1. The hybrid joint showed sufficient capacities, compared to the monolithic joint. The energy dissipation and the peak load of the hybrid joint were approximately 57% and 17% higher than the reference monolithic joint, respectively. In addition, the lowest DR reached 2.5/3.5% for push and pull directions which satisfies the requirements of CSA A23.3-07 [17] (2.5%) and ASCE 41-06 [18] (2%) for use in seismic-prone regions.

2. Based on the experimental and numerical simulation results, the CEP thickness significantly affects the dry and hybrid joint performances, such as failure mode, DR, peak load, and ED. In addition, the numerical simulation results suggested that the thickness ratio of CEP/Beam= 1.3 was an optimal value of the CEP thickness which could be considered in the design of this dry joint type.

3. GFRP bolts and reinforcements could replace the steel bolts and reinforcements to mitigate corrosion damage. The application of GFRP in this chapter provided not only ductile failure but also the great centring capability (smaller residual displacement).

4. The application of the modified concrete model well captured the failure mode and the peak load of the precast joint with a marginal variation of 4.1-6.7%.

5. The numerical simulation results illustrated that the shear and tensile stress in the middle zone of CEP mainly governed the joint failure of the dry joint. Therefore,

the assumption in the analytical model in Chapters 3 and 4 [24, 46] was numerically confirmed.

In conclusion, this chapter proposes an alternative for designing precast concrete structures which could not only reduce the construction cost but also offer more convenience in applying new technology into the construction sector.

CHAPTER 6: PERFORMANCE OF MONOLITHIC AND DRY JOINTS WITH GFRP BOLTS REINFORCED WITH DIFFERENT FIBRES AND GFRP BARS UNDER IMPACT LOADING

ABSTRACT⁵

This chapter investigates the performance of monolithic and newly proposed dry beam-column joints using GFRP bolts, GFRP reinforcements, and different types of fibres subjected to pendulum impact. Six specimens were cast and tested with increasing impact velocity until failure. The experimental results have shown that the proposed concrete dry joint reinforced with fibres and GFRP bars showed better behaviour in terms of energy dissipation (up to 51%), reduced damage level, and reduced maximum and residual displacement as compared to the monolithic joint with GFRP reinforcements. The test results suggested that steel bolts and steel reinforcements could be effectively replaced by GFRP bolts and GFRP reinforcements to mitigate the corrosion problem while still satisfy the design requirements for beam-column joints in both strength and ductility. Furthermore, the use of steel fibres (StFs) demonstrated impressive performance in the critical indices such as damage level and displacement at high impact energies, compared to synthetic fibres (SyFs). Meanwhile, the application of SyFs led to greater energy dissipation than that of StFs (between 6-30%). The proposed dry joints could be potentially applied in practice to reduce the construction costs and the damaged/deteriorated components would be easily replaced.

⁵ This work was published in **Engineering Structures** with the full bibliographic citation as follows:

Ngo TT, Pham TM, Hao H, Chen W, Elchalakani M. Performance of monolithic and dry joints with GFRP bolts reinforced with different fibres and GFRP bars under impact loading. *Eng Struct* 2021;240:112341.
<https://doi.org/10.1016/j.engstruct.2021.112341>

6.1. Introduction

Disasters related to impact and blast loads, which usually occur suddenly without any warnings, have threatened the human life worldwide. Surprisingly, there is still a lack of standards for structural designs against these loads. The performances and failure patterns of structures under impact and blast loading are different with those under static and earthquake loading. For example, flexural cracks governed the main failure of beams under static loading while shear cracks caused the failure of the identical beams under impact loading due to high loading rates [48-50]. Consequently, the current standards for static and earthquake loading could not be applied to design structures against impact and blast loads. For instance, drift ratio (e.g., 3.5% in ACI T1.1-01 [16] and 2.5% in CSA A23.3-07 [17]) is a crucial parameter to evaluate the performance of buildings under earthquake loading. This parameter, however, is not suitable to assess the performance of buildings under impact or blast load because local damage could govern the structural damage instead of the global structural responses. In other words, structures may suffer from local damage which may trigger a progressive collapse of the structure although other parts of the structure are not directly impacted by blast and impact load. Therefore, there is a need to better understand the impact behaviour of reinforced concrete (RC) structures, in particular in this chapter RC joints and develop design procedures for RC joints against impact and blast loads, which are still unavailable in current standards.

Due to the limitation of the equipment, software, and dynamic material model, there is limited research investigating the responses of structural components, especially beam-column joints under impact loads. Most of previous studies related to impact loading heavily focused on beams or columns. Pham and Hao [50] and Cotsovos [162] reported that there was a time delay between the impact forces and reaction forces on a simply-supported beam owing to the effects of stress wave propagations, and the impact force was balanced primarily by inertial resistance of the beam before the reaction force was activated. In addition, Pham et al. [163] illustrated that the contact stiffness and local stiffness significantly affected the peak impact forces of concrete beams. The local responses dominated the beam behaviour if the impact energy was sufficient in impact events [164]. Li et al. [165] conducted numerical simulations with LS-DYNA software on five common geometries of the drop hammer and two different

interlayers (i.e., steel plate and rubber pad). The results highlighted that the impact forces and failure modes on the beams were considerably affected by the shapes of the drop hammer and material properties at the impact point. These studies revealed that many parameters can significantly affect the impact responses of RC beams. Further researches are needed to better understand the performances of RC beams under different impact scenarios and develop safe and economic procedures for design of RC beams against impact loads.

Meanwhile, owing to urbanization, bridge construction is experiencing rapid growth. During their service life, bridges can be threatened by collision events from, e.g. vehicle impact, ship impact or falling rock impact. Hence, many studies have focused on bridge columns under impact loads. Sha and Hao [166] carried out both experimental and numerical investigations on the performance of the monolithic circular RC piers under impact load. It was reported that the impact velocity significantly affected the peak impact forces whereas the impactor mass dominated the impact duration of the column. Additionally, studies of the impact responses of precast segmental columns using unbonded tendons and shear keys have also been reported recently [167-169]. The results from the experiments and numerical simulations in these studies suggested that the use of shear keys effectively decreased the lateral slippage between segments and mitigated the residual displacement. Pham et al. [170] investigated impact responses of rubberized concrete columns. The experimental results indicated that the application of rubberized concrete decreased the peak impact forces by approximately 27-40% but increased the energy absorption from 58 to 63%, compared to the reference specimens. In addition, increasing the prestress forces did not increase the impact forces of the segmental column under impact loading [167]. On the other hand, only one study [51] can be found in the open literature that evaluates the performance of RC beam-column joints under impact loads.

Beam-column joints play an important role in RC frame structures. They are vulnerable structural components under impact loading [171]. Beam-column joints can be classified into four types including monolithic joints, wet joints, dry joints, and hybrid joints. Recently, dry beam-column joints in prefabrication construction attract increasing interest because they offer various advantages such as reducing the construction costs, efficiently applying the new construction materials and

technologies (e.g., geopolymer, fibre reinforced concrete, and 3D printing), easily replacing and recycling damaged components for resilient structures. Nevertheless, there remain a limited number of studies focusing on the dry joints in the open literature. A few studies [10-12] investigated the dry joints under cyclic loading using unbonded steel tendons to connect beams and columns. The disadvantages of this dry joint type are that the uncovered steel tendons are very vulnerable to corrosion and damaged components are difficult to be replaced. To resolve these limitations, Chapter 2 proposed a new dry joint type using CFRP bolts and concrete-end-plate (CEP) which possess great corrosion resistance, convenient setup, and good behaviour under earthquake loading. For beam-column joints under impact and blast loading, only two studies [51, 52] investigating monolithic beam-column joints can be found. To generate impact forces, a projectile was used with an intermediate-velocity of 30-34 m/s. Aluminium honeycomb core was applied in the previous study [51]. It was found that the application of the honeycomb sandwich plate absorbed a large amount of impact energy (49%) compared to specimens without the honeycomb plate. There has been no available research investigating dry joints under impact loads in the open literature yet. Therefore, it is imperative to investigate the performances of dry RC joints subjected to impact load in order to apply such joints in structures that impact load is a design loading case.

As mentioned previously, this project aims to propose a new joint type that can yield multiple advantages, such as construction efficiency, resilience, and environmental sustainability and multi-hazards resistance. The project was divided into three stages. The first stage successfully proposed a new dry joint type with concrete-end-plate (CEP) and CFRP bolts which are corrosion resistance, simple to construct, easy to replace the damaged components, and are cost-effective. The performances of the proposed dry joint under cyclic loading have been studied and their potentials for application in structures in seismic regions have been demonstrated [19, 44, 141]. An empirical model to design this new dry joint was also proposed in Chapters 3 and 4 [24, 46]. This chapter carried out pendulum impact tests to investigate the performances of the proposed joint subjected to impact load and compare the responses with conventional monolithic joints. In the chapter, the effectiveness of using two types of fibres, namely steel fibres (SyFs) and synthetic fibre (StFs) on enhancing the performances of the joints to resist impact loads was also investigated. It is worth

mentioning that this is the first study of the impact responses of fibre reinforced RC monolithic and dry joints with GFRP reinforcements and GFRP bolts subjected to impact loading.

6.2 Experimental program

In this chapter, six 1/3-scale beam-column joints of an eight-floor building [19] were designed and cast at the structural laboratory in Curtin University. These six scaled specimens, including 3 monolithic joints (namely M1-NF, M2-1SyF-48, M3-1StF-35) and 3 dry joints (namely P4-NF, P5-1SyF-48, and P6-1StF-35) were labelled based on their characteristics as presented in Table 6-1. The first term denoted the joint types (M-monolithic and P-precast). The second term denoted the volume fraction of fibres (i.e. 1%) and fibre types (**synthetic** vs **steel** fibres). The fibre length was presented in the last term. In this chapter, only one specimen was used to investigate one parameter due to its cost and complexity of impact tests. A pendulum impact system was used to generate impact forces onto the beams. Details of the specimen designs, test setups, and material properties are described in the subsequent sections.

Table 6-1. Descriptions of the prepared specimens

Names	Joint Types	Volume Fraction of Fibres, V_f (%)	Fibre Types	Fibre Length (mm)
M1-NF	Monolithic	N/A	N/A	N/A
M2-1SyF-48	Monolithic	1	Synthetic	48
M3-1StF-35	Monolithic	1	Steel	35
P4-NF	Dry	N/A	N/A	N/A
P5-1SyF-48	Dry	1	Synthetic	48
P6-1StF-35	Dry	1	Steel	35

Note: N/A = Not applicable.

6.2.1 Details of beam-column joints and test setup

Details of the geometries and reinforcements are shown in Figs. 6-1 and 6-2. Since there were no specific standards to design beam-column joints under impact loading, this chapter adopted the design from the previous studies under cyclic loading [19, 24, 46] with improvement in the design of all the specimens. While the prior studies used 150-mm beam width, the beam width in the present chapter was 200 mm, which

ensured that the beams of precast joints were easily fabricated to the column due to the same width. The monolithic joints had similar dimensions of the precast joints to enable relatively valid comparisons between these two joint types, except the CEP in the precast specimens. The dimensions of the beams were 200-mm width, 150-mm height, and 820-mm length whereas those of the columns were 200, 200, and 1280 mm, respectively. The beams of the dry joints included two parts, namely Beam A ($200 \times 150 \times 620 \text{ mm}^3$) and CEP ($200 \times 350 \times 200 \text{ mm}^3$), as illustrated in Figs. 6-1 and 6-2. The dimensions of the CEP were larger than those of Beam A to accommodate the bolts and nuts. The strong column-weak beam philosophy was adopted to design the exterior beam-column joints. Furthermore, steel reinforcements used in the previous studies [19, 24, 46] were replaced by GFRP reinforcements in this chapter. Considering the mechanical properties of GFRP reinforcements were different from those of steel reinforcements, ACI 440.1R-15 [152] was adopted when designing all the specimens. It is noticed that the shear strength of the GFRP bars is significantly lower than that of steel bars and shear failure usually governed the main failure of specimens under impact tests [48, 49]. As a result, the spacing of the spiral stirrups in the column and Beam A was reduced from 70 to 35 mm, compared to the spacing of the individual stirrups in the previous studies [19, 46]. Meanwhile, the spacing of spiral stirrups (70 mm) in the CEP was kept the same as in the previous studies to ensure a reasonable comparison in the result and discussion sections. Moreover, two kinds of fibres (i.e., StFs and SyFs) were also utilized as an attempt to improve the joint performances. Details of these fibre types are presented in Section 6.2.3.

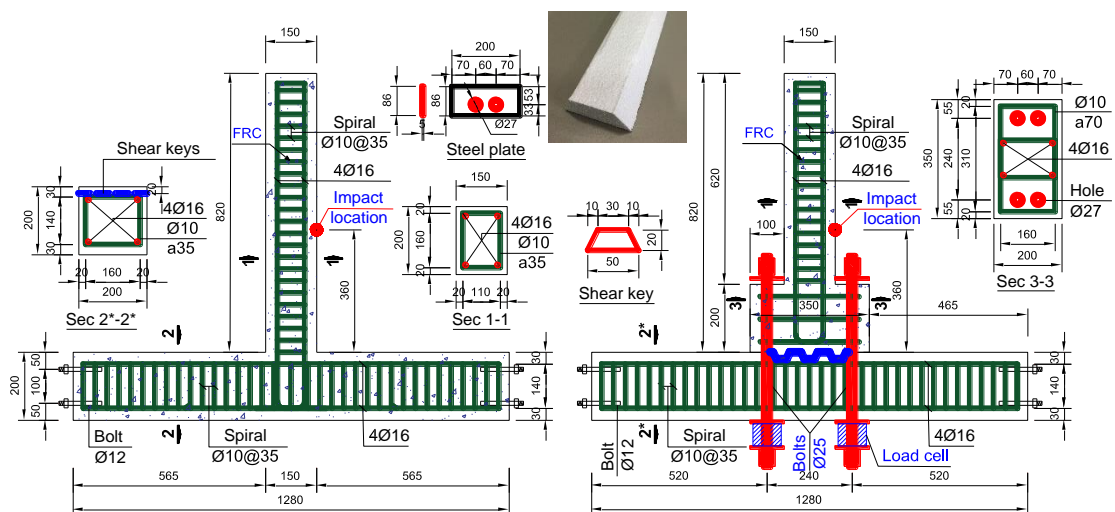


Fig. 6-1. Details of monolithic specimen (Left) and precast specimen (Right) (unit: mm).

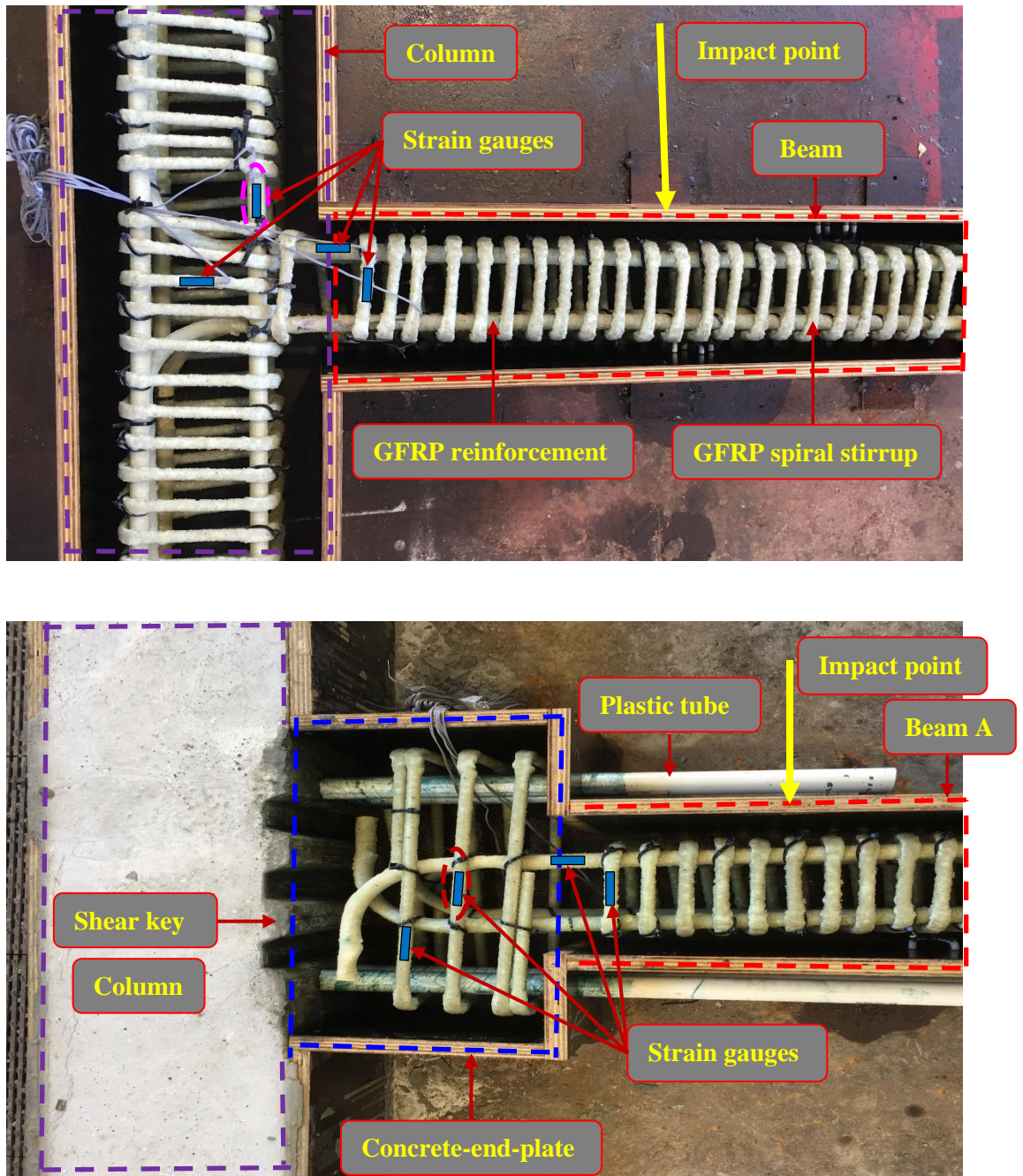


Fig. 6-2. Details of reinforcements, shear keys, and the test specimens.

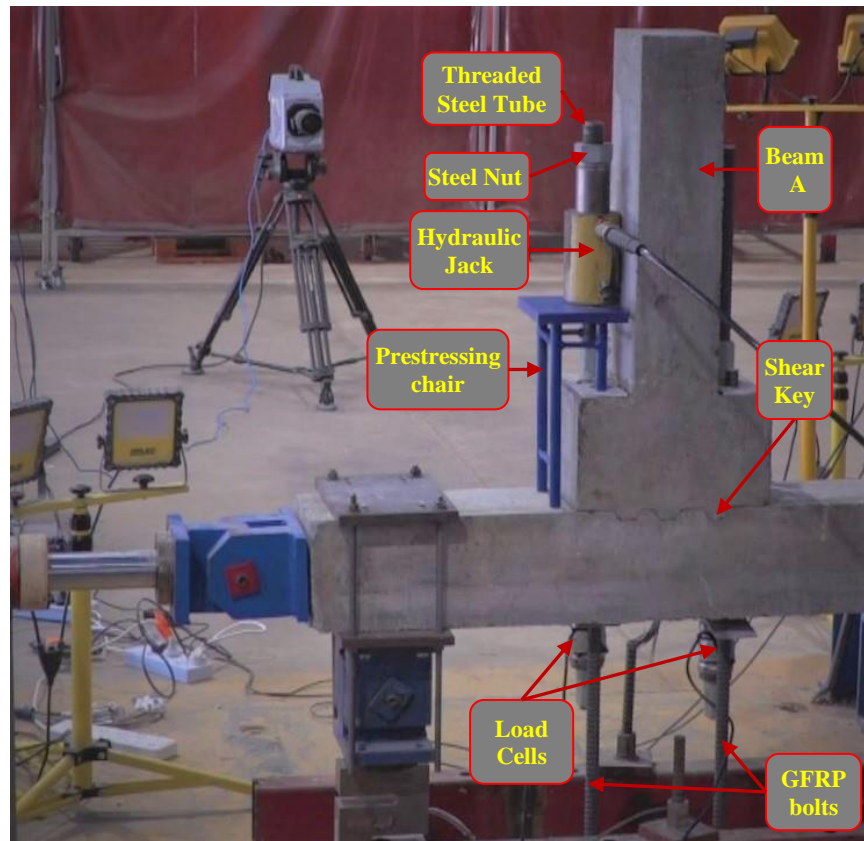


Fig. 6-3. Setup for applying prestress for GFRP bolts.

The beam was connected to the column using 4 GFRP rock-bolts with a diameter of 25 mm. GFRP bolts were applied with a higher prestress force up to 30 kN compared to only 6.5-10.5 kN in the previous studies [19, 24, 46]. The disadvantage of not being able to apply large prestress force for FRP-bolts was resolved with the design of a chair and a hydraulic jack, as illustrated in Fig. 6-3. The prestress force on the GFRP bolts was measured by load cells.

6.2.2 Pendulum impact system and data acquisition system

Fig. 6-4 shows the pendulum impact system and all measuring equipment used in the impact tests. The pendulum impact system consists of three parts including the hinge support, pendulum arm, and impactor. A square hollow steel tube (75x75x6 SHS C450) was selected to make the pendulum arm. A large steel frame was rigidly fitted on a strong floor to support all the test equipment. The top of the pendulum arm was connected to the frame with the hinge support while an adjustable 500 kg-steel impactor was placed at the bottom of the pendulum arm. The impactor head was made

of a steel cylinder of diameter 50 mm with a hemispherical nose of diameter 1 m. The length of the pendulum arm was 2,265 mm. A 360° protractor was used to measure the angle when lifting the impactor to the desired height by a 1.5-Ton winch. Afterwards, the impactor was released to collide the beam at the height of 360 mm from the column. The impact point was chosen to be the nearest to the joint area so that the most unfavourable case of joint performances could be investigated. The impact velocity in the tests was gradually increased till the specimen failure. Fig. 6-5 illustrates the impact velocities and the corresponding angles of the pendulum arm progressively applied in the tests on different specimens. After each impact, the impactor was pulled back immediately to avoid subsequent impacts on the beam.

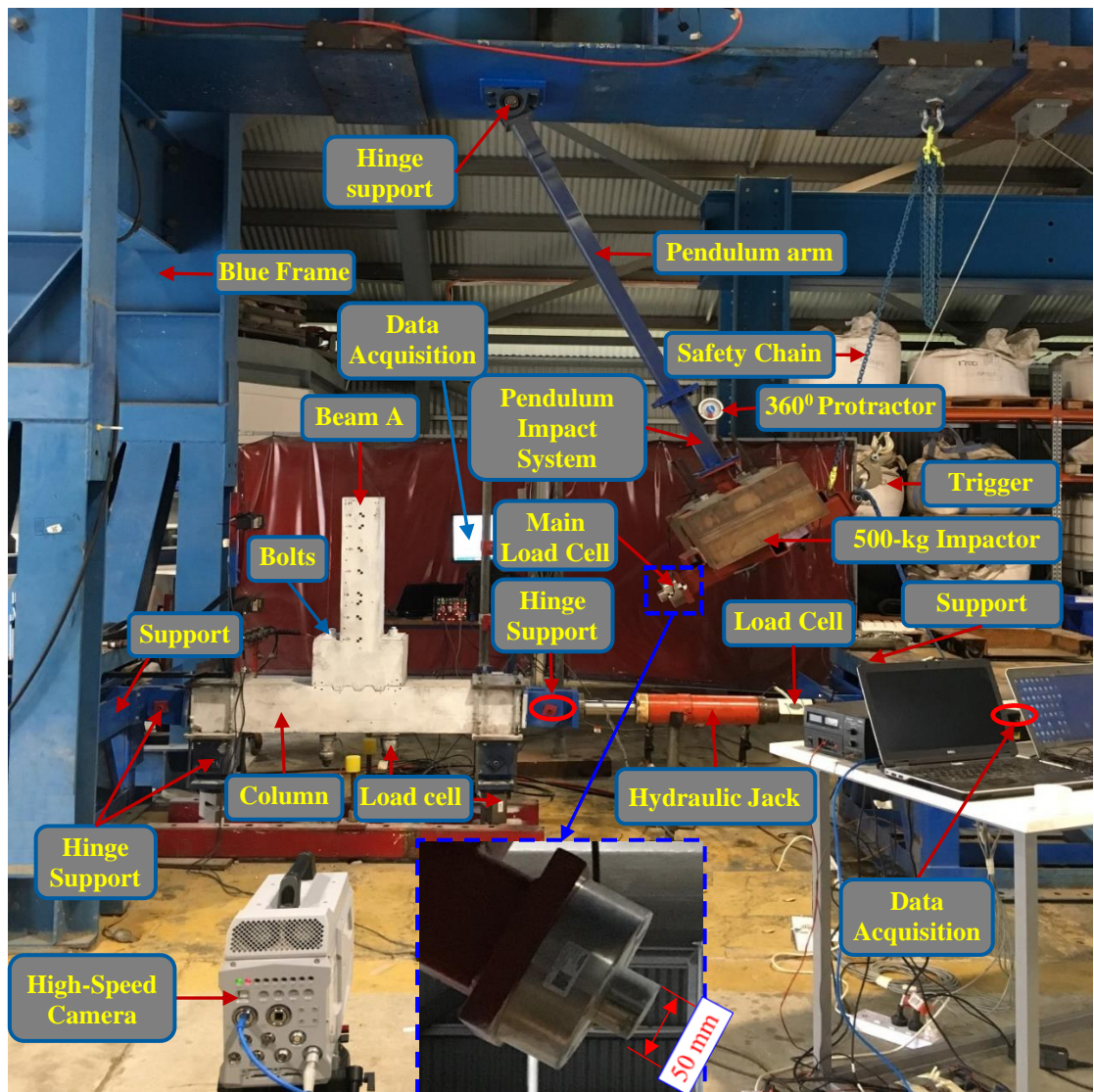
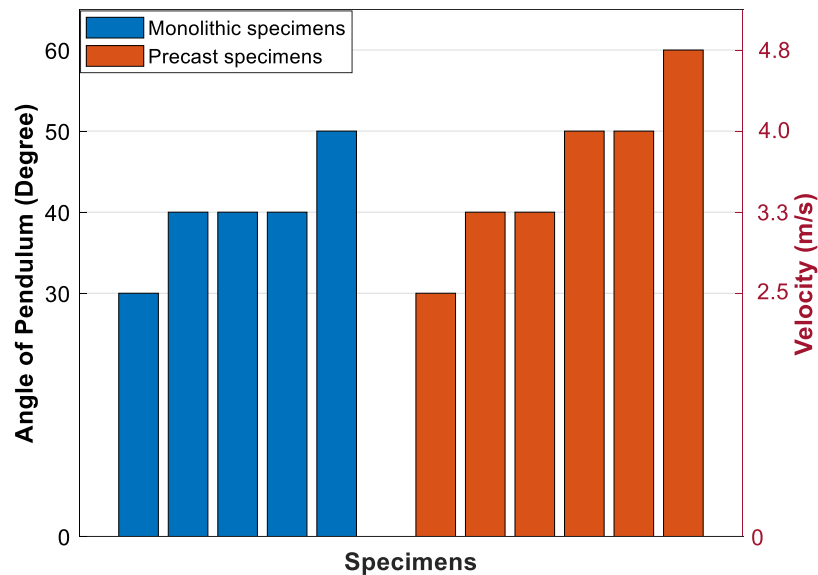


Fig. 6-4. Test setup for pendulum impact tests.

A 500-kN dynamic load cell was attached to the pendulum system to measure the impact forces. The calibration factor of this load cell was 2,080 Ton/volt. Five strain gauges (SGs) were utilized to monitor the strain of reinforcements and concrete on the CEP (see Fig. 6-2). The dynamic load cell and all SGs were connected to a data acquisition system with a sampling rate of 50 kHz. Other five load cells to measure the reaction forces at the top and bottom of the column, axial tensile forces in the GFRP bolts, and axial force on the column were connected to another data acquisition system with a sampling rate of 5 kHz (see Fig. 6-4). A prestress force of 30 kN was applied to all GFRP bolts. Meanwhile, according to the previous study of Antonopoulos and Triantafyllou [79], applying high axial force on the column top improved the capacity of the joints. Therefore, a low axial force of 65-kN ($\approx 0.03 A_c f_c$) was adopted in this chapter to minimize the beneficial effects of axial force on the capacity of the joints.



Notes: Bars indicate the angle sequence (i.e., 30°, 40°) of the pendulum impact tests in this chapter.

Fig. 6-5. Impact velocity in the tests.

A high-speed camera (HSC) was used to monitor the displacement and failure progress of the beam-column joints. This camera was set to capture 20,000 frames per second. Tracking points were glued to the dynamic load cell and the surface of the beams with

a spacing of 100 mm to track their velocity and displacement. To provide intensive light for the HSC, 6 LED lights were used in the tests. After finishing the tests, a digital image correlation software (DIC) was utilized to process the data from videos of the HSC.

6.2.3 Material properties

GFRP reinforcements were sponsored by Pultrall Inc [151] for this study. The size of the longitudinal reinforcements and spiral stirrups were #5 (17.1 mm) and #3 (10.5 mm), respectively. More details of the GFRP reinforcements are tabulated in Table 6-1. Table 6-2 presents the properties of two fibre types (i.e., Synthetic Vinyl Polypropylene fibres (SyFs) and hook-ended (3D65/35BG) steel fibres (StFs)). These two types of fibres were respectively sponsored by BarChip Pty Ltd [172] and BOSFA Pty Ltd [173]. Ready-mixed concrete was sorted from a local supplier for casting all the specimens. The compressive strength and tensile strength of plain concrete at 28 days were 59 MPa and 4.2 MPa, while the corresponding strengths of StF reinforced concrete (SFRC) were 63 MPa and 7.3 MPa, respectively. Lower compressive strength (62.5 MPa) and tensile strength (6 MPa) were recorded on SyF reinforced concrete (SyFRC), compared to SFRC. For SFRC and SyFRC mixtures, 1% volume fraction of fibres were added to the ready-mixed concrete and mixed again by a concrete mixer in the lab before pouring into the specimens. GFRP bolts and nuts were supplied by Bluey Pty Ltd [150]. The maximum capacity of GFRP bolts was governed by the maximum strength of the nuts. For example, the ultimate load of GFRP thread bars was more than 350 kN while the corresponding number of the nuts was only 70 kN. As a result, the nominal strength of the bolt-nut was 70 kN and the prestressing force of 30 kN was used for these specimens. More information provided by the manufactures is summarized in Tables 6-2, 6-3, and 6-4. The photos of StFs, SyFs, GFRP bolts, and GFRP spiral stirrups are shown in Fig. 6-6.

Table 6-2. GFRP reinforcement properties.

Bar sizes	Nom. dia. (mm)	F_u (kN)	f_u (MPa)	F'_u (kN)	f'_u (MPa)	Q_{sh} (kN)	F_{sh} (MPa)	E_s (MPa)	Area (mm ²)	Notes
#3	10.5	89.7	1259.2	42.3	593	33.6	235.8	53485	87	Stirrups
#5	17.1	268.9	1358.3	132.4	668.8	82.5	208.5	53819	230	Longitudinal reinforcements

Note: F_u and f_u = Load at the break and tensile strength of the straight portion, respectively.
 F'_u and f'_u = Load at the break and tensile strength of the bent portion, respectively.
 Q_{sh} and f_{sh} = Load at the break and transverse shear strength, respectively.

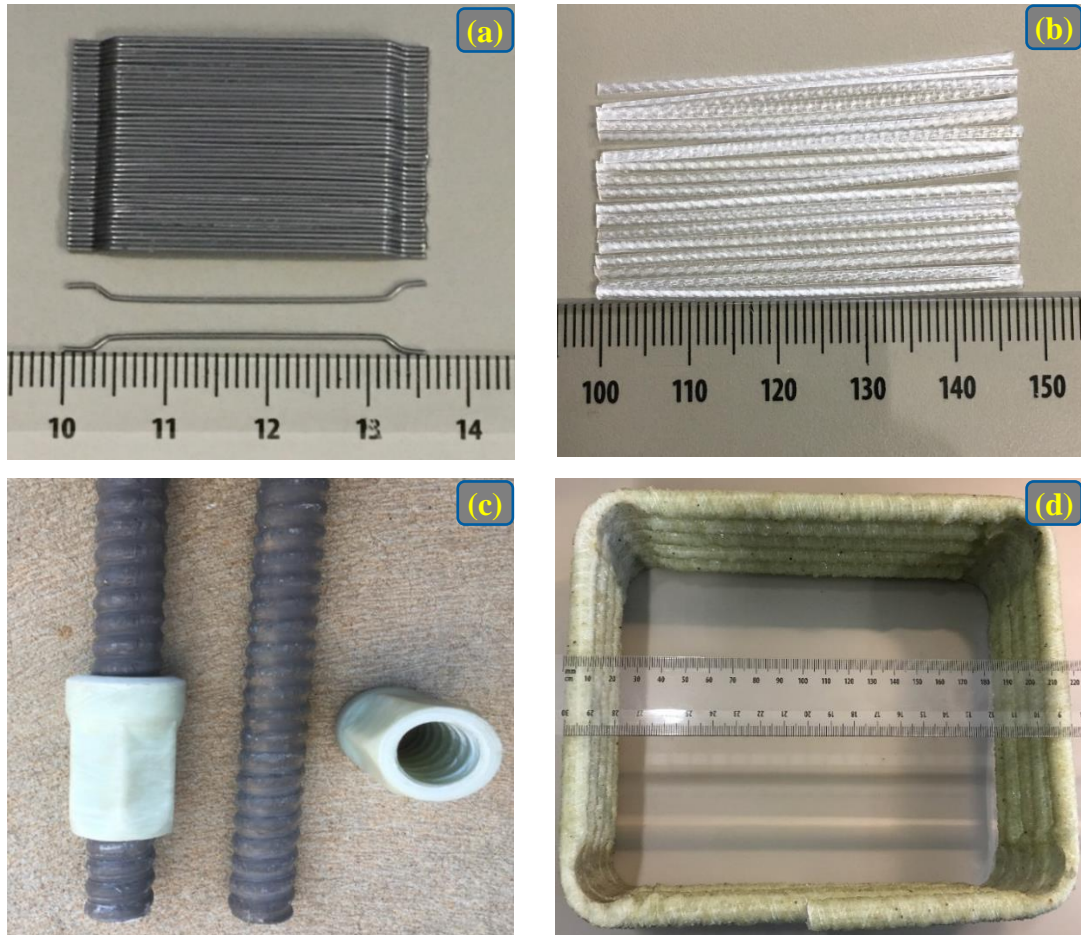


Fig. 6-6. Photos of (a) StFs; (b) SyFs; (c) GFRP bolts and nuts; and (d) GFRP spiral stirrups.

Table 6-3. Details of two types of fibres.

Fibres	Diameter (mm)	Length (mm)	Tensile Strength (MPa)	Density (g/cm ³)	Modulus (GPa)
Steel fibre	0.55	35	1,345	7.8	210
Synthetic fibre	0.85	48	640	0.9	12

Table 6-4. Details of GFRP bolts and nuts.

Names	Diameter	Tensile Stress Area	Shear @90°	Shear @50°	Ultimate Load	Elastic Modulus	Weight
	(mm)	(mm ²)	(kN)	(kN)	(kN)	(GPa)	(kg/m)
Bolt	25	346	170	345	≥ 350	60	0.9
Nut	25	N/A	N/A	N/A	70	60	N/A

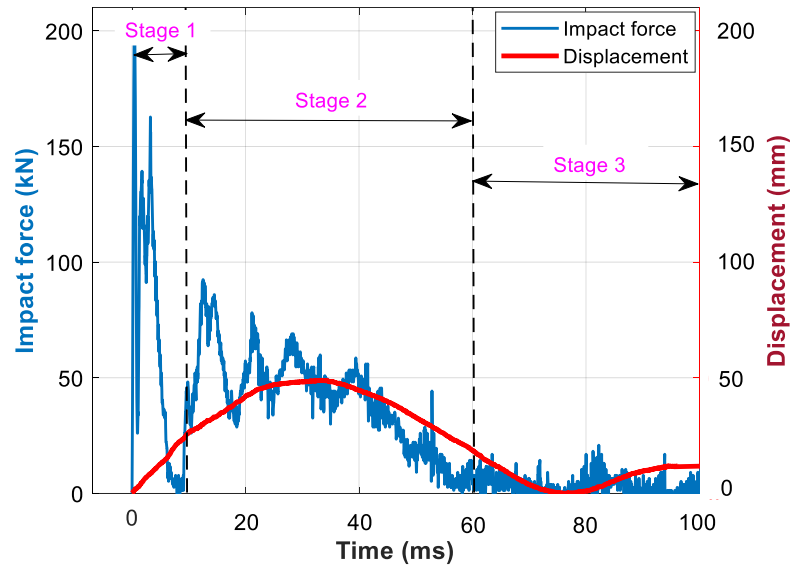
Note: N/A = Not applicable.

6.3 Experimental results and discussion

This section presents the performance of two joint types and the effects of two kinds of fibres under impact loading, followed by the discussions with respect to the deformation, crack development, and failure modes. Other important parameters, such as the impact forces, reaction forces, displacements, and energy dissipation are also presented.

6.3.1 Comparisons between monolithic joint and proposed dry joint

The impact performance of the proposed dry joint under impact loading will be presented through comparisons with the corresponding monolithic joint. For more convenience in the data analysis, the dynamic behaviour of all the specimens in this chapter was divided into three main stages, as shown in Fig. 6-7. Stage 1 was determined when the dynamic load cell stroke the beam and reached the peak impact force. Afterwards, the impact force reduced to almost zero. The second stage was defined from the end of Stage 1 to the moment when the load cell collided with the beam again and the impact force increased. After that, the impact force decreased again to zero. Stage 3 commenced when the beam was under free vibration and then rested in the stationary position.



Note: The curves were plotted from Specimens M1-NF at 3.3 m/s

Fig. 6-7. Typical impact responses of joints with 3-stage classification at the impact point.

6.3.1.1 Deformation of beams and crack development

The beam displacement of Specimens M1-NF and P4-NF at the impact velocity of 2.5 m/s was almost similar as illustrated in Fig. 6-8. For brevity, hereafter the impact velocity is briefly written. For example, the impact velocity of 2.5 m/s was denoted as 2.5 m/s. These specimens showed local response dominated with the large displacements at the impact point (360 mm), which were observed in Specimens M1-NF and P4-NF at 2 ms and 2.5 ms, respectively. This phenomenon was different from the displacement of the specimens in the previous studies focusing on cyclic loading [19, 24, 46]. A horizontal crack appeared at 0.8-1.1 ms on the rear face of the beam behind the impact point after the loading head collided the beam. The inertial forces of the beam, which were distributed throughout the beam body, resisted the lateral displacement of the beam as soon as the loading head touched the beam surface and the beam tended to move. Therefore, the above horizontal crack on the rear face of the impact point was formed owing to the bending of the beam which induced the large displacement at the impact point. When the impact force overcame the inertial force, the displacement of two joint types shifted to the first mode of the cantilever beam with the largest displacement at the free end from 5 ms. Afterwards, the beams had a tendency to rebound to its original position after the end of the impact process (see

Fig. 6-8). The speed of the beams' rebounding to their original position depended on the natural frequency, damage level and interaction with the impactor. A similar displacement response was observed for all the other specimens and was not presented here for brevity.

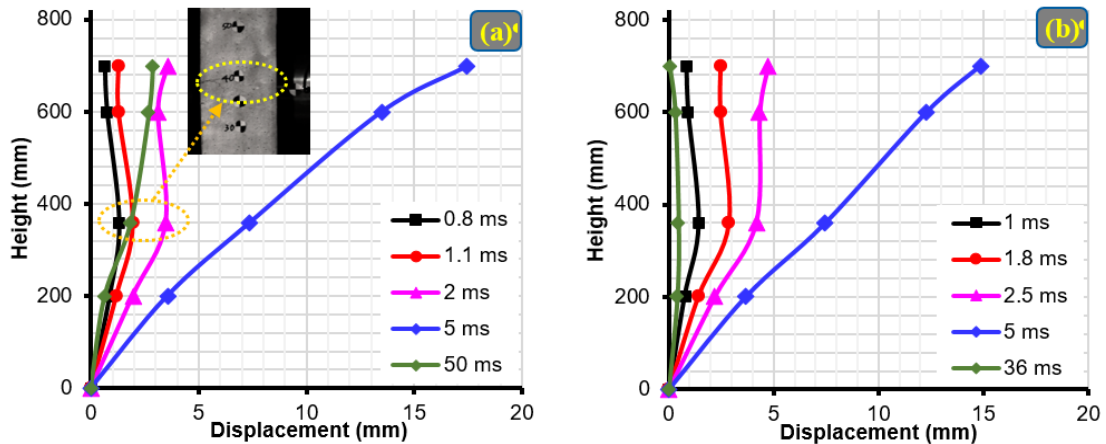


Fig. 6-8. Beam lateral displacement of (a) Specimens M1-NF and (b) P4-NF at 2.5 m/s impact.

In general, the trend of crack development of the two joint types was similar. Most of the main cracks appeared in the first and second stages of the impact process. The cracks occurred firstly at the impact point and then propagated to the fixed-end and joint area. The horizontal crack occurred immediately on the rear face of the beam at the impact point ($t = 0.8\text{-}1.1$ ms) because of the local bending. Afterwards, when the impact force overcame the inertial force, the top of the beam started to deflect to the left and the beam was bent due to the effects of the impact force. The joint performance shifted from the local responses to the global behaviour which caused the flexural cracks at the fixed-end and inclined cracks at the joint area.

Under 2.5 m/s impact, the first cracks at the impact point of Specimens M1-NF and P4-NF were similar, which were observed at 1.1 ms and 0.8 ms, respectively. However, the second cracks occurring at the fixed-ends were different. For Specimen M1-NF, a horizontal flexural crack occurred at the fixed-end whereas an inclined crack was observed in the joint area of Specimen P4-NF (Figs. 6-A1(1.5ms) and 6-A1(1.7 ms) in the appendix). This phenomenon was attributed to the effects of the lever arm. The lever arm from the impact point to the fixed-end of the monolithic specimen (360 mm) was longer than that of the precast specimen (160 mm) because of the CEP. This

led to a higher bending moment causing the horizontal flexural cracks at the fix-end of Specimen M1-NF. For Specimen P4-NF, due to the closer distance from the impact point to the fixed-end, shear stress reached the ultimate shear strength before flexural stress reached the ultimate flexural strength. Consequently, the shear stress could potentially cause the above-inclined cracks at the joint area. From 9.3 to 9.6 ms, more inclined cracks developed on the joint areas of both the joints. However, the directions of these inclined cracks were different, as reflected by the green cracks of Figs. 6-A1(9.3 ms) and 6-A1(9.6 ms) in the appendix. The inclined cracks in the joint area of Specimen M1-NF were a result of the diagonal strut mechanism as explained in the previous studies [46, 174] whereas shear and tensile stress caused the inclined cracks of Specimen P4-NF [19]. Additionally, no concrete crushing was observed on Specimen P4-NF while concrete crushing occurred at the fixed-end of Specimen M1-NF at 11.9 ms due to the larger displacement of the beam of Specimen M1-NF and thus higher compressive stress at the fixed-end, compared to that of Specimen P4-NF.

When the velocity of the impactor increased to 3.3 m/s, more shear cracks on Beam A, which occurred initially from the edges of the loading head surface 45° toward the fixed end, were observed on Specimen P4-NF, compared to the shear cracks on the beam of Specimen M1-NF. The reason for this difference will be explained in the next section of failure modes (Section 6.3.1.2). For Specimen M1-NF, a yellow crack on the face of the concrete crushing zone appeared at 12.8 ms, and then it developed to 200-mm length of the beam (Figs. 6-A1(16.1 ms) and 6-A1(31.3 ms) in the appendix). This crack induced spalling of concrete in the concrete crushing zone at the second impact with the velocity of 3.3 m/s (denoted as $3.3v_2$ m/s). Due to the significant flexural bending, the beam of Specimen M1-NF was bent and rotated with the left corner crushed against the column. As a result, the above crack indicated in yellow in the figure was generated. It is interesting to note that although large displacement was observed at the beam top (e.g., up to 103 mm (drift ratio = 12.9%) of Specimen M1-NF subjected to the 3.3 m/s impact), the beam of both the specimens almost rebounded back to its original position after the 2.5 m/s and 3.3 m/s impacts due to the linear behaviour of GFRP reinforcements and GFRP bolts. It implies that the use of GFRP reinforcements and GFRP bolts did not cause brittle failures of the joints under impact loading and they possess the good recentring capability. Both the specimens could survive the second 3.3 m/s impact. The second 3.3 m/s impact did not generate new

cracks but existing cracks were further extended and widened, which led to the large damage of the specimens after the second 3.3 m/s impact. The crack development of these specimens corresponding to the second 3.3 m/s impact will be presented in Section 6.3.1.2.

6.3.1.2 Crack patterns and failure modes

The maximum recorded tensile force (56 kN) of GFRP bolts in Specimen P4-NF did not reach their nominal tensile strength of the nuts (70 kN). Therefore, no GFRP bolt failure was observed during the tests. It is noted that the shear keys were adopted for all the precast specimens. Consequently, a combination of the shear keys and friction between two surfaces effectively mitigated the slips between the beam and the column, although there were no corbels or brackets in this dry joint. No failure on the shear keys was observed during the tests. In addition, there have been no analytical models to estimate the ultimate capacity of beam-column joints under impact loading in the open literature. Hence, there is neither definition nor criterion to quantify the failure of RC beam-column dry joint yet. This study based on the maximum displacement, residual displacement, and crack observation during the test classified the failure modes into four damage levels including minor damage (I), moderate damage (II), severe damage (III) and failure (IV). Level I was identified with minor cracks at the impact point and the fixed-end. Level II was associated with the concrete crushing, flexural crack at fixed-end and some minor cracks at the joint area. Level III corresponded to major concrete spalling, concrete crushing and shear damage at fixed-end. Large displacement and residual displacement were recorded at this level. Level IV was identified when the beam could not rebound back to its original position with a significant residual displacement. Fig. 6-9 illustrates the critical damage patterns of both the joint types under the impact. For comparison, damage modes of the similarly designed joint under cyclic loading obtained in previous studies [19, 46] are also shown. In general, both Specimens M1-NF and P4-NF showed severe damage (Level III) when subjected to the second 3.3 m/s impact.

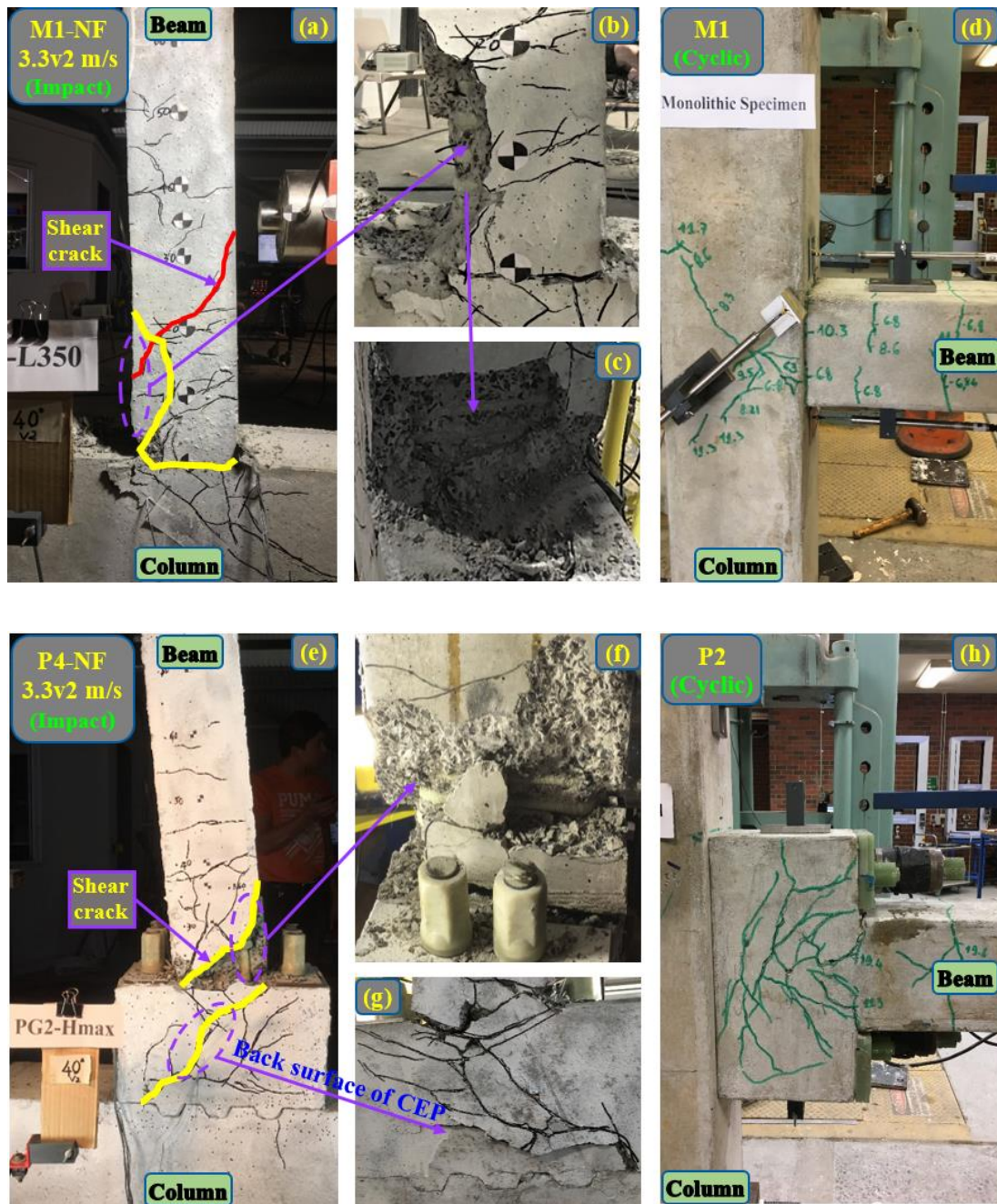


Fig. 6-9. Comparison of damage modes (Specimens M1-NF vs P4-NF; Impact loading vs cyclic loading).

In general, the main failure modes of the monolithic joint under impact and cyclic loading were relatively similar while those of the dry joints were quite different. For the monolithic joint, the concrete crushing and flexural cracks at the fixed-end governed the main failure patterns of this joint type under impact and cyclic loading. The monolithic specimen failed at the beam when subjected to either impact or cyclic loads, as shown in Figs. 6-9(a) and 6-9(d). However, some differences in the

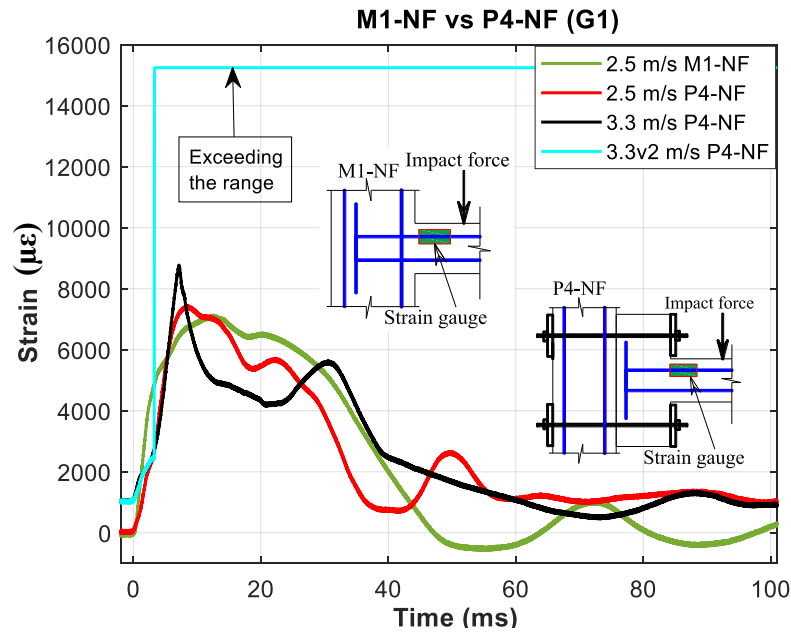
performance of the monolithic joint under impact and cyclic loading were observed regarding the crack types and damage levels. As reported in the previous study [46], no shear cracks occurred on the beam during the cyclic test while a shear crack (red line) was observed from the impact point to the fixed-end, as depicted in Fig. 6-9(a). It means that the shear mode also affected the damage of the monolithic specimen, although the beam was designed with very strong shear resistance (35-mm spacing of stirrup). In addition, a large vertical crack indicated in yellow, which appeared at the compressive zone, induced the intensive spalling of concrete in this area (see Figs. 6-9(a), 6-9(b), and 6-9(c)). This crack was induced by the reflected tensile stress wave in the beam generated by the impact load. A comparison between Figs. 6-9(a) and 6-9(d) reveals that the monolithic joint under impact loading showed severe local damage with more concrete crushing and spalling, compared to that under cyclic loading. This phenomenon is attributed to the shear dominant mechanism and large deformation of the beam, as well as impact load induced stress wave propagation [164, 175]. In addition, the compressive strain of the equivalent strut in the joint area was quite small ($-284 \mu\epsilon$) which did not reach the ultimate compressive strain of concrete. Therefore, no failure due to the compression strut occurred at the joint area of Specimen M1-NF.

By contrast, the failure modes of the dry joint under impact and cyclic loading showed some discrepancies. For example, although the crack patterns on the CEP in the cyclic and impact tests were analogous, intensive shear damage was only observed on the beam under impact loading. The intensive impact force caused this local shear damage around the impact point [164]. In addition, the tensile strain of concrete at the middle zone of the CEP ($618 \mu\epsilon$) exceeded the ultimate tensile strain of concrete ($116 \mu\epsilon$). It is noted that the ultimate tensile strain of concrete was determined based on its tensile strength (f_{ct}) and Young's modulus [46]. It means the dry joint failed at the joint area under cyclic loading while a combination of joint and beam damage was observed under impact loading.

Figs. 6-9(a) and 6-9(e) show the main damage modes of the monolithic vs precast joints under impact loading. More severe damage above the fixed-end of Specimen P4-NF was observed during the test, compared to that of Specimen M1-NF. This phenomenon could be explained by two reasons: (1) The cross-section of the CEP

(200x350 mm²) was larger than that of the beam (200x150 mm²) so the CEP was stiffer than the beam. (2) The beam length from the impact point to the fixed-end of Specimen P4-NF was shorter than that of Specimen M1-NF because of the existence of CEP. The above two reasons led to higher stress concentration along the shorter beam of Specimen P4-NF, compared to that on the longer beam of Specimen M1-NF. As a result, severe damage appeared on the beam of Specimen P4-NF. The above explanation was well supported by the data of SGs which were bonded on the stirrups close to the fixed-end. The tensile strain in this stirrup of Specimen P4-NF (6,391 $\mu\epsilon$) was higher than that of Specimen M1-NF (3,904 $\mu\epsilon$) at 3.3 m/s impact. It is attributed to higher shear stress concentrated at the fixed-end of Specimen P4-NF, compared to that of Specimen M1-NF. This phenomenon only occurred on the beam under impact loading due to the local stress wave which appeared around the impact point [164]. The impact forces induced the shear cracks on the beam of both joint types, as illustrated in Figs. 6-9(a) and 6-9(e). Therefore, it can be concluded that the shear damage needs to be considered when beam-column joints are designed to resist impact loading.

Fig. 6-10 shows the data of SGs attached to the longitudinal reinforcements. The maximum strain of the reinforcements in Specimens M1-NF and P4-NF at 2.5 m/s and 3.3 m/s impacts was 7,107 $\mu\epsilon$ and 8,775 $\mu\epsilon$, respectively. These values reached only 35% of the nominal strain at the break strength (25,238 $\mu\epsilon$). It is noted that the above nominal strain was determined based on the information provided by the supplier (Table 6-2). The strain of GFRP reinforcements under impact test was approximately 2.2 times higher than that of steel reinforcements under cyclic tests [46]. It is attributed to the lower elastic modulus (53 GPa) of GFRP reinforcements, compared to that of steel reinforcements (210 GPa). The above results indicated that there was no failure of the longitudinal reinforcements in the beam of Specimens M1-NF and P4-NF up to 3.3 m/s impact. In addition, the strain of stirrups at the joint area did not reach their nominal strain of 23,543 $\mu\epsilon$ either. Therefore, the main damage of these two specimens was not governed by GFRP reinforcements but concrete. No sign of failure of GFRP reinforcements was observed during and after the tests.



Note: Nominal strain at the break strength of longitudinal reinforcements (a) the straight portion: 25,238 $\mu\epsilon$, and (b) bent portion: 12,426 $\mu\epsilon$.

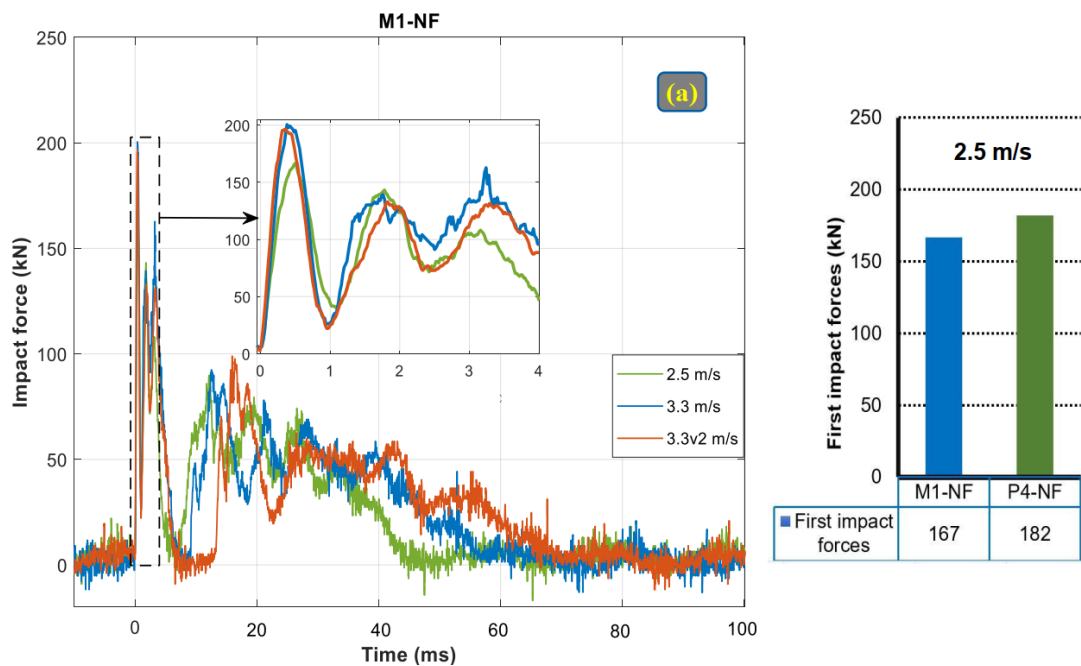
Fig. 6-10. Strain of longitudinal reinforcements on the beams of Specimens M1-NF and P4-NF.

6.3.1.3 Impact forces and reaction forces

The impact forces and reaction forces are critical parameters to evaluate the joint performance under impact loading. Fig. 6-11 illustrates the impact force-time histories of the monolithic and dry joints. The peak impact forces of Specimens M1-NF and P4-NF occurred at the first stage of the impact process, as described in Section 6.3.1.

As shown in Fig. 6-11(a), the impact force increased sharply after the impactor struck on the beam of Specimen M1-NF to the peak value of 167 kN at approximately 0.5 ms. When the impact velocity increased from 2.5 m/s to 3.3 m/s, the peak impact force also increased from 167 kN to 201 kN. Nevertheless, if the specimen was impacted the second time with the impact velocity of 3.3 m/s, the peak impact forces were almost unchanged, i.e. 201 kN in the first 3.3 m/s impact and 197 kN in the second 3.3 m/s impact. This observation indicated that the peak impact forces depended on the velocity or impact energy of the pendulum impact system. The finding was also consistent with the results of the previous study [166]. It is worth noting that there were three peak impact forces (see Fig 6-11) in the first stage which also were observed in the previous studies [166, 170, 176]. The first peak impact forces of Specimen M1-

NF and P4-NF were roughly the same. For instance, the first peak impact forces of Specimen M1-NF at 2.5 and 3.3 m/s were 167 and 201 kN whereas those of Specimen P4-NF were 182 and 203 kN, respectively. It is because the peak impact force is governed by the local stiffness [163] while these two specimens had the same section and material at the impact points. In addition, the second peak impact force of the precast specimen as shown in Fig. 6-11 was roughly the same as the first ones while the second peak force of the monolithic specimen was smaller than the first ones. This is attributed to the influence of global stiffness. After the first peak impact force, the stress wave propagated toward the supports and thus the global stiffness affected the second peak. The global stiffness of the precast specimen was greater than that of the monolithic specimen because of the great stiffness of the CEP [19, 46]. Therefore, the second peak impact force of the precast specimen was greater than that of the monolithic specimen. The third peak impact force was the lowest in the first stage because the impact energy and joint stiffness decreased after the first and second peaks. After reaching the third peak impact force, the impact force reduced sharply marking the end of the first stage of the impact process. The second stage began when the impact force increased again owing to the second collision between the loading head and the beam. The duration of this second stage was approximately 37-48 ms with 99-kN peak impact force at the second 3.3 m/s impact. After Stage 2, the impact forces gradually reduced to zero and the beam started to vibrate freely.



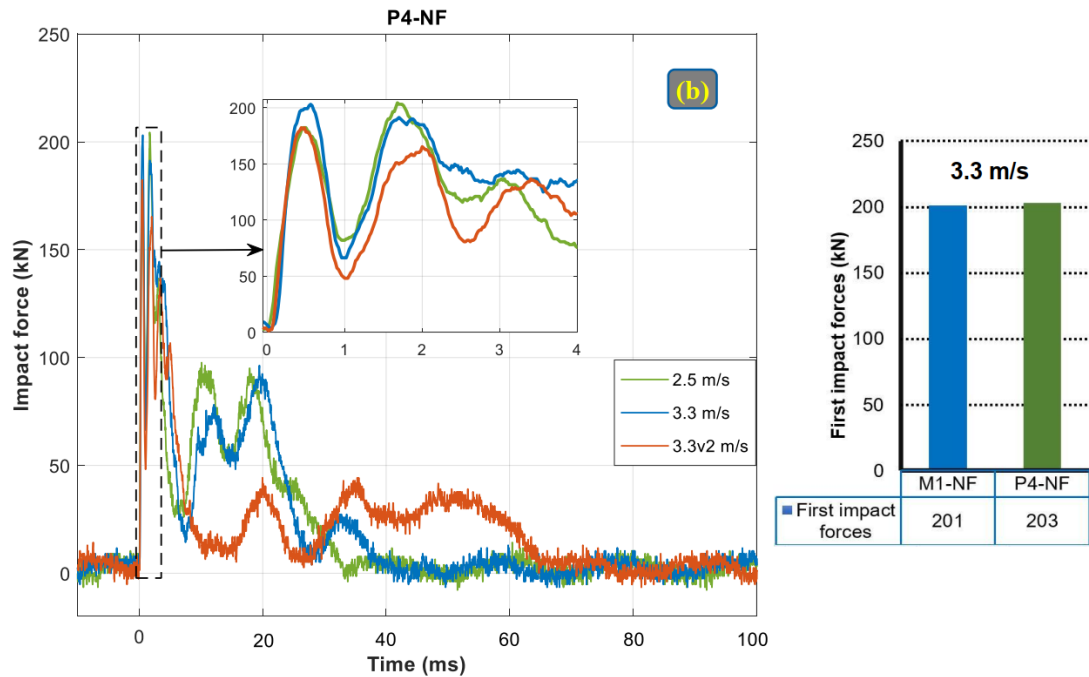


Fig. 6-11. Impact force-time histories of Specimens (a) M1-NF and (b) P4-NF.

Fig 6-11(b) shows the impact force-time histories of the dry joint (P4-NF). The first peak impact force (182 kN) at 2.5 m/s was lower than the first peak impact force (203 kN) at 3.3 m/s because of lower impact energy. After that, although the impact velocity remained unchanged at the second impact with the velocity of 3.3 m/s, the first peak impact force reduced from 203 kN to 182 kN. It is attributed to severe damage of the beam-column joint in the first 3.3 m/s impact. Hence, the stiffness of Specimen P4-NF decreased and caused the above reduction of the first peak impact force in the second impact. In addition, three peak impact forces were also observed in the first stage of the impact process as Specimen M1-NF. For the proposed dry joints, the second and third peak impact forces might be affected by the global stiffness and thus the prestressing force of the bolts. A 30-kN prestress force was applied to all the GFRP bolts to connect the beam and the column. After the dynamic load cell hit the beam, the beam deflected and there was a joint opening of approximately 0.5-1.5 mm. The GFRP bolts provided the resistance to the force and pulled the beam back to its original position. It means the rebound velocity of the beam was in the opposite direction with the impactor velocity, resulting in a higher second peak impact force, compared to the first peak impact force. Hence, a conclusion could be made that the local stiffness mainly affected the first peak impact forces whereas the second and the third peak impact forces were governed by the global stiffness and the prestress bolts.

Fig. 6-12 shows the relationship between the impact forces and reaction forces of Specimens M1-NF and P4-NF under impact loading. It is noted that the impact force and reaction forces were measured by two different computers, thus, the time lag cannot be determined and it is removed from the figure. Although Specimens M1-NF and P4-NF exhibited a similar peak impact force, the peak reaction forces were different (31 vs 54 kN at 2.5 m/s impact), which indicates the distributed inertia forces of the two specimens were very different. Under static loads, the reaction forces of the two specimens would be similar given the same applied load. The peak impact forces of 167 and 182 kN were respectively recorded for Specimens M1-NF and P4-NF at 2.5 m/s impact. If the time lag is removed and the inertia force is ignored, an estimation by using the free body diagram analysis gives the peak reaction force of 73 and 80 kN for Specimens M1-NF and P4-NF, respectively. Based on this comparison, the dynamic amplification factor (theory/measurement) of the monolithic joint was 2.3 whereas that of the precast joint was between 1.5-1.9.

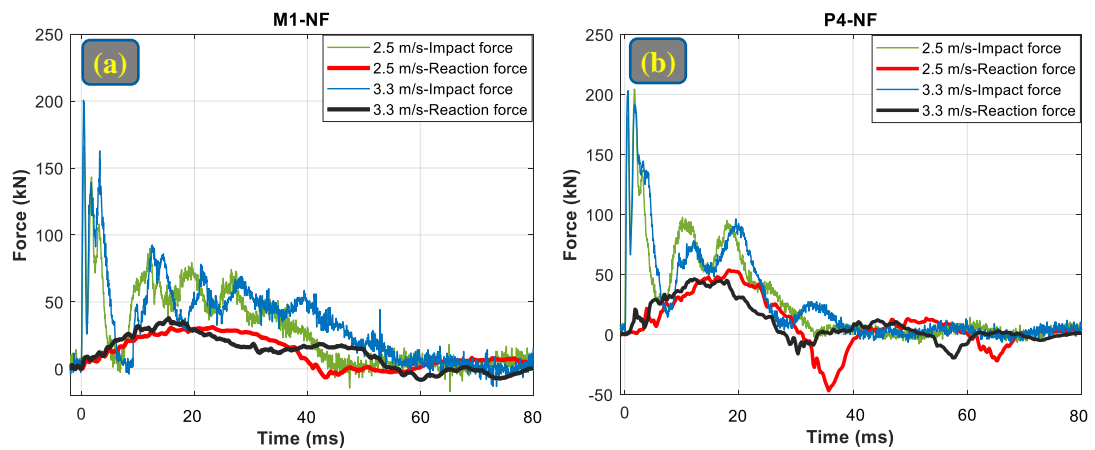


Fig. 6-12. Impact forces and reaction forces of Specimens (a) M1-NF and (b) P4-NF.

6.3.1.4 Maximum and residual displacement at the impact point

The image processing was utilized to derive the displacement-time histories of tracking points on the specimens. The displacement-time histories at the impact point of Specimens M1-NF and P4-NF are plotted in Fig. 6-13. In general, when the loading head impacted the beam surfaces, the beams of all the specimens deflected and reached the peak displacements after 25-40 ms during Stage 2 of the impact process, as shown in Fig. 6-7. Afterwards, the beam restored its original position. No brittle failure was observed during the tests. For example, the maximum displacement of Specimen M1-NF subjected to 2.5 m/s impact was 24 mm at 24 ms. When the impact velocity was

increased to 3.3 m/s, an increase of the peak displacement was recorded at approximately 49 mm at 33 ms. Afterwards, 59-mm displacement was measured at the second 3.3 m/s impact although the peak impact force was almost unchanged. This response resulted from the degraded joint stiffness induced by the previous impacts. After Stage 2, the beam of Specimen M1-NF showed the residual displacement which could be used to evaluate the damage level of this joint. As can be seen in Fig. 6-13 (a), the residual displacements of Specimen M1-NF at 2.5 m/s and 3.3 m/s impacts were 3 and 6 mm, respectively. It means the beam was capable of going back to its original position with very small residual displacement. This interesting phenomenon is attributed to the linear elastic behaviour of GFRP reinforcements which is different from the case of steel reinforcements. The use of steel reinforcements always results in residual displacement once the plastic deformation of the steel material occurs. At the second 3.3 m/s impact, 10-mm residual displacement was recorded at the impact point of Specimen M1-NF owing to severe damage (Level III) with the concrete crushing and large flexural cracks at the fixed-end (see in Section 6.3.1.2).

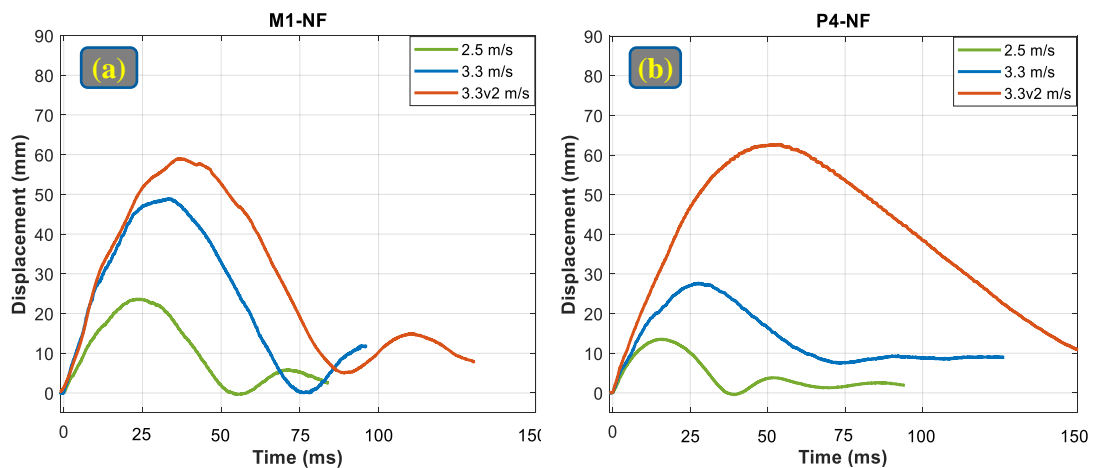


Fig. 6-13. Displacement-time histories of Specimens (a) M1-NF and (b) P4-NF.

Fig. 6-13(b) depicts the displacement-time histories of Specimen P4-NF. The peak displacement also occurred in the second stage of the impact process. Same as the M1-NF, the displacement increased with the impact velocity. The displacement at the second 3.3 m/s impact also increased even though there was no increment of the impact forces due to degraded stiffness caused by cracks and partially damaged concrete in the previous impacts. The peak displacements at 2.5 m/s and the first 3.3 m/s impacts were measured approximately 13 and 27 mm, respectively which were significantly lower than those of Specimen M1-NF. This difference resulted from a different lever

arm and thus stiffness. The lever arm of the monolithic specimen was 360 mm whereas that of the precast specimen was 160 mm because of the existence of CEP. Nevertheless, there was more severe damage at the fixed-end and joint area occurring in Specimen P4-NF, compared to Specimen M1-NF at the second 3.3 m/s impact. Hence, the maximum displacement of Specimen P4-NF was slightly higher than that of Specimen M1-NF. In addition, the above responses led to the higher residual displacement of Specimen P4-NF after 3.3 m/s and second 3.3 m/s impacts, compared to those of Specimen M1-NF. Interestingly, the displacement of the monolithic specimen exhibited the free vibration with some oscillation cycles while the vibration of the precast specimen was damped quickly after the peak displacement. It means that the precast joint showed better performance in the damping characteristic, compared to the monolithic joint. It is attributed to the greater energy dissipation in the precast joint (see more details in Section 6.3.1.5).

6.3.1.5 Energy dissipation

The energy dissipation (ED) of the beam-column joints is a critical parameter to evaluate the joint performance under the impact loading. For more convenience in data analysis, the energy was divided into three types which were determined as the closed area under the loop of the displacement and impact force (see Fig. 6-14). Type 1, namely work done (WD), marked from the beginning of the impact process to the moment when the beam started to rebound back to its original position. It was determined as the closed area from O to A in Fig. 6-14(a). Type 2, namely energy reversion (ER), indicated the reversion of the energy due to transferring energy to the supports (the area of the green part in Fig. 6-14(a)), followed by Type 3 when the energy obtained a plateau value. This plateau value was equal to the ED of the beam-column joints which was calculated by subtracting ER from WD. It is worth noting that following the energy conservation law, the WD by the impact force was equal to the imparted energy which caused the beam deformation, indentation effect, membrane component, and fracture energy. Also, the WD was equal to the sum of the ER and ED, as indicated in Fig. 6-14(b).

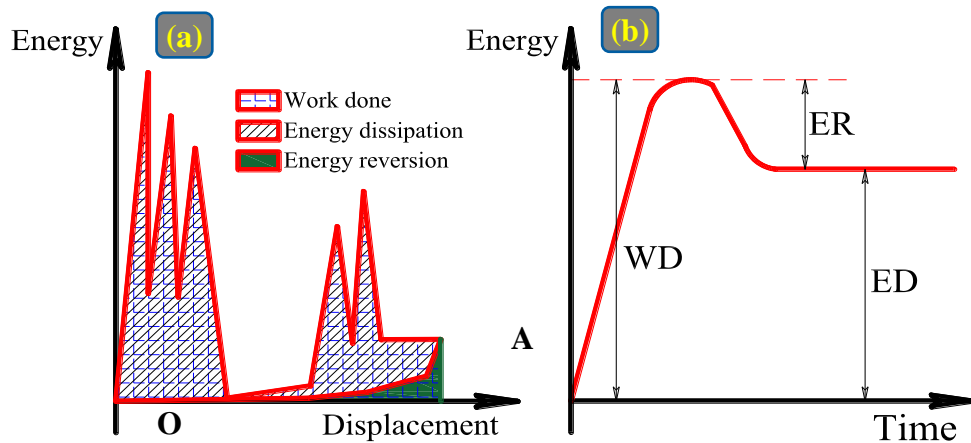
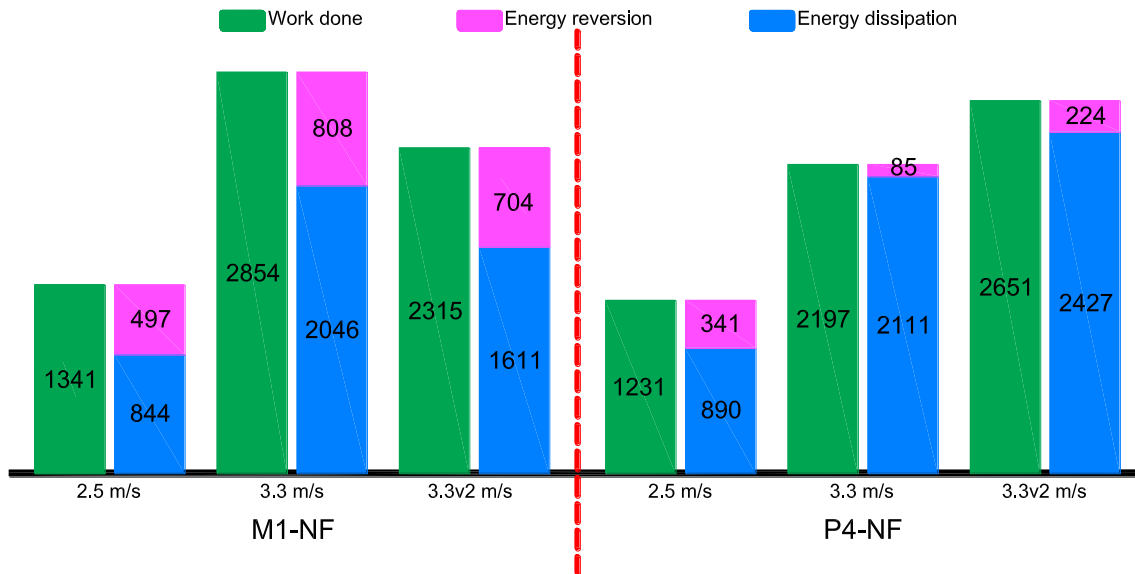


Fig. 6-14. Definition of three types of energy.

As can be seen in Fig. 6-15, WD of Specimen M1-NF was higher than that of Specimen P4-NF at 2.5 and 3.3 m/s impacts. For example, WD of Specimens M1-NF and P4-NF at 3.3 m/s impact was 2854 and 2179 kN.mm, respectively. However, at the second 3.3 m/s impact, WD of the dry joint (2651 kN.mm) was greater than that of the monolithic joint (2315 kN.mm). This different result could be explained that when these specimens did not fail at the low velocities of the pendulum system (2.5 and 3.3 m/s), the displacement of the monolithic joint was greater than that of the dry joint owing to longer lever arm (see more details in Section 6.3.1.4). Severe damage was observed on the joint and fixed-end areas of Specimen P4-NF at the second 3.3 m/s impact, compared to Specimen M1-NF. Therefore, the displacement and WD of Specimen P4-NF were greater than those of Specimen M1-NF at 3.3v2 m/s impact.

In general, ED capacities of the dry joint at 2.5 m/s, 3.3 m/s, and 3.3v2 m/s impacts were greater than those of monolithic joint with approximately 5%, 3%, and 51%, respectively. This result is consistent with the ED capacity of these specimens under cyclic loading [46]. It is attributed to less energy reversion in the dry joint, compared to the monolithic joint. For example, the energy reversion of Specimen P4-NF at 2.5, 3.3, and 3.3v2 m/s impacts was 31%, 89%, and 68% lower than that of Specimen M1-NF. In addition, under impact loading, the beam of Specimen P4-NF could considerably deform due to the joint opening and then vibrated which transferred the impact energy to kinetic energy. Consequently, the ED capacity of the proposed dry joint was better than that of the monolithic joint.



Note: Unit is kN.mm

Fig. 6-15. Energy comparison of Specimens M1-NF and P4-NF.

6.3.2 Effects of fibres and different kinds of fibres

This section discusses the test results of the two monolithic joints and two dry joints with SyFs and StFs. The effects of different fibre types on the joint performance under impact loading are also discussed.

6.3.2.1 Crack development

In this chapter, SyFs and StFs were utilized to reduce the damage of the beam-column joints under impact loading. As a result, the joints could survive under higher impact velocities. For example, Specimens M3-1StF-35 and P6-1StF-35 could respectively resist the forces at 4.0 m/s and 4.8 m/s impacts whereas both the Specimens M1-NF and P4-NF were severely damaged at second 3.3 m/s impact. The main cracks on the specimens with SyFs and StFs also occurred in the first and second stages of the impact process. In addition, the first crack appeared on the rear face of the beam at the impact point, and then the cracks propagated to the fixed-end and the joint area, which was similar to the specimens without fibres. The explanation for this phenomenon can be found in Section 6.3.1.1. The use of fibres did not prevent the formation of the first flexural crack. However, the presence of the fibres prevented the formation of the shear cracks on the beams and concrete spalling at the zone above the fixed-end.

For Specimen M3-1StF-35, no shear cracks and concrete spalling were observed on the beam up to 3.3 m/s impact while these damage modes appeared on the beam of Specimen M1-NF (see Figs. 6-A1 and 6-A2 in the appendix). The presence of StFs changed the damage patterns of the beams from a combination of the shear and flexural cracks to only flexural cracks which were also reported in the previous study where the use of steel fibres also changed the damage mode of fibre reinforced geopolymer beams under impact loading [177]. Furthermore, this observation indicated that adding fibres into the concrete mixture provides higher shear resistance, compared to flexural resistance. The flexural cracks occurred firstly at the fixed-end and then developed upwards on the beam length between the fixed-end and impact point. This trend was a result of higher bending moment at the fixed-end, compared to other regions of the beam under the global performance. On the other hand, almost no new cracks appeared after 3.3 m/s impact. The cracks at the fixed-end and joint area developed in length and width causing failure (Level IV with 41-mm residual displacement) after 4.0 m/s impact.

The application of SyFs and StFs in the two dry joints (P5-1SyF-48 and P6-1StF-35) effectively mitigated the shear cracks and concrete spalling. This phenomenon is attributed to the bridging effect of the fibres under impact loading. Therefore, less damage was observed at the same impact velocity, compared to Specimen P4-NF. In general, the crack development on Specimens P5-1SyF-48 and P6-1StF-35 was different from that of Specimen P4-NF. Vertical cracks and shear key failure on the column were observed on the specimens with fibres during the impact test. These phenomena did not happen to Specimen P4-NF. There were two reasons to explain this difference. (1) The presence of the fibres made Beam A and the CEP stiffer, compared to those with no fibres. (2) There were no fibres in the column of the precast specimens which resulted in the column relatively weaker compared to the CEP. The plain concrete was used for the columns considering reports from the previous studies [19, 46] that the columns were very strong showing no cracks under cyclic tests. Consequently, the cracks shifted from only appearing on the beams of the specimen without fibres to occurring on both of the beams and columns of the specimen with fibres under impact loading. In addition, only one shear key on the column made of plain concrete was damaged due to the joint opening.

The use of StFs showed better crack resistance under impact loading. Therefore, Specimen P6-1StF-35 showed less damage at the second 4.0 m/s impact, compared to Specimen P5-1SyF-48 at the same impact velocity. As shown in Figs. 6-A3(44.3ms) and 6-A3(42.0ms) in the appendix, the number of cracks on Specimen P6-1StF-35 was less than those on Specimen P5-1SyF-48. This result is attributed to the higher elastic modulus and better anchorage of StFs, compared to those of SyFs. The elastic modulus of StFs was 210 GPa while that of SyFs was only 12 GPa. Additionally, the SyFs were crimped and straight whereas hooked-ends StFs were used which provided better bonding and anchorage to concrete (see Figs. 6-6(a) and 6-6(b)).

6.3.2.2 Crack patterns and failure modes

This section adopted the definition of damage level in Section 6.3.1.2 to evaluate the failure modes of the specimens under impact loading. In general, the specimens with fibres showed smaller residual displacement as compared to the reference specimen under the same impact velocity. The maximum residual displacements at the impact point of Specimens M3-1StF-35, P5-1SyF-48, and P6-1StF-35 were 41, 40, and 63 mm, respectively. Figs. 6-16 and 6-17 compare the damage levels of the monolithic and precast specimens with fibres and no fibres. As previously mentioned in Section 6.3.2.1, the presence of fibres changed the damage modes of the beam-column joints. The main damage location of Specimen M1-NF was on the beam. The flexural cracks at fixed-end, concrete crushing, and concrete spalling governed the main damage of this specimen. Meanwhile, the damage patterns of Specimens M2-1SyF-48 and M3-1StF-35 were different from those of Specimen M1-NF. The damage mode was governed by a combination of the beam and joint damage (M2-1SyF-48 and M3-1StF-35). The bridging effects of the fibres increased the stress distribution on the monolithic joints which caused the above change of the damage modes. For example, in Specimen M3-1StF-35, the strain of a stirrup in the joint area was $3,029 \mu\epsilon$ at 4.0 m/s impact. This value was still lower than the nominal strain of the stirrups ($23,543 \mu\epsilon$). Therefore, the stirrups did not govern the main damage at the joint area of Specimen M3-1StF-35. The big inclined cracks of concrete at the joint were the main damage of Specimen M3-1StF-35 (see Fig. 6-16(e)). For the damage at the fixed-end of Specimen M3-1StF-35, the flexural cracks significantly opened at 4.0 m/s impact which induced the main damage in this location. On the other hand, Specimen M2-

1SyF-48 also failed due to the flexural cracks and inclined cracks. These damage modes were similar to Specimen M3-1StF-35 but at a lower impact velocity, i.e., the third 3.3 m/s impact. Additionally, more severe concrete crushing was observed on Specimen M2-1SyF-48, compared to that of Specimen M3-1StF-35 due to better performance of StFs as compared to SyFs (see Fig. 6-16).

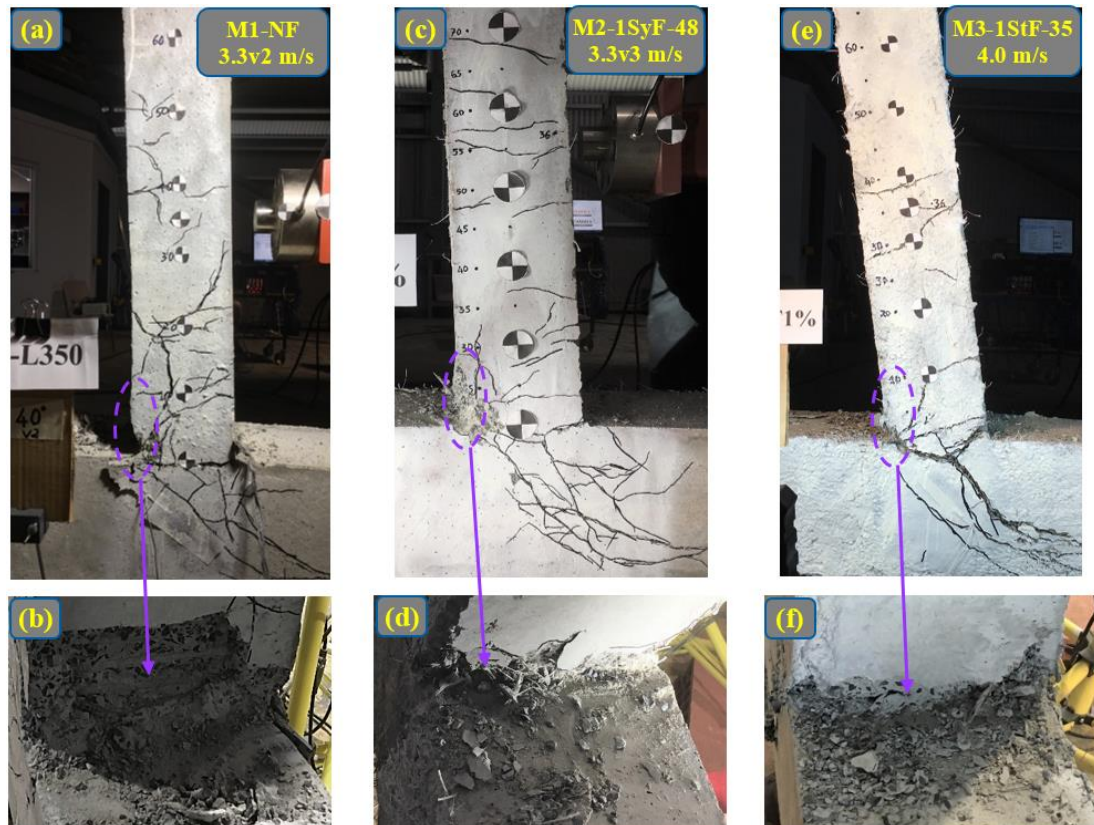


Fig. 6-16. Damage modes of the monolithic specimens.

(No fibres vs fibres; Synthetic fibres vs steel fibres).

For the precast specimens, the presence of fibres also changed the damage patterns from a combination of the beam and joint damage to the damage at the fixed-end of the beam. This trend was opposite to that of the monolithic specimens. This result could be explained that the presence of fibres significantly improved the shear resistance of the CEP. As a result, flexural stress at fixed-end reached its ultimate flexural strength before concrete reaching the ultimate shear strength in the CEP. Nevertheless, fewer inclined cracks were noticed in the CEP of Specimens P5-1SyF-48 and P6-1StF-35, as depicted in Figs. 6-17(c) and 6-17(e). Based on Fig. 6-17, there was no shear damage on the beam of Specimens P5-1SyF-48 and P6-1StF-35 while

severe shear damage was observed in the beam of Specimen P4-NF. This phenomenon was a result of the enhancement of the shear resistance of SFRC and SyFRC, as previously explained in Section 6.3.2.1. Pull-out and rupture failures of the fibres regulated the main failure of SyFs whereas only pull-out failure accounted for the primary failure of StFs. It was because the tensile strength of SyFs (640 MPa) was lower than that of StFs (1,345 MPa). Based on the above discussions, it could be concluded that (1) the presence of SyFs and StFs significantly reduced the damage level (concrete crushing, concrete spalling, and shear cracks); (2) the use of the fibres changed the damage modes of the monolithic and dry joint; (3) and the application of StFs showed better performance, compared to those of SyFs.

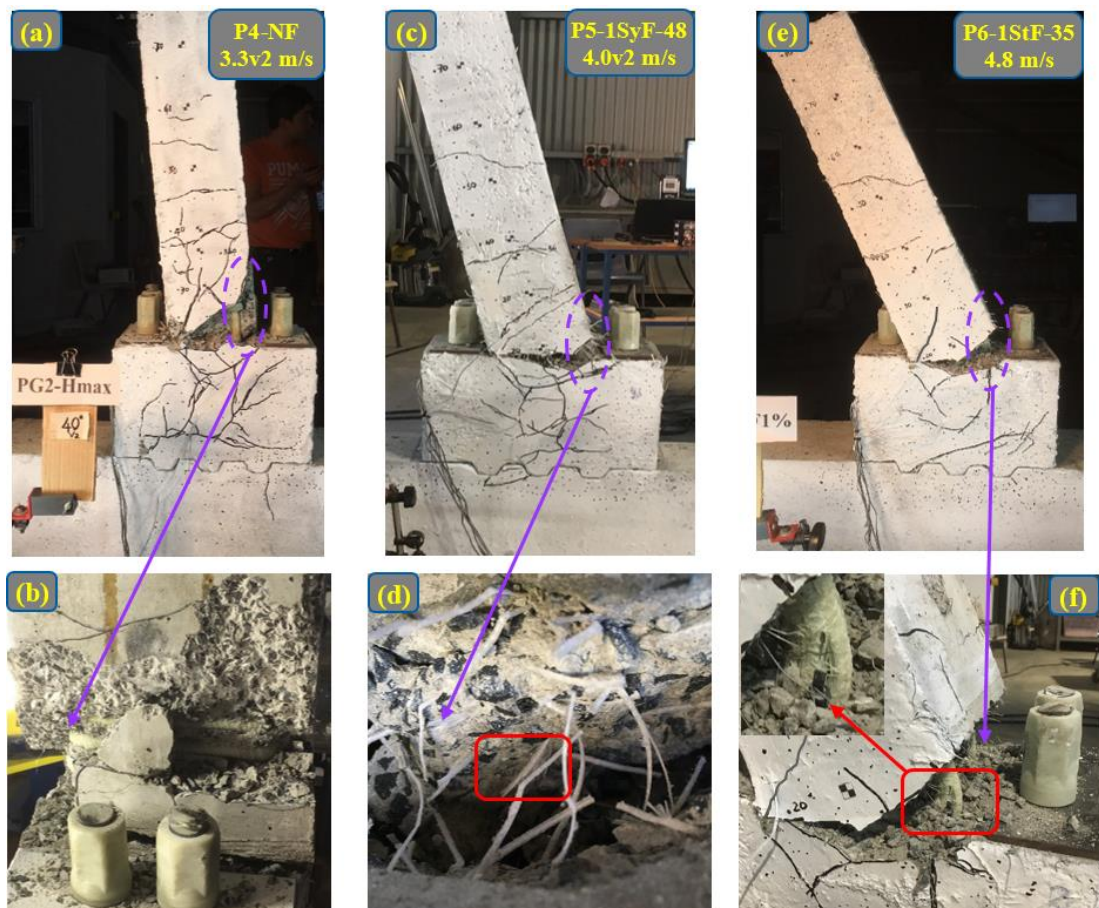


Fig. 6-17. Damage modes of the precast specimens.

(No fibres vs fibres; SyFs vs StFs).

Interestingly, the brittle failures did not occur on the beam-column joints during the test even though all the steel reinforcements and steel bolts were replaced by the GFRP reinforcements and GFRP bolts, respectively. The joints using GFRP reinforcements

showed ductile performance under impact loading. The beams could rebound back to their original positions as shown in Figs. 6-13 and 6-20. This observation was different from a common belief [62, 134] that the application of FRP materials could cause brittle failure for structures due to the linear behaviour of FRP materials. The GFRP reinforcements in this chapter failed due to splitting because of the excessive displacement of the beam as shown in Fig. 6-17(f). No rupture failure on the GFRP reinforcements was found during the tests.

6.3.2.3 Impact force-time history

According to Chapter 3, the addition of 1% StFs improved the peak loading capacity by approximately 18% under cyclic loading. Meanwhile, the impact forces of the specimens with the fibres (SyFs and StFs) were almost similar to the specimen without fibre (see Figs. 6-11, 6-18, and 6-19). For instance, the peak impact force of Specimen M3-1StF-35 at 3.3 m/s impact was 208 kN while that of Specimen M1-NF were 201 kN. It means the use of fibres did not noticeably increase the peak impact forces. This observation could be explained that the peak impact forces were affected by the local stiffness and contact stiffness between the loading head and beam surfaces [163] while the application of the fibres did not considerably improve these stiffnesses. Three peak impact forces were also observed in the specimens with fibres in the first stage of the impact process. The reasons for this observation were previously explained in Section 6.3.1.3.

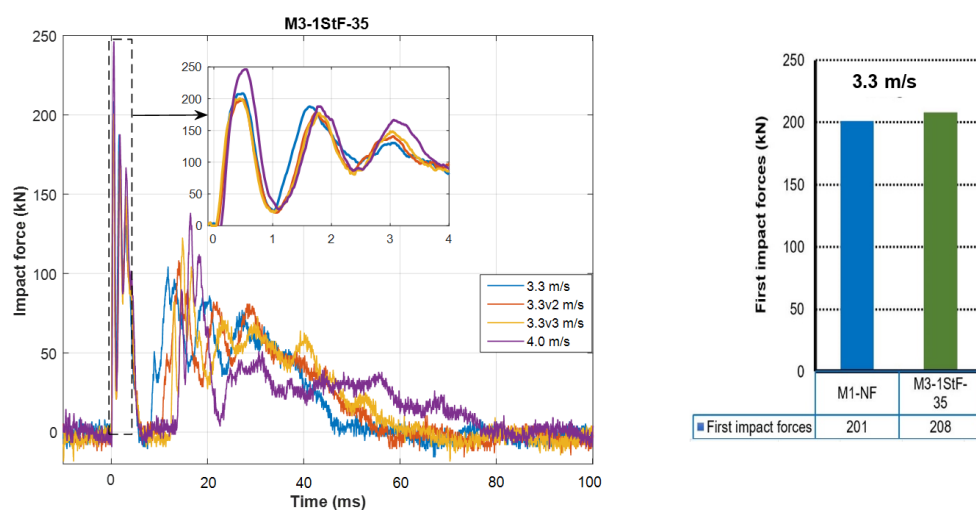


Fig. 6-18. Impact forces of Specimen M3-1StF-35.

The impact force-time histories of the specimens with fibres are presented in Figs. 6-18 and 6-19. For the monolithic joints, the peak impact forces of Specimen M2-1SyF-48 were closely analogous to Specimen M3-1StF-35. For example, the peak impact forces of these specimens were around 200 kN at 3.3, 3.3v2, and 3.3v3 m/s impacts. For the precast joints, the first peak impact forces of Specimen P6-1StF-35 (e.g., 247 kN at 4.0 m/s impact) were slightly higher than those of Specimen P5-1SyF-48 (e.g., 238 kN at 4.0 m/s impact), as illustrated in Fig. 6-19. This minor variation is attributed to testing variation, which is a result of different impact velocities (4.0 m/s of Specimen P6-1StF-35 and 3.86 m/s of Specimen P5-1SyF-48). In addition, steel fibres showed better bridging effect than synthetic fibres and thus Specimen P6-1StF-35 exhibited less local damage (less number of cracks near the impact region) as compared to that of P5-1SyF-48. This phenomenon is also attributed to a minor reduction in the impact force at 4.0 m/s impact.

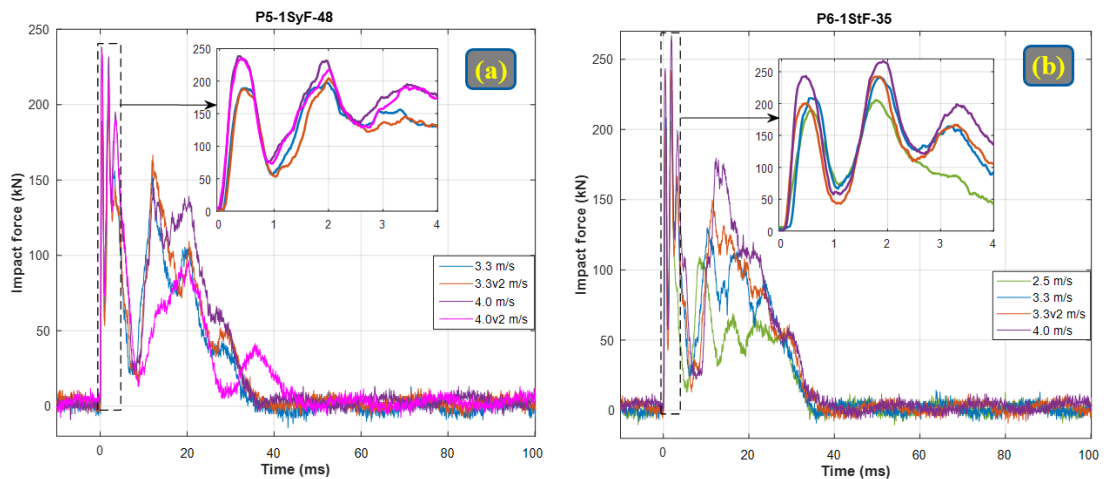


Fig. 6-19. Impact forces of two precast joints with fibres (a) P5-1SyF-48 and (b) P6-1StF-35.

6.3.2.4 Maximum and residual displacement at the impact point

Fig. 6-20 shows the displacement-time histories at the impact point of the monolithic and dry joints with SyFs and StFs. In general, the presence of the fibres effectively reduced the peak displacement of the beams at high impact velocities. As can be seen in Figs. 6-16 and 6-17, the use of the fibres considerably mitigated the number of cracks and concrete crushing on the beams and joint areas due to the bridging effect of the fibres. As a result, smaller displacement was observed on the specimens with fibres. For instance, the maximum displacements of Specimen M2-1SyF-48 at 3.3 m/s

and 3.3v2 m/s impacts were respectively approximately 41 mm and 47 mm which were smaller than the corresponding displacement of Specimen M1-NF (49 mm and 59 mm). This observation was also found in the precast specimens. For example, 14 mm and 16 mm were the maximum displacement of Specimen P6-1StF-35 at 3.3 m/s and 3.3v2 m/s impacts whereas those of Specimen P4-NF were 27 mm and 63 mm, respectively. As expected, the presence of fibres also effectively reduced the residual displacement of the beams. For instance, the residual displacements of Specimen P4-NF at 3.3 m/s and 3.3v2 m/s impacts were approximately 8 mm and 11 mm while those of Specimen P6-1StF-35 were almost zero. Consequently, the specimens with fibres could survive higher impact velocities. For instance, the precast joint with StFs (P6-1StF-35) failed at 4.8 m/s impact whereas the precast joint without fibres (P4-NF) showed severe damage and failure at the second 3.3 m/s impact. In addition, the displacements of the specimens with fibres and without fibres at a low impact velocity (2.5 m/s) were quite similar because the fibres did not activate its function in this low impact velocity as the displacements of the specimens were still minor and cracks had not opened yet. Hence, the maximum displacements of Specimens M1-NF and M2-1SyF-48 at 2.5 m/s impact were almost identical at about 24 mm.

To evaluate the effectiveness of the application of SyFs to replace StFs in the proposed dry joints, a comparison was conducted between Fig. 6-20(b) and Fig. 6-20(c). From 2.5 m/s impact to 3.3v2 m/s impact, the maximum displacement of Specimen P5-1SyF-48 was closely analogous to Specimen P6-1StF-35 with approximately 9.5 mm at 2.5 m/s impact and 16.5 mm at 3.3v2 m/s impact. This was because both SyFs and StFs did not activate yet at 2.5 m/s impact or just activated at 3.3 and 3.3v2 m/s impacts. No pull-out and rupture failures of the fibres were observed in the tests under these impact velocities. Afterwards, the concrete crushing and flexural cracks at the fixed-end and a combination of the shear and tensile cracks at the CEP significantly developed in the beams and joint areas which caused the greater peak displacements on the beam of Specimen P5-1SyF-48, compared to those of Specimen P6-1StF-35. As a result, Specimen P5-1SyF-48 failed at second 4.0 m/s impact with a large residual displacement of 40 mm whereas Specimen P6-1StF-35 still survived at this impact with only a 5-mm residual displacement. This different response could be explained by the two following reasons: (1) the elastic modulus (210 GPa) and hooked-end anchorage of StFs are more effective than the elastic modulus (12 GPa) and straight

anchorage of SyFs and (2) the use of SFRC with higher tensile strength (7.3 MPa), compared to the tensile strength of SyFRC (6 MPa), 22% improvement, showed better performance in resisting the shear and tensile cracks. Therefore, it could be concluded that the application of StFs and SyFs exhibited a similar displacement at the low impact velocities. Meanwhile, the use of StFs showed a better behaviour at high impact velocities compared to SyFs.

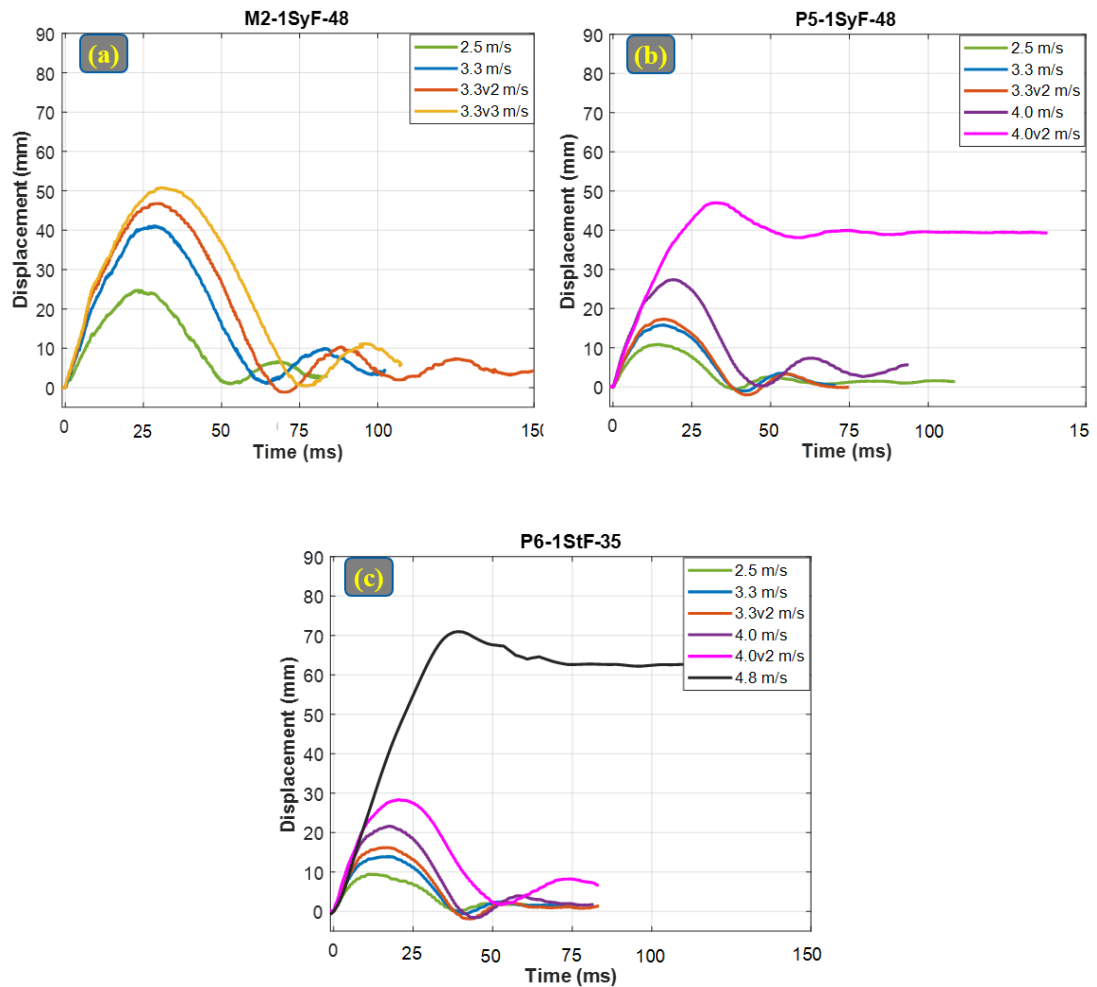
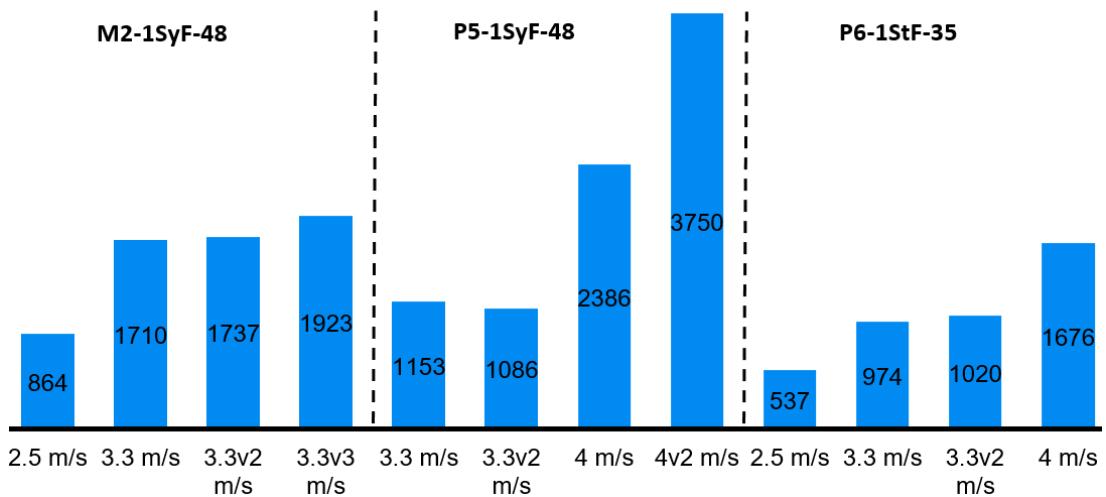


Fig. 6-20. Displacement-time histories of Specimens (a) M2-1SyF-48, (b) P5-1SyF-48, and (c) P6-1StF-35.

6.3.2.5 Energy dissipation

Fig. 6-21 shows the energy dissipations of the specimens with the fibres. For brevity, the WD and ER were not shown in this figure. In general, the presence of fibres mitigated the damage so the specimens with fibres could resist the impact force and dissipate higher impact energies. For instance, Specimen P5-1SyF-48 could resist the impact load up to the second 4.0 m/s impact while Specimen P4-NF showed severe

damage at the second 3.3 m/s impact. In addition, the use of fibres reduced the ED capacity at the same impact velocities (i.e., 3.3 and 3.3v2 m/s impacts), compared to specimens without fibres (i.e., M1-NF and P4-NF), as illustrated in Figs. 6-15 and 6-21. It is attributed to smaller displacements and less damage of the beam of the specimens with the fibres, which affected the ED (see in Section 6.3.2.4). Another comparison of the ED capacity was carried out between Specimens P5-1SyF-48 and P6-1StF-35 to evaluate the effectiveness of SyFs and StFs in the beam-column joints. As can be seen in Fig. 6-21, Specimen P6-1StF-35 exhibited less ED capacity than Specimen P5-1SyF-48 by approximately 6-30% at the same impact velocities. It is also attributed to the better performance of StFs in mitigating cracks, compared to SyFs, as discussed in Section 6.3.2.2.



Note: Unit is kN.mm

Owing to the loss of impact force data, ED at some pendulum impact velocities was not reported in this figure.

Fig. 6-21. Energy dissipation comparison of Specimens M2-1SyF-48, P5-1SyF-48, and P6-1StF-35.

6.4 Summary

This chapter investigated the performance of monolithic and dry joints made of normal and fibre reinforced concrete under impact loading. The proposed dry joints with fibres showed excellent performance in terms of the damage level, displacement, and ED compared to the reference monolithic joint. The findings from this chapter can be summarized as follows:

1. Excellent ductility with no brittle failure was observed in the beam-column joints under impact loading when steel reinforcements were replaced by GFRP reinforcements. The beams could rebound back to its original position with very low residual displacement.
2. The use of GFRP bolts did not only effectively resolve corrosion damage as often observed in precast joints with conventional steel bolts, but also effectively mitigated the residual joint opening because of the higher strength and linear elastic behaviour of GFRP. This performance is superior compared to the application of steel bolts which has lower yield strength, therefore, is more vulnerable to yield and hence leads to a residual opening.
3. The energy dissipation of the proposed dry joint was greater than that of the monolithic joint up to 51%.
4. The shear damage significantly affected the failure mode of the beam-column joints subjected to impact loading. Therefore, it needs to be carefully considered when designing the joints. The application of fibres is a potential solution to enhance the shear resistance.
5. The presence of steel fibres (StFs) and synthetic fibres (SyFs) effectively mitigated the damage level (concrete crushing, concrete spalling, and shear cracks), lateral displacement (up to 21% for the monolithic joint and 74% for the dry joint at the second 3.3 m/s impact), and residual displacement (up to 57% for the monolithic joint and 93% for the dry joint at the second 3.3 m/s impact). Nevertheless, the peak impact forces were not considerably affected by the use of fibres because the application of the fibres did not considerably improve the local stiffness and contact stiffness.
6. The use of SyFs showed greater energy dissipation than StFs, approximately 6-30% higher at the same impact velocity. Meanwhile, the application of StFs showed better performance in reducing the damage and displacement of the joint subjected to higher impact loads.
7. All the specimens under impact loading showed local response dominance with the large displacement at the impact point in the early stage of impact up to 2.5 ms. This response was not observed under cyclic loading.
8. High prestress forces can be applied on the FRP bolts with a hydraulic jack and a steel chair which effectively resolves the disadvantages of the conventional method with the use of a torque wrench.

In general, the impact behaviour of the beam-column joints under impact loads was very different from that under cyclic loads. The proposed dry joints with the GFRP bolts, GFRP reinforcements, and fibres showed better performance compared to the corresponding monolithic joint under impact loading. Therefore, this dry joint type could be potentially applied in construction to effectively replace the conventional monolithic joint and reduce the construction time, construction cost, and enhance the construction quality. It is also easy to be repaired or replaced after deterioration and damage.

CHAPTER 7: CONCLUSIONS AND RECOMMENDATIONS

7.1 Findings

This dissertation successfully developed and proposed new sustainable and resilient dry and hybrid joints with excellent behaviours under earthquake and impact loads. Various new and advanced materials were applied in this dissertation such as GFRP/CFRP bolts, GFRP reinforcements, synthetic (plastic) fibres, and GPC to mitigate corrosion damage and reduce environmental impact. The proposed precast joints were tested under cyclic and impact loading conditions. Subsequently, the results were compared with those of the conventional monolithic joints to evaluate the performances of the proposed precast joints. After studying the joint performances based on the experimental results, new analytical models were proposed to assist engineers to design the precast joints using OPC, SFRC, and GPC. In addition, 3D finite element models of the precast joints were built and validated against the experimental results to examine some assumptions in the analytical models. Some parameters which could not be straightforwardly measured from the experiments were studied from the results of the numerical models. Finally, parametric studies were conducted to determine the optimal value of CEP thickness. The main findings of this dissertation are summarised as follows:

Experimental studies

1. The proposed dry and hybrid joints showed excellent performances in terms of the loading capacity, drift ratio, ductility, stiffness, and energy dissipation, compared to the conventional monolithic joints. Therefore, they can effectively replace monolithic joints in earthquake and non-earthquake prone areas with many benefits.
2. Shear and tensile cracks at the middle zone of CEP primarily governed the main failure modes of the proposed dry joints under cyclic loading. This conclusion was different from the report of the previous study of Saqan [14] which reported that compression strut failure governed the main failure mode of the dry joint with CEP and bolts.

3. The application of FRP in this study shows outstanding behaviours. No brittle failure was observed during the tests. In addition, the use of FRP bolts, FRP plates, and FRP reinforcements did not only effectively resolve corrosion damage as often observed in precast joints with conventional steel connecting parts, but also effectively reduce the residual joint opening and residual displacement. This excellent performance is attributed to the higher strength and linear elastic behaviour of FRP material. This performance is impressive compared to the application of steel bolts and reinforcements which have lower yield strength, therefore, become more vulnerable to yielding and hence lead to a residual joint opening and residual displacement.

4. The high prestress forces in bolts could not only increase the maximum applied load but also reduce the joint opening of the proposed precast joints. Meanwhile, the initial stiffness of the precast joints is not affected by the prestress levels in the bolts.

5. GPC could potentially replace OPC, which helps to recycle industrial wastes and reduce CO₂ footprint. The crack development and crack patterns of OPC and GPC beam-column joints were similar before reaching the maximum applied loads. However, brittle failure was observed on the GPC specimens after reaching the peak load due to the brittleness characteristic of GPC. Therefore, the ductility of plain GPC specimens was lower than that of plain OPC specimens by approximately 23-43%. To increase the ductility of GPC specimens, the application of fibre reinforced concrete is a promising solution.

6. The presence of different fibre types (steel or synthetic) effectively mitigated the damage level (concrete crushing, concrete spalling, and shear cracks), lateral displacement, and residual displacement under impact loading. The peak impact forces were not considerably affected by the use of fibres because the application of the fibres did not considerably change the local stiffness and contact stiffness. Meanwhile, the use of fibres increased the load-carrying capacity and drift ratio of the proposed precast joints under cyclic loading.

7. The shear damage significantly affected the failure mode of the beam-column joints subjected to impact load. Therefore, it needs to be carefully considered

when designing the joints. The application of fibres is a potential solution to enhance the shear resistance.

Analytical studies

1. The current standards and models such as ACI 318-11 [72], BS EN 1998-1-04 [88], lower-AIJ-2010 [89], and Hwang and Lee [90] can not be used to predict the capacity of the proposed precast joints. High variations of up to 96% were observed in this dissertation.
2. The proposed strut-tie model in the previous study of Saqan [14] and Hanaor and Ben-Arroyo [13] could neither explain the failure modes nor estimate the maximum applied load of the proposed precast joints in this project due to the different failure modes.
3. The newly proposed analytical model in this study could well predict the main failure mode, failure position, and the loading capacity of the precast joints made of OPC, SFRC, or GPC. Therefore, the proposed analytical model can be used to design the proposed precast joints.

Numerical simulation

1. The application of the common concrete damage plasticity model for concrete could not capture the shear failure of the proposed precast joints while the modified concrete model which was proposed by Feng et al. [145] and Feng et al. [155] could be used to capture well the failure mode and peak load of the proposed precast joints with a marginal variation of 4.1-6.7%.
2. The numerical results proved that the shear and tensile stress in the middle zone of CEP mainly governed the failure modes of the dry joints. Therefore, the assumptions in the proposed analytical models [24, 46] and the experimental results were numerically confirmed.
3. Based on the results of the numerical simulation, it can be concluded that the CEP thickness significantly affected the performances of the precast joints, such as failure mode, DR, loading capacity, and ED. In addition, the numerical results

suggested that the thickness ratio of CEP/Beam= 1.3 was an optimal value of the CEP thickness to be considered in the design of this dry joint type.

7.2 Recommendation for future works

The findings reported in this dissertation paved a way to further research for wide application of the proposed dry and hybrid joints in practice. The following research topics are recommended:

For the experiment

- The performances of GPC dry and monolithic joints have been extensively investigated but not those of GPC hybrid joints. Therefore, investigating the performances of GPC hybrid joints could be a potential topic.
- The performances of the proposed dry and hybrid joints under impact loading are a new topic in the literature. It would be interesting to examine some parameters which may affect the precast joint performance including velocity and weight of impactor, CEP thickness, prestress level, and position of impact points.

For analytical model

Proposing an analytical model to predict the peak impact forces needs to be done in future studies.

For numerical simulation

There has been no study investigating the joint performances under blast load in the literature. Therefore, studies on blast responses of beam-column joints may be a promising topic for future work. However, it is challenging to conduct experiments to investigate blast performances of the beam-column joints due to the limitation of the experimental equipment. The use of numerical simulation is a potential method to overcome this difficulty.

References

- [1] Zhao W, Yang H, Chen J, and Sun P. A proposed model for nonlinear analysis of RC beam-column joints under seismic loading. *Engineering Structures* 2019;180:829-43.
- [2] Ngo TT, Pham TM, Hao H, Chen W, and Elchalakani M. Performance of monolithic and dry joints with GFRP bolts reinforced with different fibres and GFRP bars under impact loading. *Engineering Structures* 2021;240:112341.
- [3] Wouters JP, Kesner K, and Poston RW. Tendon corrosion in precast segmental bridges. *Transportation Research Record* 1999;1654:128-32.
- [4] Koch GH, Brongers MPH, Thompson NG, Virmani YP, and Payer JH. Chapter 1 - Cost of corrosion in the United States. In: Kutz M, editor. *Handbook of Environmental Degradation of Materials*. Norwich, NY: William Andrew Publishing; 2005. p. 3-24.
- [5] Lawler N, and Polak MA. Development of FRP shear bolts for punching shear retrofit of reinforced concrete slabs. *Journal of Composites for Construction* 2010;15:591-601.
- [6] Yunovich M, and Thompson NG. Corrosion of highway bridges: Economic impact and control methodologies. *Concrete International* 2003;25:52-7.
- [7] Bahrami S, Madhkhan M, Shirmohammadi F, and Nazemi N. Behavior of two new moment resisting precast beam to column connections subjected to lateral loading. *Engineering Structures* 2017;132:808-21.
- [8] Yekrangnia M, Taheri A, and Zahrai SM. Experimental and numerical evaluation of proposed precast concrete connections. *Structural Concrete* 2016;17:959-71.
- [9] Tran TM, Hadi MNS, and Pham TM. A new empirical model for shear strength of reinforced concrete beam-column connections. *Magazine of Concrete Research* 2014;66:514-30.
- [10] Jin K, Kitayama K, Song S, and Kanemoto K-o. Shear capacity of precast prestressed concrete beam-column joint assembled by unbonded tendon. *ACI Structural Journal* 2017;114:51.
- [11] Priestley MN, and MacRae GA. Seismic tests of precast beam-to-column joint subassemblages with unbonded tendons. *PCI journal* 1996;41:64-81.
- [12] Kaya M, and Samet Arslan A. The effect of the diameter of prestressed strands providing the post-tensioned beam-to-column connections. *Materials & Design* 2009;30:2604-17.
- [13] Hanaor A, and Ben-Arroyo A. Prestressed bolting in precast concrete beam-column connection. *Proceedings of the institution of civil engineers: Structures and buildings*: Thomas Telford Services Ltd; 1998. p. 144-53.
- [14] Saqan EI. Evaluation of ductile beam-column connections for use in seismic-resistant precast frames. USA: University of Texas at Austin; 1995.
- [15] Palmieri L, Saqan E, French C, and Kreger M. Ductile connections for precast concrete frame systems. *ACI-Special Publication* 1996;162-13:313-56.
- [16] ACI T1.1-01. Acceptance criteria for moment frames based on structural testing and commentary. *ACI T11-01*. American Concrete Institute: ACI Committee; 2001. p. 1-7.
- [17] CSA A23.3-07. Design of concrete structures. CSA A233-07. Mississauga, Ontario: CSA (Canadian Standards Association); 2007.
- [18] ASCE 41-06. Seismic rehabilitation of existing buildings. ASCE 41-06. ASCE Reston, VA: ASCE; 2006.

- [19] Ngo TT, Pham TM, and Hao H. Ductile and dry exterior joints using CFRP bolts for moment-resisting frames. *Structures* 2020;28:668-84.
- [20] Yuksel E, Karadogan HF, Bal IE, Ilki A, Bal A, and Inci P. Seismic behavior of two exterior beam-column connections made of normal-strength concrete developed for precast construction. *Engineering Structures* 2015;99:157-72.
- [21] Ngo TT, Pham TM, Hao H, Wensu C, and Ngoc San H. Experiment and numerical study on newly proposed dry and hybrid concrete joints with GFRP bolts and GFRP reinforcements under cyclic loading. 2021 (Under review).
- [22] Benhelal E, Zahedi G, Shamsaei E, and Bahadori A. Global strategies and potentials to curb CO2 emissions in cement industry. *Journal of Cleaner Production* 2013;51:142-61.
- [23] Castel A, Foster SJ, Ng T, Sanjayan JG, and Gilbert RI. Creep and drying shrinkage of a blended slag and low calcium fly ash geopolymer Concrete. *Materials and Structures* 2016;49:1619-28.
- [24] Ngo TT, Tran TT, Pham TM, and Hao H. Performance of geopolymer concrete in monolithic and non-corrosive dry joints using CFRP bolts under cyclic loading. *Composite Structures* 2020:113394.
- [25] Bakharev T. Resistance of geopolymer materials to acid attack. *Cement and Concrete Research* 2005;35:658-70.
- [26] Castel A, and Foster SJ. Bond strength between blended slag and class F fly ash geopolymer concrete with steel reinforcement. *Cement and Concrete Research* 2015;72:48-53.
- [27] Nath P, and Sarker PK. Flexural strength and elastic modulus of ambient-cured blended low-calcium fly ash geopolymer concrete. *Construction and Building Materials* 2017;130:22-31.
- [28] Xie J, Wang J, Rao R, Wang C, and Fang C. Effects of combined usage of GGBS and fly ash on workability and mechanical properties of alkali activated geopolymer concrete with recycled aggregate. *Composites Part B: Engineering* 2019;164:179-90.
- [29] Wang J, Xie J, Wang C, Zhao J, Liu F, and Fang C. Study on the optimum initial curing condition for fly ash and GGBS based geopolymer recycled aggregate concrete. *Construction and Building Materials* 2020;247:118540.
- [30] Rafeet A, Vinai R, Soutsos M, and Sha W. Effects of slag substitution on physical and mechanical properties of fly ash-based alkali activated binders (AABs). *Cement and Concrete Research* 2019;122:118-35.
- [31] Sumajouw MDJ, and Rangan BV. Low-calcium fly ash-based geopolymer concrete: reinforced beams and columns, research report GC. Perth (Australia): Curtin University of Technology; 2006.
- [32] Wallah S, and Rangan BV. Low-calcium fly ash-based geopolymer concrete: long-term properties. Perth, WA, Australia: Curtin University; 2006.
- [33] Nguyen KT, Ahn N, Le TA, and Lee K. Theoretical and experimental study on mechanical properties and flexural strength of fly ash-geopolymer concrete. *Constr Build Mater* 2016;106:65-77.
- [34] Visintin P, Mohamed Ali MS, Albitar M, and Lucas W. Shear behaviour of geopolymer concrete beams without stirrups. *Construction and Building Materials* 2017;148:10-21.
- [35] Albitar M, Mohamed Ali MS, and Visintin P. Experimental study on fly ash and lead smelter slag-based geopolymer concrete columns. *Construction and Building Materials* 2017;141:104-12.
- [36] Tran TT, Pham TM, and Hao H. Rectangular stress-block parameters for fly-ash and slag based geopolymer concrete. *Structures* 2019;19:143-55.

- [37] Teh SH, Wiedmann T, Castel A, and de Burgh J. Hybrid life cycle assessment of greenhouse gas emissions from cement, concrete and geopolymers concrete in Australia. *Journal of Cleaner Production* 2017;152:312-20.
- [38] Saatcioglu M. Cracking in concrete structures during the August 17, 1999 earthquake in Turkey. *ACI-Special Publication* 2001;204:261-76.
- [39] Mosallam A, Allam K, and Salama M. Analytical and numerical modeling of RC beam-column joints retrofitted with FRP laminates and hybrid composite connectors. *Composite Structures* 2019;214:486-503.
- [40] Abbas AA, Syed Mohsin SM, and Cotsovos DM. Seismic response of steel fibre reinforced concrete beam-column joints. *Engineering Structures* 2014;59:261-83.
- [41] Mady M, El-Ragaby A, and El-Salakawy E. Seismic behavior of beam-column joints reinforced with GFRP bars and stirrups. *Journal of Composites for Construction* 2011;15:875-86.
- [42] Hadi MNS, and Tran TM. Seismic rehabilitation of reinforced concrete beam-column joints by bonding with concrete covers and wrapping with FRP composites. *Materials and Structures* 2016;49:467-85.
- [43] Wang G-L, Dai J-G, and Bai Y-L. Seismic retrofit of exterior RC beam-column joints with bonded CFRP reinforcement: An experimental study. *Composite Structures* 2019;224:111018.
- [44] Ngo TT, Pham TM, and Hao H. Use of CFRP bolts in dry beam-column joints for sustainable prefabrication constructions. *APFIS2019. Surfers Paradise, Gold Coast, Australia*2019.
- [45] Le-Trung K, Lee K, Lee J, Lee DH, and Woo S. Experimental study of RC beam-column joints strengthened using CFRP composites. *Composites Part B: Engineering* 2010;41:76-85.
- [46] Ngo TT, Pham TM, and Hao H. Effects of steel fibres and prestress levels on behaviour of newly proposed exterior dry joints using SFRC and CFRP bolts. *Engineering Structures* 2020;205:110083.
- [47] Leiba M. Impact of landslides in Australia to December 2011. *Australian Journal of Emergency Management, The* 2013;28:28-34.
- [48] Pham TM, and Hao H. Behavior of fiber-reinforced polymer-strengthened reinforced concrete beams under static and impact loads. *International Journal of Protective Structures* 2017;8:3-24.
- [49] Saatci S, and Vecchio FJ. Effects of Shear Mechanisms on Impact Behavior of Reinforced Concrete Beams. *ACI Structural Journal* 2009;106:78-86.
- [50] Pham TM, and Hao H. Impact behavior of FRP-strengthened RC beams without stirrups. *Journal of Composites for Construction* 2016;20:04016011.
- [51] Rajeev A, Mohotti D, and Shelke A. Implications of impact experiments on honeycomb shielded exterior beam-column joint. *Engineering Structures* 2020;212:110470.
- [52] Rajeev A, Parsi SS, Raman SN, Ngo T, and Shelke A. Experimental and numerical investigation of an exterior reinforced concrete beam-column joint subjected to shock loading. *International Journal of Impact Engineering* 2020;137:103473.
- [53] Wang W, Li H, and Wang J. Progressive collapse analysis of concrete-filled steel tubular column to steel beam connections using multi-scale model. *Structures* 2017;9:123-33.
- [54] Mostofinejad D, and Akhlaghi A. Flexural strengthening of reinforced concrete beam-column joints using innovative anchorage system. *ACI Structural Journal* 2017;114:1603-14.

- [55] Feng D-C, Wu G, and Lu Y. Finite element modelling approach for precast reinforced concrete beam-to-column connections under cyclic loading. *Engineering Structures* 2018;174:49-66.
- [56] Vidjeapriya R, and Jaya KP. Experimental study on two simple mechanical precast beam-column connections under reverse cyclic loading. *Journal of Performance of Constructed Facilities* 2013;27:402-14.
- [57] Clifford LF. Durability of post-tensioned concrete structures. *Concrete International* 1991;13:58-65.
- [58] Singh V, Bansal PP, Kumar M, and Kaushik SK. Experimental studies on strength and ductility of CFRP jacketed reinforced concrete beam-column joints. *Construction and Building Materials* 2014;55:194-201.
- [59] Dalalbashi A, Eslami A, and Ronagh HR. Plastic hinge relocation in RC joints as an alternative method of retrofitting using FRP. *Composite Structures* 2012;94:2433-9.
- [60] Benmokrane B, Robert M, Mohamed HM, Ali AH, and Cousin P. Durability assessment of glass FRP solid and hollow bars (rock bolts) for application in ground control of jurong rock caverns in Singapore. *Journal of Composites for Construction* 2017;21:06016002.
- [61] Li Y-m, Ma N-j, Yang K, and Shi J-j. Research on FRP bolt-end failure mechanism. *Mining Science and Technology (China)* 2009;19:0522-5.
- [62] Mady M, El-Ragaby A, and El-Salakawy EF. Experimental investigation on the seismic performance of beam-column joints reinforced with GFRP bars. *Journal of Earthquake Engineering* 2011;15:77-98.
- [63] Mady MHA. Seismic behaviour of exterior beam-column joints reinforced with FRP bars and stirrups. 395 Wellington Street, Ottawa ON K1A 0N4, Canada: University of Manitoba (Canada); 2011.
- [64] Le TD, Pham TM, Hao H, and Yuan C. Performance of precast segmental concrete beams posttensioned with carbon fiber-reinforced polymer (CFRP) tendons. *Composite Structures* 2019;208:56-69.
- [65] Wang X, Shi J, Wu G, Yang L, and Wu Z. Effectiveness of basalt FRP tendons for strengthening of RC beams through the external prestressing technique. *Engineering Structures* 2015;101:34-44.
- [66] Schmidt JW, Bennitz A, Täljsten B, Goltermann P, and Pedersen H. Mechanical anchorage of FRP tendons – A literature review. *Construction and Building Materials* 2012;32:110-21.
- [67] Li J, Samali B, Ye L, and Bakoss S. Behaviour of concrete beam-column connections reinforced with hybrid FRP sheet. *Composite Structures* 2002;57:357-65.
- [68] Ghomi SK, and El-Salakawy E. Seismic performance of GFRP-RC exterior beam-column joints with lateral beams. *Journal of Composites for Construction* 2016;20:04015019.
- [69] Feroldi F, and Russo S. Structural behavior of all-FRP beam-column plate-bolted joints. *Journal of Composites for Construction* 2016;20:04016004.
- [70] ACI 550R-96. Design recommendation for precast concrete structures. ACI 550R-96. Farmington Hills, MI: ACI (American Concrete Institute); 1996. p. 115-21.
- [71] ACI 352R-02. Recommendations for design of beam-column connections in monolithic reinforced concrete structures. ACI 352R-02. Farmington Hills, MI: ACI (American Concrete Institute); 2002. p. 38.00.
- [72] ACI 318-11. Building code requirements for structural concrete and commentary. ACI 318-11. Farmington Hills, MI 48331: ACI (American Concrete Institute); 2011. p. 503.

- [73] Wight JK, and MacGregor JG. Reinforced concrete: Mechanics and design. 6th ed. Boston: Boston : Pearson; 2012.
- [74] AS 1012.8.1-14. Method for making and curing concrete-compression and indirect tensile test specimens. AS 10128 1-14. Sydney, NSW: AS (Australian Standard); 2014.
- [75] AS 1012.9.1-14. Methods of testing concrete-compressive strength tests-concrete, mortar and grout specimens. AS 101291-14. Sydney, NSW: AS (Australian Standard); 2014.
- [76] J and R Metalwork Industry Pty Ltd. Quotation and Properties of CFRP bolts. China2018.
- [77] GB/T 1447-05. Fiber-reinforced plastics composites-Determination of tensile properties. GB/T 1447-05. China: GB (Chinese Standard); 2005.
- [78] Hobson Engineering Pty Ltd. High tensile: Metric vs Imperial - bolts. Australia2018. p. 2.
- [79] Antonopoulos CP, and Triantafillou TC. Experimental investigation of FRP-strengthened RC beam-column joints. Journal of composites for construction 2003;7:39-49.
- [80] Turmo J, Ramos G, and Aparicio AC. FEM modelling of unbonded post-tensioned segmental beams with dry joints. Eng Struct 2006;28:1852-63.
- [81] Le TD, Pham TM, and Hao H. Numerical study on the flexural performance of precast segmental concrete beams with unbonded internal steel tendons. Construction and Building Materials 2020;248:118362.
- [82] Park R. Evaluation of ductility of structures and structural assemblages from laboratory testing. Bulletin of the New Zealand national society for earthquake engineering 1989;22:155-66.
- [83] Park RL, Park R, and Paulay T. Reinforced concrete structures: John Wiley & Sons; 1975.
- [84] Hadi MN, and Schmidt LC. Use of helixes in reinforced concrete beams. ACI Structural Journal 2002;99:191-8.
- [85] Xue W, and Zhang B. Seismic behavior of hybrid concrete beam-column connections with composite beams and cast-in-place columns. ACI Structural Journal 2014;111:617-27.
- [86] Priestley MN, Seible F, and Calvi GM. Seismic design and retrofit of bridges. 605 Third avenue, New York: John Wiley & Sons; 1996.
- [87] NZS 3101-06. Concrete structures standard - part 1: the design of concrete structures. New Zealand, Wellington: Standards New Zealand; 2006. p. 137.
- [88] BS EN 1998-1-04. Eurocode 8: design of structures for earthquake resistance - Part 1: general rules, seismic actions and rules for buildings. European Committee for Standardization; 2004. p. 112-3.
- [89] AIJ-2010. Standard for structural calculation of reinforced concrete structures. Tokyo, Japan: Architectural Institute of Japan; 2010. p. 179-82.
- [90] Hwang S-J, and Lee H-J. Strength prediction for discontinuity regions by softened strut-and-tie model. Journal of Structural Engineering 2002;128:1519-26.
- [91] Paul RG, and Melvin RR. Increased Joint Hoop Spacing in Type 2 Seismic Joints Using Fiber Reinforced Concrete. Structural Journal 1989;86.
- [92] Liu C. Seismic behaviour of beam-column joint subassemblies reinforced with steel fibres 2006.
- [93] Shafaei J, Hosseini A, and Marefat MS. Seismic retrofit of external RC beam-column joints by joint enlargement using prestressed steel angles. Engineering Structures 2014;81:265-88.

- [94] Kaya M, and Arslan AS. Analytical modeling of post-tensioned precast beam-to-column connections. *Materials & Design* 2009;30:3802-11.
- [95] Tran TM, and Hadi MNS. Shear strength model of reinforced-concrete exterior joint under cyclic loading. *Structures & Buildings* 2017;170:603-17.
- [96] Prabhakaran R, Razzaq Z, and Devara S. Load and resistance factor design (LRFD) approach for bolted joints in pultruded composites. *Compos Part B* 1996;27:351-60.
- [97] Hassan NK, Mohamedien MA, and Rizkalla SH. Finite element analysis of bolted connections for PFRP composites. *Composites Part B: Engineering* 1996;27:339-49.
- [98] Kaya M, and Arslan AS. Effect of stress levels applied to pre-stressing strands on post-tensioned beam-to-column connections. *The Structural Design of Tall and Special Buildings* 2012;21:682-98.
- [99] Nzabonimpa JD, Hong W-K, and Kim J. Experimental and non-linear numerical investigation of the novel detachable mechanical joints with laminated plates for composite precast beam-column joint. *Composite Structures* 2018;185:286-303.
- [100] Kitane Y, Aref AJ, and Lee GC. Static and fatigue testing of hybrid fiber-reinforced polymer-concrete bridge superstructure. *J Compos Constr* 2004;8:182-90.
- [101] Woodward R, and Williams F. Collapse of ynys-y-gwas bridge west glamorgan. *Proceedings of the Institution of Civil Engineers* 1988. p. 635-69.
- [102] Jiuru T, Chaobin H, Kaijian Y, and Yongcheng Y. Seismic behavior and shear strength of framed joint using steel-fiber reinforced concrete. *Journal of Structural Engineering* 1992;118:341-58.
- [103] Andre Filiatrault SP, and Jules H. Seismic Behavior of Steel-Fiber Reinforced Concrete Interior Beam-Column Joints. *Structural Journal*;92.
- [104] Oinam RM, Sahoo DR, and Sindhu R. Cyclic Response of Non-ductile RC Frame with Steel Fibers at Beam-Column Joints and Plastic Hinge Regions. *Journal of Earthquake Engineering* 2014;18:908-28.
- [105] Yoo D-Y, Shin H-O, Yang J-M, and Yoon Y-S. Material and bond properties of ultra high performance fiber reinforced concrete with micro steel fibers. *Composites Part B: Engineering* 2014;58:122-33.
- [106] Meda A, Minelli F, and Plizzari GA. Flexural behaviour of RC beams in fibre reinforced concrete. *Composites Part B: Engineering* 2012;43:2930-7.
- [107] Olivito RS, and Zuccarello FA. An experimental study on the tensile strength of steel fiber reinforced concrete. *Composites Part B: Engineering* 2010;41:246-55.
- [108] McIntyre J. *Synthetic Fibres: Nylon, Polyester, Acrylic, Polyolefin*: Elsevier; 2004.
- [109] Company T. Technical data sheet. Australia 2018.
- [110] Alavi-Dehkordi S, Mostofinejad D, and Alaei P. Effects of high-strength reinforcing bars and concrete on seismic behavior of RC beam-column joints. *Engineering Structures* 2019;183:702-19.
- [111] Ozturan T, Ozden S, and Ertas O. Ductile connections in precast concrete moment resisting frames. *concrete construction* 2006;9:11.
- [112] Turmo J, Ramos G, and Aparicio AC. Shear behavior of unbonded post-tensioned segmental beams with dry joints. *ACI Materials Journal* 2006;103:409.
- [113] Khan MZN, Shaikh FuA, Hao Y, and Hao H. Synthesis of high strength ambient cured geopolymer composite by using low calcium fly ash. *Construction and Building Materials* 2016;125:809-20.
- [114] Khan MZN, Hao Y, Hao H, and Shaikh FUA. Mechanical properties of ambient cured high strength hybrid steel and synthetic fibers reinforced geopolymer composites. *Cement and Concrete Composites* 2018;85:133-52.

- [115] Ding Y, Dai J-G, and Shi C-J. Mechanical properties of alkali-activated concrete: A state-of-the-art review. *Construction and Building Materials* 2016;127:68-79.
- [116] Noushini A, Aslani F, Castel A, Gilbert RI, Uy B, and Foster S. Compressive stress-strain model for low-calcium fly ash-based geopolymer and heat-cured Portland cement concrete. *Cement and Concrete Composites* 2016;73:136-46.
- [117] Thomas RJ, and Peethamparan S. Alkali-activated concrete: engineering properties and stress-strain behavior. *Construction and Building Materials* 2015;93:49-56.
- [118] Maranan GB, Manalo AC, Benmokrane B, Karunasena W, and Mendis P. Evaluation of the flexural strength and serviceability of geopolymer concrete beams reinforced with glass-fibre-reinforced polymer (GFRP) bars. *Engineering Structures* 2015;101:529-41.
- [119] Brooke N, Keyte L, South W, Megget L, and Ingham J. Seismic performance of green concrete interior beam-column joints. *Australian Structural Engineering Conference: Engineers Australia*; 2005. p. 982.
- [120] Datta M, and Premkumar G. Comparative study of geopolymer concrete with steel fibers in beam column joint. *IAEME Journals* 2018;9:234-47.
- [121] Raj SD, Ganesan N, Abraham R, and Raju A. Behavior of geopolymer and conventional concrete beam column joints under reverse cyclic loading. *Advances in Concrete Construction* 2016;4:161-72.
- [122] Saranya P, Nagarajan P, and Shashikala AP. Behaviour of GGBS-dolomite geopolymer concrete beam-column joints under monotonic loading. *Structures* 2020;25:47-55.
- [123] Mukherjee A, and Joshi M. FRPC reinforced concrete beam-column joints under cyclic excitation. *Composite structures* 2005;70:185-99.
- [124] Tran TT, Pham TM, and Hao H. Experimental and analytical investigation on flexural behaviour of ambient cured geopolymer concrete beams reinforced with steel fibers. *Engineering Structures* 2019;200:109707.
- [125] Chem-supply Pty Ltd. <https://www.chemsupply.com.au/>. Australia2020.
- [126] PQ-Australia Pty Ltd. <https://www.pqcorp.com/>. Australia2020.
- [127] Mahini SS, and Ronagh HR. Web-bonded FRPs for relocation of plastic hinges away from the column face in exterior RC joints. *Composite Structures* 2011;93:2460-72.
- [128] Hasaballa M, and El-Salakawy E. Shear capacity of exterior beam-column joints reinforced with GFRP bars and stirrups. *Journal of Composites for Construction* 2015;20:04015047.
- [129] Rahman R, Dirar S, Jemaa Y, Theofanous M, and Elshafie M. Experimental behavior and design of exterior reinforced concrete beam-column joints strengthened with embedded bars. *Journal of Composites for Construction* 2018;22:04018047.
- [130] Grassl P, Wong HS, and Buenfeld NR. Influence of aggregate size and volume fraction on shrinkage induced micro-cracking of concrete and mortar. *Cement and Concrete Research* 2010;40:85-93.
- [131] ACI 374.1-05. Acceptance criteria for moment frames based on structural testing and commentary. ACI 3741-05. Farmington Hills, MI: ACI (American Concrete Institute); 2005. p. 9.
- [132] Karayannis CG. Mechanics of external RC beam-column joints with rectangular spiral shear reinforcement: experimental verification. *Meccanica* 2015;50:311-22.

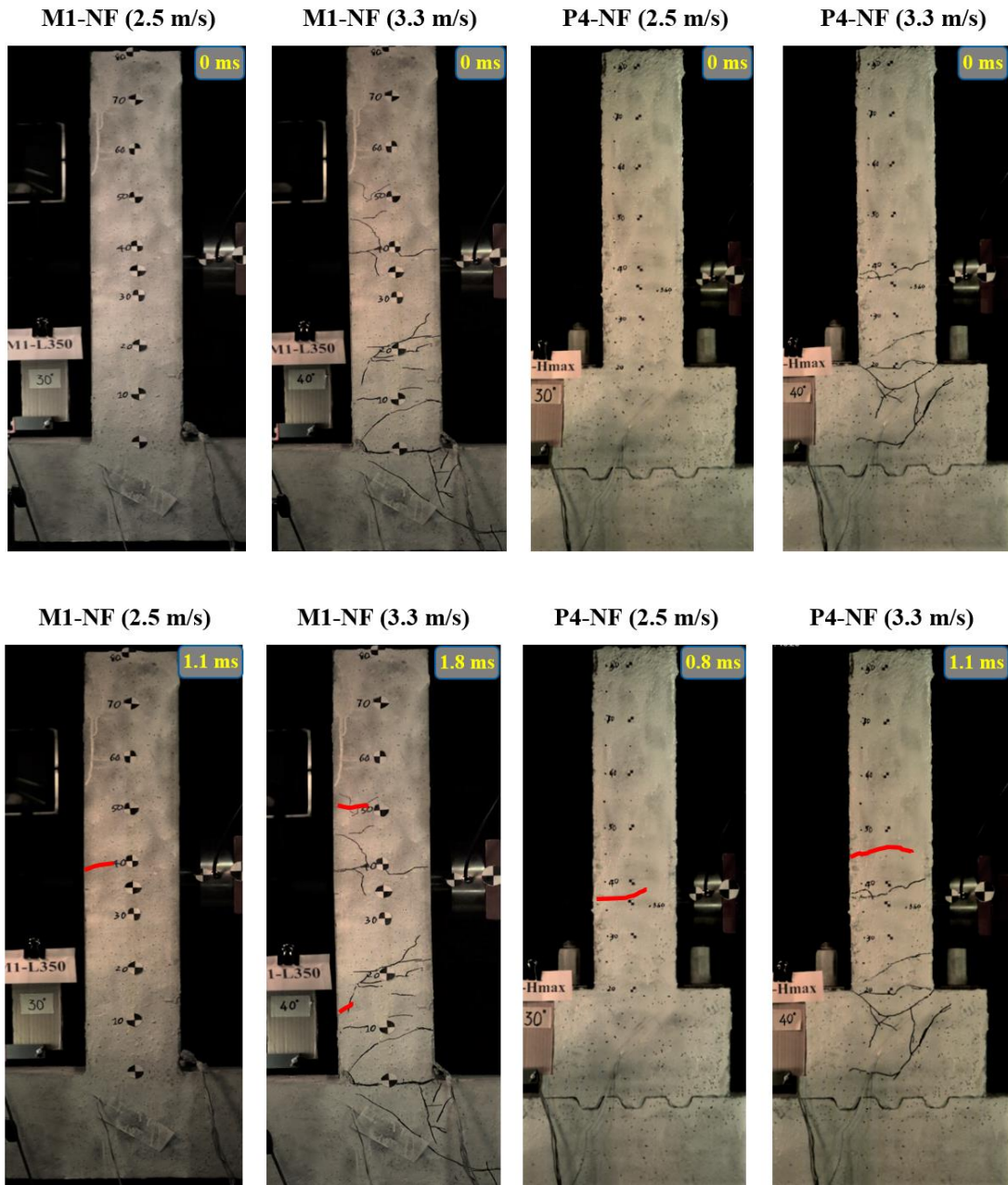
- [133] Hadi MNS, and Tran TM. Retrofitting nonseismically detailed exterior beam–column joints using concrete covers together with CFRP jacket. *Construction and Building Materials* 2014;63:161-73.
- [134] Ghomi SK, and El-Salakawy E. Effect of joint shear stress on seismic behaviour of interior GFRP-RC beam-column joints. *Engineering Structures* 2019;191:583-97.
- [135] Amr AA, and Sami HR. Serviceability of Concrete Beams Prestressed by Carbon-Fiber-Reinforced-Plastic Bars. *ACI Structural Journal* 1997;94.
- [136] Maddah A, Golafshar A, and Saghafi MH. 3D RC beam–column joints retrofitted by joint enlargement using steel angles and post-tensioned bolts. *Engineering Structures* 2020;220:110975.
- [137] Alver N, Selman ME, and Akgun OB. The effect of short cantilever beam formation on the structural behavior of precast post-tensioned connections. *Construction and Building Materials* 2012;35:232-9.
- [138] Guan D, Yang H, Ju D, Guo Z, and Yang S. Cyclic loading test on a locally post-tensioned precast concrete beam–column connection. *Advances in Structural Engineering* 2019;22:2699-711.
- [139] Wang H, Marino EM, Pan P, Liu H, and Nie X. Experimental study of a novel precast prestressed reinforced concrete beam-to-column joint. *Engineering Structures* 2018;156:68-81.
- [140] Yan X, Wang S, Huang C, Qi A, and Hong C. Experimental study of a new precast prestressed concrete joint. *Applied Sciences* 2018;8:1871.
- [141] Hao H, Ngo TT, and Pham TM. Performance of dry exterior beam-column joints using CFRP bolts and SFRC under cyclic loading. *Australian Earthquake Engineering Society 2019 Conference*. Newcastle, NSW, Australia 2019.
- [142] Alae P, and Li B. Analytical Investigations of Reinforced Concrete Beam–Column Joints Constructed Using High-Strength Materials. *Journal of Earthquake Engineering* 2020;24:774-802.
- [143] Kulkarni SA, Li B, and Yip WK. Finite element analysis of precast hybrid-steel concrete connections under cyclic loading. *Journal of Constructional Steel Research* 2008;64:190-201.
- [144] Li B, Kulkarni SA, and Leong CL. Seismic Performance of Precast Hybrid-Steel Concrete Connections. *Journal of Earthquake Engineering* 2009;13:667-89.
- [145] Feng D-C, Ren X-D, and Li J. Softened damage-plasticity model for analysis of cracked reinforced concrete structures. *Journal of Structural Engineering* 2018;144:04018044.
- [146] Feng D-C, Ren X-D, and Li J. Cyclic behavior modeling of reinforced concrete shear walls based on softened damage-plasticity model. *Engineering Structures* 2018;166:363-75.
- [147] Abu Tahnat YB, Dwaikat MMS, and Samaaneh MA. Effect of using CFRP wraps on the strength and ductility behaviors of exterior reinforced concrete joint. *Composite Structures* 2018;201:721-39.
- [148] Dabiri H, Kaviani A, and Kheyroddin A. Influence of reinforcement on the performance of non-seismically detailed RC beam-column joints. *Journal of Building Engineering* 2020;31:101333.
- [149] Boral Pty Ltd. <https://www.boral.com.au/>. Australia 2020.
- [150] Bluey Pty Ltd. <https://www.bluey.com.au/category/blugeo>. 2020.
- [151] Pultrall Inc. <https://www.fiberglassrebar.com/>. Canada 2020.
- [152] ACI 440.1R-15. Guide for the design and construction of structural concrete reinforced with FRP bars. ACI 4401R-06: American Concrete Institute; 2015.

- [153] Lubliner J, Oliver J, Oller S, and Oñate E. A plastic-damage model for concrete. *International Journal of Solids and Structures* 1989;25:299-326.
- [154] Li C, Hao H, and Bi K. Numerical study on the seismic performance of precast segmental concrete columns under cyclic loading. *Engineering Structures* 2017;148:373-86.
- [155] Feng D-C, Wu G, Sun Z-Y, and Xu J-G. A flexure-shear Timoshenko fiber beam element based on softened damage-plasticity model. *Engineering Structures* 2017;140:483-97.
- [156] Li J, and Ren X. Stochastic damage model for concrete based on energy equivalent strain. *International Journal of Solids and Structures* 2009;46:2407-19.
- [157] Wu JY, Li J, and Faria R. An energy release rate-based plastic-damage model for concrete. *International Journal of Solids and Structures* 2006;43:583-612.
- [158] Feng D, and Li J. Stochastic nonlinear behavior of reinforced concrete frames. II: Numerical simulation. *Journal of Structural Engineering* 2016;142:04015163.
- [159] Faria R, Oliver J, and Cervera M. A strain-based plastic viscous-damage model for massive concrete structures. *International Journal of Solids and Structures* 1998;35:1533-58.
- [160] Wu J. Damage energy release rate-based elastoplastic damage constitutive model for concrete and its application to nonlinear analysis of structures [Ph.D. thesis]. Shanghai: Tongji University; 2004.
- [161] Faleschini F, Bragolusi P, Zanini MA, Zampieri P, and Pellegrino C. Experimental and numerical investigation on the cyclic behavior of RC beam column joints with EAF slag concrete. *Engineering Structures* 2017;152:335-47.
- [162] Cotsovos DM. A simplified approach for assessing the load-carrying capacity of reinforced concrete beams under concentrated load applied at high rates. *International Journal of Impact Engineering* 2010;37:907-17.
- [163] Pham TM, Hao Y, and Hao H. Sensitivity of impact behaviour of RC beams to contact stiffness. *International Journal of Impact Engineering* 2018;112:155-64.
- [164] Hao H. Predictions of structural response to dynamic loads of different loading rates. *International Journal of Protective Structures* 2015;6:585-605.
- [165] Li H, Chen W, and Hao H. Influence of drop weight geometry and interlayer on impact behavior of RC beams. *International Journal of Impact Engineering* 2019;131:222-37.
- [166] Sha Y, and Hao H. Laboratory tests and numerical simulations of barge impact on circular reinforced concrete piers. *Engineering Structures* 2013;46:593-605.
- [167] Do TV, Pham TM, and Hao H. Numerical investigation of the behavior of precast concrete segmental columns subjected to vehicle collision. *Engineering Structures* 2018;156:375-93.
- [168] Do TV, Pham TM, and Hao H. Dynamic responses and failure modes of bridge columns under vehicle collision. *Engineering Structures* 2018;156:243-59.
- [169] Do TV, Pham TM, and Hao H. Effects of steel confinement and shear keys on the impact responses of precast concrete segmental columns. *Journal of Constructional Steel Research* 2019;158:331-49.
- [170] Pham TM, Zhang X, Elchalakani M, Karrech A, Hao H, and Ryan A. Dynamic response of rubberized concrete columns with and without FRP confinement subjected to lateral impact. *Construction and Building Materials* 2018;186:207-18.
- [171] Krauthammer T. *Modern protective structures*: CRC Press; 2008.
- [172] BarChip Pty Ltd. <https://barchip.com/product/>. Australia2020.
- [173] BOSFA Pty Ltd. <https://bosfa.com/products/dramix-5d-4d-3d/>. 2020.

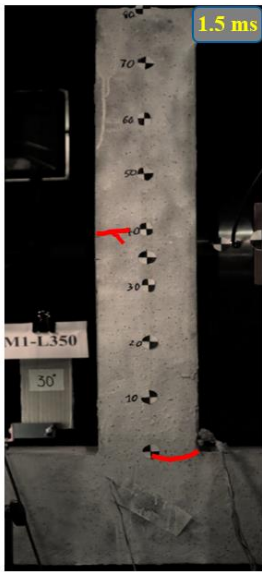
- [174] Hwang S-J, and Lee H-J. Analytical Model for Predicting Shear Strengths of Exterior Reinforced Concrete Beam-Column Joints for Sesimic Resistance. *ACI Structural Journal* 1999;96:846-57.
- [175] Pham TM, and Hao H. Influence of global stiffness and equivalent model on prediction of impact response of RC beams. *International Journal of Impact Engineering* 2018;113:88-97.
- [176] Sha Y, and Hao H. Nonlinear finite element analysis of barge collision with a single bridge pier. *Engineering Structures* 2012;41:63-76.
- [177] Tran TT, Pham TM, Huang Z, Chen W, Hao H, and Elchalakani M. Impact response of fibre reinforced geopolymer concrete beams with BFRP bars and stirrups. (Under review) 2020.

APPENDIX I: FIGURES IN CHAPTER 6

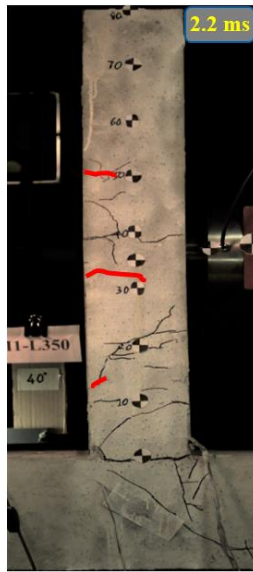
See Figs. 6-A1, 6-A2, and 6-A3.



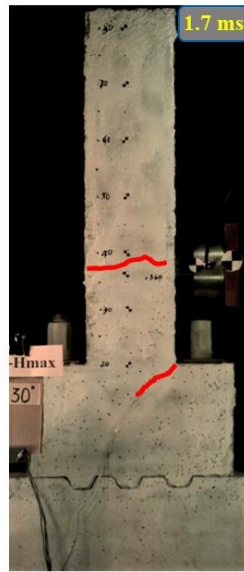
M1-NF (2.5 m/s)



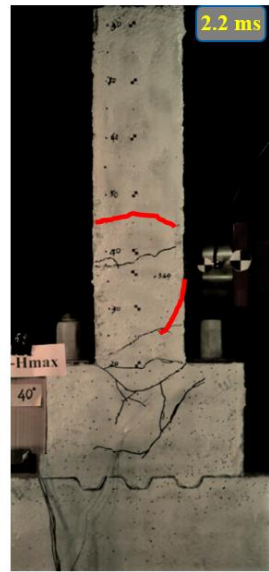
M1-NF (3.3 m/s)



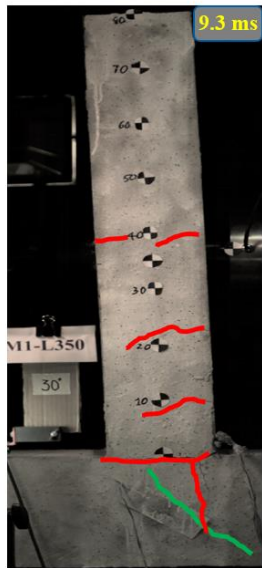
P4-NF (2.5 m/s)



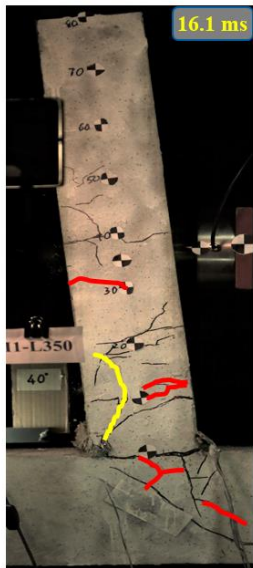
P4-NF (3.3 m/s)



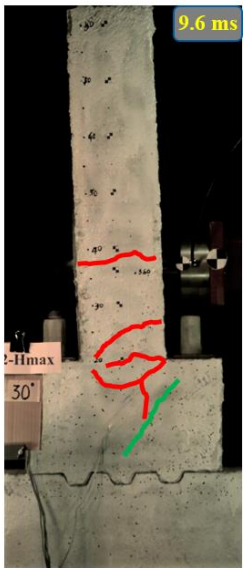
M1-NF (2.5 m/s)



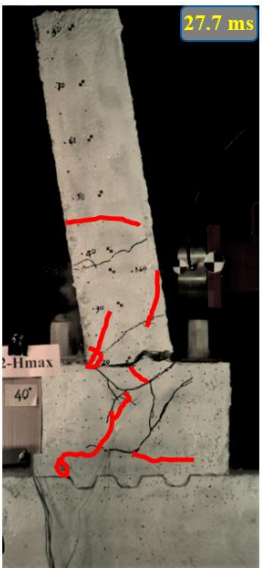
M1-NF (3.3 m/s)

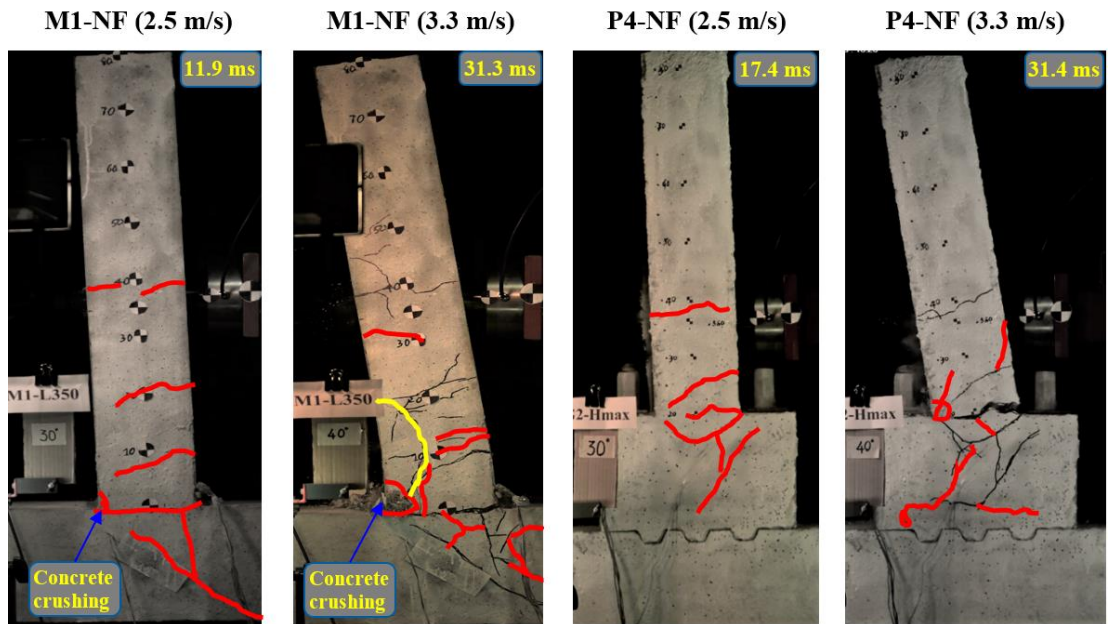


P4-NF (2.5 m/s)



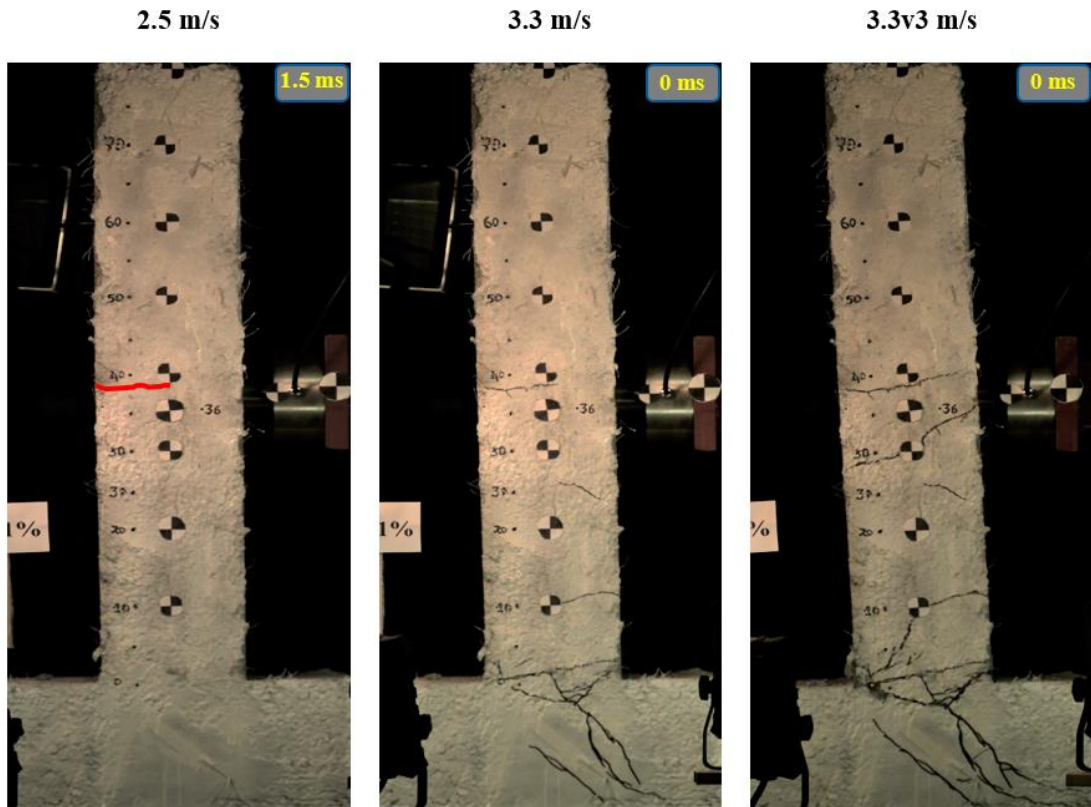
P4-NF (3.3 m/s)





Note: Highlighted lines at 3.3 m/s indicated new cracks occurred at this impact which did not appear under 2.5 m/s impact

Fig. 6-A1. Crack development of Specimens M1-NF and P4-NF at 2.5 m/s and 3.3 m/s.



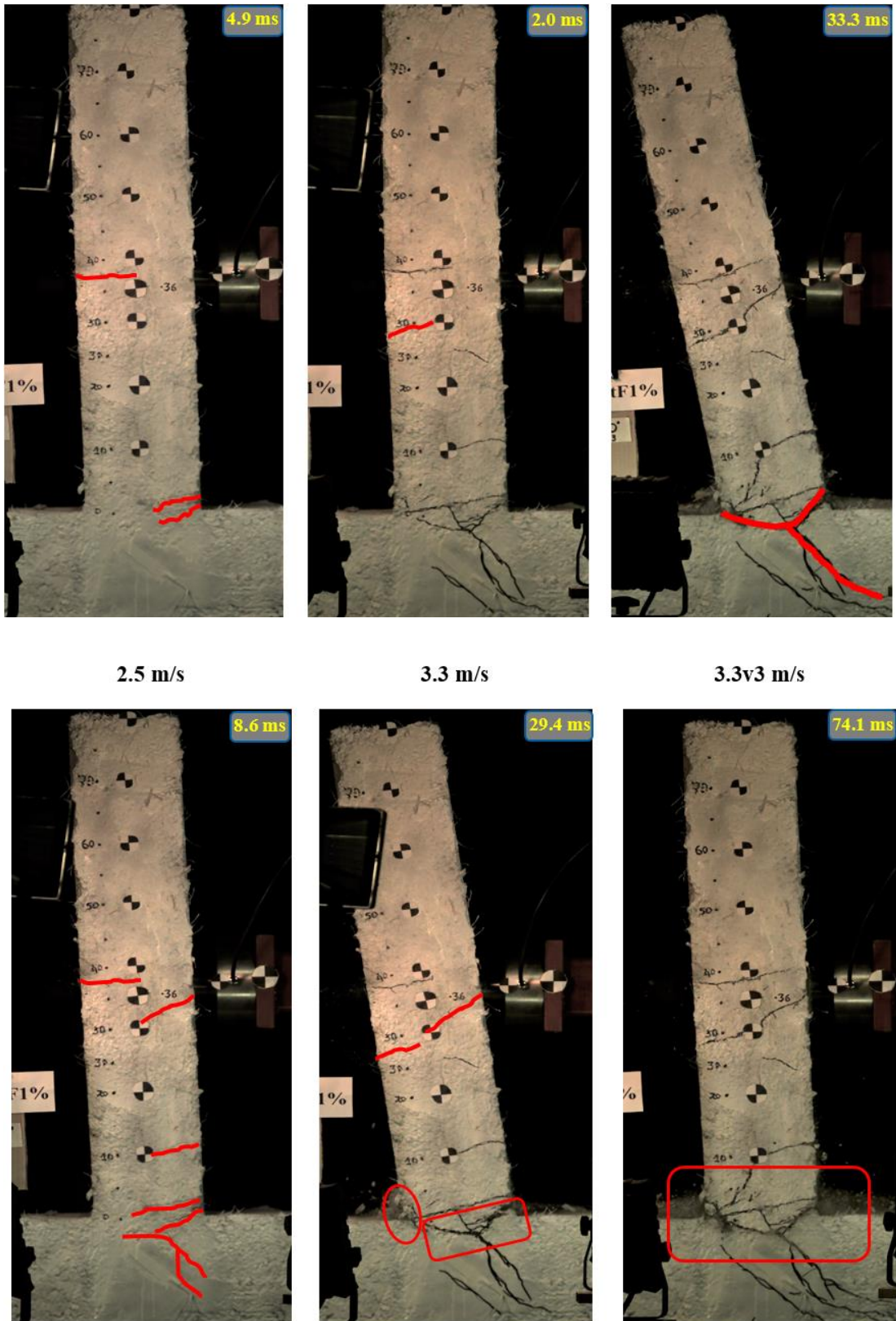
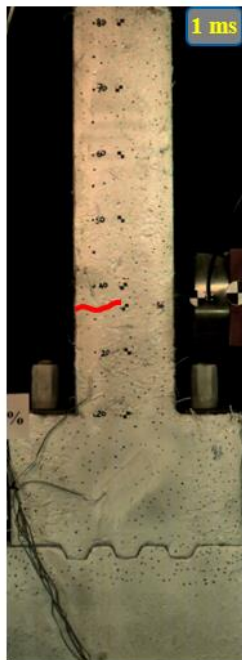


Fig. 6-A2. Crack development of Specimen M3-1StF-35.

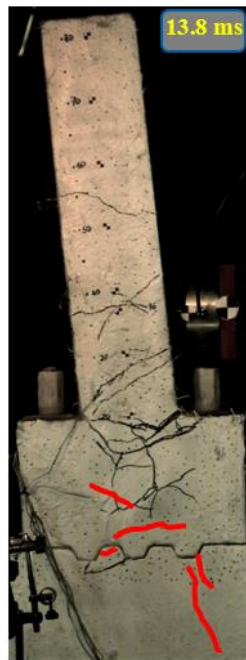
P5-1SyF-48
(2.5 m/s)



P5-1SyF-48
(3.3 m/s)



P5-1SyF-48
(4.0 m/s)



P6-1StF-35
(2.5 m/s)



P6-1StF-35
(3.3 m/s)



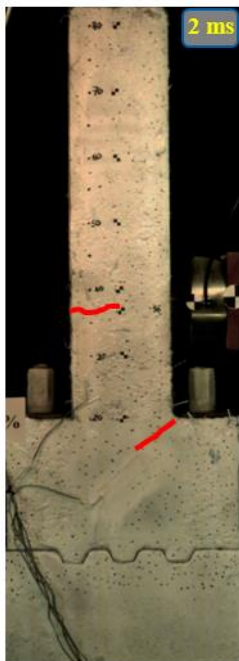
P6-1StF-35
(4.0 m/s)



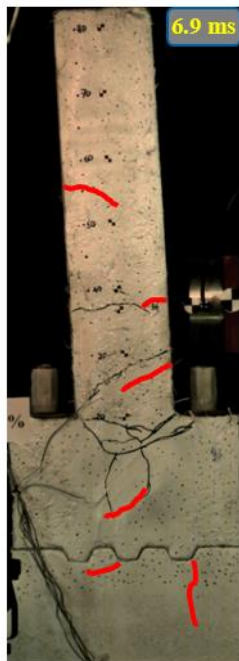
P6-1StF-35
(4.0v2 m/s)



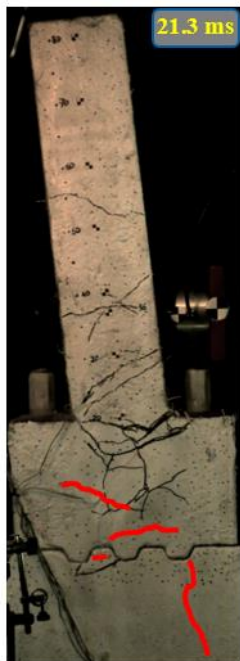
P5-1SyF-48
(2.5 m/s)



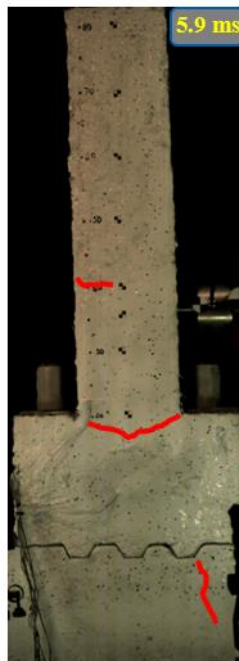
P5-1SyF-48
(3.3 m/s)



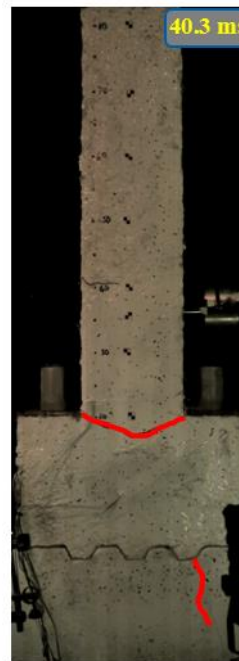
P5-1SyF-48
(4.0 m/s)



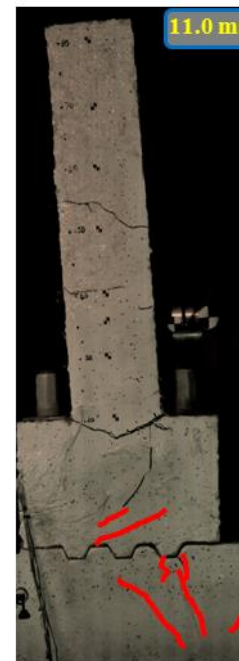
P6-1StF-35
(2.5 m/s)



P6-1StF-35
(3.3 m/s)



P6-1StF-35
(4.0 m/s)



P6-1StF-35
(4.0v2 m/s)



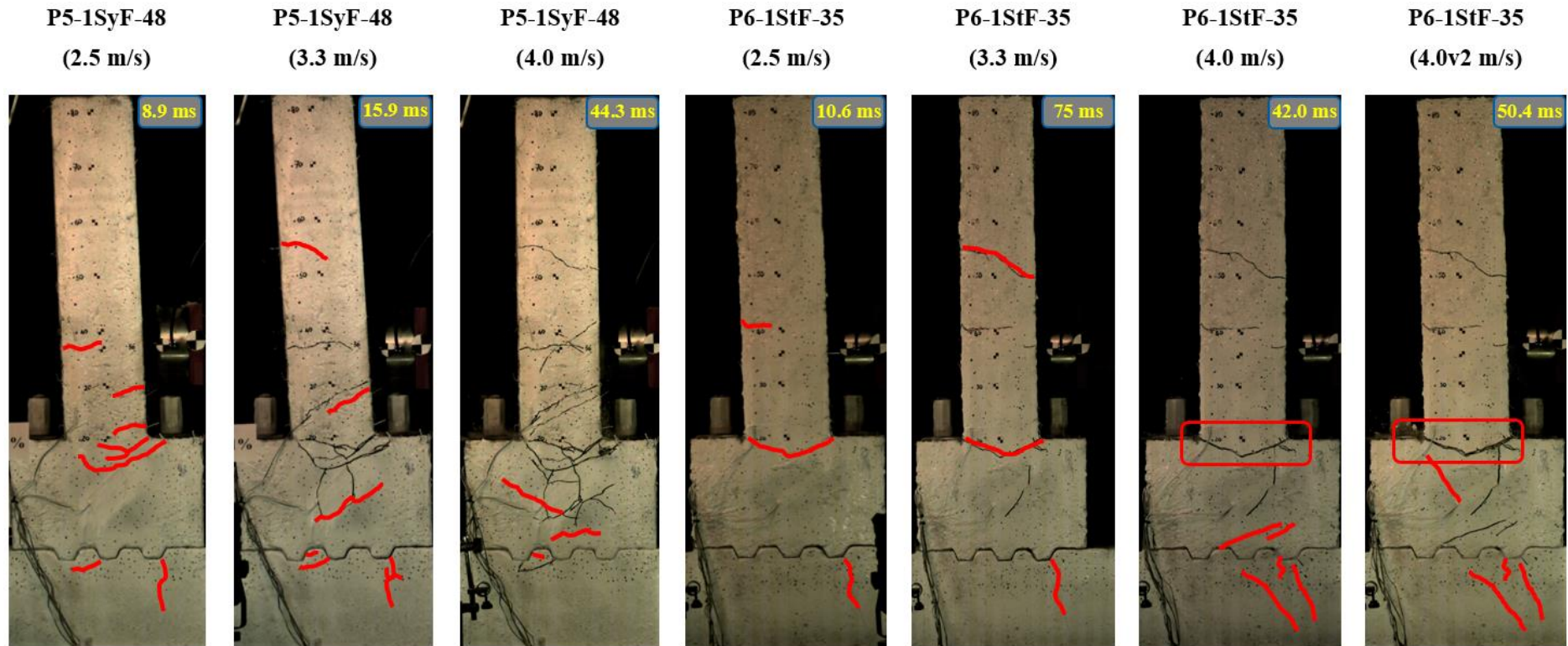


Fig. 6-A3. Crack development of Specimens P5-1SyF-48 and P6-1StF-35.

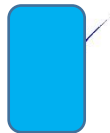
APPENDIX II: STATEMENTS OF CONTRIBUTION OF CO-AUTHORS

To whom it may concern,

I, Tang Tuan Ngo, conducted experiments, numerical and analytical investigations, data processing and analysis, and wrote the manuscripts of the papers listed below, which were reviewed and edited by the co-authors. They also provided support on experimental preparation, data processing and data analysis.

- 1. Ductile and dry exterior joints using CFRP bolts for moment-resisting frames.**
- 2. Effects of steel fibres and prestress levels on behaviour of newly proposed exterior dry joints using SFRC and CFRP bolts.**
- 3. Performance of geopolymer concrete in monolithic and non-corrosive dry joints using CFRP bolts under cyclic loading.**
- 4. Experiment and numerical study on newly proposed dry and hybrid concrete joints with GFRP bolts and GFRP reinforcements under cyclic loading.**
- 5. Performance of monolithic and dry joints with GFRP bolts reinforced with different fibres and GFRP bars under impact loading.**

Tang Tuan Ngo



I, as a co-author, endorse that this level of contribution by the candidate indicated above is appropriate.

Dr. Thong M. Pham



Prof. Hong Hao



Dr. Wensu Chen



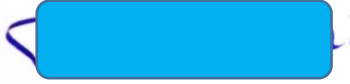
Dr. Thanh Tung Tran



Dr. Ngoc San Ha



Dr. Mohamed Elchalakani



APPENDIX III: COPYRIGHT CLEARANCE

The proof of the rights, granted by publishers for the publication that forms the chapters of this thesis are attached below.

Ngo TT, Pham TM, Hao H. Ductile and dry exterior joints using CFRP bolts for moment-resisting frames. Structures 2020;28:668-84.

<https://doi.org/10.1016/j.istruc.2020.09.020>

The screenshot shows the RightsLink interface for the article "Ductile and dry exterior joints using CFRP bolts for moment-resisting frames". It includes the Elsevier logo, author information (Tuan T. Ngo, Thong M. Pham, Hong Hao), publication details (Structures, Elsevier, December 2020), and a "Journal Author Rights" section with a disclaimer and navigation buttons.

Ngo TT, Pham TM, Hao H. Effects of steel fibres and prestress levels on behaviour of newly proposed exterior dry joints using SFRC and CFRP bolts. Eng Struct 2020;205:110083.

<https://doi.org/10.1016/j.engstruct.2019.110083>

The screenshot shows the RightsLink interface for the article "Effects of steel fibres and prestress levels on behaviour of newly proposed exterior dry joints using SFRC and CFRP bolts". It includes the Elsevier logo, author information (Tuan T. Ngo, Thong M. Pham, Hong Hao), publication details (Engineering Structures, Elsevier, 15 February 2020), and a "Journal Author Rights" section with a disclaimer and navigation buttons.

Ngo TT, Tran TT, Pham TM, Hao H. Performance of geopolymer concrete in monolithic and non-corrosive dry joints using CFRP bolts under cyclic loading. Compos Struct 2020:113394.

<https://doi.org/10.1016/j.compstruct.2020.113394>

**Performance of geopolymer concrete in monolithic and non-corrosive dry joints using CFRP bolts under cyclic loading**

Author: Tuan T. Ngo, Tung T. Tran, Thong M. Pham, Hong Hao

Publication: Composite Structures

Publisher: Elsevier

Date: 15 February 2021

© 2020 Elsevier Ltd. All rights reserved.

Journal Author Rights

Please note that, as the author of this Elsevier article, you retain the right to include it in a thesis or dissertation, provided it is not published commercially. Permission is not required, but please ensure that you reference the journal as the original source. For more information on this and on your other retained rights, please visit: <https://www.elsevier.com/about/our-business/policies/copyright#Author-rights>

[BACK](#)[CLOSE WINDOW](#)

Ngo, TT, Pham TM, Hao H, Chen W, Elchalakani M. Performance of monolithic and dry joints with GFRP bolts reinforced with different fibres and GFRP bars under impact loading. Eng. Struct 2021;240:112341.

<https://doi.org/10.1016/j.engstruct.2021.112341>

**Performance of monolithic and dry joints with GFRP bolts reinforced with different fibres and GFRP bars under impact loading**

Author: Tuan T. Ngo, Thong M. Pham, Hong Hao, Wensu Chen, Mohamed Elchalakani

Publication: Engineering Structures

Publisher: Elsevier

Date: 1 August 2021

© 2021 Elsevier Ltd. All rights reserved.

Journal Author Rights

Please note that, as the author of this Elsevier article, you retain the right to include it in a thesis or dissertation, provided it is not published commercially. Permission is not required, but please ensure that you reference the journal as the original source. For more information on this and on your other retained rights, please visit: <https://www.elsevier.com/about/our-business/policies/copyright#Author-rights>

[BACK](#)[CLOSE WINDOW](#)

BIBLIOGRAPHY DISCLAIMER

Every reasonable effort has been made to acknowledge the owners of copyright material. I would be pleased to hear from any copyright owner who has been omitted or incorrectly acknowledged.